BAND ALIGNMENTS AND INTERFACES IN ANTIMONY SELENIDE SOLAR CELLS

By

HUW SHIEL

A thesis submitted in fulfilment of
the requirements for the degree of

DOCTOR OF PHILOSOPHY

UNIVERSITY OF LIVERPOOL
Department of Physics

OCTOBER 2021

ACKNOWLEDGMENT

There is no way I could have completed this PhD without the constant support and friendship of those I worked with and all my friends and family. I feel very fortunate to have worked at the Stephenson Institute which is such a remarkably welcoming and sociable workplace as well as being full of fantastic scientists that have been a pleasure to work with.

First of all, I would not have got anywhere without my excellent supervisory team. I would like to thank Tim Veal for always being available to answer my questions, proof read anything from a slightly stressful email to an entire thesis and for providing me with a wealth of invaluable advice on all sorts of topics beyond just clearing up my understanding of science. I would also like to thank Jon Major, first of all for convincing me to apply for the PhD, and then for being a constant source of knowledge and guidance on all things PV throughout the last few years, as well as occasionally helping us out in football games (own goals aside). I would also like to thank Vin Dhanak for all his help with all things XPS.

Beyond my three supervisors I feel I've also been able to rely on and learn from every single one of my colleagues over the last few years as well as being lucky enough to call them my friends. Special thanks have to go to Oliver Hutter, Laurie Phillips and Theo Hobson for supplying me with all the antimony selenide I needed as well as sharing all their knowledge, scientific and otherwise. A massive thank you also goes to the Lab 4 dream team of Jack Swallow, Leanne Jones and Holly Edwards for all their help and for somehow keeping that place running all these years. The same goes to Vince Vasey, who was often our saviour when the labs started falling apart. I'd also like to acknowledge our collaborators at University College London and at Diamond Light Source that made much of this work possible, and NSG for providing funding and access to their equipment. Thanks also to the rest of my group and to all the other people who helped bring this work together - Nicole Fleck, Tom Featherstone, Matt Smiles, Phil Murgatroyd and Chris Don - this achievement belongs to all of you as well.

I would like to thank Pete, Silvia , Baines, Jack and Shalvey for making me feel at home straight away when I joined their office and also Matt, Luke, Jacob and Manuel for making sure it was still the funnest office (if not the most productive) to the end. Thank you also goes to Leanne for improving my Welsh and for teaching me some fun new phrases. Thanks to Luke for his excellent service as SIRE FC captain and PV meme maker, and to Shalvey for always having some reassuring words and for the many many

pints I owe him. Thank you to Theo for being an inspiration as well as an endless fountain of knowledge, and to Tom and Beaney for regularly reducing me to tears with laughter. Thank you to Bruna for always listening to my complaining and to Matt and Dan (the Birstall Boys) for keeping me sane and laughing through Lockdown 1. And a particular thank you to Nicole, for always understanding and for being my best friend throughout - words don't do it justice so suffice to say that I couldn't have done any of it without you. I would also like to thank Jacob, Alex, Scarlett, Julia, Oliver, Holly, Phil, Joe, Oliva and Kieran and everyone else who was there for the many many coffee breaks and AJ trips.

Finally I would like to thank my parents, Meinir and David, and my siblings, Elen and Owen whose love and support has allowed to me be where I am today. I would also like to thank my Liverpool family, Rich and Georgia (and Tarot and Henwen) for always being there for me with all the support and encouragement a person could need. I move on from this stage in my life with so much more than a thesis - with great friends, new perspectives, cherished memories, terrible jokes and hilarious stories. To every single one of you that made these years such an incredible experience, thank you.

ABSTRACT

This thesis explores the effect of band alignments, interfaces and electronic properties on the performance of antimony selenide (Sb_2Se_3) solar cells. It examines both the heterojunction and the back contact band alignments in photovoltaics devices, as well as the fundamental electronic properties of bulk crystals.

The band alignment between Sb_2Se_3 and both CdS and TiO_2 is measured using two methods. Natural band alignments are measured using x-ray photoemission spectroscopy (XPS) and then aligned using Anderson's rule to obtain the band offsets. This yielded spike-like conduction band offsets of 0.36 eV and 0.11 eV for CdS and TiO_2 respectively. Using the Kraut method, the band offsets were directly measured using hard x-ray photoemission spectroscopy (HAXPES). This gave a similar result for CdS of -0.01 eV but a significantly cliff-like offset of -0.82 eV for TiO_2.

The valence band (VB) spectra of bulk crystals, both as-received and *in situ* cleaved are measured using XPS and HAXPES. The difference in orbital photoionisation cross-section with incident photon energy is used to compare density functional theory calculated density of states (DOS) to the different spectra and experimentally observe partial DOS from an Sb $5s^2$ lone pair of electrons at the VB edge for the first time. The impact of this lone pair is shown to be a reduction in the ionisation potential, which has implications for the band alignments of Sb_2Se_3 with other materials.

Using ultraviolet photoemission spectroscopy (UPS), XPS and HAXPES, a depth profile of the VB-Fermi level energy separation is obtained for Cl- and Sn-doped Sb_2Se_3 bulk crystals. A solution to Poisson's equation for surface space charge layers is then found to fit this depth profile. This provides evidence of strong n-type doping ($\sim 10^{17}$-10^{18} cm^{-3}) and electron depletion in the Cl-doped crystal. The Sn-doped crystal exhibits weak p-type doping ($\sim 10^{16}$-10^{17} cm^{-3}) and a weak inversion layer.

The effects of two chemical etches, $(NH_4)_2S$ and CS_2, on the surface chemistry and back contact performance of Sb_2Se_3 are investigated. Measurements of the back contact barrier show a reduced barrier but device performance parameters show lower efficiencies after etching. XPS analysis shows removal of antimony oxide (Sb_2O_3) contamination with both etches but no reduction in elemental Se. It is concluded that the etches are beneficial for thick layers of contamination but that aggressive etching is counterproductive on lightly contaminated films.

Finally, the band alignment between Sb_2Se_3 and the Sb_2O_3 is measured using two methods - the difference spectrum of an as received and *in situ* cleaved bulk crystal, and a Kraut method measurement between thin films of Sb_2Se_3 and Sb_2O_3. The result in both cases is a straddling alignment of -1.72 eV and -1.90 eV for the crystal and the thin films respectively.

GRAPHICAL ABSTRACT

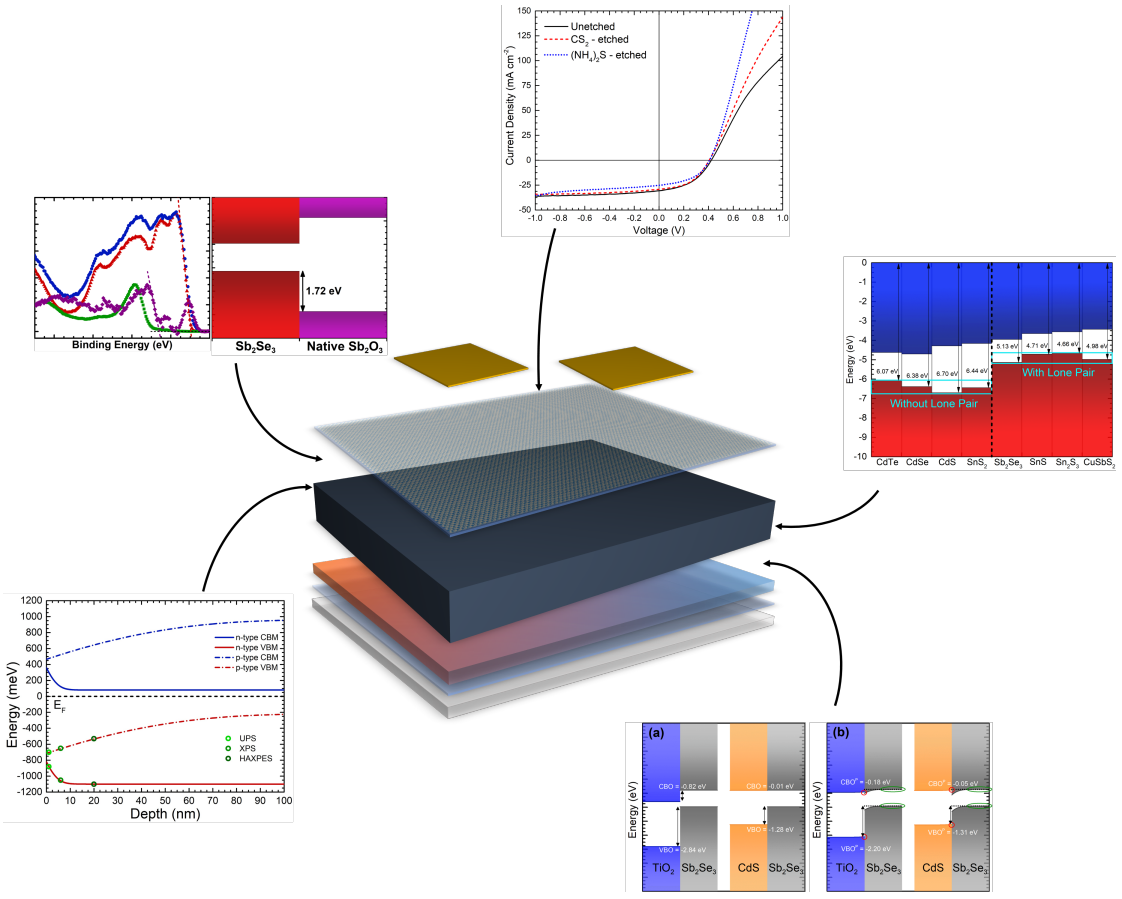

TABLE OF CONTENTS

Declaration

With the exceptions listed below, this thesis contains an account of my research carried out at the Stephenson Institute for Renewable Energy and Department of Physics, University of Liverpool between October 2017 and July 2021 under the supervision of Prof. Tim Veal, Dr. Jon Major and Prof. Vin Dhanak. Funding was provided by the EPSRC National Productivity Investment Fund and NSG Ltd. The research here has not been previously submitted, wholly or in part, for admission to a higher degree at this, or any other academic institution. Where collaborators have provided data, all analysis and interpretation is the work of the author.

- Thin film samples in Chapter 4 were deposited by **Dr. Oliver S. Hutter** and **Dr. Laurie J. Phillips**.
- HAXPES measurements for Chapters 4, 5 and 6 were collected by a team including the author, Huw Shiel, **Dr. Jack E. N. Swallow**, **Leanne A. H. Jones**, **Thomas J. Featherstone** and **Matthew J. Smiles**
- Bulk crystals in Chapters 5 and 6 were grown by **Dr. Theodore D. C. Hobson**
- DFT calculations in Chapter 5 were performed by **Dr. Christopher N. Savory**
- Thin films in Chapter 6 were deposited and etched by **Dr. Oliver S. Hutter** and **Dr. Laurie J. Phillips**
- XRD, J-V, J-V-T and EQE data and SEM micrographs in Chapter 6 were collected by **Dr. Oliver S. Hutter** and **Dr. Laurie J. Phillips**

Parts of this work are published in the following works:

- H. Shiel *et al.*, "Natural band alignments and band offsets in Sb_2Se_3 solar cells", *ACS Applied Energy Materials* **3**, 12 (2020); DOI:10.1021/acsaem.0c01477
- C. H. Don & H. Shiel *et al.*, "Sb $5s^2$ lone pairs and band alignments of antimony selenide: a photoemission and density functional theory study", *Journal of Materials Chemistry C* **8**, 36, (2020); DOI:10.1039/D0TC03470C

- H. Shiel & O. S. Hutter *et al.*, "Chemical etching of Sb_2Se_3 solar cells: surface chemistry and back contact behaviour", *Journal of Physics: Energy*, **1**, 4 (2019); DOI:10.1088/2515-7655/ab3c98

- H. Shiel *et al.*, "Band alignment of Sb_2O_3 and Sb_2Se_3", *Journal of Applied Physics **129**, 235301 (2021); DOI: 10.1063/5.0055366*

Other publications arising from work carried out during the course of this project include:

- L. J. Phillips *et al.*, "Current enhancement via a TiO_2 window layer for CSS Sb_2Se_3 solar cells: Performance Limits and High V_oc", *IEEE Journal of Photovoltaics* **9**, 2 (2018); DOI:10.1109/JPHOTOV.2018.2885836

- T. D. C. Hobson *et al.*, "Isotype heterojunction solar cells using n-type Sb_2Se_3 thin films", *Chemistry of Materials* **32**, 6 (2020); DOI:10.1021/acs.chemmater.0c00223

- N. Fleck, O. S. Hutter and L. J. Phillips *et al.* "How oxygen exposure improves the back contact and performance of antimony selenide solar cells", *ACS Applied Materials & Interfaces* **12**, 47 (2020); DOI:10.1021/acsami.0c14256

- B. A. D. Williamson and T. J. Featherstone *et al.* "Resonant Ta doping for enhanced mobility in transparent conducting SnO_2", *Chemistry of Materials* **32**, 5 (2020); DOI:10.1021/acs.chemmater.9b04845

- L. A. H. Jones *et al.* "Sn $5s^2$ lone pairs and the electronic structure of tin sulphides: A photoreflectance, high-energy photoemission, and theoretical investigation", *Physical Review Materials* **4**, 7 (2020); DOI:10.1103/PhysRevMaterials.4.074602

- E. Artegiani *et al.* "Analysis of a novel $CuCl_2$ back contact process for improved stability in CdTe solar cells", *Progress in Photovoltaics: Research and Applications* **27**, 8 (2019); DOI:10.1002/pip.3148

- E. Artegiani *et al.*, "How the amount of copper influences the formation and stability of defects in CdTe solar cells", *Solar Energy Materials and Solar Cells* **204** (2020); DOI:10.1016/j.solmat.2019.110228

List of Abbreviations

$\mathbf{Sb_2Se_3}$	Antimony Selenide
PV	Photovoltaics
LCOE	Levelised Cost of Energy
$\mathbf{E}_g$	Band Gap
$\mathbf{E}_F$	Fermi Level
VBM/CBM	Valence/Conduction Band Maximum/Minimum
J-V	Current Density vs. Voltage
PCE	Power Conversion Efficiency
CdTe	Cadmium Telluride
CIGS	Copper Indium Gallium Selenide
$\mathbf{V}_{oc}$	Open-Circuit Voltage
$\mathbf{J}_{sc}$	Short-Circuit Current
FF	Fill Factor
$\mathbf{R}_s$	Series Resistance
$\mathbf{R}_{sh}$	Shunt Resistance
EQE	External Quantum Efficiency
TCO	Transparent Conducting Oxide
CdS	Cadmium Sulphide
IP	Ionisation Potential
EA	Electron Affinity
WF	Work Function
$\mathbf{E}_{VAC}$	Local Vacuum Level
$\mathbf{E}(\infty)$	Global Vacuum Level
VBO/CBO	Valence/Conduction Band Offset

EPBT	Energy Payback Time
PVD/CVD	Physical/Chemical Vapour Deposition
MAPI	Methyl-ammonium Lead Iodide
CZTS	Copper Zinc Tin Sulphide
OPV	Organic Photovoltaics
TE	Thermal Evaporation
CSS	Close Space Sublimation
RSC	Royal Society of Chemistry
VTD	Vapour Transport Deposition
SLME	Spectroscopic Limited Maximum Efficiency
DFT	Density Functional Theory
XRD	X-Ray Diffraction
RTE	Rapid Thermal Evaporation
RF	Radio Frequency
SEM/TEM	Scanning/Transmission Electron Microscopy
TiO_2	Titanium Dioxide
DLTS	Deep Level Transient Spectroscopy
QCM	Quartz Crystal Microbalance
UPS	Ultraviolet Photoemission Spectroscopy
XPS	X-ray Photoemission Spectroscopy
HAXPES	Hard X-ray Photoemission Spectroscopy
KE/BE	Kinetic/Binding Energy
$\boldsymbol{\phi_A/\phi_S}$	Analyser/Sample Work Function
IMFP	Inelastic Mean Free Path
UHV	Ultra-High Vacuum
SEC	Secondary Electron Cut-Off
FWHM	Full Width at Half Maximum
FTO	Fluorine-Doped Tin Oxide
EDX	Energy Dispersive X-ray
DOS	Density of States
CS_2	Carbon Disulphide

$\mathbf{(NH_4)_2S}$	Ammonium Sulphide
$\boldsymbol{\phi}_b$	Back Contact Barrier

Chapter One
Introduction

1.1 The Global Energy Crisis

In the last few years the global energy crisis has become a well established issue both in politics and in everyday society. The consumption of energy by the human race continues to grow year on year. Coupled with the energy industry's continued reliance on harmful fossil fuels this presents a problem that relatively few now deny. In 2019 total global energy consumption grew to 584 exajoules, and oil, gas and coal made up a combined 84.3% of primary energy production [1]. The resulting increase in global emission of greenhouse gases means that if we do not dramatically reduce our burning of fossil fuels soon, the impact on global ecosystems will be catastrophic and irreversible. There is only one viable solution to this issue, and that is to replace fossil fuel burning with more sustainable methods of producing energy.

In 2015, 196 countries signed The Paris Agreement - a legally binding treaty committing to limiting the increase in global temperatures to 2°C above pre-industrial revolution levels [2]. This has led to a wave of new targets and commitments from these countries to reduce carbon emissions. The UK, for example, has passed legislation that requires the government to reduce greenhouse emissions to 'net-zero' compared to 1990 levels by 2050 and recently announced a fresh target to reduce emissions by 68% compared to 1990 levels by 2030 [3, 4]. These ambitious targets require changes in behaviour and infrastructure but they also require a greater capacity for producing energy for consumption.

When it comes to low-carbon sources of energy, there are two schools of thought. One of these is nuclear power, which is capable of producing vast amounts of energy without any greenhouse gas emission. However, its classification as a sustainable energy source is debated due to the issue of disposing of its extremely harmful nuclear waste products, some of which will take millennia to be safe to handle. Adding to this, high profile accidents such as those at Chernobyl and Fukushima have raised safety concerns and, as a result, many governments around the world are reluctant to invest too heavily in nuclear power.

The other camp is that of renewable energy: this is an umbrella term used for any source of energy that is not depleted upon generation of energy. The primary technologies include onshore and offshore wind power, solar photovoltaics (PV), hydroelectric power and geothermal power. It is widely accepted at this stage that no one individual renewable technology can provide for the world's energy needs single-handed. A combination of all the aforementioned technologies is the only hope for reducing the harmful burning of fossil fuels and averting a climate disaster. World renewable energy generation increased by 40% in 2019 from 2018, showing that there is a shift in momentum towards these greener technologies [1]. However, its share of the energy market remains only 11.4% (including hydro and biofuels), which shows that there is still a long way to go.

1.2 Solar Photovoltaics

Of the many available options in the renewable energy department, solar photovoltaics is one of the most reliable and widely deployable. Hydroelectric power accounts for 6.4% of the total primary energy produced worldwide and has the capacity to produce vast amounts of energy per system. However, hydroelectric plants are reliant on having the right geographical conditions and come at enormous expense. Construction costs are one aspect of this, but they also have a huge effect on ecosystems, with many species or habitats being harmed by the construction of reservoirs. Reservoirs can also lead to the displacement of communities on a huge scale and some reports show that carbon emissions from some hydroelectric plants (from decomposing plant-matter flooded by the dam) are actually on a comparable scale to coal plants [5], leading to its status as a renewable energy being called into question [1]. Geothermal power is likewise dependent on having an uncommon combination of geographical and geological conditions. Wind power and solar power, meanwhile, utilise natural phenomena which are abundant almost everywhere in the world, do not need to be gathered or constrained and, despite being somewhat intermittent, are regular and reliable. Onshore wind is currently the cheapest renewable energy source in terms of levelised cost of energy (LCOE) according to the International Energy Agency's (IEA) latest report [6], with utility-scale solar PV not far behind, at 50 USD/MWh and 56 USD/MWh respectively. These are now competitive with fossil fuel energy sources such as gas (76 USD/MWh) and coal (88 USD/MWh). [6]. Solar photovoltaics has the additional advantage of being free of any moving parts (such as turbines) that may require maintenance or have their own efficiency limits. It is also modular, which removes the requirement for a centralised power station, has a long lifetime ($\sim$30 years), produces no emissions and taps into a truly inexhaustible source of energy [7].

However, PV still has room for improvement. The report by the IEA shows that when deployed on a larger scale solar PV has a far lower LCOE [6], meaning that large-scale deployment is desirable in order to continue matching onshore wind for cost

effectiveness. The development of new technologies could allow for cheaper and more widespread large-scale deployment or deployment in new and innovative ways to bring costs down or to minimise the area required. The development of new, cheap and easily scalable PV technologies such as antimony selenide (as further discussed in sections 2.1 & 2.2) is important if we are to achieve the goal of terawatt scale deployment of PV around the world.

1.3 Overview of the Thesis

This thesis aims to shed light on some of the fundamental aspects of antimony selenide solar cells that have so far been poorly (if at all) understood. Rather than focus purely on device performance characteristics or on fundamental material properties, this work continuously tries to link the two. Particularly, data acquired from photoemission studies (often left as self-contained studies) are compared with device performance characteristics so that one can deduce what effect the measured parameters have on the performance of antimony selenide solar cells. Furthermore, the results of the thesis are not limited to one aspect of device performance, with studies carried out on the front contact, back contact and on bulk characteristics of the cell.

The layout of the thesis is as follows: in Chapter 2, the relevant background information on photovoltaics and antimony selenide will be presented. This includes the principles of operation and general history of PV, the fundamental understanding of antimony selenide (Sb_2Se_3) as a material, and the development of Sb_2Se_3 solar cells thus far. Chapter 3 will summarise the experimental and theoretical techniques used in the work carried out in this project, including fabrication, characterisation and modelling techniques. Chapters 4-6 then constitute the chief results obtained during the project before concluding remarks and comments on future work in Chapter 7.

Chapter Two
Background

2.1 Photovoltaics

In this section the fundamental principles of solar energy conversion through photovoltaics will be introduced. The operation principles of a solar cell are explained, from the fundamentals of semiconductor junctions to performance characteristics. This is followed by a brief overview of the history of the field of photovoltaics, discussing the merits and drawbacks of each technology that are the basis for the search for new alternative solar absorbers.

2.1.1 Operation

Semiconductors

When a material is in the solid state the wave functions of the electrons overlap. The Pauli exclusion principle states that no two electrons can occupy the same quantum state and therefore the electrons occupy states of a slightly different energy. On a macroscopic scale the number of electrons becomes very large and the separation between the energies of these states becomes very small, meaning that they can be considered a continuum or band [8, 9]. These bands are known as the valence band (comprising of occupied states) and the conduction band (unoccupied states). Most materials can be sorted into 3 categories - metals, insulators and semiconductors (Figure 2.1). In a metal, the valence and conduction bands overlap, meaning that the electrons can easily occupy the conduction band and there are always free carriers to carry a current. However in non-metals there exists a forbidden gap in between the valence and conduction bands in which there are no states, known as a band gap (E_g). An insulator has a large band gap ($E_g > 4$ eV) which means that it is energetically difficult to excite electrons from the valence band to the conduction band and therefore these materials for all practical purposes do not conduct electrically. Semiconductors, as the name suggests, fall in between metals and insulators - they possess a band gap which is small enough ($E_g < 4$ eV) that thermal excitations or other extrinsic sources of energy can promote an electron from the valence band into the conduction band and allow conductivity [8].

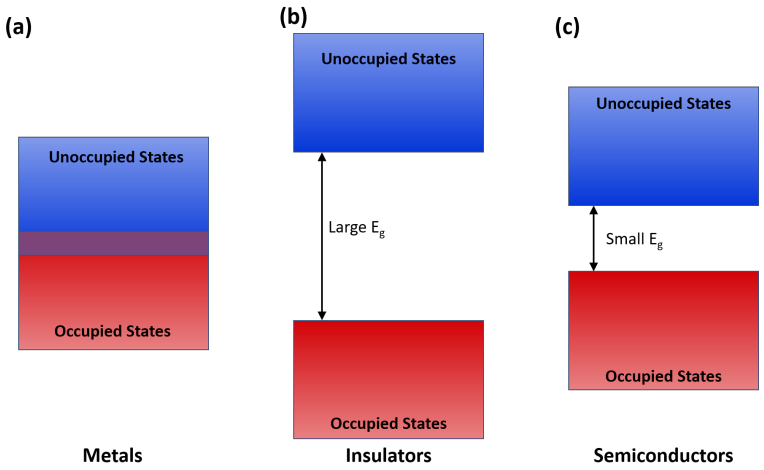

Figure 2.1 Schematic of the conduction and valence bands of (a) metals, (b) insulators and (c) semiconductors, with no band gap, a large band gap, and a small band gap respectively.

The ground state electrons occupy available states up to the Fermi level (E_F). The Fermi level is more rigorously defined as a hypothetical energy level that has a 50% chance of being occupied by an electron in a solid at thermal equilibrium. The position of the Fermi level relative to the valence and conduction bands is a crucial property defining the electrical conduction of a material. In a metal the Fermi level must lie within the overlapping valence/conduction bands, signifying the consistent conductivity of the material. In a semiconductor, however, the Fermi level most commonly lies somewhere within the band gap, and its relative proximity in energy to the valence or conduction band determines the conductivity of the semiconductor. An ideal intrinsic semiconductor at equilibrium will have a Fermi level directly in the middle of the gap at zero Kelvin because in an ideal case it will have an equal number of holes in the valence band and electrons in the conduction band. However, the introduction of impurities, either through structural defects or chemical impurities in the material, will introduce donor or acceptor states that increase the electron or hole population respectively and thereby move the Fermi level up or down in the gap. A semiconductor with a higher proportion of electrons is called an n-type semiconductor and one with a higher proportion of holes is known as a p-type semiconductor. Materials can be one or the other through native defects, or can be deliberately doped n- or p-type through the addition of small quantities of other elements. Materials that are heavily doped can have the Fermi level lie within the conduction or valence band, signifying that there are always free carriers within the respective band. These materials are referred to as degenerately-doped and are fully conducting due to the now constant existence of charge carriers within the respective band. Doping is discussed further in Chapter 5.

The Photovoltaic Effect

The operation of a typical photovoltaic device is dependent on semiconductor junctions, most-commonly a p-n junction. The simplest example is the homojunction, in which both semiconductor layers are made of the same material (and therefore have the same E_g) but are doped differently. Upon contacting a p-type material and an n-type material the electrons and holes near the interface will diffuse across and recombine with each other. The recombination of the electrons and holes at the junction leaves charged donor and acceptor ions on either side of the boundary, forming the depletion region. This depletion region experiences an electric field due to the now negatively charged region on one side and the positively charged region on the other. This is a p-n junction (see Figure 2.2), and it acts as a diode, allowing charge to flow in one direction but opposing charge flow in the other [8, 10].

When light is shone onto the junction, any photons with energy lower than the band gap will pass through the material without being absorbed. However, a photon with energy equal to or greater than the band gap can be absorbed by an electron in the valence band, promoting it into the conduction band. If this occurs within the depletion region, the electric field then sweeps the carriers towards electrical contacts on either side of the p-n junction. This is the photovoltaic effect and it explains how light can be converted into electrical current. The same effect can be achieved through a heterojunction, in which the two materials have different band gaps. However this leads to discontinuities in the bands at the interface, causing band alignments to play a huge part in device performance, as discussed further in Section 2.1.2 and Chapter 4. It is also possible to produce PV power from an isotype junction [11], where the materials are of the same doping type but sufficiently different carrier densities to form a junction, as discussed further in Chapters 4 & 5.

Photovoltaic Devices

Having reviewed the principles that allow a solar cell to produce power from sunlight, we will now examine the characteristics necessary for them to do this well. One of the first considerations when looking for a promising PV material is the band gap. When a photon is absorbed and an electron is promoted from the valence band maximum (VBM) to the conduction band, it can only contribute energy equal to the band gap to the power output. As mentioned earlier, any photons with energy less than the band gap will not be absorbed at all. Any electrons excited by a higher energy photon will be raised above the conduction band minimum (CBM), however they cannot be extracted with this energy; instead they will undergo thermal losses until they reach the CBM. For this reason, the choice of band gap in an absorber material is crucial. Too high a band gap will lead to very little light being absorbed and therefore low power generation. However, if the band gap is too low, each excited carrier will only contribute a small amount of energy to the output and the efficiency will be low. This balance was summarised by William Shockley and Hans-Joachim Queisser in what is known as

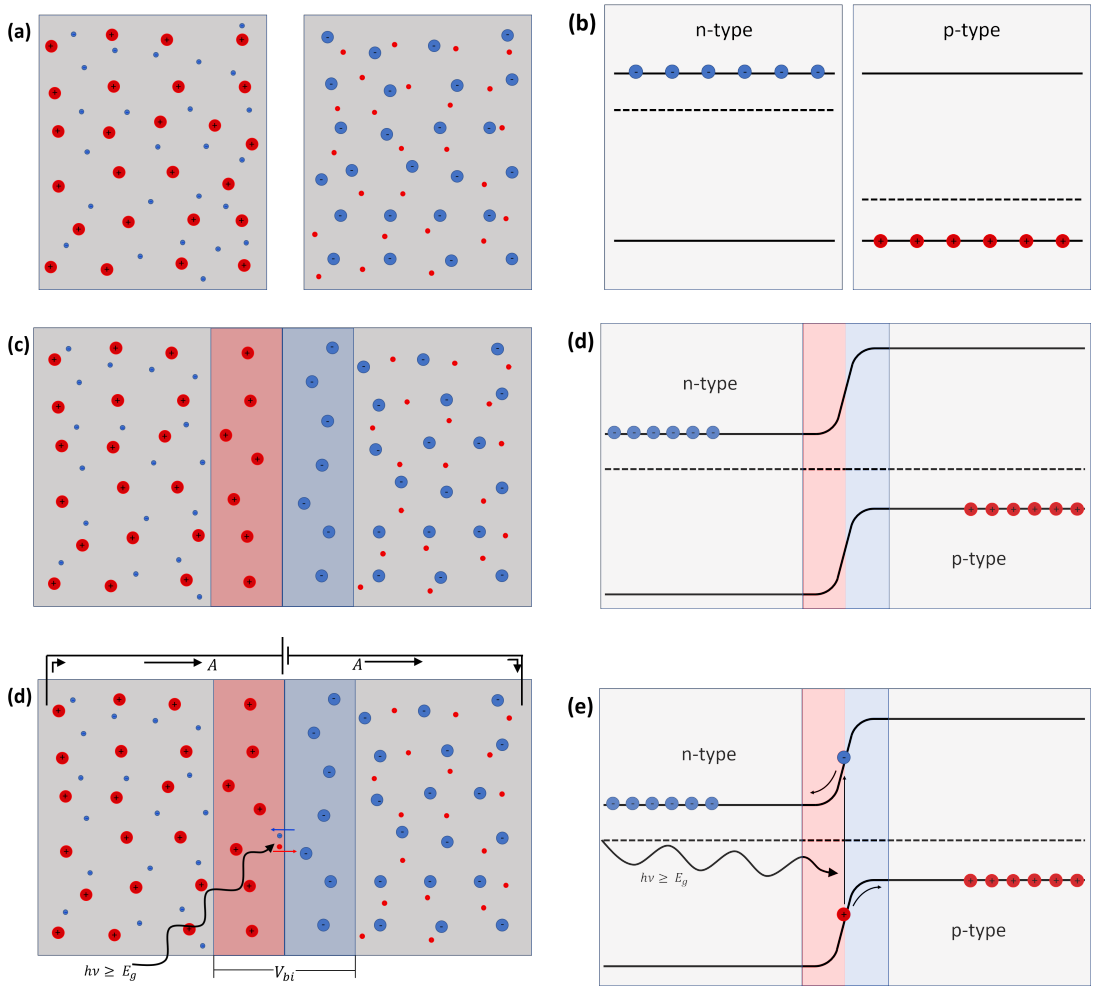

Figure 2.2 Sketches depicting (a) n- and p-type semiconductors before contacting, (c) the p-n junction after the diffusion and recombination of carriers at the interface and (e) the generation of photovoltaic current upon light absorption with (b,d,f) respective band structures.

the detailed-balance limit. This describes a fundamental limit of photovoltaic power conversion and it states that for a single p-n junction solar cell in AM1.5 illumination the optimal band gap is 1.34 eV, and would provide a maximum possible efficiency of 33.16% [12, 13]. More generally, it is shown in Figure 2.3 that a band gap in the range of 1.1 - 1.5 eV provides the best potential to reach efficiencies near the detailed-balance limit.

However, it is not enough to have a band gap of the right energy - the material should also be an effective absorber. The effective absorption of light by a solid de-

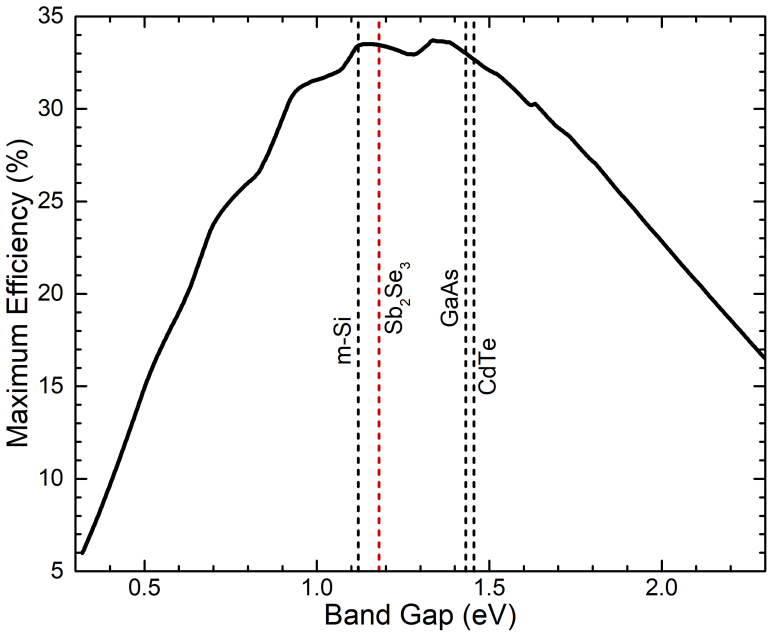

Figure 2.3 Detailed-balance limit of maximum achievable efficiency by a single p-n junction solar cell as a function of absorber band gap [12]. The band gaps of some common absorbers are shown as a comparison for Sb_2Se_3.

pends strongly on the band structure of the material. When plotting energy against momentum it is possible to see how the VBM and CBM line up in k-space. If the VBM and CBM are lined up as in Figure 2.4a, absorption of light is significantly more likely and the material usually has a high absorption coefficient. However, if the VBM and CBM are offset (Figure 2.4b), then a phonon excitation equal to the momentum difference is also required to make the transition possible, making it far less likely and the material will have a low absorption coefficient. Silicon, despite being the leading PV technology, has an indirect gap, meaning that very thick layers are needed in order to absorb a useful amount of light. Materials with a high absorption coefficient, however, can absorb the majority of incident visible light within a few hundred nanometres.

A p-n heterojunction device is usually made up of an absorber layer (with a band gap within the detailed-balance limit's optimal range and a high absorption coefficient) contacted to a layer of a semiconductor of the opposite doping type. This window layer is desired to have a relatively wide band gap (so that it doesn't absorb too much of the useful light) and good conductivity. The window layer will be contacted a transparent conductive layer as a front contact - usually a degenerately doped oxide - so that the circuit can be completed but light still be admitted to the device. Transparent conductors are a field unto themselves and will not be discussed further here. Finally, metal contacts will be deposited onto the absorber layer, completing the device. This

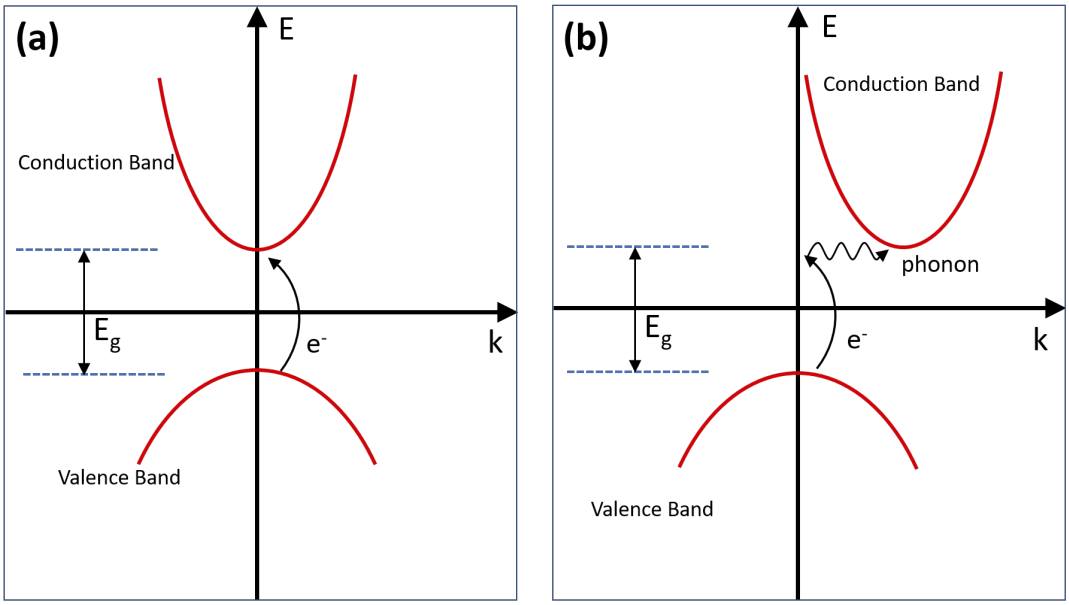

Figure 2.4 Sketch showing an example of (a) a direct band gap transition and (b) an indirect transition requiring an additional phonon excitation.

is the most basic structure of a solar cell - in reality, the highest performing devices often contain numerous other layers such as anti-reflection coatings, buffer layers and carrier-selective transport layers.

Performance Characteristics

An ideal solar cell at equilibrium in the dark behaves as a diode, with a built-in electric field across the p-n junction. At equilibrium, the drift current (in which minority carriers are swept across the depletion region by the electric field) is balanced by the opposing diffusion current (caused by carriers moving from regions of high carrier concentration to areas of lower concentration), and the net current is zero. When a bias is applied across the cell this equilibrium is broken. In forward bias, the electric field of the p-n junction is reduced, leading to an increased diffusion current. In reverse bias, the electric field is increased leading to a reduction of the diffusion current, however the drift current is limited by the number of minority carriers present in the material and therefore remains largely unchanged (until the breakdown voltage). The performance of a solar cell can be summarily characterised by a current-voltage (I-V) curve. The equation for the current output of an ideal diode in the dark is given by equation 2.1:

$$\mathrm{I}_{dark}(\mathrm{V}) = \mathrm{I}_0(\mathrm{e}^{\frac{qV}{nKT}}\text{-}1) \tag{2.1}$$

When under illumination, many more carriers are generated within the depletion

region of the cell. These carriers are separated by the electric field, increasing the drift current and breaking equilibrium. In a good working cell, the drift current will then be far greater than the diffusion current, and if the terminals of the device are connected, a light generated current will flow through the circuit, generating power. Given that the current is dependent on the illuminated area, the convention is to use the current density (J), as a more useful measure of performance. The J-V curve of a working solar cell can be considered to be a superposition of the dark J-V curve and the light-generated current (Figure 2.5). For an ideal solar cell under illumination, the ideal diode equation is given by equation 2.2, for which a complete derivation can be found elsewhere [10].

$$\mathrm{J(V)} = \mathrm{J_0}(\mathrm{e}^{\frac{qV}{nKT}}\text{-}1) - \mathrm{J}_L \tag{2.2}$$

The performance of a solar cell depends on many different factors, however it can be characterised by a few key parameters. The first, and most important, is power conversion efficiency (PCE). This describes the power output from a device as a percentage of the incident power of light. Any device with a measurable efficiency can be considered to be working. However, to be considered commercially viable, efficiencies must be over 10% and nearer 15%. It is important to remember as well that the efficiencies of modules in the field are always lower than what can be achieved in a lab setting. For example the First Solar Series 6 cadmium telluride (CdTe) module has an efficiency of 18.3% [14], while the lab record (also held by First Solar) is 22.1% [15]. Commercial copper indium gallium selenide (CIGS) cells typically have efficiencies in the range of 12%-14% [16] despite the lab record being 23.32% [15]. The benchmark, however, is set by silicon modules with >20% efficiencies available commercially [15]. The target for PV technology is always, therefore, to exceed 20% and even to push towards the detailed-balance limit, but they can be considered viable with lower efficiencies, around 15% if the production cost is sufficiently low and scale-up is straightforward.

The efficiency of a device is dependent on a few other key parameters - open-circuit voltage (V_{oc}), short-circuit current density (J_{sc}) and fill factor (FF) - as depicted in Figure 2.5. At V_{oc}, a forward bias is applied so that the potential across the depletion region is negated, and therefore describes the maximum available voltage available from the p-n junction. At J_{sc}, the applied voltage across the solar cell is zero, and therefore corresponds to the maximum available current from the cell. A solar cell in operation does not operate at either of these points, but rather at the maximum power point, which lies in between the two in the fourth quadrant of the J-V graph. According to $P = IV$, the maximum power point will be at the point with the highest combined applied voltage and current. To maximise the power output then, the maximum power point should lie at a voltage very close to the V_{oc} and a current very near the J_{sc}, meaning that it is beneficial for the J-V curve to be as 'square' as possible. However, parasitic resistances can lead to a sloping of the curve which draws the maximum power point away from this point. Therefore, it is important to minimise these resistances to ensure a high efficiency. These resistances include series resistance (R_s) and shunt resistance (R_{sh}) which will be discussed further in Chapter 6. Series resistance origi-

nates from the resistance of the metal contacts and the contact resistance between the semiconductor and contact layers, while shunt resistance is a result of manufacturing defects in the films such as pinholes. The FF is a measure of the 'squareness' of the curve and is calculated from equation 2.3, where η is the PCE and J_m and V_m are the current and voltage at the maximum power point.

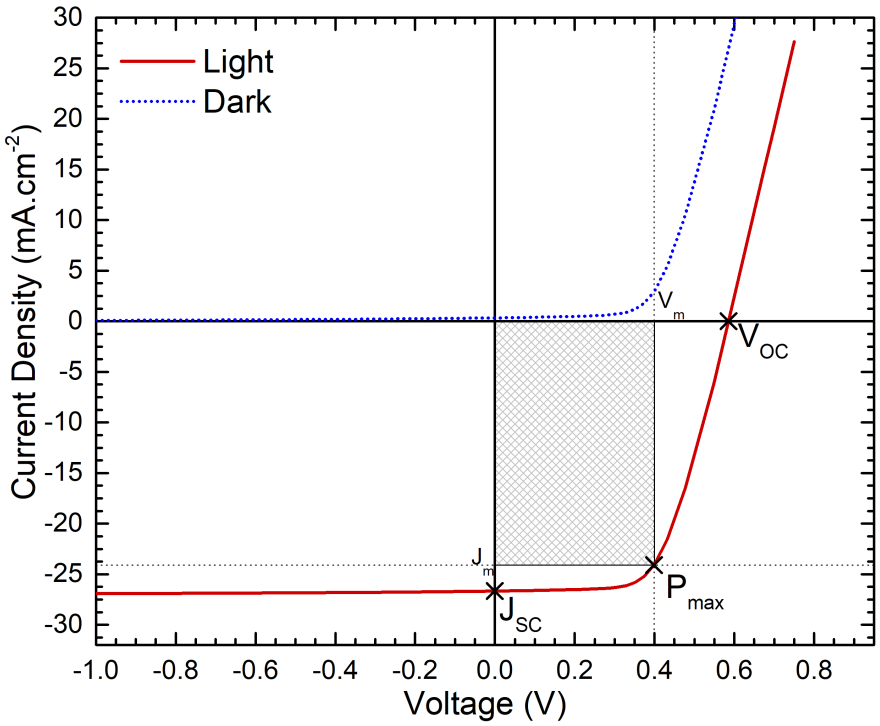

Figure 2.5 An example of a standard J-V curve for a working solar cell in the light with crosses to indicate the J_{sc}, V_{oc} and maximum power point, P_{max}.

$$FF = \frac{J_m \times V_m}{J_{sc} \times V_{oc}} \tag{2.3}$$

$$\eta = \frac{J_{sc} \times V_{oc} \times FF}{P_{in}} \tag{2.4}$$

Finally, it is prudent here to discuss the sources of loss in a solar cell. First of all, losses can occur before light is absorbed in the depletion region - some light will be reflected and some can be absorbed by the contacts or another layer, rendering it useless for power conversion. Once the light reaches the depletion region, only photons with energy greater than the band gap can be absorbed. From the light absorbed in the depletion region, an electron hole pair will be generated, which will then be separated by the electric field. However, electrons promoted to the conduction band are only

in a metastable state and are vulnerable to recombination with holes, in which they relax back down to the valence band. This can happen radiatively - where the electron transitions directly from CBM to VBM and releases a photon that can be re-absorbed - or non-radiatively. Radiative recombination is more dominant in direct band gap semiconductors due to the direct nature of the transition. Non-radiative recombination means that the carrier's energy is lost to the system and is detrimental to device performance. There are a number of things that can lead to non-radiative recombination - one instance is when the carrier encounters a defect level, usually caused by a chemical impurity or structural defect. In this case, the photon will fall into the 'trap' state before relaxing to the VBM, thereby losing the energy. In another case, carriers face a potential barrier to extraction at an interface, either due to a high density of trap states at the interface or due to a band discontinuity, causing them to 'pile up' until they recombine. These types of band discontinuities will be discussed further in Section 2.1.2 and Chapter 4. Ultimately, recombination rates can be limited by reducing the number of deep defects in the material, improving carrier mobility and lifetime and by ensuring good band alignments at interfaces.

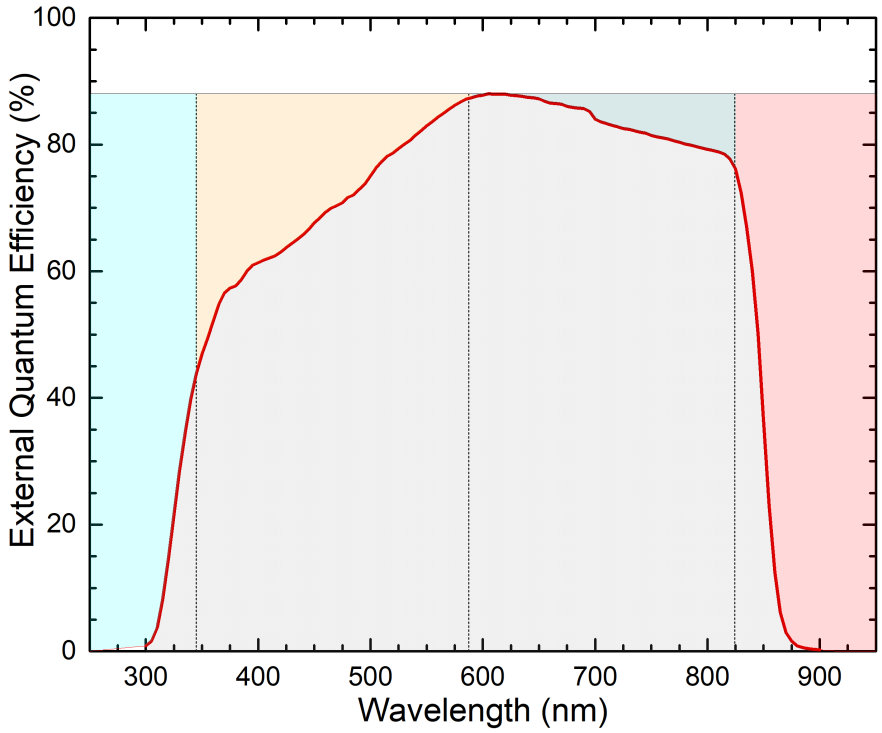

Figure 2.6 Example EQE spectrum of a standard CdTe solar cell [17] with key loss areas highlighted.

A useful tool for examining the sources of loss in solar cell performance is a measurement of external quantum efficiency (EQE) as a function of wavelength. Quantum

efficiency describes the percentage of the photons absorbed that are converted to useful current in the form of charge carriers transferred to the external circuit. External quantum efficiency takes this a step further to include those photons not absorbed by the material. EQE then is the percentage of the incident photons that are converted into extracted carriers. Figure 2.6 shows an example EQE from a standard CdTe solar cell. At lower wavelengths, in the blue highlighted sector, photons are absorbed by the transparent conducting oxide (TCO), and therefore the carriers are not separated by the electric field and will recombine without contributing to the current. In the second sector from the left, highlighted orange, a similar problem occurs with the window layer, in this case cadmium sulphide (CdS). This illustrates the need for a suitable window layer, with a wide enough band gap not to cause too much parasitic absorption, as this phenomenon is called. The data slopes upward towards higher wavelength due to the decreased probability of absorbing lower energy photons, meaning that at higher wavelengths they are more likely to be absorbed within the depletion region. In the third sector, highlighted green, the data slopes downwards towards higher wavelengths. This is also a result of the decreasing likelihood of absorption. Carriers absorbed further from the interface must travel further before reaching the interface where they can be swept into the circuit, leading to an increased likelihood of recombination. Absorbers with lower carrier lifetimes will exhibit a more dramatic downward slope in this region whereas materials with a high diffusion length will show a flatter top. The rightmost sector, highlighted red, indicates the cut-off where the energy of the photons is below the band gap energy of the absorber and so no photons are absorbed. Finally, the topmost region, unhighighted, indicates the fundamental losses due to reflection of light as well as recombination. The top of the EQE spectrum can be raised by increasing the carrier diffusion length/lifetime, or by using anti-reflection coatings to raise the amount of overall light admitted to the solar cell.

2.1.2 Band Alignments

A large part of this thesis focuses on band alignments, both fundamentally and in application. However, band alignments is an umbrella term and can refer to many aspects of a solar cell's electronic structure. In this section we will introduce the important quantities explored in this work regarding semiconductor energy bands and band alignments.

Natural Band Alignments

Here we will define some key quantities used frequently when discussing band alignments in semiconductors and semiconductor heterojunctions. As mentioned briefly in section 2.1.1, semiconductor materials are characterised by their band gap, the forbidden energy gap between the occupied electronic states of the valence band and the unoccupied states of the conduction band. Each band lies at a certain energy on an absolute energy scale and these energies are called the ionisation potential (IP) and the electron affinity (EA), respectively (Figure 2.7). The IP is defined as the energy required to remove an

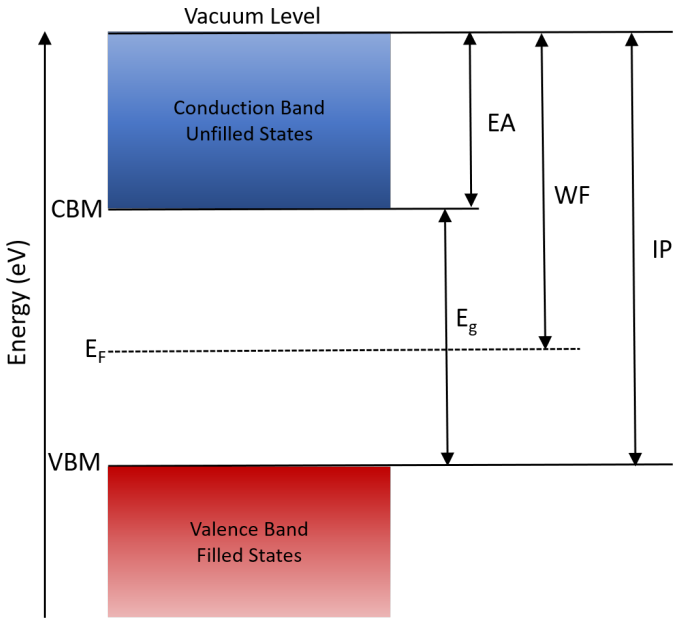

Figure 2.7 Schematic showing the electron affinity (EA), work function (WF), ionisation potential (IP) and band gap (E_g) of a typical semiconductor.

electron from the valence band maximum. To 'remove' the electron is a somewhat loose definition - the electron is considered free of the material when it lies at some point outside the material sufficiently far from the surface that it is beyond the influence of the surface dipole [18]. This is known as the local vacuum level (E_{VAC}) and will be discussed in more detail below. The EA is defined, similarly to the ionisation potential, as the energy required to move an electron from the conduction band minimum to the local vacuum level. Finally, the other quantity labelled in Figure 2.7 is the work function (WF), which is defined as the energy required to remove an electron from the Fermi level. However, given that in non-degenerate semiconductors there are no states at the Fermi level, this is a definition more based on the statistical concept of the average occupancy of the valence and conduction bands. The work function can also be defined more physically as the energy required for an electron to overcome the energy barrier between the material and free space [18, 19].

The work function is in fact a crucial quantity when one intends to deal with band alignments in solids. This stems largely from the definitions of the IP and EA being dependent on the local vacuum level, and the local vacuum level's dependence on the work function. The local vacuum level is a widely accepted concept in solid state physics however its nuances are rarely discussed. Firstly, it is useful to distinguish the local vacuum level from the global vacuum level, $E(\infty)$. $E(\infty)$ describes an energy level infinitely far away from the surface, which is global for all materials and surfaces alike. However, this global vacuum level is not accessible experimentally (as discussed by Cahen *et al.*)

and therefore only useful in a conceptual sense [19]. The local vacuum level is defined to be the energy at which the electron has escaped the surface forces, therefore it follows logically that this level would be different for different materials and surfaces with different work functions. The surface dipole is a result of the abrupt termination of the solid at the surface, causing electron density to spill out into the vacuum, creating a potential step. This would naturally vary between different materials, however variations in the rearrangement of atoms between different surface terminations can also lead to significant variation in the work function for the same material. The presence of any contamination would also influence the work function of a surface and so it is not straightforward to quantify [18]. A common example is the work function of tungsten as measured by Ishi *et al.*, which was found to be 4.47 eV for the (111) surface orientation and 5.25 eV for the (110) surface orientation [20]. This difference is significant, and highlights the importance of understanding the implications of work function variations for practical applications. It is also important that these quantities can only be truly physically measured as surface quantities, and any extrapolation into the bulk is purely conceptual. This is discussed in more detail by Cahen *et al.*, but will not be elaborated on further here [19].

Band Offsets

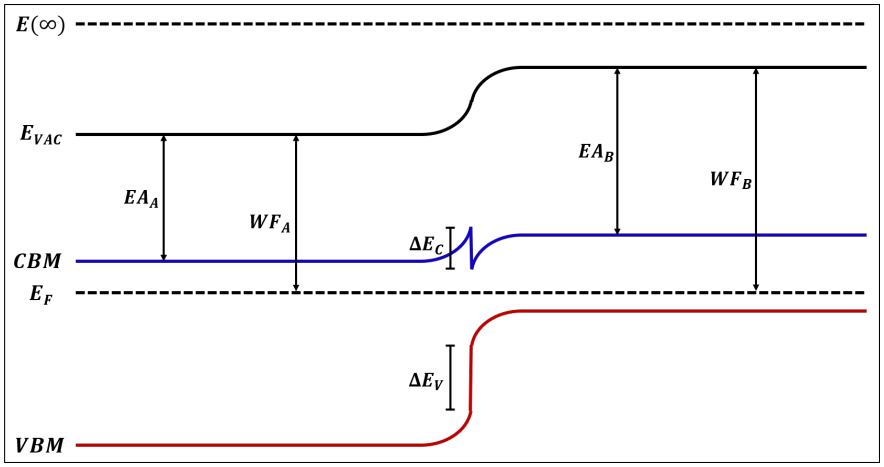

Figure 2.8 Schematic diagram of a heterojunction's bands upon contacting, in which the Fermi level becomes the reference level and the local vacuum level (dashed), conduction band (blue) and valence band (red) 'bend' to accommodate this. E(∞) represents the global vacuum level and E_{VAC} represents the local vacuum level.

When two semiconductors are brought into contact, the flow of charges across the interface causes the Fermi levels of the two materials to align. This leads to the formation of a depletion region in which there exists an electric field and band bending takes place. At thermal equilibrium, the Fermi levels of the two material align and

this becomes the fixed reference level. As discussed above, the local vacuum levels, and consequently the valence and conduction bands are positioned in reference to the Fermi level, therefore these bands are shown to bend to accommodate the alignment of the Fermi levels, as shown in Figure 2.8. Of course, a vacuum level cannot technically exist at the interface between the two solids due to the lack of a solid-vacuum interface, however the concepts can be translated to a good approximation, as is discussed in section 4.3.1.

In a heterojunction, due to the difference in band gaps between the two materials, this causes a discontinuity in the valence and conduction bands at the interface, labelled as ΔE_V and ΔE_C in Figure 2.8. These discontinuities are known as the valence band offset (VBO) and conduction band offset (CBO), and are crucial to the performance of a heterojunction solar cell. If the discontinuities are too large, they can cause barriers or recombination traps to carriers passing from one layer to another, and harm device performance. This is discussed further in Chapter 4.

Metal-Semiconductor Junctions

Metal-semiconductor junctions play a key role in solar cell device operation because no current can be extracted from the cell without the carriers having to navigate the junction between absorber and metal contact. A poor contact between these two layers can lead to a back-contact barrier which can severely impede carrier extraction from the cell and limit power output. It is therefore important to understand the considerations for designing an effective back contact.

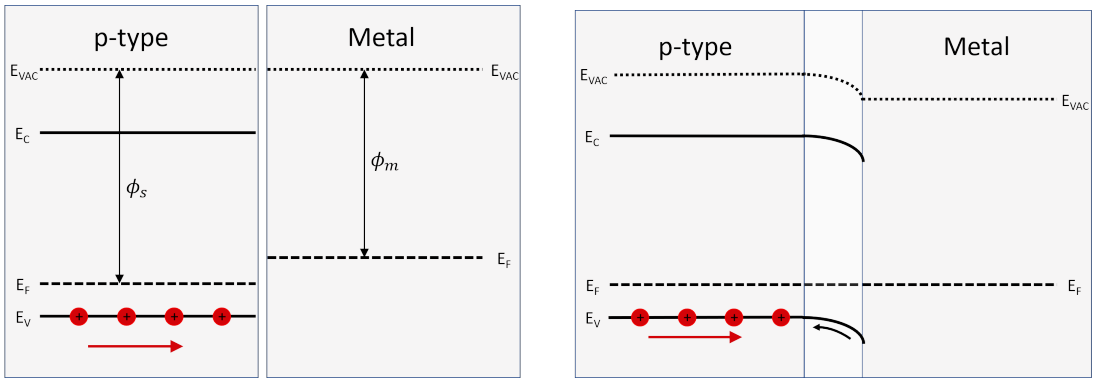

Figure 2.9 Schematic diagram of the band alignments (a) before and (b) after forming a Schottky junction.

Much in the same way that the Fermi levels of two semiconductors align upon contacting, the Fermi level of a metal and semiconductor do the same when forming a junction. The difference is the metal's lack of band gap, meaning that this is a simplified

case in many respects. To take the case of a standard, superstrate configuration solar cell with a p-type absorber layer, holes are moving towards the back contact and are seeking to move into the metal contact. There are two potential outcomes to the back contact. If the work function of the metal is less than the work function of the absorber ($\phi_m < \phi_s$) electrons will flow from the metal to the semiconductor upon contacting, creating a depletion region. Due to the high carrier concentration of metals, this region effectively lies entirely in the semiconductor (see Figure 2.9). This region of downward band bending opposes the movement of holes into the metal, and is known as a Schottky barrier. A back contact barrier such as this can be seen as rollover in a J-V curve and is known to increase series resistance (R_s) in PV devices, lowering the efficiency [21].

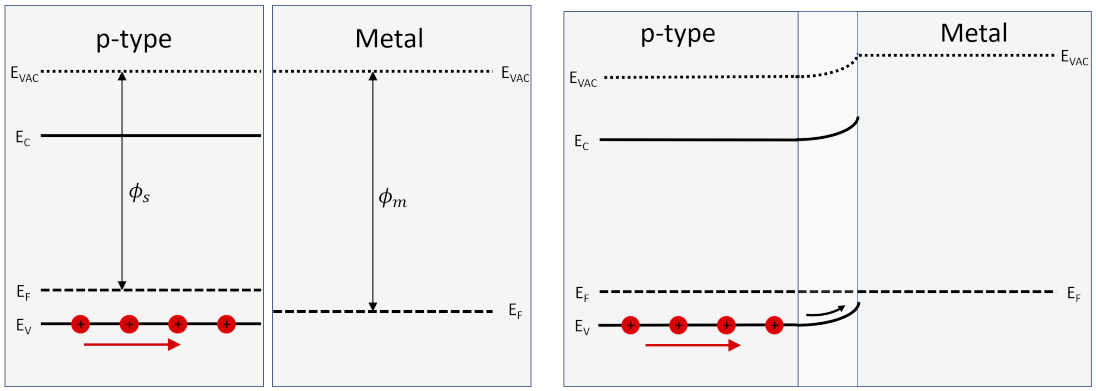

Figure 2.10 Schematic diagram of the band alignments (a) before and (b) after forming an Ohmic junction.

Alternatively, if the work function of the metal is greater than the work function of the semiconductor ($\phi_m > \phi_s$) the valence band will bend upward upon contacting, leading to an Ohmic contact (Figure 2.10). This poses no obstacle to carrier extraction and is the desired outcome from back contacting. It is therefore important to use a metal with a higher work function than the absorber being used. This is a long-standing issue in CdTe PV, with the high work function of CdTe posing great difficulties in back contacting [21, 22].

2.1.3 A Brief History of PV

In this section we will provide context for the research of Sb_2Se_3 solar cells by presenting a brief history of the field of photovoltaics thus far, from the first solar cells ever made to the next generation materials being researched today. This section will focus on each technology as a whole, the advantages that made them successful, and the drawbacks that lead people to continue searching for better alternatives.

Photovoltaic power is named after the photovoltaic effect, discovered in 1839 by

Edmond Becquerel [23]. The first PV device was created much later in 1883 by Charles Fritts [24, 25] which consisted only of a piece of selenium covered in a layer of gold and had a power conversion efficiency less than 1%. However, the field of photovoltaics was not truly sparked to life until another century had passed, with the creation of the first silicon solar cell in 1954 [26]. This device, utilising a p-n junction (see section 2.1.1), achieved a power conversion efficiency of ∼6% and began the first generation of PV technologies.

First Generation: Silicon PV

Silicon-based PV makes up roughly 95% of the PV market share, with the vast majority of that being wafer based silicon [27, 28]. Based on a homojunction made up of p- and n-type doped wafers, these solar cells provide high efficiencies and are made primarily using silicon - a highly abundant material that is already widely used in the electronics industry. Monocrystalline silicon achieves the highest efficiencies, however the production of wafers of high quality monocrystalline silicon is an energy intensive and wasteful process. Polycrystalline silicon cells were developed to try to mitigate these issues and achieve respectable efficiencies (>20%) at a lower production cost. Finally, amorphous silicon was developed as an even cheaper and more scalable alternative, however efficiencies of amorphous silicon do not exceed those of thin film technologies (see below) and therefore usage is not as widespread.

Mono- and poly-silicon PV is without a doubt the backbone of the PV industry. High efficiencies and a rapidly falling cost of production mean that they are unlikely to be displaced by any other PV technology as the majority shareholders of solar energy production. However, there are inherent flaws to silicon as a PV material that cannot be overlooked: silicon has an indirect band gap, meaning that absorption rates are low. This leads to wafers with thicknesses of ∼200 μm being used [29], with a reduction of this thickness coming at the cost of efficiency. Couple this with the wastefulness of the process of cutting these wafers and the silicon industry leaves a lot to be desired in terms of production efficiency. It is not straightforward to calculate the energy payback time (EPBT) of silicon technologies because they largely use silicon recycled from the microelectronics industry and, as a result, estimates of the energy required to produce them vary widely. However, one report by the U.S. Department of Energy in 2004 estimated the EPBT to be approximately 4 years. Thin film PV, which will be discussed in the following section, was already reported to have an EPBT less than 1 year. Given the improvement in both silicon and thin film efficiencies since the publication of said report both can be considered to have even shorter EPBTs but it is clear that thin film technologies hold a significant advantage over silicon in terms of EPBT [30].

Second Generation: Thin Film PV

The main advantage of thin film PV is that, for certain materials with a high absorption coefficient, a large percentage of the AM1.5 solar spectrum can be absorbed in films

with thickness between a few hundred nanometers and a few microns. This means that a fraction of the material is required to produce an efficient solar cell compared to the amount of silicon used in crystalline wafers. Additionally, the films can be deposited by simpler means than the costly and wasteful growing and joining of monocrystalline wafers. The majority of thin film technologies are deposited by physical vapour deposition (PVD) or chemical vapour deposition (CVD) techniques or even solution processes such as slot dye or bar coating. This means that the material and production cost of thin film PV technologies are massively reduced compared to silicon. The use of such thin films also opens the door to depositing onto flexible substrates, something which wafer-based PV cannot do. This would allow solar panels to be incorporated into buildings and other structures in an entirely new way

The success of thin film technologies has come primarily through two technologies - cadmium telluride and copper indium gallium selenide. The former was first worked into a PV device in 1957 [31] and has since progressed to a record efficiency of 22.1% [15]. CdTe has the shortest energy payback time of any PV technology [32]. CIGS, meanwhile, was first developed in the mid-1970s in an attempt to limit copper diffusion and tune the band gap of Cu_2S cells. It has since reached a record efficiency of 23.4% [15]. A mention should be made also for gallium arsenide PV, which currently holds the record for the highest PCE obtained from a single-junction solar cell (29.1% [15]). While they are by definition a thin film technology, these films have to be grown epitaxially due to the severe negative impact of grain boundaries, making them extremely costly.

The production of thin film PV is growing year on year but its overall market share is steadily decreasing [28]. This is primarily due to the rapidly increasing production of silicon technologies, however both CIGS and CdTe do have their drawbacks. A key component of CIGS is the indium, an expensive element that is in high demand in the electronics industry. This means that production costs are not as low as CdTe or even some silicon technologies. There is also a downside to being a quaternary material - the processing of good quality CIGS is complex and requires a high degree of control, meaning that commercially produced modules do not match laboratory cells in terms of efficency [7]. CdTe is cheaper than CIGS and is relatively simple to produce. However, cadmium is a toxic heavy metal and, while safe within the CdTe compound, some of the processes involved in the making of the cells have harmful cadmium-containing waste products. This has raised concerns over the environmental impact of CdTe production [33]. Additionally, tellurium is a very scarce metal, which raises questions over its suitability for terawatt scale-up.

Next Generation PV

Next generation PV is an umbrella term encompassing any and all PV technologies trying to improve on the current thin film technologies. There are many and varied candidates for the next generation of solar cells. One of the primary contenders is

the perovskite solar cell, which has achieved a remarkable growth in terms of both efficiency and publications in the last few years. The name perovskite actually refers to a certain crystal structure (ABX_3) but in the field of solar cells it has become an umbrella term for methyl-ammonium lead iodide (MAPI) and its many, organic, inorganic and hybrid variants. Perovskites have many advantages, that include tuneable properties, low production and material cost and high efficiencies. The barrier to their wide scale deployment currently lies with their poor stability, although a lot of effort is going into improving the lifetime of these cells. Another popular material is copper zinc tin sulphide (CZTS), also known as kesterite for its structure, which aims to replace the expensive indium and gallium in CIGS with cheap abundant elements zinc and tin. While a maximum lab efficiency of 12.6% has been achieved [34], the field has stagnated recently due to the poor phase stability of the material. Other noteworthy technologies include dye-sensitized solar cells and organic PV (OPV) which have also achieved efficiencies over 10%, but will not be discussed further here.

These are just some examples of emerging PV technologies but there are dozens of others that are still at a fledgling stage with low efficiencies. The priorities for next generation technologies can be boiled down to a few key goals. Firstly, they must achieve a competitive efficiency: it is generally accepted that once a technology reaches over 15% efficiency it is considered to be of commercial interest. The materials used should be both cheap and non-toxic, in order to provide good scalability. The compound should be stable and not too complex, again to ensure that large scale processing is not an issue. Finally, the production methods should be well established and, preferably, cheap and simple so as to provide easy assimilation to existing industrial processing facilities.

2.2 Antimony Selenide

The focus of this thesis is the improvement of the understanding of certain fundamental properties and behaviours of Sb_2Se_3 in the context of photovoltaic devices. Sb_2Se_3 is a material of rapidly growing interest in the field of next generation PV and since 2014 it has improved remarkably quickly, from $\sim$2% to $\sim$10% with a relatively small number of groups working on it (Figure 2.11). In terms of existing technologies, Sb_2Se_3 could be seen as a potential successor to CdTe, given that it has many of the same advantages while being free of some of the drawbacks. Despite its promise, however, Sb_2Se_3 remains an emerging material, and many of the fundamental questions over how best to use it remain unanswered. This section will aim to summarise what is known of antimony selenide, both in terms of material properties and cell development, and highlight the avenues of research that still need to be pursued in order to better understand this material.

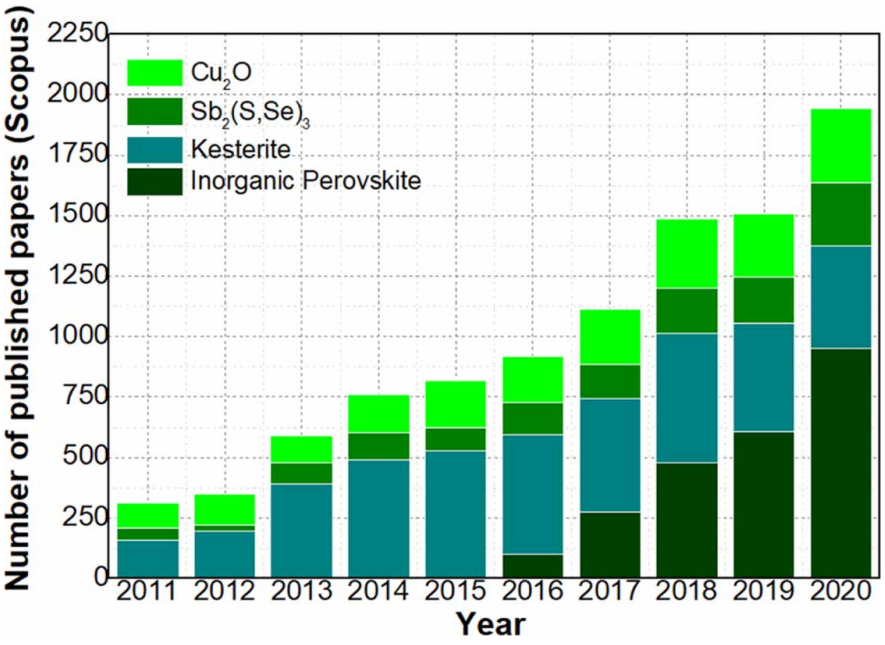

Figure 2.11 Number of published papers each year for a number of emerging PV materials [35].

2.2.1 Material Properties

Basic Material Properties

One of the key advantages of Sb_2Se_3 is that it is a simple binary compound with no common secondary phases [36]. To the best of our knowledge there are no reports in the literature of any secondary phases of Sb_2Se_3 being formed during thin film deposition. Some groups report selenium deficiency post-deposition as well as oxidation of the surface layer [37–39], but they have never posed any significant barrier to device performance, as will be discussed further in Chapter 6. The lack of problematic secondary phases makes Sb_2Se_3 an attractive prospect for industry scale-up because it promises ease of deposition by any cheap method. CZTS, by contrast, struggles to achieve phase purity by most methods due to the many other favourable Sn-, Zn-, or Cu-based compounds [40–42], and this has been a barrier to its development. High quality Sb_2Se_3 films have been made by thermal evaporation (TE), magnetron sputtering, closed-space sublimation (CSS), vapour transport deposition (VTD), e-beam evaporation and some progress has been made with solution processing [38, 43–46]. While performance differs, any of these techniques are capable of producing phase pure Sb_2Se_3 thin films, giving it massive potential. Sb_2Se_3 also has a lower melting point (885 K) than CdTe (1366 K), making the energy cost of depositing films lower [36], another appealing property for manufacturers.

Another attractive property of Sb_2Se_3 as a PV material is the relative cost and toxicity of its constituent materials. The high and fluctuating cost of In [47] makes it problematic for commercial use, especially given the incredibly high demand for In in the touch-screen electronics industry. Tellurium is a very scarce resource (crustal abundance of 0.001 ppm according to Royal Society of Chemistry (RSC)) and western nations are almost entirely reliant on imports from China [48]. Antimony and selenium are considerably cheaper and easier to acquire than both (crustal abundance of 0.2 & 0.13 respectively according to RSC) [49]. In the CdTe industry, the use of a $CdCl_2$ treatment during fabrication leads to harmful Cd containing waste products [33], something which has limited the widespread production of CdTe PV. Sb and Se, while harmful if inhaled, are far less problematic to work with and, as far as we know, do not require any activation steps such as the $CdCl_2$ treatment.

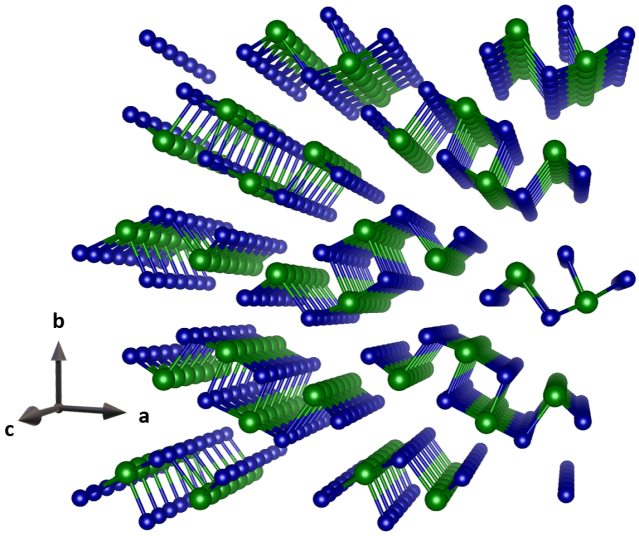

Figure 2.12 Crystal structure of Sb_2Se_3 with Sb atoms shown in green and Se atoms in blue.

Sb_2Se_3 adopts an orthorhombic structure in the Pbnm space group setting. In some cases it is referred to as being of the Pnma space group, which is also correct, but can cause confusion [50]. The different space group settings do not correspond to any physical differences in the crystal structures, but are merely a different way to define the symmetries of the structure. However, it is important to distinguish between the two so as to be clear which planes are referred to in the hkl notation. In the interests of simplicity, Pbnm is used throughout this work as it is what is used in the majority of the literature surrounding Sb_2Se_3 and because of the convenience of naming the nanoribbon direction as [001]. This non-centrosymmetric crystal structure means that Sb_2Se_3 forms $[Sb_4Se_6]$ chains, usually referred to as nanoribbons (Figure 2.12). Within these nanoribbons Sb and Se atoms bond covalently and these nanoribbons are in turn

held together by van der Waals interactions. This anisotropic nanoribbon structure is a common property of materials containing a stereochemically active s-orbital lone-pair [51]. Sb_2Se_3 is also one of a number of materials recently proposed to undergo metavalent bonding. This group of materials known as metavalent solids possess a unique set of properties that does not entirely fit with the classical picture of covalent nor ionic solids as discussed by Raty *et al.* [52]. This is discussed further in Chapter 5.

Basic Optical Properties

Sb_2Se_3 is known as a near-direct band gap material. This means that the lowest energy transition (also known as the fundamental gap) is indirect, however there is a direct band gap of only slightly higher energy. The indirect gap is reported to be in the region of 1 - 1.1 eV [53], with the direct gap being 1.18 eV [54, 55]. This means that it is in the ideal region on the detailed-balance limit graph (Figure 2.3). The associated problems of an indirect material do not apply in this case given the near-direct nature of the band structure, and Sb_2Se_3 actually boasts an incredibly high absorption coefficient, $\sim 10^5$ cm^{-1}. This is 10 times greater than the absorption coefficient of CdTe [36] which is itself considered to be an effective absorber [56].

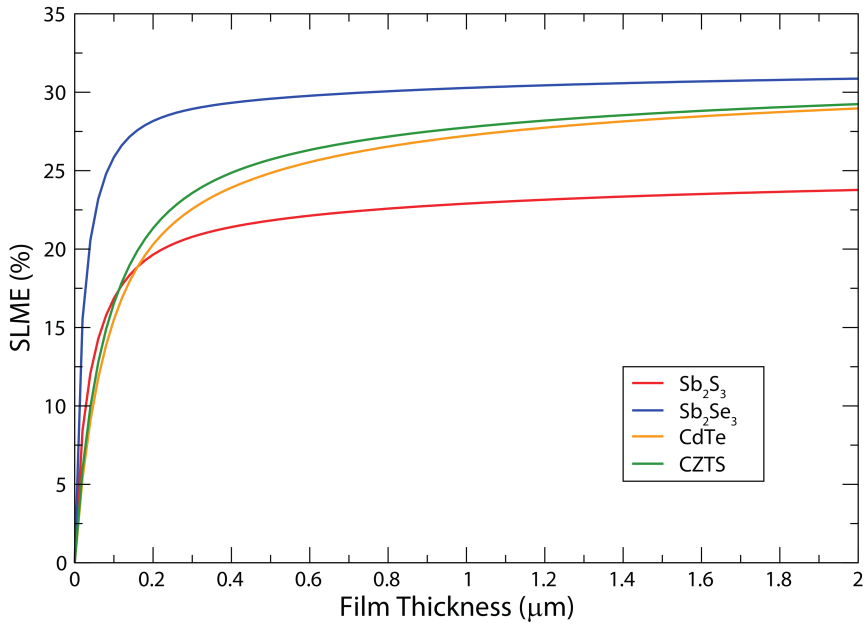

Figure 2.13 Spectroscopic limited maximum efficiency as a function of absorber thickness for a selection of popular absorbers [57].

A useful metric of the impact of absorption coefficient on device performance is spectroscopic limited maximum efficiency (SLME). This is a density functional theory (DFT) calculated measure of the maximum theoretical efficiency taking into account absorption coefficient as well as the band gap. Plotting this as a function of absorber

thickness (Figure 2.13) we can compare Sb_2Se_3 to a number of popular PV materials. As can be seen in Figure 2.13, the maximum efficiency of Sb_2Se_3 rises to near 30% for only a couple of hundred nanometers, meaning that high efficiencies can be achieved with much thinner layers than CdTe or CZTS, for which the onset is much more gradual and the plateau lower [57].

Electronic Structure and Properties

The DFT calculated band structure of Sb_2Se_3 is shown in Figure 2.14. It shows a complex structure with a multitude of valence and conduction bands. The VBM and CBM are both situated between the gamma point (Γ) and the z-point (Z). The direct fundamental gap lies in between, only slightly wider than the fundamental indirect gap [58].

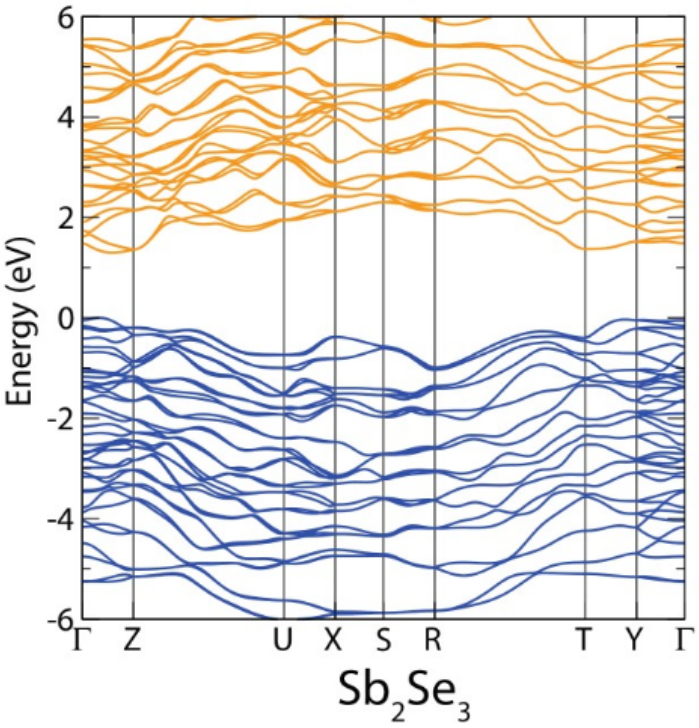

Figure 2.14 HSE06+SOC calculated band structure of Sb_2Se_3 with VBM set to 0 eV [57].

From the calculated band structure it is possible to determine carrier effective masses at the band edges. Carrier effective mass is related to the dispersiveness of the band edge - the flatter the band the greater the effective mass. It is related to mobility according to equation 2.5, where μ is the mobility, e is the electronic charge, τ is the average scattering time and m^* is the effective mass.

$$\mu = \frac{e\tau}{m^*} \tag{2.5}$$

As can be seen in Figure 2.14, the flatness of the bands is different for the different k directions, meaning that the carriers will have different effective masses moving in different directions in the crystal. For the a, b and c directions (represented by $\Gamma - X$, $\Gamma - Y$ and $\Gamma - Z$ in Figure 2.14) these effective masses have been calculated from the curvature of the bands between these points for the valence and conduction bands (see Table 2.1). At the VBM, the hole effective mass is considerably greater in the b direction, which corresponds to the direction with the largest spacing in between nanoribbons. This makes intuitive sense as it would be expected for carriers to have a lower mobility when having to 'hop' between the loosely bound ribbons. It also corresponds to a much lower low-frequency dielectric permittivity, an order of magnitude lower for the b direction than for the other two. The low-frequency permittivity describes the polarisability of charges within the material under a static electric field and is closely related to electric susceptibility and screening length within the material. A lower permittivity would lead to shorter screening lengths and shallower space charge layers, as discussed in Chapter 5.

Direction	m_e^*	m_h^*	ϵ_0	ϵ_∞
a	$0.514m_0$	$0.332m_0$	68	19.6
b	$1.135m_0$	$2.246m_0$	3.5	13.7
c	$0.211m_0$	$0.501m_0$	56	18.7

Table 2.1 Values for electron effective mass (m_e^*), hole effective mass (m_h^*), low frequency dielectric constant (ϵ_0) and high frequency dielectric constant (ϵ_∞) as calculated from DFT computed band structure [58].

Sb_2Se_3 is typically thought to exhibit p-type conductivity [36] and a number of studies show conductivity data to back this up [59–61]. However, in a paper by Hobson *et al.* it was shown that the Sb_2Se_3 made from a certain source material (purchased from a mainstream manufacturer) showed strongly n-type conductivity as a result of chlorine impurities in the source material [62]. This ties in with other reports that Sb_2Se_3 is only very weakly natively doped (if at all) [63], and likely its doping type depends mainly on extrinsic doping [64]. This is discussed further in Chapter 5.

2.2.2 Cell Development

The Importance of Orientation

In a paper published by Zhou *et al.* in 2015 - which included the first report of an Sb_2Se_3 solar cell with greater than 5% PCE - it was stated that "carrier transport in the [211]-oriented grains should be much easier than in the [120]-oriented grains because in the former carriers travel within the covalently bonded ribbons and in the latter carriers are required to hop between ribbons held together by van der Waals forces". While this is

not backed up experimentally - rather it is based on an intuitive assumption of carrier transport mechanisms - there is a strong trend within the literature that supports this hypothesis.

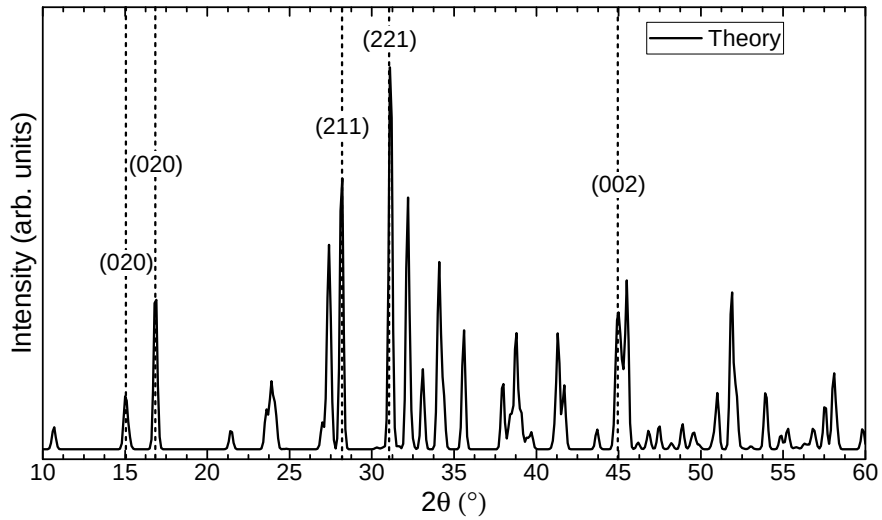

Figure 2.15 Theoretical powder x-ray diffraction pattern for Sb_2Se_3 with a Cu Kα x-ray source with significant reflections for film characterisation labelled.

The x-ray diffraction (XRD) pattern of Sb_2Se_3 contains many peaks, however certain characteristic peaks can be used as indicators of the film's preferred orientation. The 020 and 120 peaks lie at 15° and 17° and are easily identified in the otherwise busy pattern. Meanwhile, the 211 and 221 peaks, at 28° and 32° respectively, are often prominent and easily identified in well-oriented films. Using the 020 and 120 as an indicator of the unfavourable {hk0} planes, and the 211 and 221 peaks to represent favourably oriented {hk1} planes, we can identify a clear trend in the literature. For example, reports by Phillips *et al.* showed that the switch from one deposition method to another significantly reduced the contribution of the 020 and 120 peaks in favour of the 211 and 221 peaks, accompanied by an increase in efficiency [57]. Similarly, in 2018 Wen *et al.* achieved a world record efficiency by switching from rapid thermal evaporation (RTE) to VTD, significantly increasing the relative contribution of the 211 and 221 peaks along with an efficiency increase of 2% [46]. Finally, the current world record for Sb_2Se_3 solar cells is held by Li *et al.*, owing largely to the development of highly oriented nanorods. The XRD pattern for this film had no visible 020 or 120 peaks, but very strong 211 and 221 peaks as well as an unusually prominent 002 peak [43]. This trend can also be seen in studies in which either a deposition condition or post-deposition treatment is varied so as to give a range of film orientations and device efficiencies. In almost all cases, there is a clear correlation between the relative intensities of 211/221 and 020/120 orientations and the power conversion efficiency [61, 65–70]. As an example, Li *et al.* showed in a study on the effect of varying source and substrate

temperature in CSS deposition that, upon increasing substrate temperature, the 020 and 120 XRD reflections were reduced and the device efficiency improved. However, when the substrate temperature was taken too high, 020 and 120 peaks were significantly increased, accompanied by a large reduction in device performance. The same can be said of the reverse case, with a convincing correlation between low efficiency devices and poor orientation of the nanorribbons [71–74].

In the work by Zhou *et al.*, two potential reasons for the importance of orientation are given. Firstly, that it is more favourable for carriers to travel within the nanoribbons and not have to hop in between them. The other is the much hypothesised phenomenon of benign grain boundaries in Sb_2Se_3 when the grains are well oriented. The former seems intuitively sensible but is not backed up with any experimental evidence in this study. However, a study of anisotropic carrier mobilities (amongst other quantities) in Sb_2Se_3 by Chen *et al.* in 2017 supports this hypothesis. It was found by time of flight measurements that for three films, with strong [020], [120] and [221] orientations respectively, the latter had the highest hole mobility of 1.25 $cm^2V^{-1}s^{-1}$, compared with 0.69 $cm^2V^{-1}s^{-1}$ and 0.81 $cm^2V^{-1}s^{-1}$ for the [020] and [120] films. Further confirmation is gained from DFT calculations which find the anisotropic carrier effective mass to be lower for the direction along the ribbons [58].

It has long been claimed in the Sb_2Se_3 literature that grains terminated along the [hk1] directions will be terminated along the atomic spacings bound by van der Waals forces and therefore possess no dangling bonds - thereby removing a major potential source of recombination. However, this would rely on grain boundaries being perfectly aligned with the nanoribbon van der Waals termination axis, something which is unlikely to be achieved throughout the film. However, a recent work by Williams *et al.* used a combination of aberration-corrected scanning transmission electron microscopy and DFT calculations to show that likely all grain boundaries in Sb_2Se_3 are defect-tolerant [75]. They found that at a number of grain boundaries between differently oriented grains, theory calculations showed that mid-gap states attributed to dangling bonds would disappear upon structural relaxation, making these grains self-healing. While the hopping of carriers across grain boundaries is still less favourable than transport directly along the nanoribbons, the absence of dangling bonds at grain boundaries is a huge advantage for Sb_2Se_3 over other popular absorbers such as CdTe.

Deposition Method

As mentioned in section 2.2.1, Sb_2Se_3 can be deposited by a number of different deposition techniques. Most of the earliest efforts to make solar cells with Sb_2Se_3 concentrated on thermal evaporation, a simple and scalable technique (discussed in section 3.1.1). TE generally utilises a straightforward filament wrapped boat that is heated by passing a current through the filament. Both source and substrate are housed in an evacuated chamber and the substrate is generally some distance away from the source material ($\sim$30 cm). TE will deposit amorphous films at room temperature, requiring either

substrate heating during deposition or some post-deposition annealing of the films to achieve crystallinity [76]. It has been shown that the device performance is extremely sensitive to these heating conditions [59, 76]. Through optimisation of the deposition conditions efficiencies exceeding 5% were achieved and this was primarily due to the discovery and compensation of Se losses during the Sb_2Se_3 deposition [61, 77]. Liu *et al.* reported that an abundance of Se vacancy traps were a limiting factor in the performance of Sb_2Se_3 solar cells, and by depositing in a Se rich atmosphere the number of Se vacancies could be reduced [61].

Much of the progress made in Sb_2Se_3 was achieved through work carried out by the Tang group from Wuhan National Laboratory in China. Their favoured deposition technique, labelled rapid thermal evaporation, succeeded in driving the efficiencies further, and was the basis for a number of trials of different device structures (discussed below). This approach is similar to CSS in that the distance between source and substrate is much smaller, $<$1 cm. The deposition is carried out at low pressure and over a short time period ($\sim$35 seconds per deposition) [46, 78]. The progress made with this deposition technique likely owed largely to these factors aiding good crystallinity and orientation, as well as the numerous innovations attempted in terms of device structure [38, 39, 72, 79, 80].

The next step in device development came along in two simultaneous prongs - the shift of the Tang group from RTE to vapour transport deposition and the development of CSS deposition by a number of other groups. According to Wen *et al.* the move to VTD was motivated by a desire to gain independent control of the source and substrate heating as well as reduce defect formation by increasing the distance between source and substrate [46]. This is done using a horizontal single temperature zone tube furnace, where the substrate temperature is modified by changing the distance between source and substrate. The deposition time was increased only slightly to $\sim$2 minutes and deposition was still carried out under vacuum. This approach achieved a record PCE of 7.6%, an increase of over 1% from the previous record [46, 80]. While other studies using the VTD approach have also exceeded 7% PCE (showing it to be a reproducible achievement) 7.6% remains the highest efficiency achieved by this approach.

CSS is a similar but distinct form of PVD that has long been used to fabricate CdTe solar cells, making it appealingly scalable. The first report of Sb_2Se_3 solar cells fabricated using CSS was by Li *et al.* in early 2018 with an efficiency of 5.2%, however this was more similar to the RTE process than to conventional CSS therefore will not be discussed further here [67]. Hutter *et al.* reported 6.6% efficiency by CSS, using a two step process in which a seed layer was initially deposited to aid uniformity, followed by a longer deposition achieving large, well-oriented grains. The CSS process is distinct from RTE and VTD in two key aspects - firstly that the deposition is slower ($\sim$45 minutes), and secondly that growth is performed in an inert gas ambient, specifically N_2 [57, 81]. Since then CSS has become arguably the most popular deposition method for

Sb_2Se_3, consistently achieving efficiencies between 6% and 8% [37, 62, 68, 79, 81, 82]. The current world record efficiency for Sb_2Se_3 was also achieved via CSS in 2019, with Li *et al.* reaching 9.2% [43]. However, even films produced by CSS can be very sensitive to deposition conditions and research is ongoing to better understand the contributing factors to grain size, orientation and grain packing [79, 81].

Attempts have also been made to develop Sb_2Se_3 films deposited via sputtering, and in recent year efficiencies of cells made using this method have started to catch up with CSS and VTD [44, 83, 84]. The most popular process for sputtering Sb_2Se_3 layers is to deposit an Sb layer as a precursor and then selenise this by annealing in a selenium atmosphere. Efficiencies using this method have reached 6.84%, competitive with CSS and VTD although not quite matching them yet. Radio frequency (RF) sputtering is attractive as a scalable technique, with many existing technologies making use of sputtered layers in their devices. The use of a separate selenisation step also introduces opportunities to control the selenium content in the films which could prove useful for controlling defects introduced by selenium vacancies [61, 85].

Finally, a mention will be made for solution processed films. Solution processing generally refers to the dropping, spinning or printing of an Sb_2Se_3-containing solution directly onto a substrate at room temperature, often followed by an annealing step to help evaporate the remaining solvent and achieve good crystallinity. It is extremely desirable in terms of industrial scale up due to its low cost and simplicity although no solar technology has yet been produced on a large scale via solution processed methods. While some forms of solution processing (such as spin casting) are limited to deposition on individual substrates, others are very scalable and extremely cheap due to there being no more need for the high temperatures required to evaporate materials. There have been a number of reports of solution processed Sb_2Se_3 solar cells, however the highest efficiency achieved thus far is 3.9% [45], which in 2019 was some way below the record. It is likely that this is due to issues with crystallinity and orientation, with every report found for this work showing strong [010] and [120] orientations (see section 2.2.2) in the XRD patterns and smaller grain sizes than would usually be seen for PVD approaches in the scanning electron microscope (SEM) images [45, 73, 86]. This could potentially be a result of the presence of some solvent in the Sb_2Se_3 during the annealing step inhibiting crystallisation.

Configuration

The configuration of a solar cell refers to the order/direction in which the solar cell is made. In superstrate configuration, the window layer is first deposited onto a TCO-coated glass substrate and the absorber and metal contacts are in turn deposited atop these initial layers. In substrate configuration, the absorber is deposited first onto a metal layer (either on a glass or flexible substrate), with the window layer followed by a TCO deposited on top (2.16). There are advantages and disadvantages to both approaches and it varies with absorber technology which has the best success. The best

CIGS solar cells are made in substrate configuration while CdTe solar cells are typically made in superstrate configuration (although they also work in substrate). The pros and cons of each configuration depend largely on the individual layers, the way they deposit onto each other and the treatments they require pre- or post-deposition. For example, in CdTe there is a Cl_2 activation step which works best when applied to CdTe deposited on CdS because it has beneficial effects on the interface. Substrate solar cells, however, lend themselves better to depositing on flexible substrates, making them a better prospect for flexible solar cells.

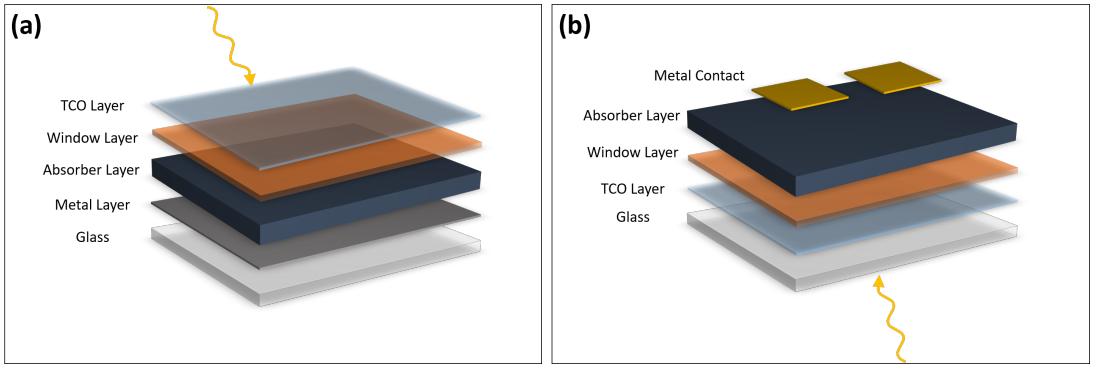

Figure 2.16 Schematic diagram of the basic cell design of (a) substrate and (b) superstrate configuration solar cells.

With Sb_2Se_3 solar cells still in a relatively early stage of development, it is not yet clear which configuration is preferred (if one is at all). It is straightforward to note that the record efficiency is currently held with a substrate cell [43]. However, this work had many innovations from the existing literature, including a nanorod Sb_2Se_3 structure and a titanium dioxide (TiO_2) interlayer at the interface between CdS and Sb_2Se_3. Looking further into the literature there ceases to be any trend in performance, with the next tier of efficiencies (>7%) being dominated by superstrate devices [46, 62, 68, 82, 87]. It must also be considered of course that the majority of works published on Sb_2Se_3 utilise the superstrate configuration, although this is not necessarily a reflection of its suitability for one configuration over the other and more likely a result of many Sb_2Se_3 researchers drawing on previous knowledge of CdTe solar cells. Ultimately, both configuration still hold promise and more research is needed to establish whether there is one better suited to Sb_2Se_3 than the other.

Window Layer Choice

The choice of window layer to partner an absorber is critical to the effective operation of the solar cell. One must consider the band gap of the material (as shown in section 2.1.1, too narrow a band gap can lead to losses), its lattice parameter (overly mismatched lattice parameters can cause interface defects) and all of the same scalability factors that

are considered for the absorber layer itself. The band alignment between window layer and absorber is also critical, and this will be discussed at length in Chapter 4.

The majority of the existing literature on Sb_2Se_3 solar cells uses one of two window layer choices - CdS or (TiO_2). CdS was the standard window layer for cadmium telluride for many years, making it well understood and familiar to many researchers. However, its band gap (2.45 eV) is a little low for an ideal window layer and it contains cadmium which is highly toxic (see section 2.1.3). TiO_2 is a popular window layer choice in solution-processed technologies, such as dye sensitised solar cells and perovskites, and has a wider band gap. It has multiple phases (brookite, rutile and anatase) of which anatase is the most popular as a window layer in PV. High efficiency devices have been achieved using both CdS and TiO_2 [46, 62, 87], as well as good efficiencies for alternative window layers such as ZnO [82], SnO_2 [88], CdS:O [68], and CdZnS [89]. There have also been a number of attempts with SnO_2 as a window layer, with slightly less success [45, 90, 91].

It has been reported that under certain circumstances the deposition of Sb_2Se_3 onto CdS can lead to significant interdiffusion of elements across the interface [57, 79, 92], which is not beneficial to device performance. Interestingly, the record Sb_2Se_3 cell uses a combination of CdS and TiO_2, incorporating a thin TiO_2 interlayer to block this interdiffusion. Window layers will be discussed further in Chapter 4.

Contacting

In many PV technologies additional layers or treatments are included to aid in the separation and transport of carriers. In perovskite solar cells, an intrinsic absorber layer is sandwiched by an electron transport material (ETM) and a hole transport material (HTM), forming an electron or hole selective contact on each side of the absorber. Many groups have postulated that, due to the weakly doped nature of Sb_2Se_3 [63, 80, 93], Sb_2Se_3 solar cells would benefit from the use of a HTM to aid carrier transport from Sb_2Se_3 to metal contact. The first example of a HTM being used in a conventional Sb_2Se_3 solar cell was by Chen *et al.*, who incorporated a PbS quantum dot layer between Sb_2Se_3 and Au in order to increase carrier lifetime and reduce the back contact barrier [80]. The 6.5% efficiency was a certified record at the time of publication, however PbS has not been reported in Sb_2Se_3 solar cells since. Many groups favour organic HTMs such as P3HT, spiro-OMeTAD or PCDTBT [45, 67, 81], although good efficiencies have also been achieved with inorganic HTMs [94, 95]. Organic layers have the advantage of being cheap and easy to deposit and many are already used in the perovskite field. Li *et al.* reported an increase in both J_{sc} and V_{oc} upon inclusion of spiro-OMeTAD or CZ-TA as HTMs, in part due to improved carrier collection at the long wavelength end of the EQE [67]. Guo *et al.* similarly reported improved J_{sc} and V_{oc} with the use of a NiO_x HTM attributed to improved collection as well as an electron reflection barrier at the back contact reducing recombination [94].

In the work carried out at the University of Liverpool, however, the use of a HTMs does not provide much benefit to the peak efficiency of the devices, but does improve the average efficiency of the devices [81]. In this case, the organic P3HT or PCDTBT layers act more as a pinhole blocking agent, filling pinholes and reducing the number of losses through shunting pathways or short circuited cells [96]. This is in some cases counteracted by a slight reduction in peak efficiency due to the addition of a resistive layer at the back contact. The difference in the effect of HTMs in this work compared to that of Chen *et al.* and Li *et al.* is attributed to the difference in carrier density in the Sb_2Se_3 films. Chen *et al.* quote the hole density of their films to be in the region of $10^{13}cm^{-3}$, whereas the films grown at the University of Liverpool have been found to exhibit n-type conductivity with a carrier density of roughly 10^{16}-$10^{17}cm^{-3}$ [62, 80].

Another technique often used to aid the performance of the back contact is chemical treatment of the Sb_2Se_3 layer prior to contacting, which will be discussed further in Chapter 6.

Defects

The defect chemistry of Sb_2Se_3 is complex and has recently come to be considered by many to be the most significant obstacle to the development of Sb_2Se_3 into a competitive PV technology. Defect chemistry is crucial to the performance of a material within a solar cell due to its influence on carrier density, carrier lifetime and carrier diffusion length. Defects are electronic states within the band gap that are introduced via a crystallographic or compositional defect in the material. These defects include vacancies (V_X), in which an atom of element X is missing from its position in the lattice, interstitials (X_i), in which an atom of element X lies away from a lattice site, and antisites (X_Y) in which an atom of element X sits in the place of an atom of element Y. Electrons and holes within the valence and conduction bands that encounter one of these defects can relax into occupying one of these defect levels. Defects can be broadly separated into two categories - shallow defects and deep defects. Shallow defects lie close to the valence or conduction band edges and can act either as electron donors (increasing the n-type conductivity of the material) or as electron acceptors (increasing the p-type conductivity of the material). Carriers that drop into these traps can return to the bands if the energy separation is sufficiently small and the energy available to the system sufficient. Shallow defects, therefore, do not cause such a detriment to the carrier lifetime and in fact are beneficial to increasing the overall carrier concentration of the material. However, deep defects lie far in energy within the gap and carriers that are caught in these so-called traps will recombine. A high density of deep defects is therefore extremely deleterious to device performance due to an increase in recombination rates and reduction in carrier lifetime and diffusion length.

In 2017, Liu *et al.* reported that Sb_2Se_3 photovoltaic device performance could be improved through compensation of Se vacancies in the material [61]. DFT calculations were performed for both Se-rich and Se-poor Sb_2Se_3 and the formation energies

of the 5 primary defects were calculated for different Fermi level energies. They found that under Se-rich conditions, the dominant defects (those with the lowest formation energy) were Se_{Sb} and Se_i, both shallow acceptors and therefore beneficial for p-type Sb_2Se_3 such as that studied in that work. For the Se-poor calculations, it was found that the V_{Se} and Sb_{Se} became dominant, both deep lying donors and therefore harmful to the device performance of p-type Sb_2Se_3. This work highlighted the key role that defect control could have in the design and performance of Sb_2Se_3 solar cells, and the conclusions were supported by experimental evidence of improved device performance when depositing Sb_2Se_3 in a Se-rich environment. Savory *et al.* carried out a similar but more thorough study in 2019, in which they showed a deeply complex defect chemistry [85]. This work showed the various defect formation energies for both Se-rich and Sb-rich (called Se-poor here for easy comparison) with an added layer of specificity for the vacancies and antisites of each different Sb and Se site. The conclusions of this work backed up the conclusions of Liu *et al.* [61], with Se vacancies and Sb_{Se} antisites dominating in the Se-poor regime and lying deep in the band gap. Additionally, it is suggested that the transition energies of the different defects could lead to Fermi level pinning mid-gap through compensation. In the Se-rich regime, many of the problematic defects (V_{Se} & Sb_{Se}) are much higher in formation energy, indicating that they will be less prevalent in the material. These are replaced by V_{Sb}, Se_{Sb} and Se_i, with only the Se_i state lying deep within the gap. However, it is still shown that the Fermi level is likely to be pinned at 0.62 eV above the VBM, in the middle of the gap. This highlights the role that defect states can play in carrier density as well as in recombination, with the Fermi level pinning a sign that the maximum achievable carrier density of Sb_2Se_3 would be limited unless the problematic defects could be eliminated.

Experimental evidence has also been provided for the presence of deep defects in Sb_2Se_3, however the experimental results are to some extent inconsistent. In 2018, Hu *et al.* used admittance spectroscopy to identify three deep lying defects in Sb_2Se_3 solar cells, situated at 300-400, 200-600 and 500-600 meV above the VBM. Later, in 2020, Hobson *et al.* used deep level transient spectroscopy (DLTS) to identify four deep lying defects in Sb_2Se_3 bulk crystals and devices, situated at 358-378, 447-460, 685-690 and 505 meV below the CBM (802-822, 720-733, 490-495 and 675 meV above the VBM). Wen *et al.* achieved similar results in 2018, also using DLTS of efficient devices, with deep levels at 480-490, 710-740 and 580-590 meV above the VBM. Consistently across all three studies there is report of a defect state lying $\sim$500 meV above the valence band, and Wen *et al.* and Hobson *et al.* both report another level $\sim$700 meV above the VBM, however this is where the similarities end. While the results are confusing, this highlights the complexity of the defect chemistry of Sb_2Se_3 thin films, with the deposition process and film quality likely having a significant impact on the defect properties of the film. The combination of bulk crystal and CSS-deposited thin film results in the work by Hobson *et al.* goes some way to suggesting that grain boundaries do not contribute significantly to the defect density, however the films grown for the study (as well as those in the study by Wen *et al.*) consist of large, well-oriented grains with a

high device efficiency (>7%), therefore the impact of grain boundaries in lower efficiency devices cannot be discounted.

The conclusion that can be drawn from both theory and experiment regarding the defect chemistry of Sb_2Se_3 is that it is complex and likely to limit device efficiency if not addressed. It seems likely that Se-rich Sb_2Se_3 goes some way towards passivating some of the more harmful defects, as well as enhancing the p-type conductivity of the absorber. However, this raises further questions regarding the desired conductivity of Sb_2Se_3, with some reports of high efficiency devices using extrinsically doped, n-type Sb_2Se_3 [62, 97]. This extrinsic doping in fact ties in well with work carried out by Stoliaroff *et al.*, in which they performed calculations that indicated a good solar cell performance from halogen doped, n-type Sb_2Se_3. This hints at a potential solution which may include passivating deep level defects through the introduction of an extrinsic dopant which would simultaneously improve the conductivity of the material.

Other Antimony Chalcogenides

It is noteworthy here that there is a parallel avenue of investigation into the PV applications of Sb_2S_3. Sb_2S_3 bears many of the same advantages for PV as Sb_2Se_3, having the same nanoribbons structure in the same space group setting and similarly cheap and safer elements. The band gap of Sb_2S_3 is higher at ~1.7-1.8 eV [98], making it well suited to be a top cell in a tandem cell with a Si bottom layer. Meanwhile, the solid solution $Sb_2(S,Se)_3$ has also attracted attention. The mixing of the sulfide and selenide compounds allows for band gap engineering and greater control over the structure, grain size and defect chemistry through adjusting the S/Se ratio. $Sb_2(S,Se)_3$ recently achieved the significant milestone of a record efficiency of 10% through the use of hydrothermal deposition and careful tuning of the S/Se ratio [99]. Both of these fields of research naturally hold great relevance to Sb_2Se_3 research and advances in these technologies are useful and informative to the development of Sb_2Se_3 solar cells. However, they are not discussed further in this work so as not to extend the scope beyond what can be reasonably contained within a thesis.

Summary

This review summarises the progress made in the field of Sb_2Se_3 PV up to March 2021. It shows that Sb_2Se_3 solar cells have been subject to much development and innovation in recent years, and the rate of improvement in efficiency has been remarkable. Many of these advancements have been made during the last 4 years in parallel with this project and the understanding of Sb_2Se_3 as a PV absorber is continually developing. Certain aspects of the device making process have become established standards, such as orientation control and deposition method. However in other areas there remain many questions, such as the best configuration, window layer choice and back contact treatment. Coupled with a gap in knowledge of certain fundamental properties such as electronic conductivity, there remains a wealth of knowledge to be gained. The answers

to these questions are likely the key to taking Sb_2Se_3 solar cells to the next level in performance.

Author	Year	Journal	Efficiency	Certification	Deposition Method	Configuration	Window Layer	HTM	Reference
Li *et al.*	2019	Nature Comms.	9.2%*	Yes	CSS	Substrate	CdS+TiO_2	None	[43]
Wen *et al.*	2018	Nature Comms.	7.6%*	Yes	VTD	Superstrate	CdS	None	[46]
Tao *et al.*	2019	Nano Energy	7.5%	No	VTD	Superstrate	CdS	None	[87]
Shen *et al.*	2020	Advanced Science	7.45%	No	CSS	Superstrate	CdS	Trigonal Se	[100]
Hobson *et al.*	2020	Chemistry of Materials	7.3%	No	CSS	Superstrate	TiO_2	None	[62]
Guo *et al.*	2019	Solar RRL	7.01%	No	CSS	Superstrate	CdS:O	None	[68]
Li *et al.*	2019	ACS Appl. Mater. & Int.	6.71%	No	CSS	Substrate	CdZnS	None	[89]
Shiel *et al.*	2019	J. Phys Energy	6.63%	No	CSS	Superstrate	TiO_2	None	[37]
Hutter *et al.*	2018	Sol. Mat.	6.6%	No	CSS	Superstrate	TiO_2	PCDTBT	[81]
Chen *et al.*	2017	ACS Energy Lett.	6.5%*	Yes	RTE	Superstrate	CdS	PbS QD	[80]
Zhang *et al.*	2019	Solar Energy	6.5%	No	VTD	Superstrate	CdS	NiO_x	[101]
Williams *et al.*	2020	ACS Appl. Mater. & Int.	6.18%	No	CSS	Superstrate	TiO_2	None	[75]
Hutter *et al.*	2018	WCPEC-7	6.06%	No	CSS	Superstrate	TiO_2	P3HT, PTB7	[65]
Tang *et al.*	2019	Nano Energy	6.06%	No	RF Sputtering	Substrate	CdS	None	[44]
Wang *et al.*	2017	Nature Energy	5.93%	Yes	RTE	Superstrate	ZnO	None	[39]
Liu *et al.*	2017	Progress in PV	5.76%	No	TE	Superstrate	CdS	None	[61]
Chen *et al.*	2017	Adv. Energy Mater.	5.6%	No	RTE	Superstrate	TiO_2	None	[38]
Zhou *et al.*	2015	Nature Photonics	5.6%*	Yes	RTE	Superstrate	CdS	None	[78]
Phillips *et al.*	2019	IEEE JPV	5.48%	No	CSS	Superstrate	TiO_2	P3HT	[57]
Guo *et al.*	2019	Solar Energy	4.5%	No	RTE	Superstrate	CdSe	Graphite	[102]
Li *et al.*	2018	Solar Energy	4.45%	No	RTE	Superstrate	MZO	None	[72]
Tiwari *et al.*	2018	WCPEC-7	4.3%	No	e-beam	Substrate	CdS	None	[103]
Wang *et al.*	2019	Sol. Mat.	3.9%	No	Solution	Superstrate	TiO_2	P3HT	[45]
Leng *et al.*	2014	Appl. Phys. Lett.	3.7%*	No	TE	Superstrate	CdS	None	[77]
Liu *et al.*	2014	ACS Appl. Mater. & Int.	2.1%*	No	TE	Substrate	CdS	None	[59]
Luo *et al.*	2014	Appl. Phys. Lett.	1.9%*	No	TE	Superstrate	CdS	None	[104]

Table 2.2 Table summarising notable publications on Sb_2Se_3 solar cells between 2014 and March 2021. High reported efficiencies have been included along with unusual device structures or deposition techniques and notable landmark publications in the history of Sb_2Se_3 solar cell development. An asterisk is used to mark efficiencies that were a world record at the time of publication.

Chapter Three

Methods

In this chapter the principles behind the experimental methods used throughout the work are presented. This includes a short overview of the fabrication methods used to deposit thin films or grow bulk crystals as well as the methods used for materials and device performance characterisation. Particular attention was given to photoemission techniques, as these were a central and common factor running through all of the work carried out in this project.

3.1 Fabrication

In this section is a brief overview of the methods used to deposit thin film layers for the solar cells studied in this thesis, as well as the method used to fabricate bulk crystals for photoemission studies.

3.1.1 Thermal Evaporation

Thermal evaporation is a straightforward PVD technique but a very useful one. The source material (usually in the form of powder or small pieces) is placed into a crucible or boat. Depending on the deposition temperature required and the reactivity of the material being deposited different metals can be selected, with metals such as molybdenum and tungsten being popular choices. The boat is heated by passing a direct current through it until the source material melts and evaporates. Boat and substrate are held in a chamber which is evacuated to a high vacuum in order to ensure a long mean free path of the vapour phase. The deposition rate can be monitored using a quartz crystal microbalance (QCM) allowing excellent control of the film thickness ($\sim$1 nm precision). Additionally, during deposition the substrate can be heated to aid crystallisation of the film, or the substrate can be left unheated (usually meaning an amorphous film). In order to avoid non-uniformities as a result of a variation in working distance, the substrate is usually rotated during deposition [105].

The evaporation system used in this work operated at a base pressure of approximately $\sim 5 \times 10^{-5}$ mbar with a working distance (between boat and substrate) of approximately $\sim$20 cm. Deposition rate was monitored using a QCM and samples were rotated

during deposition.

3.1.2 Close Space Sublimation

CSS is a specialised form of PVD in which the source material sublimes (rather than melting and evaporating), allowing vapour deposition at a temperature below the material's melting point. Due to the higher pressure (∼10 mbar) than typically used for thermal evaporation or sputtering, the substrate is held very close to the source material to account for the reduced mean free path of the vapour phase [106, 107]. In CSS deposition, the source and substrate temperatures can be controlled independently (although due to the close proximity, some heating of the substrate from the source heating is unavoidable) and an inert or reactive gas atmosphere can be employed during deposition to aid crystallisation. Figure 3.1 shows a schematic diagram of a typical CSS setup. CSS is an industrially scalable technique and has achieved great success in the CdTe industry.

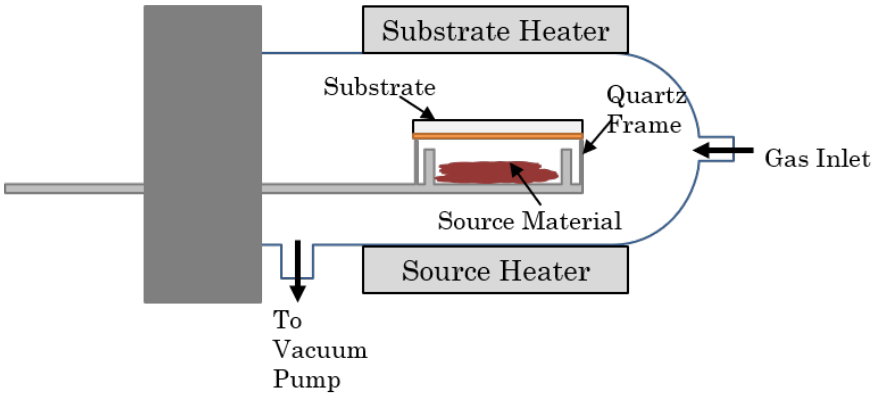

Figure 3.1 Schematic diagram of the typical CSS setup used to deposit the films studied in this work.

The CSS system used in this work was comprised of a high purity quartz glass chamber, substrate holder and source tray, a tungsten coil heater for the source and an infrared ceramic heater for the substrate. The working distance between source and substrate was approximately 5 mm. A range of gases are available for deposition however N_2 was used for all depositions in this work. More detailed deposition parameters are provided in the relevant results chapters.

3.1.3 Radio Frequency Sputtering

RF magnetron sputtering is a well-established PVD technique used in industrial thin film deposition. It is a versatile technique for depositing pure and uniform films of a wide variety of materials. It particularly holds an advantage for materials with very high melting points, which would be difficult to evaporate via resistive heating, because the

source material does not need to be evaporated [105, 106]. It works instead by exposing a target of the source material to an Ar^+ ion plasma. With the aid of an electric field, the ions bombard the target and cause atoms to be ejected from the target surface. The material then diffuses to the substrate and deposits onto the surface. A schematic diagram is shown in Figure 3.2. The electric field can be generated in a number of ways - in this case a radio-frequency alternating current is used. Magnetrons are also employed to aid in the formation of the plasma at lower chamber pressures by trapping electrons in a magnetic field and enhancing ionisation. They also help to localise the plasma at the target surface and prevent unintentional sputtering of other surfaces which could lead to contamination in the deposited film [105]. The deposition is carried out at a high vacuum to maximise the mean free path of the atoms ejected from the target. Substrate heating can be employed to aid in crystallisation of the material on the substrate and the substrate is usually rotated during deposition to ensure uniformity.

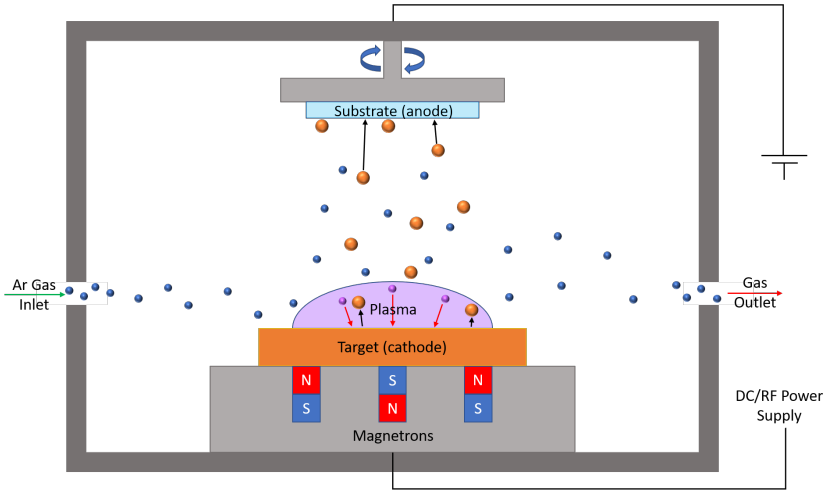

Figure 3.2 Schematic diagram of the typical sputtering chamber used to deposit the thin films studied in this work.

In this work, sputter deposition was carried out via RF sputtering in AJA International Inc. ATC Orion chambers, with a base pressure of $\sim 10^{-6}$ mbar. The working distance between source and sample was approximately 15 cm and the working gas used was Argon, at a pressure of $\sim 5 \times 10^{-3}$ mbar. More specific deposition parameters are included in the relevant results chapters.

3.1.4 Spin Casting

Spin casting is a form of solution processing popular on the laboratory scale due to its proficiency in achieving uniform films easily for a variety of materials [106]. While not suitable for industrial scale (due to difficulty in spinning large substrates) it can be seen as a stepping stone to far more scalable solution processing techniques which are

desirable in industry. Spin casting works by placing the substrate on a turntable and rotating it at a speed usually several thousand rpm. The solution is then dropped in the centre and the substrate and the centrifugal force drives the solution to the edges of the substrate, leaving a uniform film. The air flow during the spinning process also dries off the solvent, although it also leads to a lot of material being cast off the edges of the substrate, meaning that it is a somewhat wasteful process. The thickness of the films can be controlled by varying the concentration of the solution and the spin speed. It is also common to utilise multiple spinning steps with slightly different conditions [106].

3.1.5 Bridgman Melt Growth

Bridgman melt-growth is a well-established and reasonably straightforward method used to grow bulk crystals. The method involves putting granules or powder of the desired material in a container (in this case a quartz tube) and heating it until the material, or mix of materials, is melted and has had time to homogenise. It is possible to do this with purchased Sb_2Se_3 granules or by weighing out the correct quantities of Sb and Se. The weighing of one's own material allows for a high degree of tunability as well as the controlled introduction of extrinsic dopants into the melt. The tube is sealed, usually containing either a vacuum or inert gas to prevent any contamination from the air.

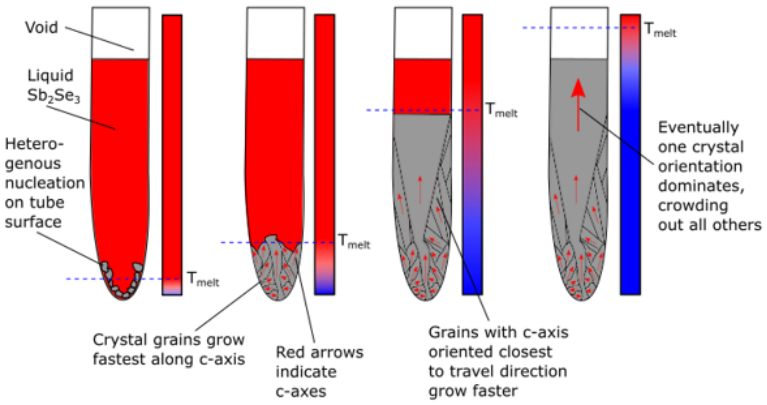

Figure 3.3 Diagram showing the formation of bulk crystals during melt growth with preferred growth direction coming to dominate [34].

Once the melt has had time to fully homogenise (to avoid regions of Sb or Se richness within the crystal) it is cooled at one end of the container, forming a temperature gradient. The container is then drawn, very slowly, through the temperature gradient, as depicted in Figure 3.3, while also being rotated to ensure even heating and cooling of the melt on all sides. As the melt cools, crystals are formed. As the container passes through the temperature gradient, the crystals at the end act as a seed crystal to those being formed further along and the preferred orientation will begin to dominate (because

growth is faster along that direction). This means that the crystals increase in size as the growth progresses and ultimately large crystals can be grown (Figure 3.3).

3.2 Photoemission

Photoemission spectroscopy is an exceptionally powerful and versatile group of techniques for characterisation of the chemical and electronic properties of a material. There are numerous variants depending on the source of electromagnetic radiation and the acquisition setup. Photoemission techniques can be used to investigate the chemical composition of a material, the valence band density of states (DOS), natural band alignment positions, surface band bending, band offsets between materials and many other quantities. It does, however, require great care and precision when making measurements, as well as a very specific and somewhat challenging measurement environment. In this section we will discuss the principles and theory of photoemission as well as the practicalities of data talking and data analysis. We will also lay out the differences, strengths and weaknesses of the different variants used within this thesis, including x-ray photoemission spectroscopy (XPS), ultraviolet photoemission spectroscopy (UPS) and hard x-ray photoemission spectroscopy (HAXPES).

3.2.1 Principles & Theory

The Photoelectric Effect

The principle of photoemission spectroscopy relies on the photoelectric effect. When electromagnetic waves are incident on a material, bound electrons can absorb the energy from these photons and acquire enough energy to escape the material with some kinetic energy (KE). First, an electron must absorb the energy of a photon that has energy greater than the binding energy (BE) of that electron. This electron is then ejected from its orbital and moves to the surface of the material. The electron may or may not undergo inelastic scattering during this step. When the electron reaches the surface of the material it must then have enough energy to overcome the work function of the surface, ϕ_S in order to escape. If it does this, it will escape the surface with a given kinetic energy which can be measured by the analyser.

$$\mathrm{BE} = \mathrm{h}\nu - \mathrm{KE} + \phi_S \tag{3.1}$$

Ignoring possible scattering interactions for the moment, the kinetic energy of the electron can be used to determine the binding energy of the orbital it originated from using equation 3.1. The energy of the photon ($\mathrm{h}\nu$) is completely absorbed and the kinetic energy of the electron after leaving the sample would therefore be equal to the photon energy minus the energy required to remove the electron first from the orbital (BE) and then from the surface of the material (ϕ). If the electrons were to escape the surface material without undergoing any scattering processes, the spectrum measured would consist only of very sharply defined peaks at the energies characteristic of the orbitals

of the studied material. In reality, many of the electrons undergo inelastic scattering which reduces their energy, leading to background signal across the spectrum, with the characteristic peaks superimposed on top. There are a number of other features in the spectrum which will be discussed below.

Photoionisation Cross-Sections

The interaction between bound electrons and incoming photons that leads to an electron being liberated from its parent atom has a given cross-section. This cross section varies with both the energy of the photon and the electronic environment of the electron. The photoionisation of an electron is a dipole transition between an initial state, Ψ_i, and a final state, Ψ_f, that lies in the continuum (equation 3.2). The cross section, σ, is therefore proportional to the sum of the squares of the dipole transition moment, M_{fi}, over all available final states (equation 3.3) [108].

$$\mathrm{M}_{fi} = \langle \Psi_f | \mathrm{r} | \Psi_i \rangle \tag{3.2}$$

$$\sigma \propto \sum \mathrm{f} |\mathrm{M}_{fi}|^2 \tag{3.3}$$

As the incident photon energy increases, the kinetic energy of the electrons increases and the wavelength of the continuum states shortens. As the wavelength of the continuum states becomes comparable with the radial extension of the orbitals, terms in the transition moment matrix cancel and the cross section decreases. The different geometries of the various orbitals cause the cross sections to decay at varying rates - in particular, s orbitals are more contracted and therefore the cross sections decrease more gradually than p, d or f orbitals. This phenomenon has a number of implications on the use of varied energy synchrotron-based photoemission. For example, light contaminant elements such as C or O show far less prominently in the core level spectrum at higher photon energies because the only detectable core levels are s-orbitals. Perhaps more interesting is the influence on the valence orbitals, in which the orbital contributions can vary significantly. This changes the shape of the valence band spectrum and can shed light on the electronic structure of the valence band and bonding mechanisms. This will be discussed further in Chapter 5.

Escape Depth

All photoemission spectroscopies are considered surface sensitive techniques. While the incoming x-rays penetrate deeply into the material (depending on how high their energy), the escape depth of the photoelectrons is determined by their inelastic mean free path (IMFP). This describes the distance on average that an electron will travel between undergoing some sort of inelastic scattering event and losing kinetic energy. Depending on the material and the kinetic energy of the electrons, this can vary but generally falls within the range of 0 - 10 nm. The IMFP can be calculated for any given material and

any electron energy by using the TPP-2M equation, as shown in equations 3.4 & 3.5. This equation was first proposed by Tanuma, Powell and Penn (TPP) and was derived from theoretical calculations of the IMFP of 27 different compounds [109, 110].

$$\lambda = \frac{\mathrm{E}}{E_p^2 \left[\beta \ln(\gamma \mathrm{E}) - \left(\frac{C}{E}\right) + \left(\frac{D}{E^2}\right)\right]} \tag{3.4}$$

$$\beta = -0.10 + 0.944 \left(E_p^2 + E_g^2\right)^{-0.5} + 0.069\rho^{0.1} \tag{3.5}$$

where $\gamma = 0.191\rho^{-0.5}$, $\mathrm{C} = 1.97 - 0.91U$, $\mathrm{D} = 53.4 - 20.8U$ and $U = \frac{N_\nu \rho}{M} = \frac{E_p^2}{829.4}$. If one knows the density of the material, ρ (g.cm^{-3}), the number of valence electrons per atom/molecule, N_ν, the band gap, E_g (eV), and the atomic or molecular weight, M, the IMFP, λ (Å), can be calculated for any electron kinetic energy, E.

The intensity decay of a beam of electrons travelling from a depth, d, through a solid is given by the Beer-Lambert law as:

$$\mathrm{I(d)} = \mathrm{I}_0 e^{-d/\lambda} \tag{3.6}$$

Accordingly, 63% of the electrons that escape the sample during photoemission will have originated within one IMFP of the sample surface, 86% within two IMFPs of the surface and 95% within three IMFPs of the surface. It is clear therefore, that while the signal is dominated by the near surface of the sample, information can be obtained about regions much further from surface. It is also evident that increasing the IMFP of the electrons leads to a significantly greater effective probing depth of the measurement.

3.2.2 Detection

Analyser

One factor which is predominantly unchanged across any photoemission technique is the electron energy analyser. The analyser receives the photoelectrons emitted from the sample and measures their kinetic energy, outputting a spectrum of counts/intensity with respect to the binding energy (kinetic energy is sometimes used but binding energy is the common convention). The most common type of electron energy analyser (and the type used in this work) is a hemispherical analyser, which is shown in Figure 3.4. The operation of a hemispherical analyser can be broken down into three stages. First, a series of electromagnetic lenses is used to focus and accelerate/decelerate the incoming electrons (depending on the kinetic energy of the incoming electrons). Secondly, the electrons enter the hemisphere where they are subject to a potential which causes their path to bend. The potential is set so that only electrons of a certain narrow range of energies (known as the pass energy, E_{Pass}) will reach the other side without colliding with the walls of the hemisphere. Lastly, the electrons that are channelled to the other side of this hemisphere are collected, usually by a number of channeltrons. To sweep through

the assigned range of kinetic energies the retardation potential (a potential applied by the lenses to reduce the kinetic energy of the incoming electrons) is varied, and therefore the pass energy of the hemisphere remains unchanged throughout the sweep.

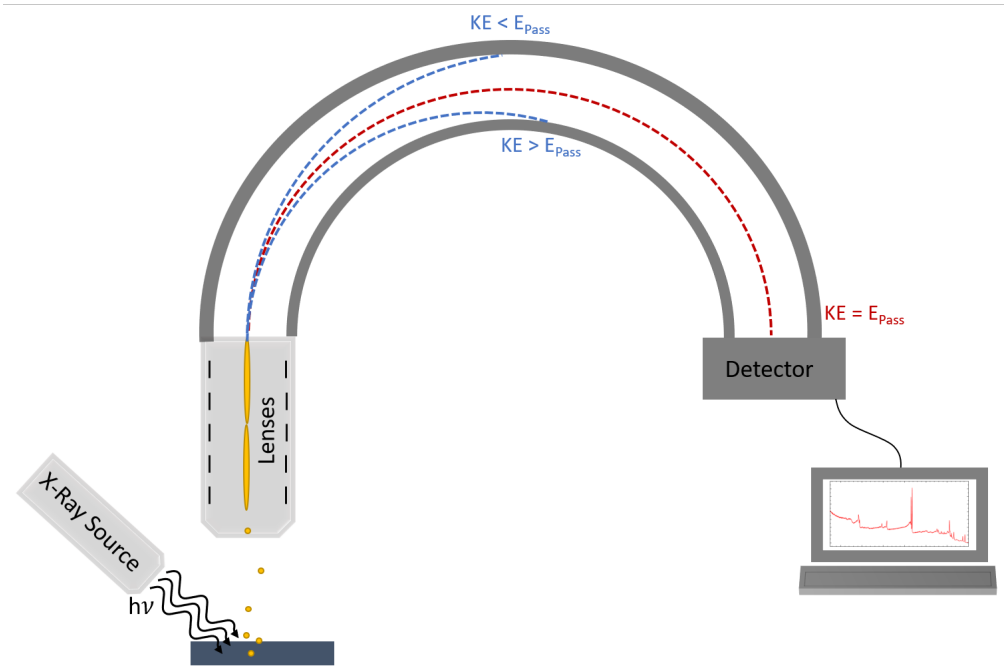

Figure 3.4 Schematic diagram of an electron energy analyser. Blue dashed lines show the trajectory of electrons with kinetic energy greater or less than the pass energy. The red dashed line shows how electrons with kinetic energy equal to the pass energy will be directed into the detector.

As mentioned above, electrons undergo a loss of kinetic energy upon leaving the sample due to the need to overcome the sample work function, ϕ_S. This means that the kinetic energy of an electron upon leaving the sample is given by

$$\mathrm{KE}^* = \mathrm{h}\nu - \mathrm{BE} - \phi_S \tag{3.7}$$

A similar process occurs in reverse upon the electron entering the analyser; the analyser has its own work function, ϕ_A, and the electron will gain some kinetic energy upon entering it. Therefore, the kinetic energy measured, KE, is different to the kinetic energy of the electron upon leaving the sample and is dependent on both work functions. However, because the analyser and the sample are connected electrically for photoemission measurements, the Fermi levels of the analyser and sample align. Therefore, as shown in Figure 3.5 and equations 3.8 & 3.9, if ϕ_A is known, the measurement becomes independent of the work function of the sample, ϕ_S.

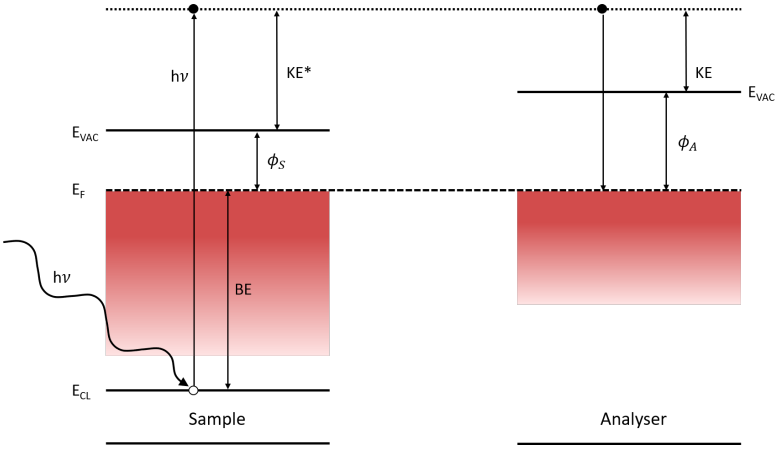

Figure 3.5 Band diagram showing the relation between binding energy, kinetic energy and work functions during photoemission measurements.

$$\mathrm{KE} = \mathrm{h}\nu - \mathrm{BE} - \phi_S - (\phi_A - \phi_S) = \mathrm{h}\nu - \mathrm{BE} - \phi_A \tag{3.8}$$

$$\mathrm{BE} = \mathrm{h}\nu - \mathrm{KE} - \phi_A \tag{3.9}$$

Ultra-High Vacuum

As mentioned above, the IMFP of electrons through a solid is of the order of a few nanometres. While this is significantly greater in a gaseous medium, it is still necessary to reduce as far as possible any possibility that electrons will collide with gas molecules before being detected. This is one of the reasons that photoemission measurements are almost exclusively carried out under ultra-high vacuum (UHV), typically within the range of 10^{-11} - 10^{-8} mbar for standard XPS. UPS requires a supply of He gas into the chamber (as discussed in more details below) and therefore will operate at pressures nearer 10^{-5} mbar.

Another reason for the use of a UHV environment is the need for a clean environment, with no reactive gases present. In particular, oxygen is of course abundant in atmospheric conditions, but its reactivity can cause issues in a photoemission experiment. A simple example is the use of a heated filament and anode in the x-ray source - in an oxygen containing atmosphere the metals that make up these components will oxidise, meaning the incoming x-rays would no longer be well known or uniform in energy. It is also important to keep any foreign contaminants from adsorbing onto the sample surface. It is naturally very difficult to completely prevent a sample from being exposed to atmospheric contamination, however it is crucial to prevent any alteration of the sample during the measurement, lest the results be affected.

Sample Requirements

Photoemission measurements can be carried out on practically any material, however for sustainable usage of a laboratory setup the samples must comply to certain criteria. As mentioned above, while it is difficult to completely prevent low levels of contamination, every effort should be made to keep samples clean of contamination such as dust, fingerprints or moisture. Furthermore, samples need to be stable under both x-ray irradiation and vacuum - some materials are prone to out-gas and this can negatively affect the UHV setup as well as ruin the reliability of the measurement. For the same reason, it is always recommended that it be well known what elements make up the sample, as the presence of a foreign element that is not stable under UHV conditions could lead to unanticipated consequences.

3.2.3 X-Ray Photoemission Spectroscopy

XPS is the most common form of photoemission experiment and generally uses x-rays of energy between 1 keV and 1.5 keV (although some sources can have energies up to 2-4 keV). It is widely used for a range of applications and gives a large amount of information about chemical composition, electronic structure and electronic behaviour simultaneously.

Source

XPS can be performed with a range of x-ray sources but all work on the same principle. A filament is heated by a direct current until thermionic emission of electrons begins. These electrons are accelerated toward an anode of a carefully selected metal by a high voltage. The bombardment of these electrons into the anode material generates characteristic x-rays with energies as shown in Figure 3.7. The anode is likely to heat up a great deal upon being bombarded and is therefore continuously cooled by circulating water throughout operation. The x-rays are directed onto the sample, passing through a very thin piece of aluminium foil as they exit the gun. The most common x-ray anode used is aluminium, and has a characteristic Kα x-ray energy of 1486.6 eV. However, dual anodes are also popular because they provide a choice of two x-ray energies (the uses are discussed in section 3.2.6) and magnesium and silver are two examples of popular choices of anode to partner Al.

When plotting the XPS spectrum it is assumed that all of the incident x-rays are of the same energy, however as shown in Figure 3.7, a range of x-ray energies are produced. Some x-rays are generated via bremsstrahlung radiation, in which electrons that are slowed by the nuclei of the target metal emit a continuum of x-ray energies. Additionally, some characteristic x-rays are generated by electrons interacting with bound electrons in the target material and causing secondary electrons to be ejected. A higher energy electron may then relax into this vacated state, discharging an x-ray of a characteristic energy in the process. These characteristic peaks are shown superimposed on

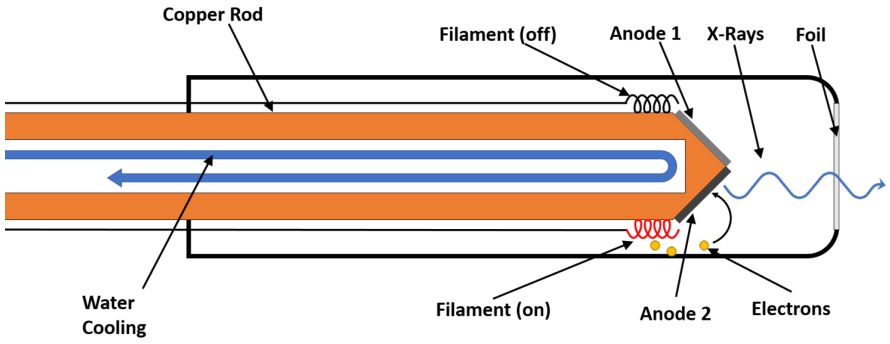

Figure 3.6 Schematic drawing of a standard dual-anode x-ray source.

the bremsstrahlung continuum in Figure 3.7. The bremsstrahlung x-rays are largely suppressed by the aluminium foil window, however the other characteristic x-ray peaks, from less dominant transitions, lead to smaller peaks, a shadow of the Kα spectrum, to slightly lower binding energy throughout the spectrum. These satellite peaks, as they are known, can be removed from the spectrum by monochromating the x-ray source. It is important to remember that these lines to not represent any distinct orbitals in the sample. The binding energy of the electron is in fact the same, however the peak is shifted due to the way the spectrum is plotted using equation 3.1.

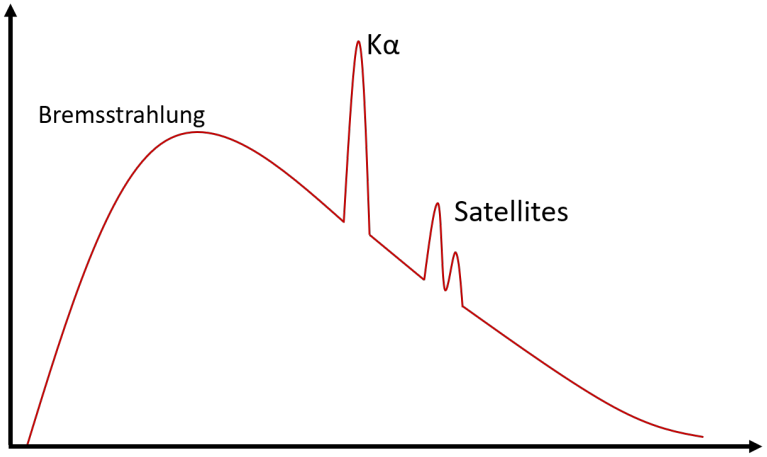

Figure 3.7 Sketch depicting the x-ray emission spectrum including a bremsstrahlung background and characteristic x-ray peaks.

X-rays can be monochromated upon exiting the x-ray source by taking advantage of Bragg's condition for diffraction (equation 3.10). The x-rays are directed towards a crystal, for example a quartz $(10\bar{1}0)$ crystal, with a well known lattice separation, d. In order to select the desired wavelength, λ, the crystal is oriented so that the Bragg angle,

θ, allows constructive interference of the desired wavelength and redirection of the now monochromated beam towards the sample. The crystal can also be curved, which allows for a focused beam of monochromated x-rays with a spot size far smaller then what can be achieved with an unmonochromated source.

$$2\mathrm{d}\ \sin(\theta) = \mathrm{n}\lambda \tag{3.10}$$

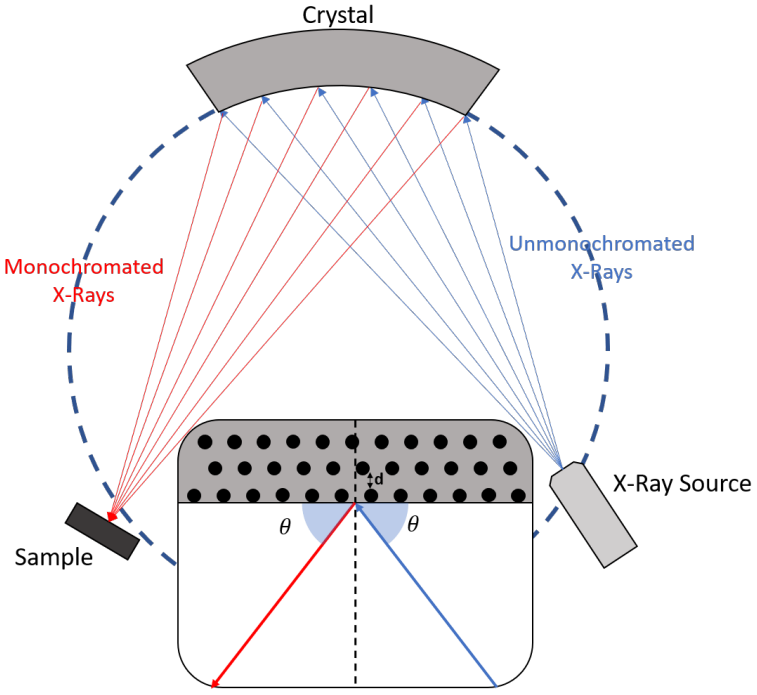

Figure 3.8 Schematic diagram of how x-rays are monochromated using Bragg diffraction.

Spectral Features

A typical XPS spectrum contains within it numerous features. The most obvious and most commonly used are the core levels (labelled in red in Figure 3.9). These are electrons ejected from core orbitals in the atom and appear at characteristic binding energies of the orbital they originated in. They therefore act as a fingerprint of the element they originated from. The core level peak positions can also be altered according to the bonding environment of the parent atom [111]. This phenomenon is known as a chemical shift and is invaluable in identifying things such as phase impurities, contamination or degradation in a material [37, 112]. It is also extensively used to identify different bonding environments in materials that have many bonding environments such as in polymers [113, 114]. This shift is not an artefact of the x-ray source, but represents a physical difference in the sample. When an atom is bonded to another atom this causes the binding

energies of the electron orbitals to be altered slightly due to variations in bond lengths and oxidation states, which means that an electron ejected from a metallic copper atom (for example) would have a subtly different binding energy to an electron ejected from a copper atom within Cu_2O. These binding energy differences can be resolved in XPS, and often a core level spectrum will contain two or more chemically shifted peaks for the same element. This makes core-level XPS a very useful tool for identifying contamination or secondary phases in a material.

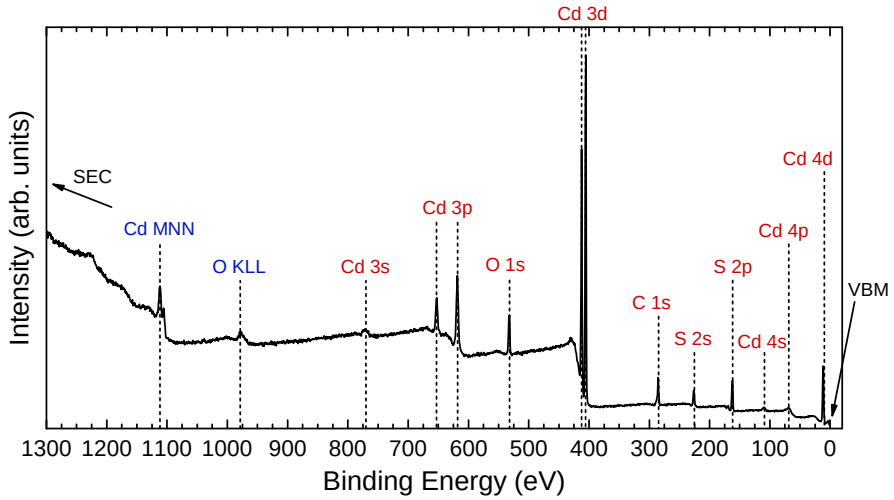

Figure 3.9 An example XPS spectrum from a measurement of a cadmium sulphide sample. Core levels are labelled according to their element and orbital in red and auger lines are labelled according to the orbitals involved in the auger transition in blue.

In most XPS spectra there are also Auger lines (labelled in blue in Figure 3.9). These look similar to core levels but are usually broader and are composed of a few clusters of very closely spaced peaks. These signals are from Auger electrons. When a core level electron is ejected from an atom (Figure 3.10a), sometimes an electron from a higher shell will drop down to take its place, usually emitting an x-ray in the process (Figure 3.10b). However, occasionally the electron will instead transfer its energy to another electron, which is then ejected with a characteristic energy of the transition (Figure 3.10c). The ejected electron is known as an Auger electron and its kinetic energy is independent of the energy of the original incoming photon. For this reason, the positions of Auger peaks on a binding energy scale vary with different photon energies (because they have fixed kinetic energy in equation 3.9) [111]. This is one of the advantages of using different anode materials in XPS - if an Auger line is inconveniently placed in the binding energy spectrum so that it is obscuring a core level feature that one wishes to analyse, using a different photon energy effectively moves the Auger peaks.

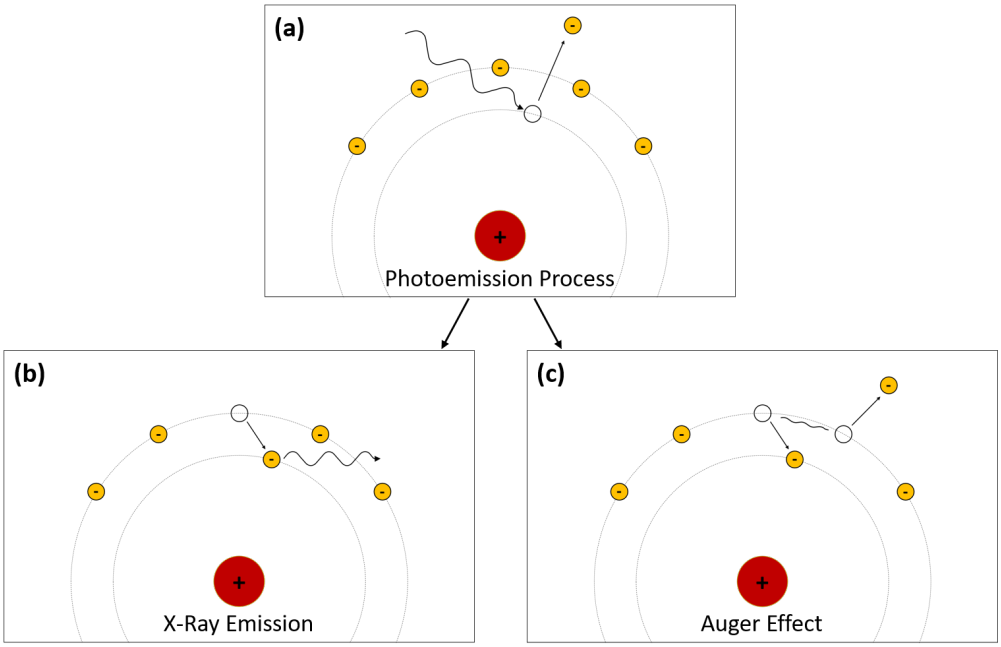

Figure 3.10 (a) The photoemission process with the two possible modes of relaxation - (b) the emission of an x-ray and (c) the Auger process.

At each end of the XPS spectrum is a cut-off. To the higher binding energy side, the spectrum rises until it reaches what is known as the secondary electron cut-off (SEC), as shown in Figure 3.11a. At this cut-off the signal is completely made up of secondary electrons and inelastically scattered electrons with only just enough kinetic energy to overcome the work function of the sample surface (effectively zero kinetic energy when leaving the sample). Therefore, from equation 3.7, $\phi_s = h\nu$ - SEC. This cut-off is therefore an extremely useful quantity to measure [115]. However, because of the exceptionally high count rate at the SEC it is difficult to measure without saturating the detector with too many electrons. It is necessary to reduce the flux of photons significantly as well as employ slits in the analyser to prevent too many electrons from entering the detector. Another complication is the SEC of the analyser itself, which lies near the sample SEC. Electrons colliding with the inside walls of the hemisphere will release secondary electrons within the analyser, meaning that another peak is present at BE = $h\nu$. To get around this, the sample is applied with a negative bias which alters the kinetic energy of the entire spectrum uniformly. This removes the overlap of SECs and the bias can be accounted for before analysis [7].

At the other end of the spectrum is a cut-off of the highest kinetic energy electrons - those most loosely bound within the material (Figure 3.11b). The XPS spectrum is referenced to the Fermi level, which is always calibrated to be at zero. Therefore, for metal samples the spectrum cuts off following a Fermi-Dirac distribution function at zero

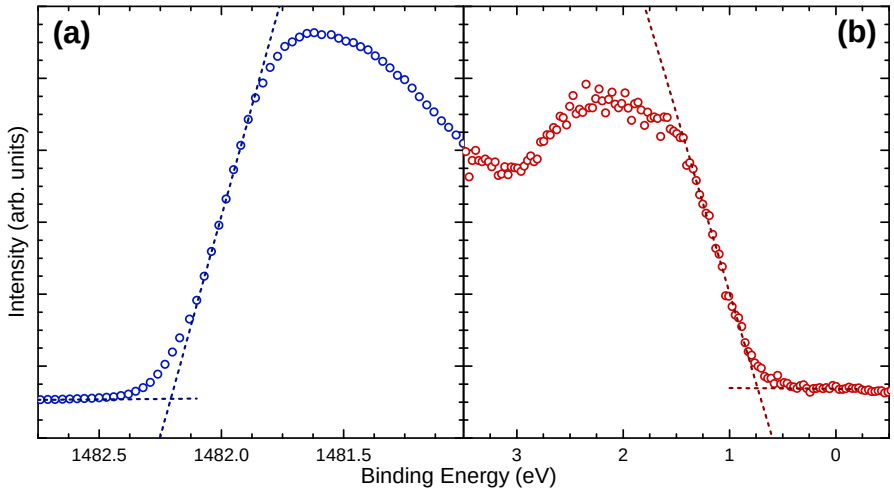

Figure 3.11 An example of (a) secondary electron cut-off, and (b) valence band edge in a typical XPS spectrum. The intensity scales have been normalised and the SEC would usually be many times more intense than the VBM. The SEC has been corrected to account for the applied bias and the whole spectrum has been calibrated to set the Fermi level to zero.

(see Figure 3.15). In semiconductors, however, there are no occupied states at the Fermi level, therefore the cut-off lies at slightly higher binding energy at what is called the valence band edge (VBM). This cut-off gives the energy separation between the Fermi level and valence band and, if the band gap is known, can be combined with the work function obtained from the SEC to learn the natural band positions of the material (see Figure 3.12). Additionally, if compared with calculated valence band DOS, the shape of the region immediately preceding the valence band edge provides certain information about the relative contributions of various valence orbitals to the valence band DOS (as discussed in detail in Chapter 5) [7, 116].

Determination of the position of the SEC and VBM is usually done by fitting a straight line to the steepest part of the edge feature. This is accepted to be an accurate representation in most cases, however the resolution of the measurement should always be taken into consideration before employing this method. As will be explored further in the next section, there is a certain amount of Gaussian broadening present in the photoemission data which will shift the measured binding energy slightly. It should be ensured, therefore, that the resolution of the measurement is sufficiently good to keep the associated error low. It is sometimes possible to determine the position of the edge by fitting broadened DFT calculated DOS to the valence band edge, however this depends on the availability of the calculations and is much more time consuming to do correctly.

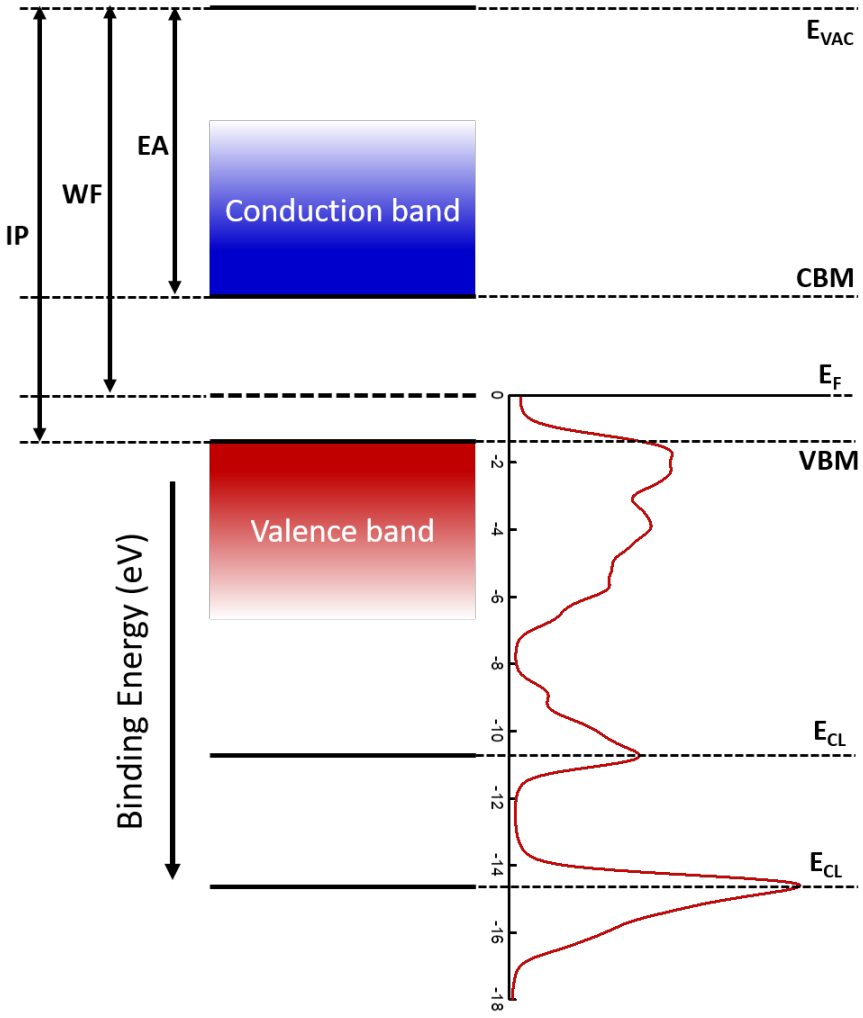

Figure 3.12 Schematic of a semiconductor's band structure and how the different levels relate to features in an XPS spectrum. The electron affinity (EA), work function (WF) and ionisation potential (IP) are also labelled.

Resolution

The resolution of XPS is determined by a number of factors. Firstly, if the x-ray source is unmonochromated, the resolution will be poorer due to the additional x-ray energies that are incident on the sample. A monochromated source, however, gives only a single x-ray energy and therefore, in a perfect setup, the core level lines should be unbroadened lines. However, there are broadening effects both in the photoemission process itself and in the detection. Upon excitation of an electron from an orbital within the material, the resulting ion exists in an excited state until the core-hole left by the emitted electron is filled by another electron from a higher orbital. The uncertainty in the lifetime of this core-hole (as described by Heisenberg's uncertainty principle) determines the minimum broadening of the detected peak according to a Lorentzian distribution [117]. Upon detection of the photoelectron there are other broadening effects, which are a consequence of the other factors such as detector resolution and the line width of the x-rays. This applies a Gaussian broadening to the detected kinetic energy of the photoelectrons. Between the two effects, the peaks in the photoemission spectrum exhibit a shape that is a mix of Gaussian and Lorenzian, and this must be taken into account when fitting them. A Voigt function is a convolution of Gaussian and Lorenzian distributions and furthermore can be adjusted to have more Gaussian character or more Lorenzian character. CasaXPS uses an approximation of a Voigt function as explained elsewhere [118]. This can be adjusted during the fitting procedure to give the best representation of the data in the fit. The better the resolution of the detector, the more Lorenzian the peaks will appear, and vice versa.

The instrumental resolution of the measurement can be determined by fitting the Fermi edge of a metal sample measured by the same instrument. In metals, the Fermi edge appears as a Fermi-Dirac step function but with some instrumental broadening. By fitting a Fermi-Dirac function (equation 3.11) convolved with a Gaussian distribution (equation 3.12) with a given variance, σ, the full width at half maximum (FWHM) of the instrumental broadening can be determined. The lifetime broadening effects are assumed to be negligible at the Fermi edge due to the very low binding energy in this region.

$$f_{FD}(\mathrm{E}) = \frac{1}{1 + \exp\left(\frac{\mathrm{E}-\mathrm{E}_F}{\mathrm{kT}}\right)} \tag{3.11}$$

$$f(x) = \frac{1}{\sigma\sqrt{2\pi}} \times \exp\left(-\frac{1}{2}\left(\frac{x-\mu}{\sigma}\right)^2\right) \tag{3.12}$$

which, for the case of a Fermi level at zero, becomes:

$$f(x) = \frac{1}{\sigma\sqrt{2\pi}} \times \exp\left(-\frac{\mathrm{E}^2}{2\sigma^2}\right) \tag{3.13}$$

This is shown for a silver sample measured with monochromated XPS in Figure 3.13 and a breakdown of the resolution of XPS, HAXPES and UPS is given in Table 3.1. The measured FWHM of the XPS Fermi edge was 0.45 eV, as calculated using equation 3.14.

$$\text{FWHM} = 2\sigma \times \sqrt{2 \times ln(2)} \tag{3.14}$$

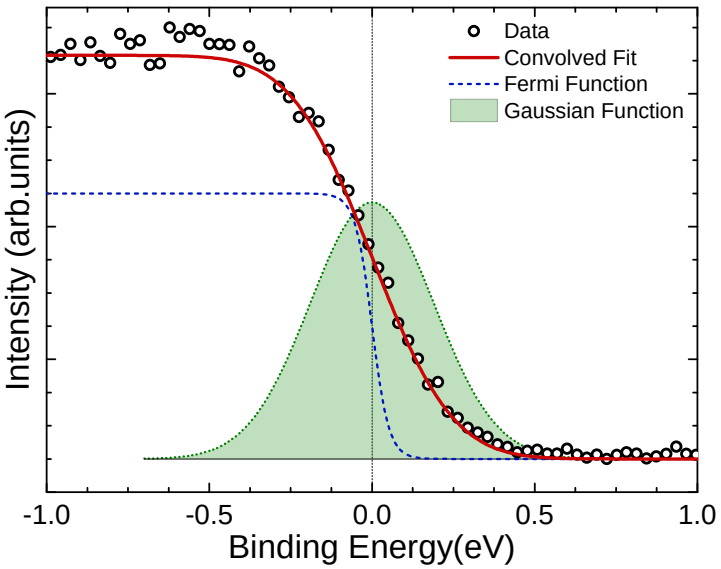

Figure 3.13 Fermi edge of a Ag sample measured with monochromated XPS with a Gaussian broadened Fermi-Dirac distribution function fit.

Technique	FWHM (eV)
Monochromated XPS	0.45
HAXPES	0.25
UPS	0.12

Table 3.1 The FWHM of the Fermi edge measured by different photoemission techniques as determined by fitting a Gaussian broadened Fermi-Dirac distribution to the Fermi edge data.

3.2.4 Ultraviolet Photoemission Spectroscopy

UPS is a variant of the photoemission technique that utilises ultraviolet rays, instead of x-rays. This means that the technique is far more surface sensitive, probing less than 5 nm from the surface. It also has a spectrum of a much narrower range than XPS, meaning that core levels are not distinguishable in the same way. It is therefore primarily used for measuring the two extrema of the spectrum; in particular it is the most commonly

used photoemission technique for measuring the work function of a material because it does not pose the same difficulties as XPS for measuring the SEC.

Source

The typical UPS setup uses a He discharge lamp to produce UV light. Helium gas is pumped into the lamp and is partially ionised by a high voltage. The positively charged ions will eventually collide with a neutral gas atom and receive an electron from it. The relaxation of the electron into a lower energy state is accompanied by the release of a characteristic photon, in this case either He(I) (21.2 eV) or He(II) (40.8 eV). The choice between the He(I) and He(II) lines can be controlled through tuning of the gas pressure and voltage.

Spectral Features

Some of the features in a UPS spectrum are very similar to those found in an XPS spectrum. In particular, the SEC and VBM are almost identical, albeit the exact shape of the valence band might be slightly different (as discussed in section 3.2.6). In between these two edges the spectrum contains far fewer features than an XPS spectrum, with the photon energy only high enough to include the valence states, and much of the spectrum is at least partially obscured by the secondary electron background tail. For this reason, peak fitting is not commonly done for UPS measurements, and it is the SEC and VBM positions that are obtained from the measurement.

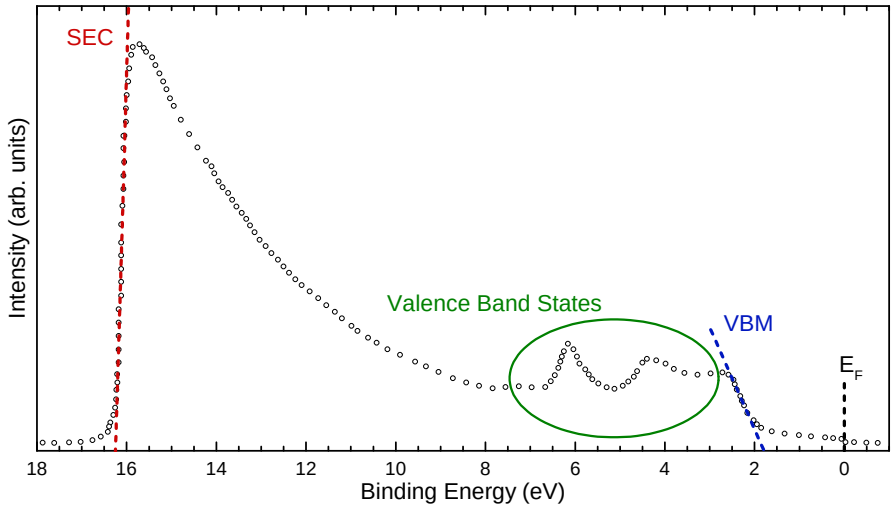

Figure 3.14 An example of a UPS spectrum with a secondary electron cut-off to the left hand side, valence band edge to the right-hand side and the Fermi level at zero binding energy. Reproduced from xpssimplified.com [119].

Resolution

The UV source is not monochromated, but benefits from a much narrower natural line width of the photon energy. Therefore the measurement generally has a sharper resolution than XPS, but can suffer from satellite signals in the spectrum from secondary emission lines from the source [7]. A Gaussian broadened Fermi-Dirac distribution fitted to the Fermi edge of a silver sample (Figure 3.15) yielded a FWHM of 0.12 eV, much narrower than that of XPS.

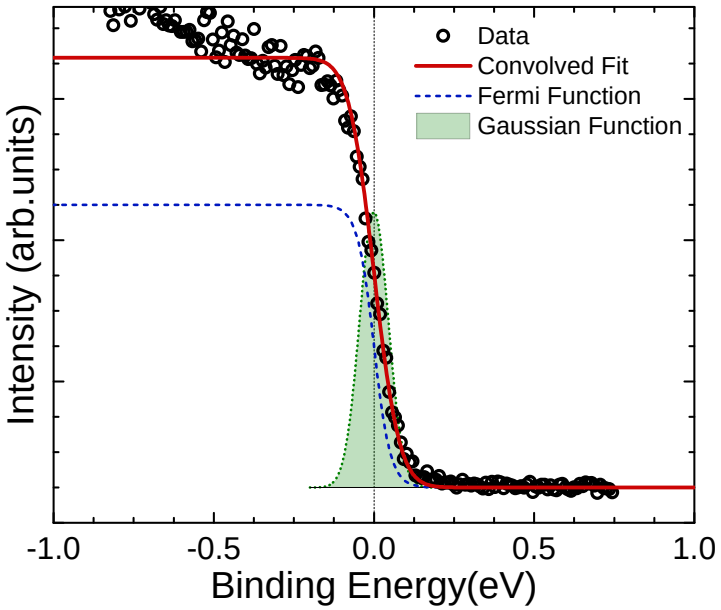

Figure 3.15 Fermi edge of a Ag sample measured with He(I) UPS with a Gaussian broadened Fermi-Dirac distribution fit.

3.2.5 HAXPES

HAXPES is a traditionally synchrotron-based variant of XPS which can call upon photons of a wide range of energy, but is predominantly used for high energy x-rays (known as hard x-rays) with energies anywhere between 2 keV and 20 keV. There are many advantages to using such a technique, including an incredibly high available intensity of incident photons, excellent resolution as well as the spectral implications of using higher energy x-rays. The intensity and resolution mean that certain features that might show up too weakly to be resolved in a traditional XPS measurement, can be studied when using HAXPES. The use of a higher photon energy also increases the effective probing depth of the measurement (by increasing the IMFP of the photoemitted electrons), meaning that deeper lying regions of the sample can be probed. There is also opportunity to take advantage of the change in photoionisation cross section with increasing photon energy, as explained in more detail in Chapter 5.

There has recently been developed a lab-based HAXPES system, however the technology is still in its infancy and lab-based HAXPES systems are not common [120]. For this reason, they will not be discussed further in this thesis.

Source

HAXPES facilities utilise a synchrotron light source to produce x-rays. This consists of a beam of accelerated electrons, moving radially within a storage ring (a type of synchrotron). The redirection of the electrons by the bending magnets causes them to emit x-ray radiation of a very high energy. For more control of the x-ray energy, beamlines can also use insertion devices. These are periodic magnetic structures that disrupt the electron beam (by either 'undulating' or 'wiggling') so that synchrotron radiation is produced, and the periodicity of the magnets can be adjusted to tune the energy of the emitted radiation. These insertion devices allow for a very brilliant light source with tunable photon energy - an incredibly useful tool for a number of experimental techniques.

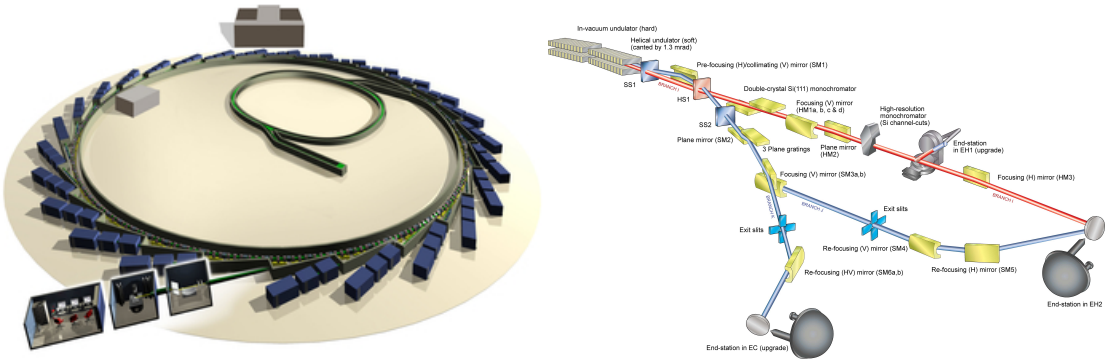

Figure 3.16 (a) Illustration of the Diamond Light Source beamline [121] and (b) the layout of the I09 beamline and end-station at Diamond Light Source [122].

A light source facility will typically have a number of end stations around the storage ring, with the exact number depending on the scale of the facility and size of the ring. Each end station will produce a beam of x-rays from the storage ring, following which a series of complex lenses, collimators and monochromators making up the 'beamline' will be used to tune the x-ray beam to the individual needs of the end station. In this way, light source facilities are extremely versatile because they can have multiple different end stations that run entirely different experiments operating simultaneously and independently of each other, each using a beam tailored to the needs of the individual experiment.

Spectral Features

A HAXPES spectrum is very similar to the spectrum obtained from XPS measurements, however the higher photon energy introduces some interesting differences. Firstly, there are no Auger lines in this spectrum. This is because Auger electrons have a fixed kinetic energy that is too low to be included on this binding energy scale. At much higher binding energy the Auger lines would be present, however the count rate in that region would likely be too high to be measurable. Similarly, the SEC is not a quantity that can be measured using HAXPES - the intensity of the illumination in HAXPES means that the number of secondary electrons would be too great for any analyser.

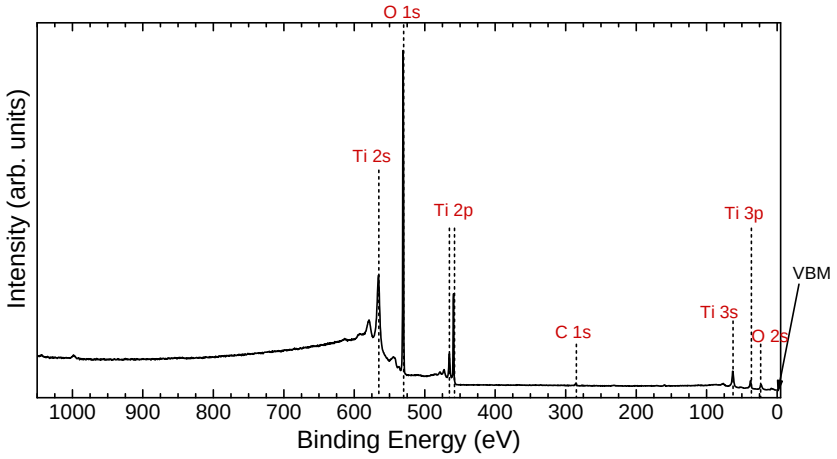

Figure 3.17 Example spectrum of a TiO_2 sample taken with HAXPES using a 5921 eV x-ray source.

There are also differences within the measured region. The background is flatter and does not rise at higher binding energy, a result of the secondary electron cut-off being far removed on the energy scale and scattering events being less likely at such high kinetic energies. The intensity of contaminant peaks such as the C 1s (often an indicator of surface contamination) is extremely low, in part due to the reduced surface sensitivity of HAXPES and also due to the difference in photoionisation cross section. There are also plasmon lines present for the most intense core level peaks, a satellite feature shifted to higher binding energy from the core level. The plasmons are a peak signifying a particularly probable energy loss, in this case as a result of collective oscillations of free electrons known as plasmons. The signal to noise ratio is also excellent, a product of the intensity of the beam and the dearth of secondary and inelastically scattered electrons at such high kinetic energies.

Resolution

The resolution of HAXPES is generally better than traditional lab based XPS due to the advanced beam optics and monochromators used in producing the x-ray beam. While not

as sharp as UPS, the FWHM determined by fitting a Gaussian broadened Fermi-Dirac distribution to the Fermi edge of a Au sample measured with 6 keV photons (Figure 3.18) was 0.25 eV, almost twice as good as the resolution of XPS.

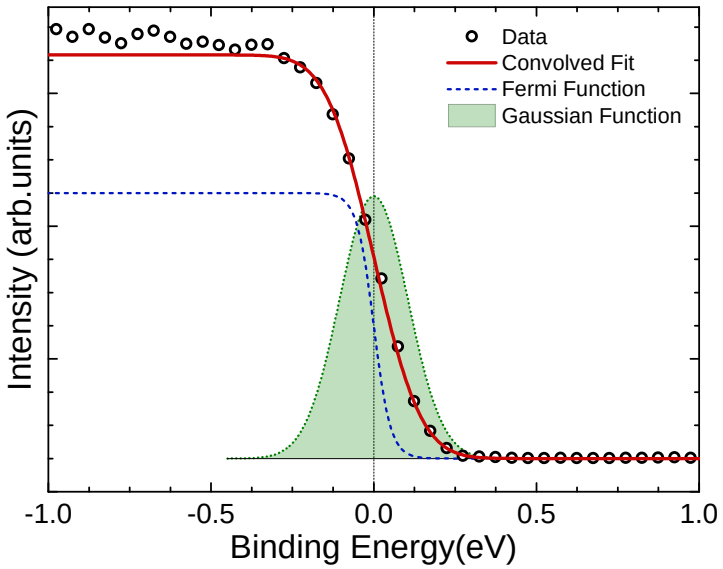

Figure 3.18 Fermi edge of a Au sample measured with 6 keV HAXPES with a Gaussian broadened Fermi-Dirac distribution fit.

3.2.6 Analysis

There is a variety of information that can be gained from photoemission, and a number of features that can be analysed. In this section, a brief overview will be provided of the analysis approaches used in this project. This by no means covers all the aspects of photoemission analysis, but only the ones relevant to this work.

Core Level Fitting

Often the first task when analysing an XPS spectrum is to identify all of the core levels. Each material has a series of characteristic core levels that are well documented [111]. In theory, every core level should correspond to an element that is expected to be in the sample, with oxygen and carbon usually present as well as a result of contamination and exposure to air. However, in practice there is occasionally an unexpected element present in the spectrum, and every core level should be identified and assigned to an orbital before any further analysis is carried out.

Core levels with an orbital angular momentum greater than zero will experience spin-orbit splitting, and this can be resolved in XPS as two peaks, for most core levels. The total angular momentum of an electron is given by $j = l \pm \frac{1}{2}$, where j is the total angular

momentum and l is the orbital angular momentum. This means that for p, d and f orbitals two peaks are resolved, one for each total angular momentum. s orbitals only have one peak due to there being only one possible value for the total angular momentum.

Orbital	l	j	Ratio
s	0	1/2	-
p	1	1/2, 3/2	1:2
d	2	3/2, 5/2	2:3
f	3	5/2, 7/2	3:4

Table 3.2 Orbital angular momentum, total angular momentum and doublet area ratios for the different orbitals in an XPS spectrum.

Each total angular momentum state for the p, d and f shells have a degeneracy originating from the different possible geometries of the sub-shells. This leads to a fixed ratio in the intensity of each peak within the doublet set. These ratios are summarised in Table 3.2 and are a useful tool when peak fitting the core-level spectra. Another well defined quantity is the energy separation between the two peaks within a doublet, and these can be found in works such as 'The Handbook of X-ray Photoelectron Specroscopy' by Moulder *et al.* [111]. In most cases, the FWHM of the two peaks is also identical (exceptions such as the Coster-Kronig effect will be discussed later). All of these quantites can be constrained in the fitting software 'CasaXPS' and can be constrained relative to each other. By constraining these known quantities the margin for error in the fitting procedure is significantly reduced and it is ensured that the necessary conditions for the fit to make physical sense are ensured.

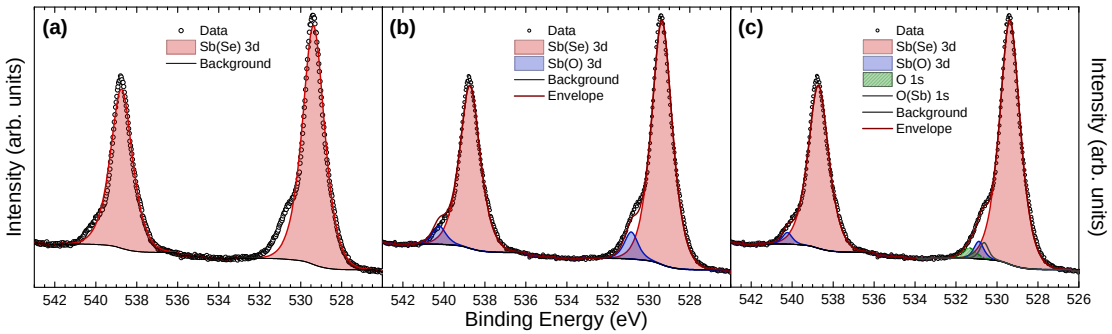

Figure 3.19 An example of the improvement of the core level fit of the Sb 3d region of an Sb_2Se_3 sample with the addition of more components.

Often there will be multiple contributions from a certain element in more than one chemical environment. For example, Sb_2Se_3 is usually subject to surface oxidation meaning that there will be a contribution to the Sb core levels from Sb_2Se_3 and from Sb_2O_3. One of the useful aspects of XPS is that these two contributions will be shifted in energy,

meaning that for most cases the two contributions can be distinguished by careful peak fitting. For example, in Figure 3.19a, the doublet (constrained according to the rules laid out above) clearly does not provide a good fit for the data, evidencing that another, chemically shifted doublet is needed to account for the data. In Figure 3.19b, the fit is much improved by the addition of another doublet that is attributed to the native oxide that grows on the surface of Sb_2Se_3. However, there still exists a discrepancy between the envelope and the data. The Sb 3d region overlaps significantly with the O 1s peak and the presence of an Sb_2O_3 signal means that some O must be present in the spectrum. Additionally, spectra from samples that have been exposed to air almost always contain an O peak due to adventitious oxygen weakly adsorbed onto the surface. The inclusion of a peak for each of these contributions in the fit (Figure 3.19) gives a very good agreement between the envelope and the data, suggesting that all contributions have been accounted for.

The addition of components to a spectrum will always improve the fit, however this improvement might not necessarily represent any true physical information about the sample. It is therefore important to cross check any peak positions with those reported in the literature as well as ensuring that the results of the fitting are consistent across all core levels within the spectrum.

Valence Band Density of States

The valence band DOS is a useful tool for investigating the electronic structure of a material. A commonly used technique is to use computational techniques such as DFT to predict the valence band DOS and from that the spectrum from photoemission. This total DOS can be separated into the contributions from each orbital (as shown in Figure 3.20) and, through comparison with photoemission data, can be used to understand more deeply the electronic structure of the material. Certain features in the spectrum can be correlated to the calculated DOS to determine its accuracy and to then understand the orbital contributions to different regions of the valence band.

The investigation of valence band DOS requires the aligning of theoretical prediction to the experimental data. However, the DFT calculations are computed with no broadening of the photoemission signals to account for lifetime effects or instrumental resolution, and therefore must be broadened in order to match the experimental data (Figure 3.20). The photoionisation cross sections of each orbital must also be taken into account, for each orbital possesses a different cross section for absorbing an incoming photon and producing a photoelectron. The photoionisation cross sections of each orbital vary with photon energy and vary at a different rate to each other. Each of these factors must therefore be taken into consideration when fitting the data, however these subtleties can also be used to an advantage when analysing data.

The photoionisation cross sections of various elements are well documented in works such as Yeh & Lindau and Scofield [123, 124]. The theoretical spectrum must then

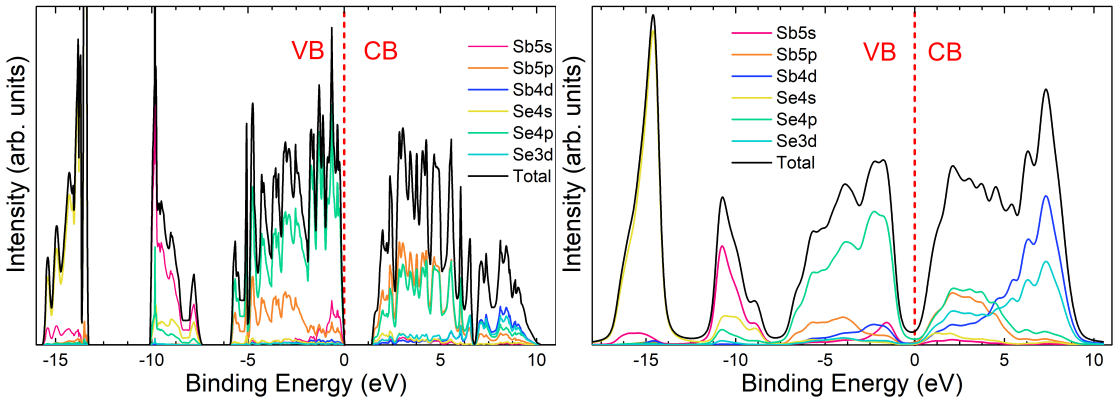

Figure 3.20 Example of calculated valence band DOS of Sb_2Se_3 (a) before and (b) after Gaussian-Lorenzian broadening

be broadened using a convolution of a Gaussian distribution (equation 3.15) with a Lorentzian distribution (equation 3.16). The correct Gaussian broadening parameter, σ, is determined by fitting a Gaussian broadened Fermi-Dirac function to the Fermi edge of a metal (Au or Ag) sample measured using the same system, as shown in section 3.2.3. This Gaussian broadening can then be fixed in the fitting procedure and the Lorentzian width, γ, varied until the agreement between theory and experimental data is good. The results are shown in Figure 3.20.

$$f_G(x) = \frac{1}{\sigma\sqrt{2\pi}} \times \exp\left(-\left(\frac{\mathrm{E}}{\sigma}\right)^2\right) \tag{3.15}$$

$$f_L(x) = \frac{1}{\pi} \times \frac{\gamma}{\left(\mathrm{E}^2 + \gamma^2\right)} \tag{3.16}$$

$$FWHM = 2 \times \sqrt{2 \times ln(2)} \times \sigma \tag{3.17}$$

This fitting method can also be used to determine the valence band maximum with greater accuracy than the more commonly used linear fitting method. When using the linear fit method a linear fit is applied to the steepest part of the edge and another to the background and the intercept of the two lines is taken as the VBM. However, the broadening effects are not taken into account and therefore the result can vary by up to 0.5 eV, depending on the shape of the valence band edge and the resolution of the measurement. This is not such an issue if one is comparing two samples of the same material measured with the same spectrometer, which will have similar valence band shapes and resolutions. However, for different materials and experiments, the slope of the edge can change significantly. Fitting the DOS to the valence band spectrum can work around this problem because it accounts for the broadening effects both from sample and spectrometer. Given that DOS calculations uniformly place the VBM at 0 eV, the DOS (once broadened) is shifted along the x-axis until it lines up perfectly with the

experimental data. This shift is therefore an accurate measurement of the VBM binding energy.

3.2.7 Experimental Setup

In this section the experimental setup for photoemission in this work will be briefly described. The majority of the photoemission data acquired for this work at the Stephenson Institute was collected using the same equipment, but some data in Chapter 6 was acquired on a similar but slightly different setup. Here we will give an overview of the principle setup used as an example and the specific differences in the alternative kit used will be covered in the relevant results chapter.

The monochromated XPS system at the Stephenson Institute was designed to be able to perform a wide variety of sample preparations and photoemission measurements *in situ*. The central chamber is equipped with a hemispherical electron energy analyser, a monochromated Al Kα x-ray source, an unmonochromated dual anode (Al Kα & Mg Kα), an inverse photoemission electron gun and detector, charge neutralising electron flood gun, a He lamp UV source and an Ar^+ ion sputtering gun for *in situ* surface cleaning. The acceptance angle of the analyser was $\pm 3^\circ$. The central chamber was maintained at a base pressure of 1×10^{-10} mbar using an ion pump. The chamber pressure was monitored by an ion gauge, accompanied by a mass spectrometer for checking contamination levels and a hydrogen getter. Two turbo pumps were also available to the main chamber, however these were only used when baking the system or when carrying out UPS measurements (where the chamber pressure was too high for the ion pump).

Samples were loaded into the system via two stages: the loading arm that opened directly onto the central chamber (prep arm) was kept under UHV conditions (1×10^{-8}) at all times, maintained by one of the turbo pumps. In this arm there was also an Ar^+ ion sputtering gun so that samples could be cleaned under UHV conditions without compromising the pressure of the main chamber. This arm was only capable of holding on sample at a time but was supplied by a second arm (loading arm) which could hold 4 samples simultaneously. The loading arm was regularly vented to atmospheric pressure in order to transfer samples in and out of the system and was pumped down to UHV using a scroll pump followed by the second of the two turbo pumps. Using the two arms simultaneously allowed for *in situ* exfoliation of crystals (see Chapters 5 & 6) by affixing double sided carbon tape to the loading arm while the crystal was held in the prep arm and pressing the tape to the surface of the crystal.

Samples were affixed to steel sample plates using double-sided carbon tape and were grounded to the spectrometer using a top electrical contact (either a tantalum or nickel strap) to help prevent any surface charging effects. For bulk crystal measurements this top contact was excluded to allow for *in situ* exfoliation. Typically, survey scans were collected at a pass energy of 50 eV and core levels were collected at a pass energy of 10 eV. The core level step size was 0.1 eV with a dwell time of 0.2 seconds at each step and

the x-ray source was operated at 250 W. For secondary electron cut-off measurements the x-ray source was operated at 9 W and a bias was applied to the sample stage. This bias was accounted for before binding energy determination by measuring the strongest core level in the spectrum under bias and under normal conditions so that an exact calibration of the bias shift could be determined.

HAXPES measurements were carried out at the I09 beamline at Diamond Light Source (see Figure 3.16b). A double crystal Si(111) monochromator was used to select x-rays with an energy of 5921 eV and a high resolution Si(004) monochromator resulting in energy resolution of 0.25 eV (see Figure 3.18). The spectra were acquired using a high-energy hemispherical electron energy analyser with an acceptance angle of $\pm 28°$. Data was collected at a pass energy of 200 eV and a step size of 0.5 eV. Samples were affixed to steel plates in the same manner as for XPS measurements but using a thin strip of conductive carbon tape as a top contact instead of a metal strap.

3.3 Device Performance

In this section we will provide a brief overview of the characterisation methods used to measure solar cell device performance.

3.3.1 Current-Voltage

Current-voltage measurements are the primary characterisation technique used for measuring photovoltaic device performance, and it is from J-V curves that device efficiency is calculated. A solar cell that is in use for producing power will always be operated at the maximum power point - the voltage at which the power output is highest. However, much can be learned about the device's performance from the output at other applied voltages. J-V measurements sweep through a range of voltages (usually between -1 and 1 V) and measure the current output at each voltage. This can be done in the dark or under AM1.5 illumination, a standard that matches the solar irradiance spectrum at ground level. Dark curves provide information on the rectifying behaviour of the p-n junction in the dark when it behaves as a regular diode (see section 2.1.1). Under illumination the cell produces a light-generated current and quantities such as the V_{oc}, J_{sc} and FF can be measured, and therefore the efficiency calculated. During J-V measurements an electrical contact is attached to the metal back contact and another to the transparent front contact, which must be exposed either by masking during cell fabrication or by removal of a part of the layers atop it. This front contact is often aided by the use of some silver paint to help ensure a reliable front contact.

For further details on J-V analysis see section 2.1.1.

Temperature-Dependent Current-Voltage

Current voltage measurements are typically carried out at room temperature, however, by varying the temperature at which the measurement is made, some interesting effects can be seen. Devices in which there is a potential barrier between the absorber layer and the back contact typically exhibit 'rollover'. This appears in the curve as a plateauing of the curve at high forward bias and is a result of carriers building up at the back contact due to the need for thermionic emission to transport them into the metal. As the temperature of the system is dropped, the probability of thermionic emission is reduced and this 'rollover' becomes more pronounced. This can be quantified by measuring the degree of rollover with respect to temperature and the size of the back contact barrier can be determined. A number of models exist for determining the back contact barrier from temperature-dependent current-voltage (J-V-T), of which the favoured in this work was that proposed by Bätzner *et al.* [21, 125].

The method used by Bätzner *et al.* measures the series resistance at different temperatures and uses equation 3.18 to determine the back contact barrier. In an ideal system, the series resistance in a device would rise linearly with temperature as the Ohmic resistance in the film increased. However, when there is a Schottky barrier present, the trend is dominated by the exponential decay of the barrier's effect as the temperature rises.

$$\mathrm{R}_s(\mathrm{t}) = \mathrm{R}_{\Omega 0} + \frac{\partial \mathrm{R}_{S0}}{\partial \mathrm{T}} + \frac{\mathrm{C}_{SK}}{\mathrm{T}^2} \cdot \mathrm{e}^{\frac{\Phi_{SK}}{kT}} \tag{3.18}$$

Equation 3.18 accounts for this by using three terms: $\mathrm{R}_{\Omega 0}$ describes the Ohmic resistance at 273 K, $\frac{\partial \mathrm{R}_{S0}}{\partial \mathrm{T}}$ describes the temperature dependence of the series resistance and $\frac{\mathrm{C}_{SK}}{\mathrm{T}^2} \cdot \mathrm{e}^{\frac{\Phi_{SK}}{kT}}$ describes the exponential decay of the back contact barrier contribution. Φ_{SK} denotes the back-contact barrier (in eV) and C_{SK} is a fitting parameter. By fitting equation 3.18 to the experimentally measured series resistance at the rollover for a range of temperatures, the back contact barrier can be calculated.

3.3.2 External Quantum Efficiency

External Quantum Efficiency measurements are carried out in a similar way to J-V measurements. The front and back contact are contacted and the cell is placed under illumination. In these measurements the illumination is a monochromatic source that is swept through a range of wavelengths (between 300 and 1100 nm in the case of Sb_2Se_3). The light generated current is measured at each wavelength. No potential is applied in conventional EQE, meaning that the current measured represents the J_{sc} at each wavelength and the integrated area of the curve should be equal to the J_{sc} of the cell overall.

For further details on EQE analysis see section 2.1.1.

Chapter Four

TiO_2 vs. CdS: Examination of Absorber-Window Layer Band Alignments in Antimony Selenide Solar Cells

Parts of this work are published as:

H. Shiel *et al.*, "Natural band alignments and band offsets in Sb_2Se_3 solar cells" *ACS Applied Energy Materials* **3**, 12, (2020), DOI:10.1021/acsaem.0c01477

4.1 Introduction

Sb_2Se_3 solar cell technology has progressed rapidly in recent years, with efficiencies growing from ∼2% to ∼10% in only 6 years and with a relatively small number of research groups working on it [43, 59]. However, Sb_2Se_3 PV remains an emerging technology, with a significant amount of fundamental understanding still missing from the literature. The impact of this is felt particularly in the design of various device structures utilising different window layers (Figure 4.1). The junction between the two semiconductors is the central and most fundamentally important aspect of a thin film photovoltaic solar cell. CdS and TiO_2 are both used frequently, with some studies finding CdS to offer superior performance [39, 46, 78] and others finding the switch to TiO_2 extremely beneficial [57, 81]. There are many aspects of these alternative device structures that are not understood, particularly the role of band alignments in influencing the device performance.

This study provides band alignment measurements between Sb_2Se_3, identical to that used in high efficiency photovoltaic devices, and its two most commonly used window layers, namely CdS and TiO_2. Band alignments are measured via two different approaches: Anderson's rule was used to predict an interface band offset from measured natural band alignments, and the Kraut method was applied to hard x-ray photoemission spectroscopy results to directly measure the band offsets at the interface. This allows examination of

the effect of interface formation on the band alignments. Finally, these results are related to device performance, taking into consideration how these results may guide the future development of Sb_2Se_3 solar cells and providing a methodology which can be used to assess band alignments in device-relevant systems.

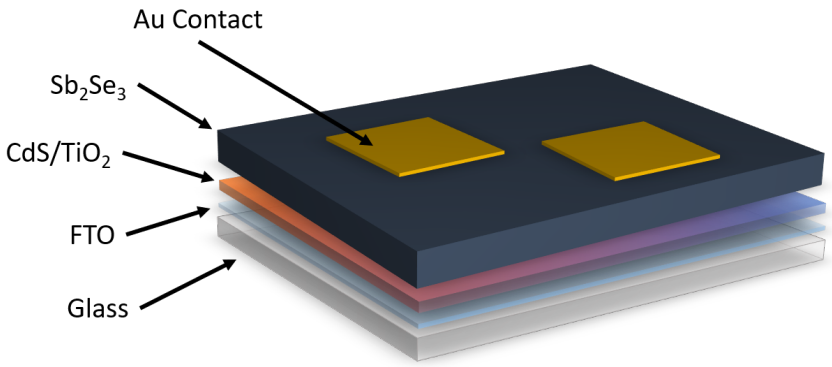

Figure 4.1 Schematic of the typical superstrate device structure used in Sb_2Se_3 solar cells.

4.2 Background

Band alignment is a general term used to describe the way the valence and conduction bands of two materials line up to perform a certain function. The 'natural' band alignment of two materials describes the positions of the band extrema with respect to the vacuum level when not in contact with each other. The term band offset refers to the discontinuity between the band extrema between the two materials once contacted. A 'spike-like' band offset is defined as where the CBM of the window layer lies above the CBM of the absorber, and a 'cliff-like' offset as when the CBM of the window layer lies below that of the absorber. Too positive an offset (Figure 4.2a), and electrons excited in the absorber will face a potential barrier opposing their drift into the window layer and lowering the J_{sc} (and efficiency) of the cell. Too negative a CBO (Figure 4.2b) leads to a potential source of back-transfer carrier recombination at the interface between conduction band of the window layer and the valence band of the absorber. This recombination, in which electrons in the window layer recombine with holes in the absorber via interface states, is more likely the narrower the gap between the two energy levels [126]. A cliff-like offset also limits the built-in voltage (V_{bi}) of the junction, leading to a lower V_{oc}. The J_{sc} and V_{oc} are crucial aspects of the solar cell performance, therefore it is vital that a good band alignment is obtained for a PV technology to be successful [127, 128].

One of the best ways to measure band alignments is through photoemission techniques such as XPS. Through use of the valence band and secondary electron cut-offs

in an XPS spectrum, the ionisation potential and work function of a material can be measured relative to the vacuum level [129, 130]. These quantities do not describe the interface itself, but via a method called Anderson's rule the band alignment can be predicted. Another technique often employed is the Kraut method [131, 132], which allows the direct measurement of valence band offset (VBO) between two materials. Both methods employ a number of assumptions that will be discussed below.

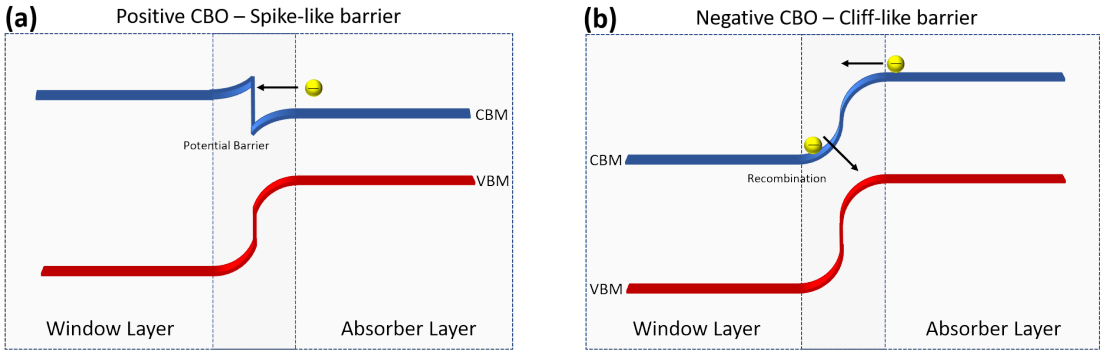

Figure 4.2 Schematic diagram showing (a) a very positive CBO leading to a potential barrier in the conduction band and (b) a very negative CBO leading to a recombination centre and low built-in voltage.

In this study, the powerful photoemission techniques of traditional lab-based XPS and synchrotron-based HAXPES were used to measure and compare band alignments using both Anderson's rule [133] and the Kraut method [131]. By examining the differences between the two sets of results, conclusions can be drawn about the effect of interface formation on the two different band alignments. Furthermore, by comparing these results to previous device studies, we assess the influence and impact of the band alignments on device performance characteristics.

4.3 Measuring Band Alignments by Photoemission

The measurement of the natural band alignments via photoemission is a commonly used procedure when screening materials for use as a junction partner to an absorber in a PV device [134, 135]. While most studies use UPS, a highly surface sensitive technique for studying work functions, it is also possible to use XPS which is slightly less surface sensitive (albeit still limited to the top few nanometres). This method involves measuring the ionisation potential of a material, which describes the position of the valence band maximum relative to the vacuum level, and then using either a measured or literature quoted band gap to determine the electron affinity, which describes the position of the conduction band relative to the vacuum level. When measuring ionisation potential, taking advantage of the fact that all XPS spectra are referenced to the Fermi level, the

position of the Fermi level in the band gap can also be determined. Knowing that when two semiconductors are contacted the Fermi levels of the two must be aligned, there is a need for a model of how this affects the alignments of the conduction and valence bands at the interface.

4.3.1 Anderson's Rule

One widely used approach is known as Anderson's rule or the electron affinity rule [133, 134]. This method states that the Fermi levels of the two materials align, while maintaining the difference in natural electron affinity at the interface (Figure 4.3). This is an extension of the local vacuum level principles discussed in section 2.1.2. The local vacuum level for each material is a fixed energy from its Fermi level and so to resolve the discontinuity at the interface, this school of thought states that the local vacuum levels experience band bending at the interface. The conduction band and valence band, being defined in relation to the local vacuum level, also bend, however it is stipulated that the difference in electron affinity between the two materials should remain fixed. However, this approach does not take into account the role of charge transfer, orientation or interface induced gap states upon contacting two materials. Therefore, if the two materials have significantly different electronegativities or lattice spacing, this approximation could differ significantly from the real band alignment [134, 136, 137]. It also relies either on some assumptions, or complex additional measurements to determine how the band bending is distributed across the two sides of the interface. Either the band offsets either side of the interface could be measured directly which, as mentioned below, is achieved with great difficulty and effectively renders the Anderson rule redundant, or else complex computational methods could be employed to calculate the band bending, which would also require such levels of work as to defeat the objective of a simple prediction. It is possible, however, to make an educated guess at the shape of the band bending through knowledge of how depletion layers are formed and a good understanding of the materials involved.

4.3.2 The Kraut Method

The alternative method used in this study, the Kraut method [131], uses a combination of measurements to take into account the charge transfer across the interface between two materials. First, the binding energy of high intensity core levels (E_{CL}) and the VBM (E_V) are measured for both materials in vacuum. Then a film of one material is deposited onto the other, thin enough that photoelectrons from the lower layer can still escape and be detected during an XPS measurement. This allows an interface-sensitive measurement in which peaks from both materials are resolved. Then by measuring the separation between core levels in the two materials (ΔE_{CL}) and exploiting the fact that the core level shift upon interface formation is equal to the shift in the valence and conduction bands ($|\delta E_{CL}| = |\delta E_V| = |\delta E_C|$), the valence band offset between them can be directly determined, as shown in Figure 4.4 and equations 4.1:

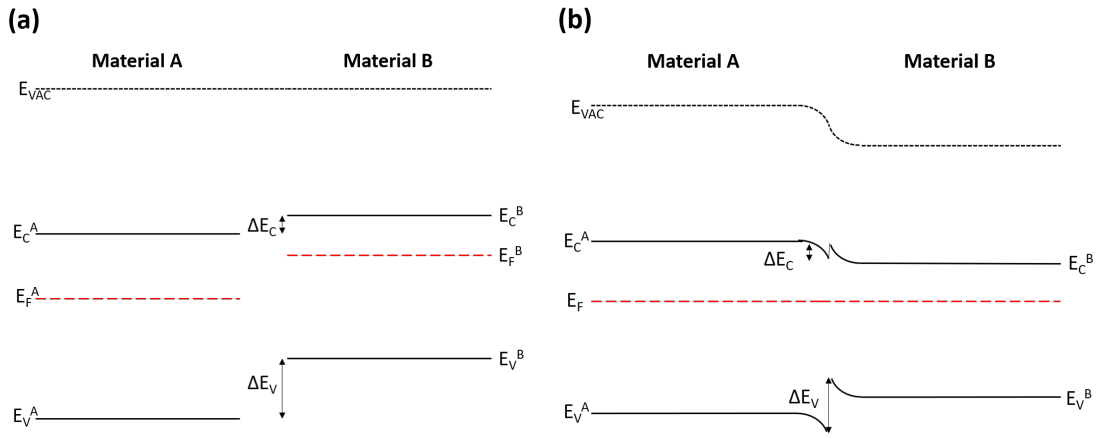

Figure 4.3 Schematic diagram of how band alignments are predicted using the Anderson rule with (a) showing the natural alignments referenced to the vacuum level and (b) showing band alignment after aligning Fermi levels.

$$\Delta E_V = (E_{CL}{}^B\text{-}E_V{}^B) - (E_{CL}{}^A\text{-}E_V{}^A) + \Delta E_{CL} \tag{4.1}$$

where A and B denote material A and material B and $\Delta E_{CL} = E_{CL}{}^A$ - $E_{CL}{}^B$. The key difference between the Kraut method and Anderson's rule, therefore, is that Anderson's rule is a prediction of the band alignment based on measurements of the separate materials, whereas the Kraut method is a direct measurement of the band offset albeit with some simplifications. The Kraut method approach is an abrupt interface approximation, meaning that an abrupt transition from one material to the other is assumed and the band bending is not measured. A drawback to this method, however, is sample preparation. As shown in Figure 4.6, the IMFP of a photoelectron is dependent on its kinetic energy and, according to the Beer-Lambert law, 95% of the signal originates within three IMFPs of the surface. Accordingly, the sampling depth of XPS is then roughly 10 nm, and a film thinner than this is required to carry out any Kraut method studies using conventional lab-based XPS.

4.3.3 Choosing the Most Device Relevant Sample

Many of the recent advances in Sb_2Se_3 device performance have come via the use of CSS or VTD of Sb_2Se_3 [37, 57, 67, 81]. CSS allows for the formation of large grain sizes with good preferred orientation for carrier transport. However, deposition of films thin enough to carry out the Kraut method was not possible by CSS with complete coverage. Any significant loss in coverage would invalidate the Kraut method measurements due to the presence of an unattenuated signal from the window layer interfering with the band alignment measurement. There were numerous options for getting around this problem, each with an element of compromise as summarised below.

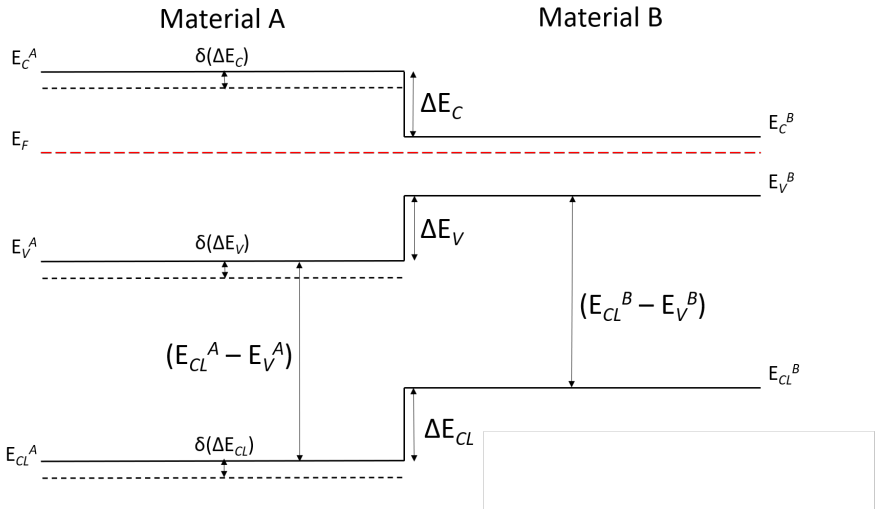

Figure 4.4 Schematic showing the band alignments measured by the Kraut method where δ signifies the band energy shift due to interface formation and ΔE signifies the band offsets.

Evaporated Films

An easy solution to the issue of CSS coverage would be to deposit Sb_2Se_3 by another technique with more uniform coverage, such as thermal evaporation. However, devices made using thermal evaporation (as covered in section 2.2.2) perform much worse than those made via CSS. This could be a result of any of a number of potential differences in the films or the material, such as crystallinity, crystal orientation, material purity or stoichiometry. For whatever reason, the performance of thermally evaporated Sb_2Se_3 thin film solar cells is some way below that of CSS films ($\sim$3-5% compared to $\sim$7%) and therefore it was decided that a measurement of a CSS film was required for relevance to device performance progression.

Reverse Junction

Another solution that was considered for the measurement was to deposit a thin layer of CdS or TiO_2 onto a Sb_2Se_3 layer and measure the junction upside-down. Unfortunately, however, this is complicated by the roughness of the Sb_2Se_3 surface when deposited by CSS and when using FTO as the TCO layer, meaning that uniform layers with good coverage are hard to achieve. There is also doubt over how representative this measurement would be of the actual interface in a device given that CdS, TiO_2 and Sb_2Se_3 are deposited in different atmospheres, at different temperatures and for different periods of time. All of these factors could affect the interface formation and so for a device relevant measurement it is not ideal.

Sputter Down

An often employed method of accessing these ultra thin layers is to deposit a thicker film and then use Ar^+ ion sputtering to etch away layers of the material until only a thin layer remains. There are two reasons that this method was not employed in this study. Firstly, the very act of sputtering the surface away by bombarding it with Ar^+ ions will alter the surface structure and chemistry - the surface of a film following sputtering is often made amorphous and there is potential for certain elements to be preferentially removed or for Ar to be implanted in the surface. Secondly, the roughness of the FTO TCO layer used in device fabrication means that all the layers deposited (window layer and Sb_2Se_3) have a distinct surface roughness as well. This means that a uniform sputtering of the surface risks exposing the substrate at certain points while still having thick layers of Sb_2Se_3 at other points (see Figure 4.5). Exposed regions of the window layer will interfere with the attenuated signal of the window layer photoelectrons coming through the top layer. This effect was observed when sputter depth profiling was attempted using the high-throughput XPS system at NSG Ltd.

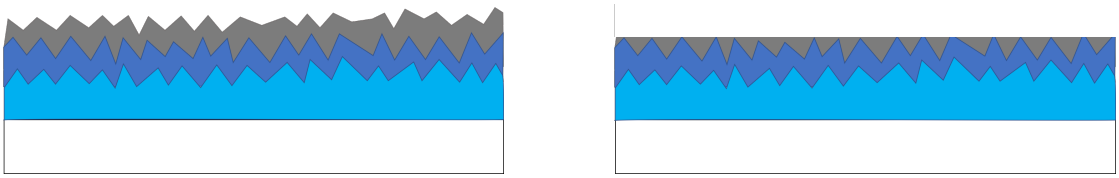

Figure 4.5 (a) A schematic depicting the rough nature of layers deposited onto FTO and (b) an illustration of how this can lead to the layer below being exposed while sputtering away the surface layer by layer.

Smoother Substrate

An obvious solution to the problem of sputtering down or of achieving good coverage with CSS would be to use a smoother substrate than FTO. A smoother substrate would likely aid in achieving good coverage with thin layers of CSS deposited Sb_2Se_3 as well as enabling better use of the sputter down approach. However, the use of FTO layers as the TCO layer is integral to the device making process, with the surface roughness aiding in achieving the 'upright' standing orientation of the Sb_2Se_3 grains. As discussed in section 2.2.2, this is crucial for producing high performance devices as well as being likely to influence the band alignment at the interface. Replacing the FTO layer would require re-optimisation of the entire deposition processes for the window layer and Sb_2Se_3, a process which could lead to significant differences between the measurement and the high efficiency devices produced by the group. The FTO layers currently used are also industry standard layers produced by NSG Ltd.; films which are used in products such as the First Solar CdTe Series 6 module, and therefore replacing the layers with a less

competitive and scalable product would be counter-productive [14]. Therefore, in the interests of device relevance once again, this wasn't a favourable option.

The Solution

HAXPES, is a synchrotron based technique that uses hard x-rays of an energy anywhere in the range of 2 eV to 20 keV. The increased x-ray energy allows for photoelectrons to have a higher kinetic energy and therefore higher IMFP, meaning that electrons originating from deeper within a sample can be detected. Figure 4.6 shows the IMFP of an electron moving through Sb_2Se_3 (as calculated by the TPP-2M equation [138]) with respect to its kinetic energy. According to the Beer-Lambert law, 63% of the detected signal will originate within one IMFP of the surface and 95% within three IMFPs of the surface.

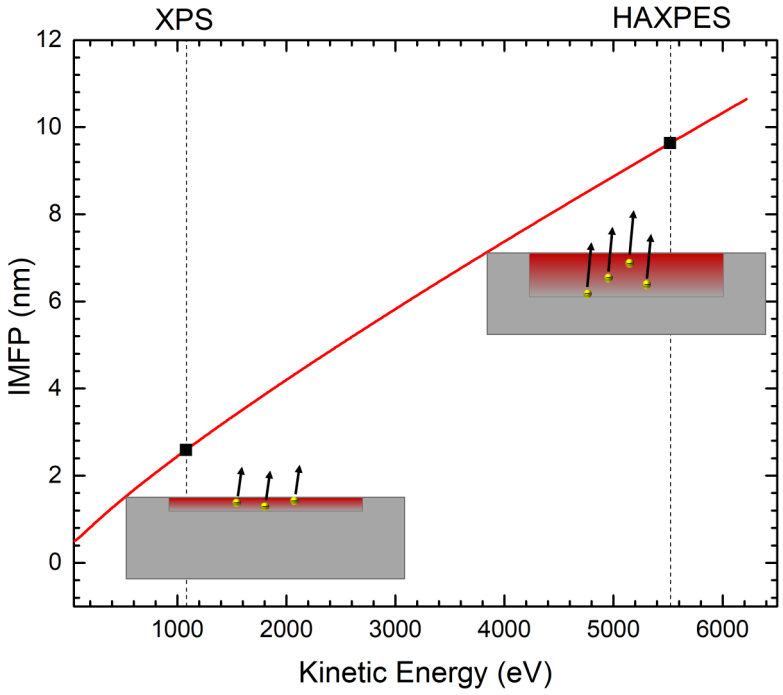

Figure 4.6 The inelastic mean free path of photoelectrons in Sb_2Se_3 with respect to kinetic energy [138]. Black points show the kinetic energy of an electron escaping the Sb 3d orbital for both conventional Al Kα XPS (1486.6 eV) and HAXPES (assuming a photon energy of 5921 eV) and the inset sketches illustrate the relative probing depths of the two techniques.

The majority of the signal originates within one IMFP but the overall probing depth (or the measurement's detection range) can be considered equal to three IMFPs. An electron excited from the Sb 3d orbital will have a kinetic energy of hν minus the binding energy of ~500 eV. For standard lab based XPS (hν = 1486.6 eV) this means an IMFP

of ~3 nm and a total probing depth of ~9 nm, hence the requirement for Sb_2Se_3 films of 5 nm. The equivalent IMFP of an electron excited in HAXPES is ~9 nm, meaning it has a probing depth of nearly 30 nm. This significantly increases the thickness of Sb_2Se_3 layer that can be used for the Kraut method. At a thickness of ~20 nm, good coverage is achievable using CSS, allowing for Kraut method measurements of device-relevant Sb_2Se_3.

This route comes with its own set of compromises much like the ones listed above. The deposition of a 20 nm-thick layer meant using only the seed layer growth of Sb_2Se_3 from what is usually a two step process. This would be unavoidable however for any method except the reverse junction method and given that the seed layer is the layer that would form the initial junction with the window layer it was deemed an acceptable compromise. The other compromise comes with the photoemission measurement via HAXPES; while sensitive to photoeletrons from a greater depth, the HAXPES signal would still be dominated by regions closer to the surface, meaning that the abrupt interface approximation of the Kraut method becomes a greater consideration. Depending on the degree of band bending and the depth over which it takes place, this approximation's accuracy could vary. However. on the scale of a device with a combined thickness of over 2 μm, this measurement is still considered to be reasonably interface-sensitive.

4.3.4 Band Alignments in Sb_2Se_3 Solar Cells

There have been numerous investigations of band alignments between Sb_2Se_3 and potential partner materials. However, these studies have mostly be done on novel window layers such as ZnS, $Cd_xZn_{1-x}S$ and CdS:O [89, 139, 140]. The band alignment of Sb_2Se_3 and CdS has been reported, once via the Kraut method and once via natural alignment measurements. In a study by Li *et al.*, the band alignment between $Cd_xZn_{1-x}S$ and Sb_2Se_3 was measured for various concentrations of Zn, with CdS without Zn being one of the samples measured. These band alignments were measured via the Kraut method, however the Sb_2Se_3 films deposited had a thickness of 60-80 nm, meaning that in order to carry out the Kraut method they will have had to be thinned, presumably via Ar^+ ion sputtering. It is also significant that the measurements were carried out on a sample in a substrate solar cell configuration, with the Sb_2Se_3 (deposited onto Mo) acting as substrate to the CdS. The result of the measurement was a valence band offset of -1.28 eV which, as will be shown later, matches well with the results of this work.

In another study, by Wang *et al.*, the natural band alignments of Sb_2Se_3 were measured using UPS, claiming an IP of 4.93 eV [45]. This was aligned with the natural alignments of TiO_2 and CdS in a stacked structure with CdS acting as an interlayer between TiO_2 and Sb_2Se_3. However, the natural alignments of TiO_2 and CdS were taken from the literature of work with quantum dots and nanorods, meaning that there is no guarantee that these values are representative of thin films. Furthermore, the alignment of a $TiO_2/CdS/Sb_2Se_3$ stack does not provide the information desired on the relative merits of CdS and TiO_2 as window layers independently. Ou *et al.* also measured natu-

ral band alignments of Sb_2Se_3 using UPS, and they also measured the natural alignments of CdS (similarly to Li *et al.*) as a starting point for varying concentrations of CdS:O. These measurements yielded ionisation potentials of 5.01 eV and 6.34 eV for Sb_2Se_3 and CdS respectively. However this study did not use Anderson's rule as in this work, using a different, unspecified method to draw the band alignment [139].

The Kraut method, too, has been used to measure the band alignments of Sb_2Se_3. However, this was a study of the band alignments between Sb_2Se_3 and ZnS, a material that has never seen great success as a window layer for Sb_2Se_3 solar cells [140]. This study used the Kraut method to great effect, depositing 'wedges' of ZnS onto Sb_2Se_3 and measuring different points along the thickness gradient. This allowed the band offset to be measured at multiple thicknesses of Sb_2Se_3 and thereby the band bending could be plotted. This is similar to other approaches in which layers of a material can be deposited sequentially *in situ* with photoemission measurements taken for each increasing thickness and the band bending plotted [141]. However, while incredibly powerful as a methodology, there are limitations to the device relevance of such experiments. Wedges of Sb_2Se_3 could not be deposited by CSS due to the unique geometry of the technique. Meanwhile, only a limited number of deposition methods could be used to deposit thin films and carry out photoemission measurements without breaking vacuum (in this case sputtering was used) and CSS and VTD in particular would be extremely difficult to connect to a vacuum transfer system. Without this vacuum transfer system, the films would be exposed to atmospheric conditions in between measurements, which would introduce surface contamination to the bulk. Additionally, the use of sequential depositions can have implications for the film quality, crystallinity and contamination levels. Nevertheless, this study was a very interesting use of the Kraut method's principles and proved beyond doubt that ZnS would not make a suitable window layer partner for Sb_2Se_3 due to the large spike-like CBO.

Finally, a recent paper published after the submission of this work for publication measured the band offsets between Sb_2Se_3 and three different window layers (CdS, ZnO & TiO_2) achieved results that were broadly consistent with the results of this work [142]. A negative conduction band offset between TiO_2 and Sb_2Se_3 was consistent with our results but different in magnitude to the one measured in this work due to the in-situ measurement carried out having the capability to measure the band bending. However, the VBO result was very similar to the result of this work when predicting the nature of the band bending as discussed later (and shown in Figure 4.14b). The conduction band offset between CdS and Sb_2Se_3 was measured to be a small spike-like offset, again consistent with the results of this work.

While there are very few cases of dedicated band alignment studies of Sb_2Se_3, there are many cases of band alignments being proposed as an explanation for some device performance characteristic. However, these alignments are based on unconnected natural alignment measurements and line-ups without rigorous consideration for the complex

processes that occur upon contacting two materials [57, 80]. A recent review paper on voltage losses in antimony chalcogenides identified interface recombination losses as a significant barrier to achieving high device efficiencies, highlighting the importance of studies such as this [143]. This study provides in depth and rigorous consideration for the complexities of band alignment measurements while maintaining a firm connection to practical device applications throughout.

4.4 Methods

4.4.1 Film Deposition

CdS films were deposited onto TEC10 fluorine-doped tin oxide (FTO) coated glass substrates (supplied by NSG Group) by RF-magnetron sputtering at 60 W, 5 mTorr of Ar gas and a substrate temperature of 200°C for 24 minutes. The CdS films were ∼80 nm thick as determined by an Ambios xp200 profilometer. Anatase TiO_2 films were deposited by a two step process; first an RF-magnetron sputtered film was deposited at room temperature at 150 W and 5 mTorr for 30 minutes, and secondly an established spin casting process [144] was carried out for a total film thickness of ∼60 nm.

Sb_2Se_3 films were deposited by CSS at a source temperature of 390°C with substrate heating at 330°C and a base pressure of ∼0.05 Torr. Interfacial films for band alignment measurements were deposited for only 30 seconds in order to achieve a film thin enough to carry out the Kraut method (∼20 nm). For the 'bulk' samples, a thicker layer (∼50 nm) was deposited so that the signal from the layer beneath was not seen in the HAXPES measurements. Detailed structural characterisation (including cross-sectional transmission electron microscopy and x-ray diffraction) of similar films can be found in the work by Williams *et al* [75].

4.4.2 Photoemission

HAXPES measurements were carried out at the I09 beamline at Diamond Light Source, Oxfordshire, UK. The experimental setup is described in detail in section 3.2.7. Lab-based XPS data was collected using the monochromated XPS system, also described in section 3.2.7.

4.5 Results

4.5.1 Natural Alignments

Initially, the ionisation potential and work function of Sb_2Se_3, CdS and TiO_2 films that were deposited under the same conditions used for fabrication of devices were measured [57, 81]. Figure 4.7 shows the SEC and VBM of TiO_2, CdS and Sb_2Se_3 that are used to measure the valence band and Fermi level positions of each material with respect to the the vacuum level. Each cut-off was fitted with a linear fit. As can be seen in Figure

4.7, while the gradients naturally vary between the samples, there are no unusual shapes to any of the cut-offs. The 'foot' of the TiO_2 SEC is slightly more pronounced than the others, however this has been accounted for by fitting the straight line to the steepest part of the edge.

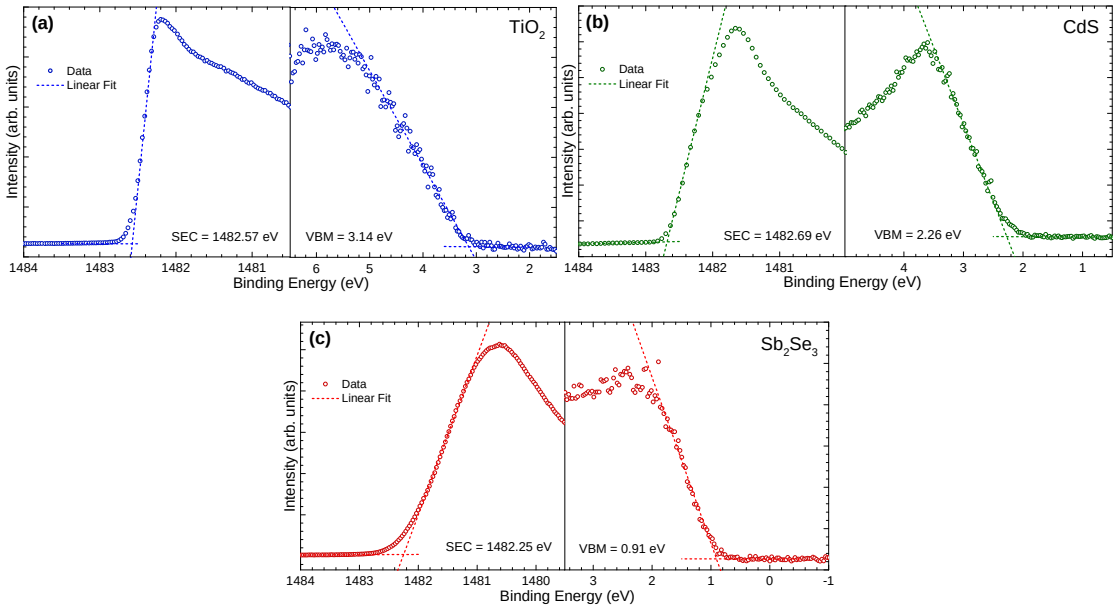

Figure 4.7 Secondary electron cut-off and valence band maximum obtained by XPS for 'bulk' samples of (a) TiO_2, (b) CdS and (c) Sb_2Se_3 with linear fits.

Using the data from Figure 4.7 and literature band gap values [54, 145–147], the EA of each material can be inferred and subsequently a band diagram drawn (Figure 4.8a). The materials in question are well studied and therefore reliable and consistent values for their band gaps can be found from previous studies. From Figure 4.8a, it can be seen that all three materials are n-type. The n-type conductivity of Sb_2Se_3 is a result of the presence of chlorine impurities in the purchased source material. These impurities are unintentional contaminants in standard high purity Sb_2Se_3 granules, however the manufacturer's guarantee of purity accounts only for metallic impurities. This makes the Sb_2Se_3 films studied in this work different from many reports of Sb_2Se_3 in the literature. However, these films have still been used in high efficiency devices [37, 81]. A more detailed discussion of n-type Sb_2Se_3 as well as the formation of an isotype heterojunction between Sb_2Se_3 and an n-type window layer partner is provided by Hobson *et al.* [62] and in Chapter 5.

Figure 4.8b shows the alignment between Sb_2Se_3 and TiO_2 and between Sb_2Se_3 and CdS if the Fermi levels are aligned according to Anderson's rule. According to this rule, the difference in EA is fixed at the interface, leading to a small spike of 0.36 eV

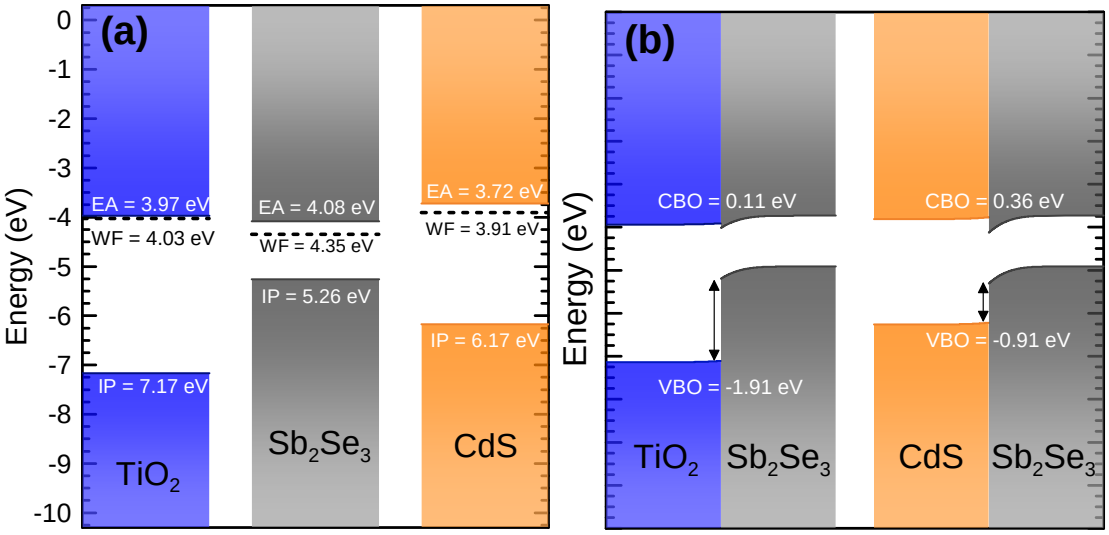

Figure 4.8 (a) Natural Alignments of Sb_2Se_3 (grey) alongside TiO_2 (blue) and CdS (orange) with the Fermi levels aligned. (b) Band alignments when the Fermi levels of the window layers are aligned with that of Sb_2Se_3. The band gaps used for TiO_2, Sb_2Se_3 and CdS were 3.2 eV, 1.18 eV and 2.45 eV respectively.

between CdS and Sb_2Se_3 and a smaller spike of 0.11 eV between TiO_2 and Sb_2Se_3. The bulk band positions of each material are determined from Figure 4.8a and are shifted up/down to align the Fermi levels. Band bending is then incorporated to resolve the discontinuity. An assumption has to be made regarding the distribution of the band bending - in this case it is almost entirely in the Sb_2Se_3 given that the majority of the band bending will occur in the material with the lowest carrier density [137] and that Sb_2Se_3 is known to undergo significant band bending at the surface [62]. However, the distribution of the band bending does not affect the offset itself, which is dependent on the difference in EA. Other interpretations of the distribution of band bending on either side of the interface could be argued but would, in most cases, have little bearing on the overall result. From this it would appear that Sb_2Se_3 and CdS have a good alignment for effective carrier transport in a PV device - a small spike up to 0.4 eV is widely considered to be conducive to achieving high efficiencies [127, 148, 149] by maximising available voltage and minimising the chance of recombination while maintaining a CBO small enough for carriers to overcome.

4.5.2 Band Offset Measurements

The Kraut method approach takes into account the charge transfer between the two materials by directly measuring the interface between them. In this study, HAXPES was used in order to enhance the IMFP of the photoemitted electrons, thereby allowing

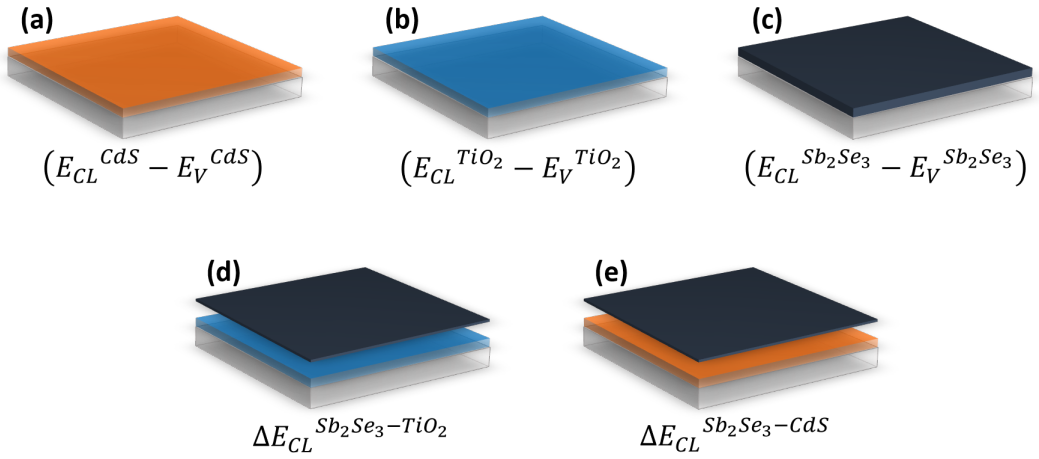

Figure 4.9 Sample set used for Kraut method band offset measurements along with quantities measured from each one: (a-c) show 'bulk' samples of (a) CdS, (b) TiO_2 and (c) Sb_2Se_3, and (d-e) show 'interfacial' samples of (d) Sb_2Se_3 on TiO_2 and (e) Sb_2Se_3 on CdS.

us to measure band alignments with a thicker layer of Sb_2Se_3 (~20 nm). Figure 4.10 shows the photoemission data collected for the band alignment between Sb_2Se_3 and either CdS or TiO_2 (sample set shown in Figure 4.9). In Figures 4.10a-c the survey scans for TiO_2, CdS and Sb_2Se_3 respectively are shown including insets of the detailed valence band scans used to determine VBM positions for each material. Figures 4.10d & 4.10e show survey scans of the interfacial samples with insets showing the separately measured core levels from the window layers. In the original survey scans, the core level signals from the substrates were especially weak but distinctly visible. Only the strongest core level from the substrate material was resolvable however. Figures 4.11, 4.12 & 4.13 show the core level and valence spectra from TiO_2, CdS and Sb_2Se_3 used for the Kraut method.

The VBOs were obtained using a number of characteristic Sb_2Se_3 peaks (Sb 3d, Sb 4d and Se 3d) but only one window layer peak was used as only the most intense one was resolvable (Cd 3d & Ti 2p) due to the attenuation of the window layer photoelectrons by the Sb_2Se_3 overlayer. The results of the band alignment measurement depend strongly on the positions of the core level peaks which, as discussed in section 3.2.6, can vary significantly with different fitting procedures. For both CdS and TiO_2, the fitting procedure was very straightforward as only one Cd and Ti species was present in the core level spectra (Figure). However, as discussed in detail in Chapter 6, Sb_2Se_3 is prone to surface oxidation and this Sb_2O_3 signal, as well as the accompanying O 1s peak, interferes with the Sb core level spectra. Therefore, careful fitting is required to ensure accurate core level positions are determined.

The fitting of the Sb 3d region is complicated by the presence of the O 1s peak at

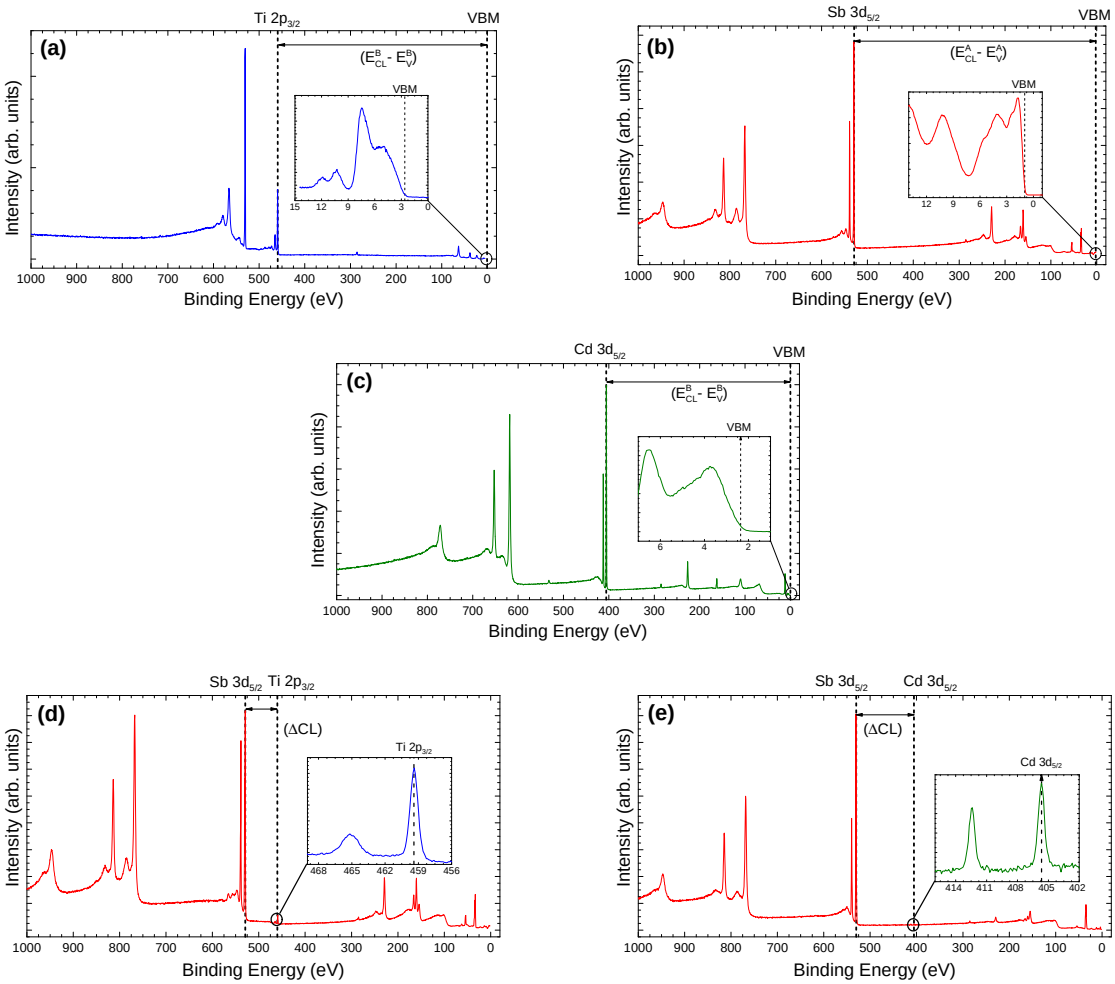

Figure 4.10 HAXPES data used to calculate band offsets. (a-c) show survey scans of 'bulk' (a) TiO_2, (b) Sb_2Se_3 and (c) CdS with separately measured VBMs shown in insets. (d-e) show the 'interfacial' samples of (d) Sb_2Se_3 on TiO_2 and (e) Sb_2Se_3 on CdS with the separately measured core level peaks from the substrates shown in the inset.

a very similar binding energy, but can also be helped by the fitting of the Sb 4d region which does not overlap with any other core levels. Upon examination of the spectrum in Figure 4.11g it was evident that some additional intensity was required beyond the single Sb 4d doublet and this was accounted for by adding an additional Sb 4d doublet. The doublet separation was constrained for both doublets to 1.24 eV, consistent with literature reports [111] and the intensity of the Sb $4d_{5/2}$ components constrained to be 1.5 times the intensity of the Sb $4d_{3/2}$ components. The addition of the doublet to higher binding energy accounted for the additional intensity and the position relative to the

Sb_2Se_3 doublet was consistent with that of Sb_2O_3.

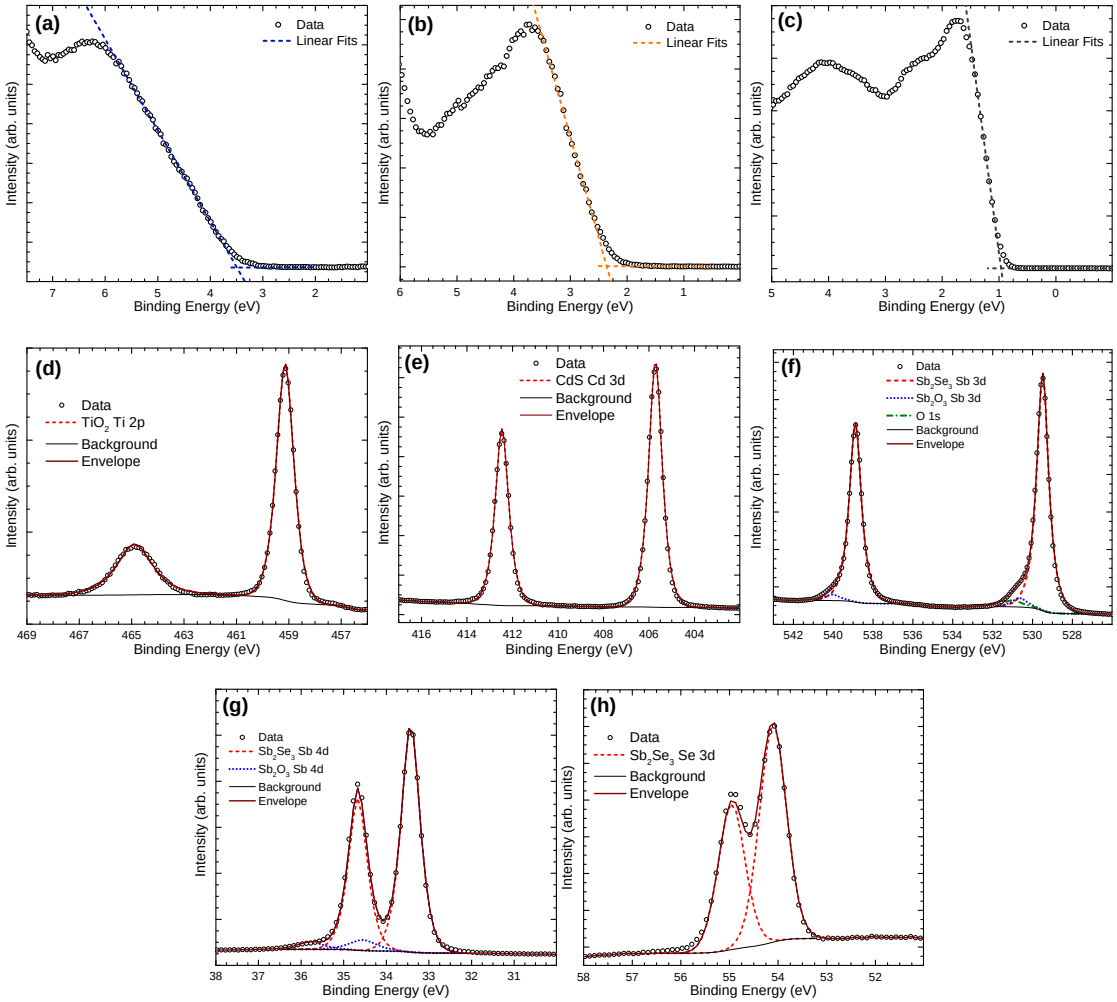

Figure 4.11 (a-c) Valence band and (d-f) core level XPS spectra taken from a 'bulk' (a & d) TiO_2 sample, (b & e) CdS sample and (c & f) Sb_2Se_3 sample. No secondary chemical environments are present in the (d) Ti 2p and (e) Cd 3d spectra and the positions are in good agreement with those expected for TiO_2 and CdS [111]. The (f) Sb 3d and (g) Sb 4d regions show small contaminant signals known to indicate the presence of slight surface oxidation [37, 39, 80].The (h) Se 3d core level shows no secondary chemical environments. The positions are consistent with those expected for Sb_2Se_3 & Sb_2O_3 [37, 111].

Based on this fitting then, the same Sb_2Se_3 and Sb_2O_3 doublets could be included in the Sb 3d core level region (Figure 4.11f) with the addition of an O 1s peak. Once again the doublet separations and intensity ratios were constrained as set out in section

3.2.6. Due to the presence of only two components in the higher binding energy core level region and the applied constraints, this is expected to control the intensity ratios of the Sb_2Se_3 and Sb_2O_3 components, leaving the fitting program (CasaXPS) to fix the O 1s contribution to account for the missing intensity in the lower binding energy peak. The ratios between the Sb_2Se_3 and Sb_2O_3 are consistent with those seen in Figure 4.11g, however these ratios cannot be constrained due to the different depth sensitivity of the different core level regions.

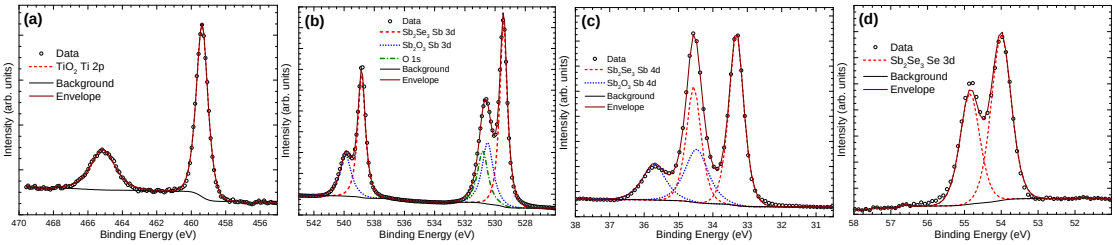

Figure 4.12 (a) Ti 2p, (b) Sb 3d, (c) Sb 4d and (d) Se 3d core level HAXPES spectra taken from an interfacial Sb_2Se_3-on-TiO_2 sample. The Sb 3d and 4d regions show contaminant signals known to indicate the presence of slight surface oxidation [37, 39, 80]. The positions are consistent with those expected for Sb_2Se_3 & Sb_2O_3 [37, 111].

The fitting of the Sb regions in Figures 4.12b and 4.12c and Figures 4.13b and 4.13c are consistent with the fitting in Figures 4.11f and 4.11f and support the conclusions of the fitting due to the much more prominent Sb_2O_3 contribution. The energy separation between Sb components originating from Sb_2Se_3 and Sb_2O_3 is consistent across all samples. The Sb 4d region in Figure 4.13c possesses a small contribution attributed to metallic Sb which was included in order to improve the agreement between envelope and data but did not measurably change the positions of the other two components. It is not included in the Sb 3d region as the other two components were so intense as to obscure any measurable signal from this metallic component. It is also worth noting the unexpectedly intense contribution of Sb_2O_3 to the spectra in Figure 4.13. This is not ideal but is not expected to impact the results of the Kraut method at the heterojunction interface because the Sb_2O_3 is known to grow on the surface as a separate layer and the signal from the Sb_2Se_3 is distinct and intense enough to still carry out the Kraut method calculations.

Finally, the choice of background model will be discussed. The Shirley background is a popular and widely used method of subtracting the inelastically scattered electron background in XPS spectra. For the majority of the peaks fitted in this work the use of a Shirley background (or on occasion, an convolution of linear and Shirley background) is used appropriately to match the background profiles on either side of the core level peak. However, in Figures 4.11h, 4.12d, 4.13a and 4.13d the background signal can be seen to increase towards lower binding energy. This is not the type of background that a

Shirley background is designed to model, given that the inelastically scattered electron background is generally observed to increase towards higher binding energy. In the case of Figures 4.11h, 4.12d, and 4.13d this discrepancy is known to be due to the Se 3d peak sitting atop a plasmon loss signal from the Sb 4d peaks (as discussed in detail in Chapter 5) and the Shirley background seems to accurately fit the rising slope of the loss signal. However, in the case of Figure 4.13a, to the best of our knowledge there is no reason for the background to be increasing in this region. It is likely that this phenomenon is a result of the difference in background profiles between HAXPES and conventional lab-based XPS (for which the Shirley background function was designed. In HAXPES the photoelectrons have a much higher kinetic energy and therefore a much lower probability of inelastic scattering. For this reason, there is not the same characteristic step in background intensity to the higher binding energy side of core level peaks. Ultimately, the nature of the background does not alter the peak positions in any of these four core level regions and therefore it was decided to proceed with the unusual inclining Shirley background.

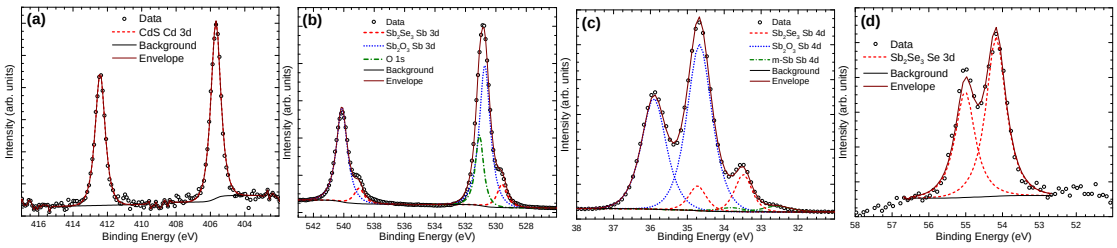

Figure 4.13 (a) Cd 3d, (b) Sb 3d, (c) Sb 4d and (d) Se 3d core level HAXPES spectra taken from an interfacial Sb_2Se_3-on-CdS sample. The Sb 3d and 4d regions show significant contaminant signals known to indicate the presence of surface oxidation [37, 39, 80] as well as a very small signal attributed to metallic Sb [37, 111]. Despite the relative size of these peaks, due to the nature of photoemission data acquisition it is expected that the oxidation is a thin surface layer. The positions are consistent with those expected for Sb_2Se_3 & Sb_2O_3 [37, 111].

Figure 4.14a shows the band offsets drawn from the VBOs measured by the Kraut method using HAXPES of Sb_2Se_3 on both CdS and TiO_2. In the Kraut method approach, no bulk band positions are measured and the offsets acquired are representative of the interface only. The values presented in this work are an average of the VBOs calculated from the different core levels - the full breakdown of values is included in Table 4.2. The Sb_2Se_3/CdS interface has a small CBO of -0.01 eV. The band alignment between Sb_2Se_3 and TiO_2 corresponds to a large cliff-like CBO of -0.82 eV. These appear significantly different to the natural alignment results at first glance. However, before the two measurements can be compared, the impact of the assumptions and approximations involved in the two approaches must be considered.

Sample	Peak	Energy (eV)
Sb_2Se_3	Sb $3d_{5/2}$	529.49
	Se $3d_{5/2}$	54.11
	Sb $4d_{5/2}$	33.43
	VB	0.967
TiO_2	Ti $2p_{3/2}$	459.49
	VB	3.76
CdS	Cd $3d_{5/2}$	405.72
	VB	2.36
TiO_2/Sb_2Se_3	Ti $2p_{3/2}$	459.37
	Sb $3d_{5/2}$	529.44
	Se $3d_{5/2}$	54.00
	Sb $4d_{5/2}$	33.32
CdS/Sb_2Se_3	Cd $3d_{5/2}$	405.68
	Sb $3d_{5/2}$	529.60
	Se $3d_{5/2}$	54.18
	Sb $4d_{5/2}$	33.48

Table 4.1 Core level and valence band positions for each sample measured using HAXPES for Kraut method calculations.

Interface	Peaks used	VBO (eV)
CdS/Sb_2Se_3	$Cd3d_{5/2}$ + $Sb3d_{5/2}$	-1.25 ± 0.14
	$Cd3d_{5/2}$ + $Se3d_{5/2}$	-1.29 ± 0.14
	$Cd3d_{5/2}$ + $Sb4d_{5/2}$	-1.31 ± 0.14
TiO_2/Sb_2Se_3	$Ti2p_{3/2}$ + $Sb3d_{5/2}$	-2.81 ± 0.14
	$Ti2p_{3/2}$ + $Se3d_{5/2}$	-2.87 ± 0.14
	$Ti2p_{3/2}$ + $Sb4d_{5/2}$	-2.87 ± 0.14

Table 4.2 Calculated valence band offsets for different core level peak combinations.

It is of interest to note that the differences in the calculated valence band offset from different Sb_2Se_3 core levels, while small, follow a trend. The calculated VBO is greater for peaks of decreasing binding energy. As mentioned in section 3.2, the depth profiling ability of photoemission measurements is greater for peaks of lower binding energy, and therefore we can assume that the VBO calculated using the $Se3d_{5/2}$ peak will represent an aggregate depth nearer to the interface than a VBO calculated using the $Sb3d_{5/2}$ core level. This trend in fact contradicts the direction of band bending given by Anderson's rule. Given that the differences in calculated VBO are small enough to be within error, this trend could be dismissed simply as an artefact of the measurement.

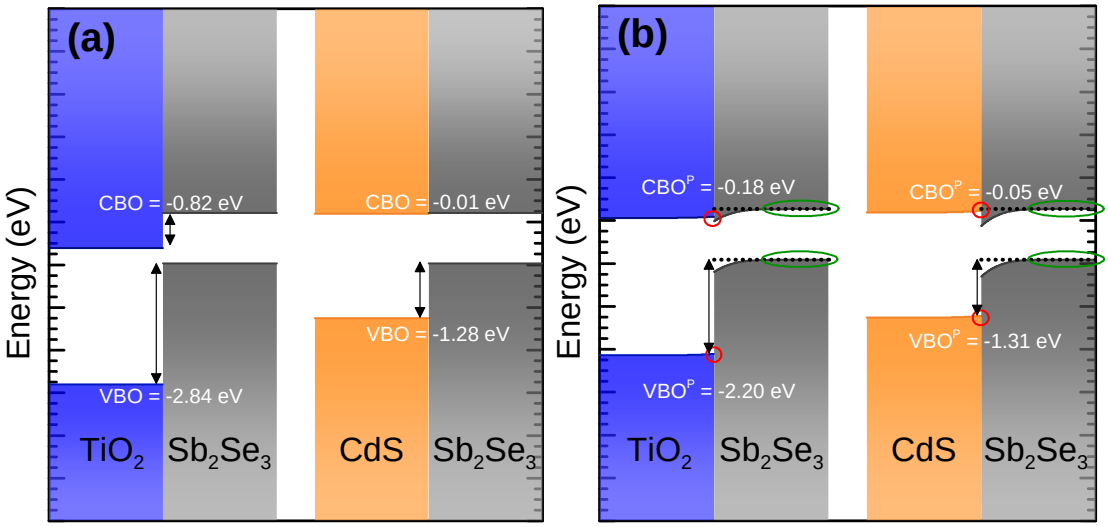

Figure 4.14 (a) Band offsets measured via the Kraut method using HAXPES and (b) natural alignments calculated by Anderson's rule (Figure 4.8b), with red and green circles indicating the equivalent regions probed by the Kraut method in window layer and Sb_2Se_3 respectively.

4.6 Discussion

The measurement of the band offsets via the Kraut method assumes flat bands and an abrupt junction. However, we must consider which regions of the interface contribute most strongly to the photoemission spectra. From the weakness of Ti 2p signal from the TiO_2 layer in Figure 4.10d (and similarly for Cd 3d from the CdS), it is clear that only a very thin part of the window layer would be detected, right at the interface with Sb_2Se_3 (red circles in Figure 4.14b). Fortunately, the Cd 3d and Ti 2p core levels have a very similar binding energy, therefore there is no need to consider any difference in depth profiling between the two peaks For the Sb_2Se_3, we can be sure that the bulk band position (green circles in Figure 4.14b) will dominate the signal considering that, as shown in Figure 4.6, the Beer-Lambert law dictates that 63% of the signal will originate from the top 9 nm. This leads us to assume that the most relevant comparison between the natural alignments and the Kraut method is as depicted in Figure 4.14b. Figure 4.14b shows the same data as presented in Figure 4.8b, with coloured circles to indicate the equivalent regions that would be probed by the Kraut method. The predicted offsets (CBO^P and VBO^P) presented in Figure 4.14b show the energy separation between these circled regions of the Sb_2Se_3 and respective window layers, for easy comparison with Figure 4.14a. Therefore the predicted band offsets quoted in Figure 4.14b are not measured, but are rather a projection of what the interface predicted by Anderson's rule (Figure 4.8b), in the absence of interface charge transfer, would yield if measured via the Kraut method.

Based on this assumption, comparing Figures 4.14a and 4.14b we can see that for the CdS/Sb_2Se_3 interface there is very good agreement between the Kraut method and Anderson's rule. This strengthens the conclusion that CdS and Sb_2Se_3 have excellent band alignments for good device performance in photovoltaics and suggests that the band alignment between CdS and Sb_2Se_3 predicted by Anderson's rule is an accurate prediction of the true band alignment. However, for the TiO_2/Sb_2Se_3 interface, there is a significant difference between VBO and CBO given by the Kraut method and the modified Anderson's rule results. Even when taking into account the differences between the two approaches regarding band bending (Figure 4.14b), the predicted offset (CBO^P) between the flat band position in the Sb_2Se_3 and the edge of the TiO_2 band is only -0.18 eV in the modified Anderson model, compared to a CBO of -0.82 eV measured by the Kraut method. According to the Kraut method here, even with an equivalent amount of band bending as predicted by Anderson's rule, the CBO would actually be cliff-like at the interface (Figure 4.14a), rather than the 0.11 eV spike predicted by Anderson's rule (Figure 4.8b). This suggests that there is a large degree of charge transfer upon contacting which increases the VBO (and CBO) from the natural value. The existence of a cliff-like offset is supported by the observation of a similar alignment for Sb_2S_3 and TiO_2 reported elsewhere [150].

There is a significant difference in how closely matched the natural alignment and Kraut method results are for Sb_2Se_3/CdS and Sb_2Se_3/TiO_2. For the Sb_2Se_3/CdS interface, the difference is minimal. The similitude of sulphur and selenium as anions in terms of both valency and electronegativity could play a part in this. While the electronegativity of all three cations (Ti, Cd and Sb) are all reasonably similar (1.54, 1.69 and 2.05), the electronegativity of O (3.44) is far greater than that of S and Se (2.58 and 2.55), for which it is almost equal [151–153]. This means that CdS and Sb_2Se_3 will possess more covalent bonding than TiO_2 which would be expected to have more ionic bonding. A smaller ionicity difference between the two contacted materials means less charge transfer upon contacting and a smaller interface dipole [151, 154].

From a device performance perspective, the results of the band alignment measurements show that the CdS/Sb_2Se_3 interface has a better alignment than TiO_2/Sb_2Se_3 - according to the Kraut method, TiO_2 would form a large cliff-like barrier at the interface with Sb_2Se_3, leading to a limited available voltage from these kinds of devices. CdS, however, has a conduction band which is perfectly aligned with the conduction band of Sb_2Se_3, showing that this would provide a near-perfect window layer partner, at least in terms of band alignment - a small interfacial spike between 0.3 eV and 0.4 eV has been shown to be ideal for PV devices with materials such as CZTS and CdTe [127, 148, 149]. Additionally, the difference between the natural alignment and Kraut method offsets presents some interesting insights into the formation of these interfaces.

Interestingly, however, CdS-based devices do not necessarily perform better than TiO_2-based devices. It has been shown by our group previously that for Sb_2Se_3 films

grown by CSS, the devices utilising a CdS window layer perform very poorly compared to those using TiO_2 [57]. Phillips *et al.* reported a power conversion efficiency of only 1.44% for a CdS-based device compared to 5.48% for a TiO_2-based device. While the V_{oc} and FF were somewhat lower for CdS (0.42 V & 45.48%) than for TiO_2 (0.45 V & 48.96%), the most significant difference was in the J_{sc}: only 7.57 mA.cm^{-2} for CdS compared to 25.44 mA.cm^{-2} for TiO_2. This is the opposite of what would be expected from the band alignments measured in this study - the cliff-like offset of the TiO_2/Sb_2Se_3 interface would be expected to cause a lower V_{oc} than CdS/Sb_2Se_3, and the small CBO of the CdS/Sb_2Se_3 lead to a very good current. This discrepancy is attributed to interdiffusion of the anions, S and Se, across the interface during the high temperature growth stage of the Sb_2Se_3 devices, a process which leads to the formation of a CdSe layer in between the Sb_2Se_3 and CdS. [57] This is evidenced by time-of-flight secondary ion mass spectrometry (see Figure 4.15) and external quantum efficiency measurements by Phillips *et al.* [57] and significantly reduces the efficiency of the carrier transport from absorber to window layer (the intermixing is not present in the samples used for the band alignments measurements, as discussed below). This is further illustrated by Williams *et al.* where the overlapping presence of Cd, S and Se at the interface, as well as the possible presence of metallic Sb is shown with cross-sectional transmission electron microscopy with elemental mapping (see Figure 4.15) [75]. The implication of this is that it may be possible to achieve a superior device performance if the interdiffusion can be prevented in such a way that the favourable band alignment between CdS and Sb_2Se_3 can be retained.

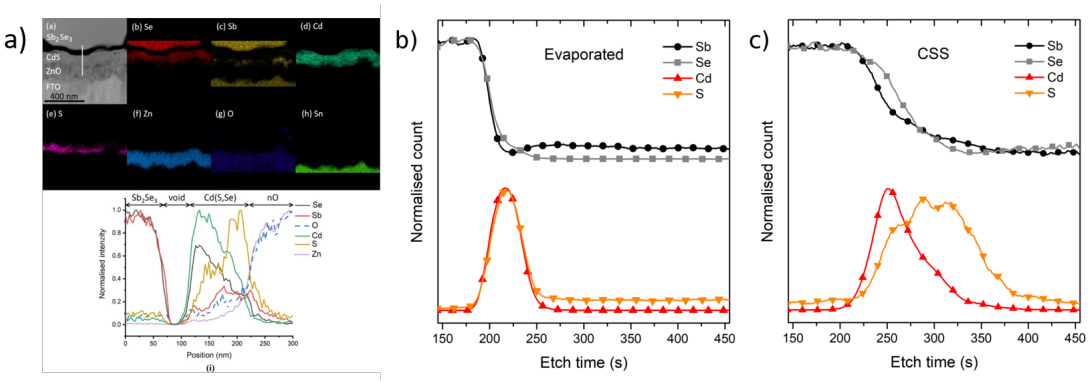

Figure 4.15 (a) shows the cross sectional TEM with EDX mapping of an interface between CSS deposited Sb_2Se_3, and CdS, taken with permission from Williams *et al.* [75]. (b, c) show the SIMS depth profile of (b) CSS and (c) evaporated Sb_2Se_3 on CdS, reproduced with permission from Phillips *et al.* [57].

While the intermixed region is usually present in the working devices using CdS, it is noted here that intermixing is not expected to occur in the samples presented here. Ideally this would be evidenced through the use of cross sectional techniques such as transmission electron microscopy (TEM) with energy dispersive x-ray (EDX) mapping,

but this was not available at the time of writing. There are a number of reasons to assume that no intermixing will take place, however. Sb_2Se_3 films deposited by CSS for devices are made via a two step process, an initial step at lower temperature to lay down a seed layer and then a longer, higher temperature deposition in order to achieve a good grain size/structure. Interfacial samples were deposited using the conditions used for the seed layer, given that this is the layer that forms the initial interface with the window layer. This deposition was therefore carried out at a lower temperature to the full thickness films, which will have reduced the probability of intermixing. It also lasted only 30 seconds, to achieve such a thin layer, leaving very little time for significant intermixing to occur. The photoemission data was studied carefully for any evidence of chemically shifted CdSe or Sb_2S_3 core level components but none were observed, supporting the conclusion that if any intermixing did occur, it was not at a level high enough to be detected by XPS.

It is noteworthy here that the current record efficiency for any Sb_2Se_3 solar cell is held by Li *et al.* [43], and that in their study, a thin TiO_2 interlayer deposited by atomic layer deposition was used between CdS and Sb_2Se_3 to block a similar interdiffusion process. While it must be acknowledged that the devices made by Li *et al.* contained a number of differences from the standard Sb_2Se_3 device structure considered in this work (the use of a substrate configuration and a nanorod structure among them), it is promising to the conclusions of this work that to the best of our knowledge the only study in which steps have been taken to prevent the interdiffusion between CdS and Sb_2Se_3 has achieved such outstanding performance. A similar approach was briefly attempted during the course of this project - ultra-thin layers of TiO_2 and Al_2O_3 were deposited by atomic layer deposition (ALD) onto CdS window layers before deposition of Sb_2Se_3 by CSS. This was not immediately successful, with optimisation of the Sb_2Se_3 deposition conditions for the altered substrate not carried out in full. It is entirely possible that this approach could still provide success with more in-depth research into the best parameters for depositing the ALD layers and subsequent CSS deposition. It is postulated that the band alignments between TiO_2 and Sb_2Se_3 are a limit to the potential efficiency of Sb_2Se_3 devices that use TiO_2 as a window layer. Furthermore, by utilising CdS as a window layer (while blocking interdiffusion with an interlayer thin enough not to interfere significantly with the band alignments), the efficiencies of Sb_2Se_3 solar cells could be improved beyond 10%.

4.7 Conclusion

In this work photoemission techniques were used to thoroughly study the band alignments between Sb_2Se_3 and two of its most commonly used window layers - CdS and TiO_2. Two methods were used - Anderson's rule and the Kraut method - and the results compared. Consideration was given to the merits and limiting factors of both methods and this was used to inform comparison of the two results.

The result of natural alignment measurements showed CdS and Sb_2Se_3 to have a small CBO of 0.36 eV, while the Kraut method gave a practically flat offset of -0.01 eV. A small spike in the conduction band offset is considered ideal for PV applications and flat bands are also a favourable outcome, because there is no barrier to carrier transport, without significant loss of built-in voltage. This is a positive result for CdS as a window layer in band alignment terms, however the use of CdS has caused problems due to the interdiffusion of anions across the interface when depositing at high temperatures. Alterations to the deposition temperature have unfortunately yielded poor grain size and orientation. The band alignments being favourable encourages research into blocking this interdiffusion, potentially using a blocking layer thin enough for carriers to tunnel through. Alternatively, investigating different structures in which materials with very similar band alignments to CdS are used might yield promising results, or different configurations in which CdS could be deposited onto Sb_2Se_3 so as to avoid interdiffusion. Both the use of an interlayer and a substrate configuration have achieved success in achieving the current record efficiency for Sb_2Se_3 cells [43].

The natural band alignment and Anderson's rule interpretation of the TiO_2 and Sb_2Se_3 interface predicted a spike-like conduction band offset of 0.11 eV, in the optimal range for PV performance. However, this result was contradicted by the Kraut method results, which showed a cliff-like offset of -0.82 eV. The discrepancy can be attributed to significant charge transfer upon interface formation, due to the different electronegativities of the two materials, something which is not the case between CdS and Sb_2Se_3. The results suggest that while CdS has an optimal band alignment with Sb_2Se_3, TiO_2-based devices are likely limited by a cliff-like offset leading to recombination and a limited built-in voltage. While some groups prefer to use TiO_2 as a window layer due to the lack of interdiffusion, these results indicate that a better window layer could likely be found with more favourable band alignments.

Chapter Five

Photoemission of Sb_2Se_3 Crystals: Lone Pairs, Band Alignments and Surface Band Bending

Parts of this work are published as:

C. H. Don & H. Shiel *et al.*, "Sb $5s^2$ lone pairs and band alignments of antimony selenide: a photoemission and density functional theory study", *Journal of Materials Chemistry C* **8**, 36, (2020); DOI:10.1039/D0TC03470C

5.1 Introduction

In this work, the primary aim is to obtain a better understanding of the fundamental natural band alignment of Sb_2Se_3. In Chapter 4, the band offsets at the interface between Sb_2Se_3 and its window layer were measured and it was shown how they differ from the band offsets predicted from natural band alignments measurements of Sb_2Se_3. Nevertheless, these natural band alignments play a crucial role in determining the band offsets. The electron affinity and ionisation potential are key quantities used in screening for suitable absorbers for PV and the nature of the surface band bending plays a key role in the formation of band discontinuities at a heterojunction. It is therefore useful to understand the factors that determine these quantities. The distorted structure of Sb_2Se_3, such an important part of its success as a PV material and the challenges to its fabrication, is also rooted in its electronic structure. In this Chapter, the electronic structure of the valence orbitals in Sb_2Se_3 will be explored in depth - how it is influenced by the bulk doping level and how it plays a key role in determining the distorted structure of Sb_2Se_3.

This Chapter is split into two parts. In the first part, a combination of photoemission data and DFT calculated DOS is used to investigate the electronic structure of the valence band in Sb_2Se_3 and the presence of a stereochemically active lone pair of electrons is evidenced. In the second part, the surface band bending of the valence band is

investigated by using a combination of different photoemission techniques and Python modelling of the surface space charge layers. This study is carried out for two types of Sb_2Se_3 - one doped with chlorine with n-type conductivity and the other doped with tin with p-type conductivity.

5.2 Part 1 - Lone Pairs

The aim of this study is to show experimentally the presence of a stereochemically active lone pair orbital at the valence band edge of Sb_2Se_3 (which has been predicted by theory [155]), and how this influences the ionisation potential and natural band alignment of the material. The study was carried out on highly-oriented bulk crystals of Sb_2Se_3 grown by a melt growth technique. The use of these bulk crystals allowed for *in situ* cleaving or exfoliation to remove surface contaminants and to reveal a pristine surface with one dominant orientation. This allows for an investigation of the fundamental properties of Sb_2Se_3 without the complication of contamination from the device making process, mixed orientations or any other device related factors. The influence of surface contamination on the valence band spectra is also shown. The different photon energies of HAXPES ($h\nu = 5.921$ keV) and XPS ($h\nu = 1.487$ keV) are used to discriminate between different orbitals within the valence band when comparing to density functional theory (DFT) calculations. The ionisation potential was measured using traditional lab-based XPS of the valence band and secondary electron cut-off.

5.2.1 Background

The Stereochemically Active Lone Pair

The physical properties of any material are strongly influenced by its electronic structure. This in turn is intertwined with the chemical bonding of the compound, something which also determines its electronic properties. The chemical bonding environment therefore lies at the root of all understanding of a material's properties. One such example of this is the case of lone pair materials. A lone pair refers to a pair of valence electrons that do not play a role in chemical bonding. This allows the element containing the lone pair to occupy a valence state two lower than its natively expected state. However, some lone pairs are known to be strereochemically active (meaning that they play a role in determining the crystal structure), despite being inactive in bonding. A brief overview of stereoactive lone pair theory (both classical and revised) will be provided below. For a fuller discussion see works by Dunitz *et al.* [156] and Walsh *et al.* [51].

The Classical Model

In the classical model laid out by Dunitz and Orgel in 1960, the lone pair is formed of non-bonding cation s and p orbitals. Due to the different parity of these orbitals, mixing cannot occur on cation sites with inversion symmetry, and the structure must be

distorted for the hybridisation to be allowed. This explains the distorted structures of lone pair containing materials - electron repulsion causes the structure to be deformed which leads to s-p hybridisation becoming allowed between the cation orbitals. The distorted structure is stabilised by the lowering of the energy of the system via a pseudo Jahn-Teller effect. However, this model does not explain why some lone pair containing materials (such as Sb_2Te_3, PbS and SnTe) do not show a distorted structure. It also fails to account for cases in which the cation s and p orbitals are well separated energetically, which should prevent mixing from occurring [156].

The Revised Model

It was generally accepted that the classical model for stereochemically active lone pairs was incomplete, and in 2011 the revised lone pair model was presented [51], based on work by A. Walsh, G. W. Watson and S. C. Parker on PbO and SnO, two materials that have polymorphs with distorted and undistorted structures [157–160]. Through DFT calculation of both distorted and undistorted structures of these two materials, they showed that the cation ns^2 valence electrons were in fact not chemically inert, and interacted strongly with the anion valence p orbitals to form bonding and anti-bonding states. These states would appear at the bottom and top of the valence band, respectively, and contradict the classical model of a non-bonding lone pair of electrons. The distortion of the lattice is the result of a subsequent mixing of the anti-bonding state with the unoccupied cation p state (see Figure 5.1b). This provides a stabilising effect for the occupied states. Without lattice distortion there would not be a net stabilising effect for the p orbitals and the hybridisation would be crystal-symmetry forbidden. The lattice distortion causes electron density to become asymmetric, effectively being 'pushed' out into the 'structural void' [51]. These stereochemically active lone pairs therefore only conform partially to the classical definition - the electron density is not fully shared between cation and anion in a traditional understanding of chemical bonding, however it is not entirely chemically inert either.

This theoretical understanding of the revised lone pair model has also been used to predict materials that will have sterically active and inactive lone pairs. The Sb chalcogenide series is one such example, with Sb_2O_3, Sb_2S_3 and Sb_2Se_3 being predicted to have distorted structures while Sb_2Te_3 has a centrosymmetric crystal structure. This difference is attributed to the energy separation between the cation s orbital and the anion p orbital. For a strong stabilising effect, the anti-bonding states that mix with the cation p-orbitals must have a strong s component, and this requires the cation s state and the anion p state to be close in energy. As shown in Figure 5.1a, this energy separation increases down the Sb chalcogenide series, meaning that in Sb_2Te_3 there is not a sufficient stabilising effect for lattice distortion to occur [155]. While this is strong circumstantial evidence for stereochemically active lone pairs in Sb_2Se_3, experimental evidence has not been provided until now.

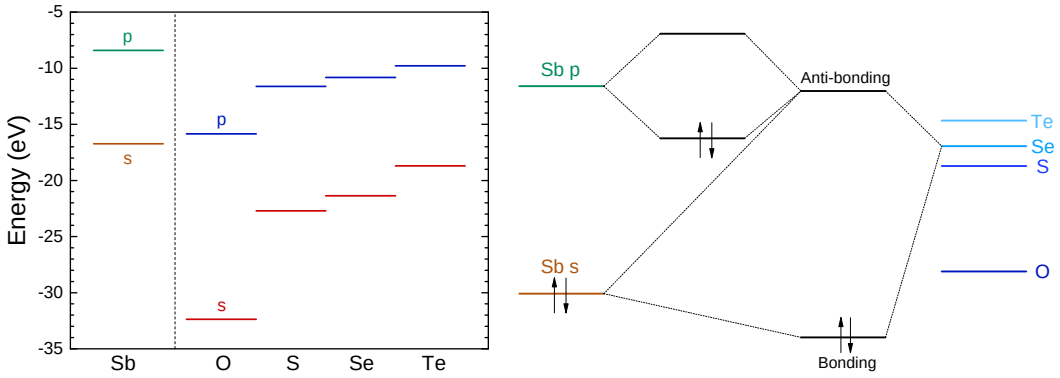

Figure 5.1 (a) Energy of s and p valence orbitals in antimony and the chalcogenide element series and (b) a schematic diagram of the orbital mixing that takes place in the revised lone pair model.

Lone pair materials in PV

Lone pair containing materials are attracting increased interest in the field of photovoltaics in recent years. This is largely as a result of the unprecedented success of MAPI, the leading perovskite material that has achieved such rapid growth as a PV technology [161]. Many believe that a significant factor in MAPI's success is the Pb $6s^2$ lone pair of electrons [161–163]. In 2015 Brandt *et al.* stated that "Materials that contain a lone $6s^2$ or $5s^2$ pair of electrons on the cation have the potential to share the high dielectric constant, low effective masses, and VB antibonding character that lead to defect tolerant transport properties" [162]. It is argued that the presence of ns^2 lone pairs encourages the formation of shallow defects only, meaning less detriment from imperfections in the material [162, 163]. Additionally, Yin *et al.* claim that "the extremely high optical absorption coefficient is due to the perovskite symmetry and the direct band gap p-p transitions enabled by the Pb lone-pair s orbitals" [164]. According to Yin *et al.*, the presence of p orbital character at both the VBM and CBM greatly enhances the transition probability and leads to a greater absorption coefficient in lone pair materials. This is tempered by the counteracting effect of increased anisotropy and propensity for indirect gaps in lone pair materials [162].

The search for other successful PV materials with ns^2 lone pairs is already underway, with a number of alternative perovskites being researched, along with Sn^{2+}, Ge^{2+}, Bi^{3+} and Sb^{3+} containing compounds. Indeed, Sn chalcogenides have long been an area of interest in PV circles, with SnS being reported as a potential PV material as early as 1994 [165]. Tin sulphide has three phases (SnS, SnS_2 & Sn_2S_3), of which SnS and Sn_2S_3 possess lone pairs and a suitable band gap for PV application [116, 166]. While Sn_2S_3 is sparsely studied, SnS has been studied extensively in a PV context. However, efficiencies have yet to surpass 5%, attributed largely to difficulties with microstructure and band

alignments [167, 168]. Ge-based absorbers are somewhat less well studied, although there has recently been renewed interest following the successes of Sb chalcogenides. GeS and GeSe both have suitable band gaps for PV and near-direct band gaps similar to Sb_2Se_3 [169], anisotropic crystal structures and are made up of earth abundant and cheap elements. Currently the record efficiency stands at 5.2% for GeSe, albeit with very limited research thus far [170, 171]. Of Bi containing compounds, only Bi_2S_3 has attracted any great attention [161, 172]. Bi_2S_3 has a similar 1D crystal structure to Sb_2Se_3 and an optical gap in the range 1.3-1.6eV [161]. The record efficiency for a planar heterojunction cell currently stands at 3.3%, however progress has also been made by pairing it with PbS quantum dots [173].

Finally there are the Sb^{3+} compounds, namely Sb_2S_3 and Sb_2Se_3. The presence of a lone pair of ns^2 electrons at the valence band maximum of Sb_2Se_3 and its implications has been referenced previously by a number of authors. In 2017, Ganose *et al.* discussed the prospects of lone pair materials in PV, highlighting some of their key advantages [161]. Firstly, as mentioned above, materials with anti-bonding states at the top of the valence band have been theorised to be defect tolerant [162, 163]. It is also stated that the presence of a lone pair would influence the magnitude of the band gap of a material and the energy of the valence band maximum (and by extension the band alignment with other materials), as discussed further in this Chapter [161]. The projection of the lone pair states into the structural void also provides Sb_2Se_3 with its much discussed 1D-nanoribbon structure. This was proposed by Zhou *et al.* to allow benign grain boundaries and effective carrier transport, as discussed in detail in section 2.2.2 [78].

Other references to Sb_2Se_3's lone pair electronic structure have been made in the literature, however these are mentioned in passing with no detailed discussion of the implications [57, 85]. To the best of our knowledge this work is the first study to show experimental evidence for its existence. In this work, the implications of the presence of a lone pair for the band gap and band alignment are also presented experimentally and in the context of its relevance to PV applications.

Photoionisation Cross-Sections

The energy dependence of photoionisation cross-sections refers to the way in which an orbital's photoionisation probability varies with different incident photon energies. As discussed in section 3.2.1, the rate of photoemission tends to decrease with increasing incident photon energy (at least sufficiently far from the threshold energy). This decrease is the result of the wavelength of the incident photon becoming more comparable with the radial extension of the valence band orbitals and the resulting cancellation of terms contributing to the transition matrix element (see section 3.2.1 for more details). In general, s orbital photoionisation cross-sections decrease more gradually with increasing photon energy relative to other orbitals because of the more contracted nature of the orbitals (see Figure 5.2). Therefore, the relative contribution to the valence band photoemission spectrum from s orbitals is generally expected to be greater in measurements

taken with hard x-rays than with soft x-rays. The cross sections for the Sb and Se orbitals are also compared in Table 5.1 for the two photon energies used in our photoemission measurements.

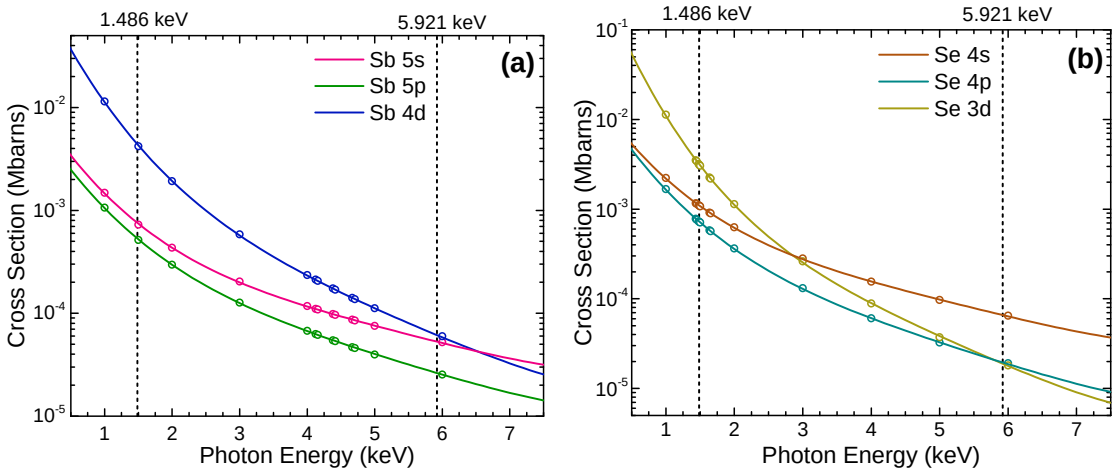

Figure 5.2 Photoionisation cross-section energy dependence for each valence orbital in (a) antimony and (b) selenium [124].

This photoionisation cross-section energy dependence can be exploited to identify the presence of various orbitals in different parts of the valence band. DFT calculations such as the ones employed by Watson and Parker [157] to identify which materials will possess a lone pair can predict the valence band DOS of a material split into the individual orbital contributions. By applying suitable cross section corrections for the different photon energies, this DOS can be directly compared to the experimental data. Valence band data collected with different photon energies will have subtly different shapes and the orbital contributions that are manifest in the difference can be identified. This approach has been used previously to identify the presence of a lone pair in some tin sulphide phases and not in others [166, 174].

	Cross Section (Mbarns)	
Orbital	1486 eV	5921 eV
Sb 5s	754.7	52.33
Sb 5p	531.9	25.32
Sb 4d	4390	59.74
Se 4s	1101	64.94
Se 4p	726.1	19.12
Se 3d	3170	18.06

Table 5.1 Photoionisation cross sections of the Sb_2Se_3 orbitals at the two different photon energies used for the photoemission measurements.[124]

5.2.2 Experimental Details

Fabrication

The Sb_2Se_3 single crystals utilised in this work were prepared by T. D. C. Hobson, via the Bridgman melt-growth technique, as laid out in section 3.1.5. More specific details are provided by Hobson *et al.* [62]. The identity and crystallographic orientation of Sb_2Se_3 was confirmed by x-ray diffraction and Raman spectroscopy as described in detail for these crystals by Fleck *et al.* in [175]. Its chemical composition was further confirmed as 40% Sb and 60% Se by EDX analysis in an SEM, this being consistent with the expected 2:3 stoichiometry. An SEM image and some EDX data are included elsewhere [34]. Extracted crystals were found to cleave easily in one plane to reveal parallel reflective facets, demonstrated to be the (010) crystal plane (using the *Pbnm* space group setting) [176]. Given that the weakest van der Waals interactions lie along the b axis, this behaviour is expected [177]. This (010) crystal surface was exposed to air and is the "as-received" crystal referred to below as opposed to the "*in situ* cleaved" crystal which refers to the crystal cleaved under UHV. For the synchrotron photoemission measurements, this was done by gluing a post to the crystal surface, and cleaving by hitting the post with a wobble stick. For the laboratory XPS measurements, this was done by exfoliating surface layers of the crystal using carbon tape attached to a sample-transfer arm.

Photoemission

HAXPES measurements were carried out at the I09 beamline at Diamond Light Source, Oxfordshire, UK. The experimental setup is described in detail in section 3.2.7. The crystals were first measured as-received and then were cleaved *in situ* to expose a pristine (010) surface and to prevent any re-oxidation of the surface. All peak positions from curve fitting are reported with an error of ± 0.05 eV. Lab-based XPS data was collected using the monochromated XPS system, also described in section 3.2.7. Photoemission spectra were curve fitted using CASAXPS software with Voigt lineshapes after subtracting a Shirley background [178].

DFT calculations were performed within periodic boundary conditions using the Vienna Ab Initio Simulation Package [179–182]. The screened hybrid exchange correlation functional HSE06 was used [183], for geometry optimization and electronic structure calculations of Sb_2Se_3. To account for the ribbon nature of the Sb_2Se_3 structure, the D3 dispersion correction from Grimme *et al.* was also included in DOS calculations [184], while spin-orbit coupling was included for all calculations. For more details see work by Savory *et al.* [85].

5.2.3 Results

Core Level HAXPES

Core level analysis of photoemission measurements allows for the identification of surface chemical composition and the extent to which surface contamination has chemically altered the surface through examination of the chemical shift in characteristic elemental lines. It is generally preferred in PV to use materials that are not strongly affected by exposure to atmospheric conditions due to the potential instability and lifetime limitation that this might introduce when modules are in use and exposed to the elements. It is also inconvenient to need to manufacture materials in ultra-clean environments. Surface contamination can also have an effect on the formation of favourable interfaces in photovoltaic devices, as will be discussed in Chapter 6. Therefore, a good understanding of how to identify these contaminants is essential. A list of core level peak positions and full widths at half maximum (FWHM) values for an as-received and *in situ* cleaved Sb_2Se_3 bulk crystal can be found in Table 5.2.

	As-received		*In situ* cleaved	
Peak	BE (eV)	Width (eV)	BE (eV)	Width (eV)
Sb(Se) $3d_{5/2}$	529.53	0.71	529.71	0.62
Sb(O) $3d_{5/2}$	530.72	0.90	-	-
Sb(Se) $4d_{5/2}$	33.41	0.56	33.47	0.46
Sb(O) $4d_{5/2}$	34.62	0.83	-	-
Se(Sb) $3d_{5/2}$	54.11	0.68	54.16	0.58
Se(Elem.) $3d_{5/2}$	55.78	1.13	-	-
O(Sb) $1s$	530.66	0.60	-	-
O(Adv.) $1s$	531.17	0.60	-	-

Table 5.2 Core level binding energy (BE) and width (FWHM) of all fitted peaks in the HAXPES spectra from an as-received and an *in situ* cleaved Sb_2Se_3 bulk crystal. The element in brackets denotes the what species is responsible for the chemical shift. "Sb(Elem.)" denotes elemental selenium and "O(Adv.)" denotes adventitious oxygen.

Figure 5.3 shows Sb $3d_{3/2}$ and $3d_{5/2}$ peaks before and after *in situ* cleaving to expose a pristine surface. The core level fitting procedure was the same as that described in Chapters 3 and 4. In both Figure 5.3a and Figure 5.3b, the agreement between the data and the fitted envelope is good. The highest intensity peaks seen in both Figure 5.3a and Figure 5.3b are from antimony bonded to selenium (red dotted line). The spectrum recorded from the contaminated sample in Figure 5.3a is complicated by the overlap of peaks due to the O $1s$ state (yellow and green), as well as chemically shifted Sb $3d$ states bonded to oxygen (blue solid lines). This feature is attributed to Sb_2O_3 due to the $3d_{5/2}$ peak position of 530.7 eV coinciding with literature values for Sb_2O_3 [185]. Despite this agreement, the evidence is not enough to be conclusive – a previous paper reported Sb $3d_{3/2}$ positions of Sb_2O_3 and Sb_2O_5 as 539.8 eV and 540.4 eV respectively

[186], compared to a position measured here of 540.1 eV. The smallest of the fitted peaks in Figure 5.3a (yellow) has a measured peak position also of 530.7 eV which broadly agrees with current literature for the O 1s state in an Sb_2O_3 environment (529.8 eV)[187] and this same conclusion has been reached in related work [146].

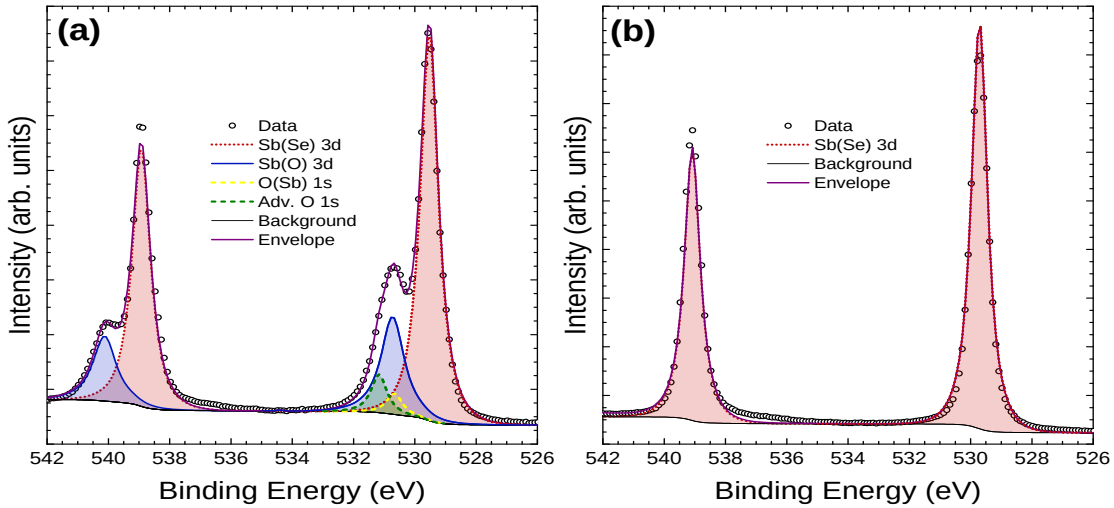

Figure 5.3 Sb 3*d* HAXPES data from an Sb_2Se_3 crystal (a) before and (b) after *in situ* cleaving.

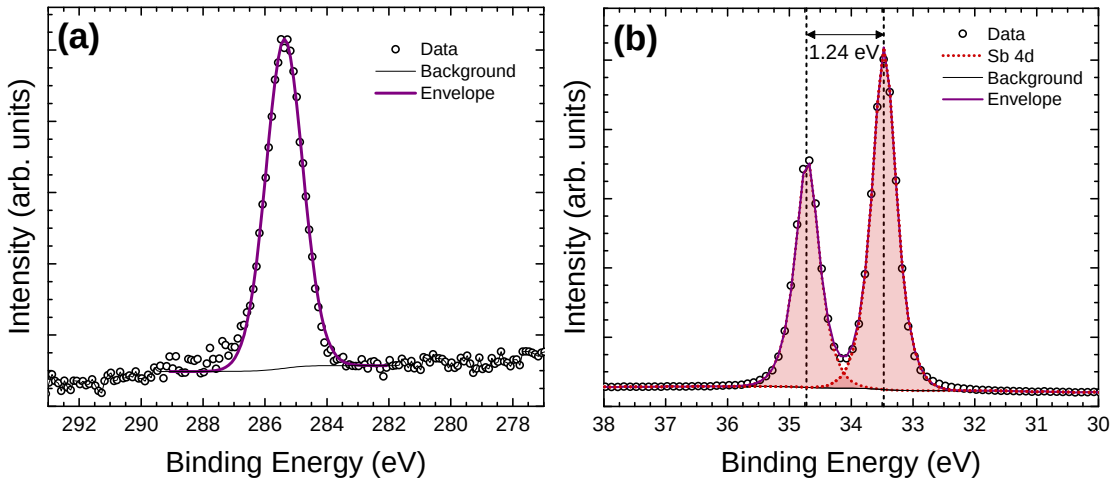

Figure 5.4 (a) Carbon 1s core level peak from the as received Sb_2Se_3 crystal. No chemical shifts are visible, indicating that the carbon is not bonded to any elements other than hydrogen. (b) Sb 4d core level peaks with the doublet separation used to fit plasmon loss lines.

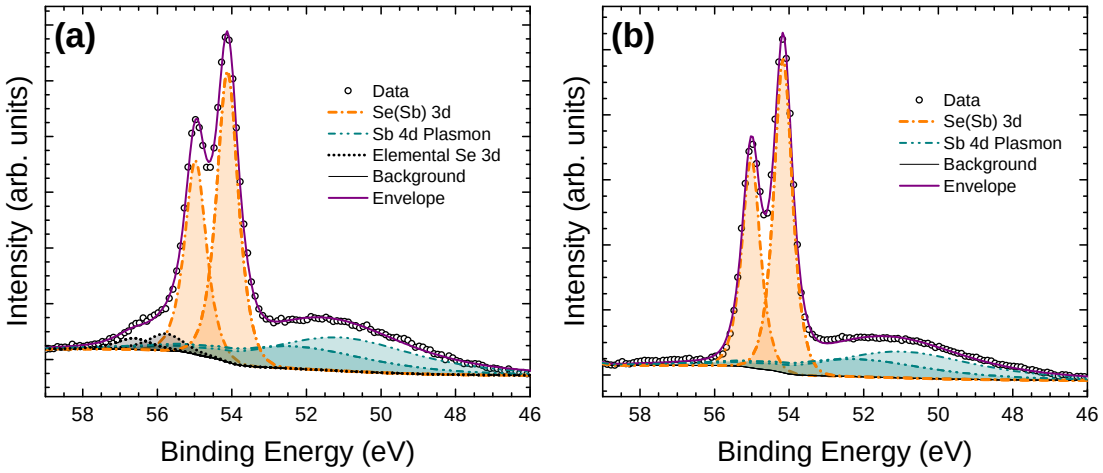

Figure 5.5 Se 3*d* HAXPES data from an Sb_2Se_3 crystal (a) before and (b) after *in situ* cleaving.

The remaining O 1s peak (green) has been labelled as adventitious oxygen weakly adsorbed on the surface, but could also be a result of atmospheric CO_2 surface physisorption. However, if this were the case we would expect to also see a chemical shift in the carbon 1s core level. As shown in Figure 5.4a the position of the carbon 1s peak at 285.4 eV which is the expected position for adventitious hydrocarbon and there are no additional chemical shifts present, indicating that there is no CO_2 contamination. The carbon signal is likewise attributed to adventitious carbon weakly adsorbed onto the surface. The assignment of all these extra peaks in Figure 5.3a to oxygen-related species caused by atmospheric exposure is further supported by the data from the *in situ* cleaved crystal in Figure 5.3b which shows only clean, sharply defined selenium bound antimony 3*d* peaks in this binding energy region.

A comparison of Se 3*d* data from a contaminated as-received and an *in situ* cleaved crystal is presented in Figure 5.5. Unfortunately, the spectra are complicated by the presence of valence band plasmon loss features from the Sb 4*d* states. This was confirmed by measuring the positions of each plasmon peak in relation to the parent core level (Figure 5.6). It was determined that the plasmon loss energy was 17.9 eV and this was consistent with the position of the spectral features in the Se 3d core levels. By fitting the Sb 4d region of the cleaved crystal, the separation of the plasmon features could also be determined, as it would be equal to the separation of the Sb 4d doublet (1.24 eV). Knowing the plasmon position relative to the Sb 4d core levels and the separation allowed for very accurate fitting of the plasmon loss features in the Se 3d region, removing any uncertainty over the rest of the fit. Since the selenium from the pure Sb_2Se_3 crystal must become unbound when it is replaced by oxygen to form Sb_2O_3 on the surface, the chemically shifted peaks in Figure 5.5a (blue dotted line) were assigned

to free elemental selenium at the surface, consistent with previous reports [37, 111]. As expected, the peaks associated with elemental Se are also absent after *in situ* cleaving, further confirming that exposure to standard atmospheric conditions does not impact the bulk chemistry of the material, only the surface.

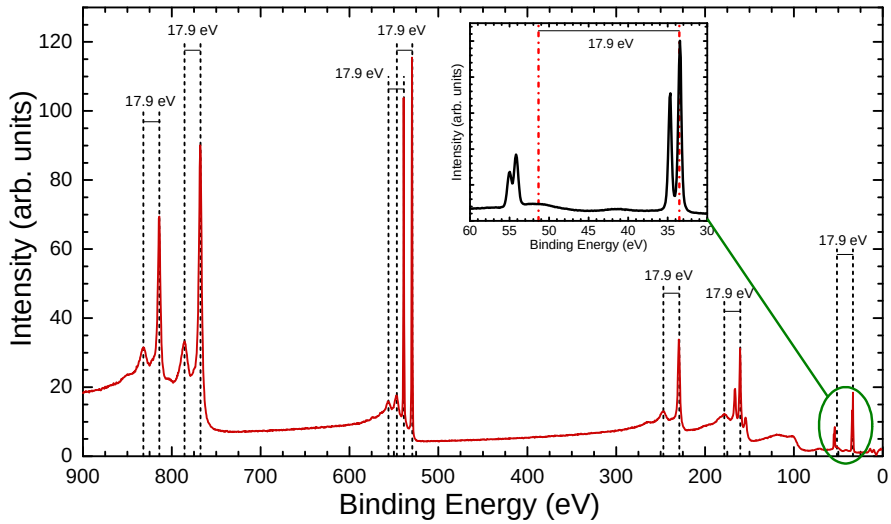

Figure 5.6 HAXPES survey spectrum from cleaved Sb_2Se_3, showing plasmon loss features at a binding energy of 17.9 eV above each core level peak, corresponding to lower kinetic energy due to energy loss to the plasmon excitations.

Valence Band Photoemission

Valence band (VB) spectra were obtained by collecting photoelectrons excited by monochromatic x-rays of 5.921 keV both before and after *in situ* cleaving of the crystal, to look at the effects of surface contamination on VB states. An additional data set was taken from an *in situ* exfoliated crystal using traditional lab Al Kα (soft) x-ray energy of 1.4866 keV to utilise the energy dependence of photoionisation cross sections as a way of verifying valence orbital contributions from the changing intensities of VB features. DFT is used here to calculate the contributions of the different orbitals to the overall valence band occupation in Sb_2Se_3. Then, comparison of the theory with experimental results enables orbital hybridisation and its effect on the VB spectra and band alignment to be determined. The DFT calculated DOS is shifted to line up with the Sb_2Se_3 valence band for ease of comparison.

In Figure 5.7 it can be seen that there are broad similarities in the data from as-received and *in situ* cleaved crystals. This is expected because the 5.921 keV x-ray energy is not very surface sensitive - the resulting photoelectron inelastic mean free path is such that the effective probing depth is about 20 nm (see Chapter 4). Therefore, the

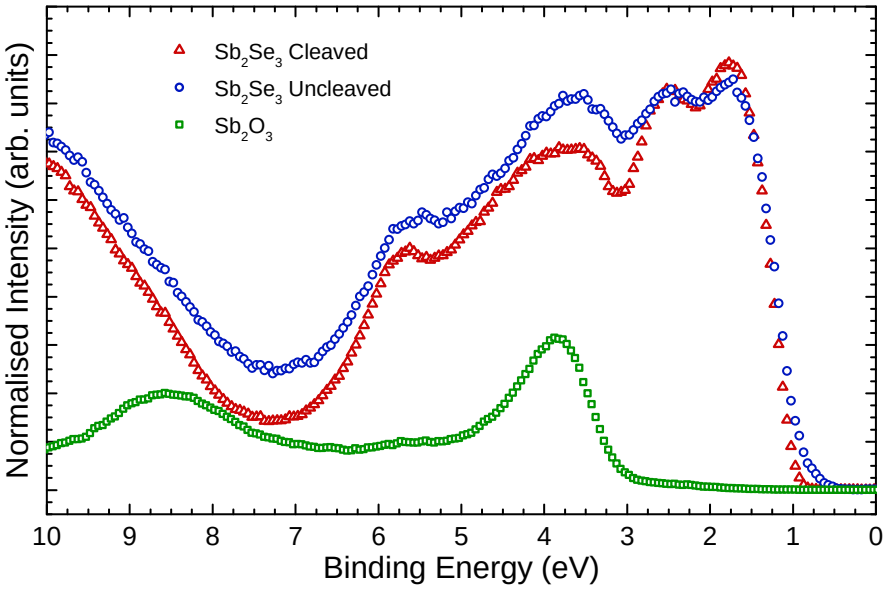

Figure 5.7 Normalised valence band spectra of the as-received (blue) and *in situ* cleaved (red) Sb_2Se_3 crystals with the valence band spectrum of an Sb_2O_3 thin film (green) overlaid for comparison.

contribution to the spectrum from the surface oxidised layer is relatively small. The main differences can be seen between 3 eV and 4 eV where the data from the *in situ* cleaved crystal is of significantly lower intensity. The additional intensity for the as-received crystal is attributed to a thin surface layer of Sb_2O_3, which is known to be present from the core level analysis. This is supported by overlaying the data with a valence band spectrum obtained from an Sb_2O_3 thin film measured with the same photon energy. The region with the greatest disparity between the as-received and cleaved crystals lines up perfectly with the highest intensity point of the Sb_2O_3 valence band. The other region in which the difference is more pronounced, between 7 eV and 8 eV lines up very closely with the secondary peak in the Sb_2O_3 valence band. No significant change in the spectra at low binding energy is seen after *in situ* cleaving, which indicates that the Sb_2O_3 contribution to the data from the contaminated crystal does not affect the spectrum in the vicinity of the VBM.

The data from the *in situ* cleaved crystal agrees well with the theoretically predicted DOS at low binding energies (Figure 5.8, however the intensities fall off increasingly with binding energy despite replicating the overall shape of the total DOS (red line) fairly well. This effect is most likely due to final-state relaxation effects which have been observed to shift high binding energy valence band features to lower binding energies [146, 174, 188]. Other possible contributors to this lack of intensity arise from DFT inaccuracies in dealing with the van der Waals bonding present in this material and also the lack of a well established or optimal method for background subtraction of valence band photoe-

mission data. The DOS predicts a large contribution to the spectra from the Sb $5s$ state at low binding energy which is supported by the strong agreement with the experimental data in this region. This result is significant because it suggests a lone pair of electrons in the Sb $5s$ state, causing this group V element to be in an Sb(III) oxidation state, instead of the naïvely expected Sb(V) state for a group V element. The presence of this lone pair Sb $5s$ state contributes to the observed layer-like ribbon structure as summarised by Walsh *et al.* [51]

Due to the photoionisation cross-section energy dependence (Figure 5.2), the cross-section corrected DOS for 1.487 keV in Figure 5.8b predicts lower relative contributions to the spectra from s orbitals, and additional intensity from d and p orbitals, compared with the calculated cross-section corrected DOS for 5.921 keV in Figure 5.8a. This is consistent with the experimental data, which shows reduced relative intensity in the initial feature near the VB onset, confirming that the Sb $5s$ lone pair state is in fact occupied and contributing intensity in this region. It is the strong interaction between the cation s and anion p orbitals that results in high-energy anti-bonding states with a considerable degree of cation s character at the top of the upper valence band [51]. The hybridization of the Sb $5s$ states with Se $4p$ states results in intensity from the Se $4p$ states also occurring at the VBM. In other words, in the absence of the Sb $5s$ lone pair states at top of the valence band, the VBM would be lower in energy, further from the vacuum level.

5.2.4 Discussion

The implications of the presence of stereochemically active lone pairs at the valence band edge has been explored previously, such as the work on the different tin sulphide phases by Whittles *et al.* and Jones *et al.* [166, 174]. The mixing of the anion p orbitals with the ns^2 lone pair effectively 'drags' the valence band edge to a lower binding energy and leads to the phases that possess this lone pair to have a significantly lower band gap and ionisation potential than those without. The significance of the lone pair on Sb_2Se_3 band alignments can be put into context by comparing this work with those results on tin sulphides and similar work performed by the same group on $CuSbS_2$,[146]. It can be seen in Figure 5.10 that the ionisation potentials of $CuSbS_2$, SnS and Sn_2S_3 (the tin sulphide phases possessing a lone pair) range from 4.66 eV to 4.98 eV. However, chalcogenide materials that are similar but lack an ns^2 lone pair at the top of the valence band, such as SnS_2 and CdS, have ionisation potentials ranging from 5.67 eV to 6.70 eV, significantly greater than the lone pair materials. In order to see how Sb_2Se_3 fits in with this trend, the ionisation potential of an identical crystal as used in the HAXPES was determined. By measuring the VBM and SEC of the XPS spectrum, as shown in Figure 5.9, and using equation 5.1 (in which hν is the incident x-ray excitation energy, hν=1486.6 eV) the ionisation potential can be calculated.

$$\mathrm{IP} = \mathrm{h}\nu - (\mathrm{SEC} - \mathrm{VBM}) \tag{5.1}$$

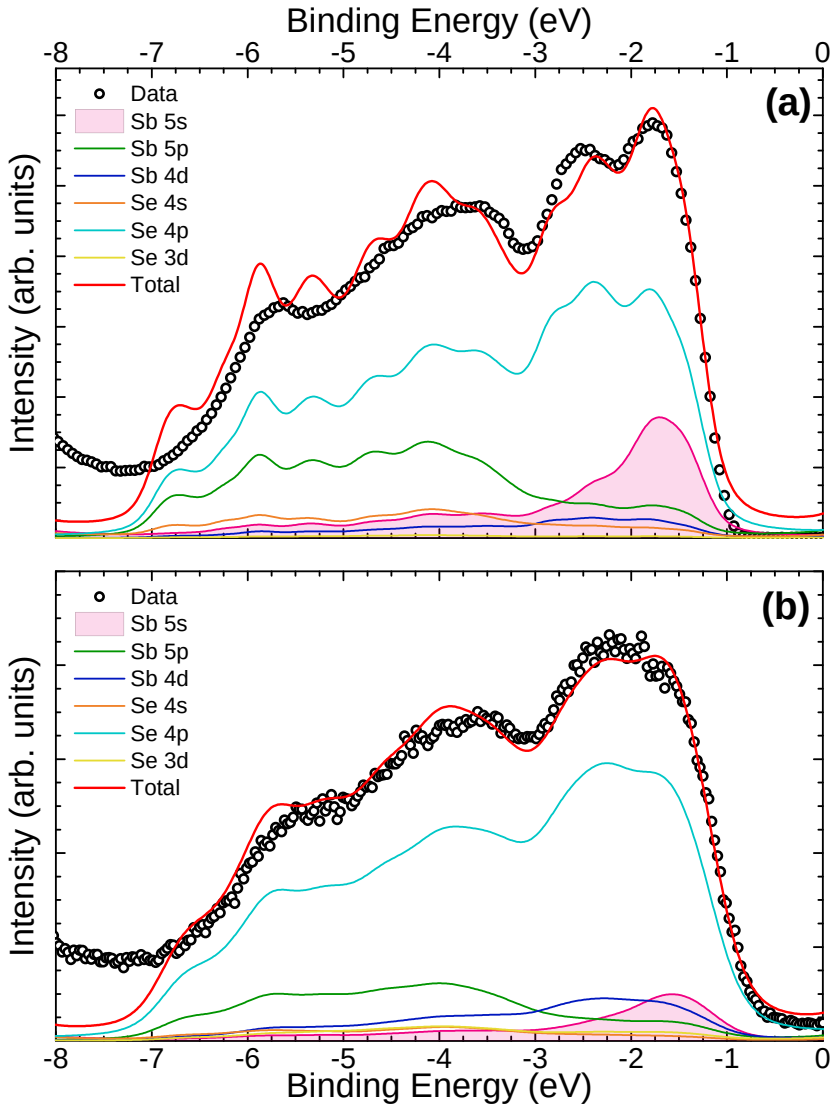

Figure 5.8 VB XPS spectra from an Sb_2Se_3 single crystal sample for (a) hard x-rays with a photon energy of 5.921 keV after *in situ* crystal cleaving and in (b) soft x-rays with a 1.487 keV photon energy after *in situ* exfoliation. Both are plotted with total and partial theoretical VB DOS calculations.

The measured ionisation potential for the Sb_2Se_3 crystal in this study was found to be 5.13 eV. This is consistent with the ionisation potential of 5.26 eV measured for a CSS grown thin film measured in Chapter 4 (Figure 4.8a). While consistent, these two values are not identical and the difference could be attributed to a number of factors. The most likely cause is the difference in the measured surfaces. The Sb_2Se_3 surface measured in this study was the pristine b plane of a bulk crystal, whereas the surface measured in

Chapter 4 was an air-exposed polycrystalline surface made up of a number of different orientations. Nevertheless, the two measured values are in good agreement with each other.

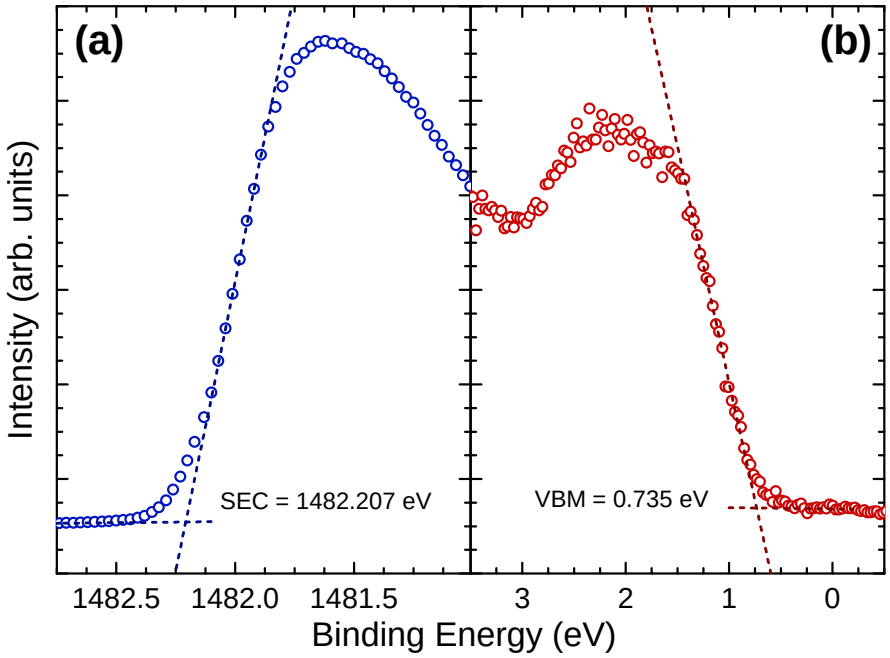

Figure 5.9 (a) Secondary electron cut-off (blue) and (b) valence band maximum (red) of *in situ* cleaved Sb_2Se_3 bulk crystals with straight line fits used to determine the binding energy of the cut-offs. The incident photon energy is 1486.6 eV.

Figure 5.10 shows this ionisation potential along with the band gap known from literature [54] alongside the above-mentioned chalcogenide materials. Sb_2Se_3 is towards the upper end of the values for other ns^2 lone-pair-containing materials, but certainly well below many of the materials without lone pairs, putting it firmly in the former group. This demonstrates that not only is understanding the lone pair model important from a structural perspective, but it also affects the electronic properties of a material. In the context of photovoltaics, understanding the dependence of the ionisation potential on lone pairs could inform band alignment engineering between absorber and window layers for improving performance of Sb_2Se_3 solar cells. The ionisation potential and band gap, along with the associated electron affinity, are crucial factors in determining how the conduction and valence bands align when forming a heterojunction. It could also prove invaluable in the research and development of other solar cell technologies. As well as the selection of materials possessing lone pairs as absorbers, this understanding of the electronic structure could greatly reduce the time spent searching for suitable partner layers. For example, based on unfavourable band alignments, CdS has previously been suggested to be a non-optimal solar cell junction partner for SnS [174, 189] and $CuSbS_2$

[146]. Someone looking to identify a new window layer for an absorber should therefore take into consideration the electronic structure of the material, not simply its material properties, and design the cell structure accordingly. For example, a material with a particularly high ionisation potential and medium sized band gap is likely to form a cliff like interface with Sb_2Se_3 which would limit a cell's performance. This kind of reasoning can speed up the process not only of finding promising material combinations, but of determining why performance is low or high.

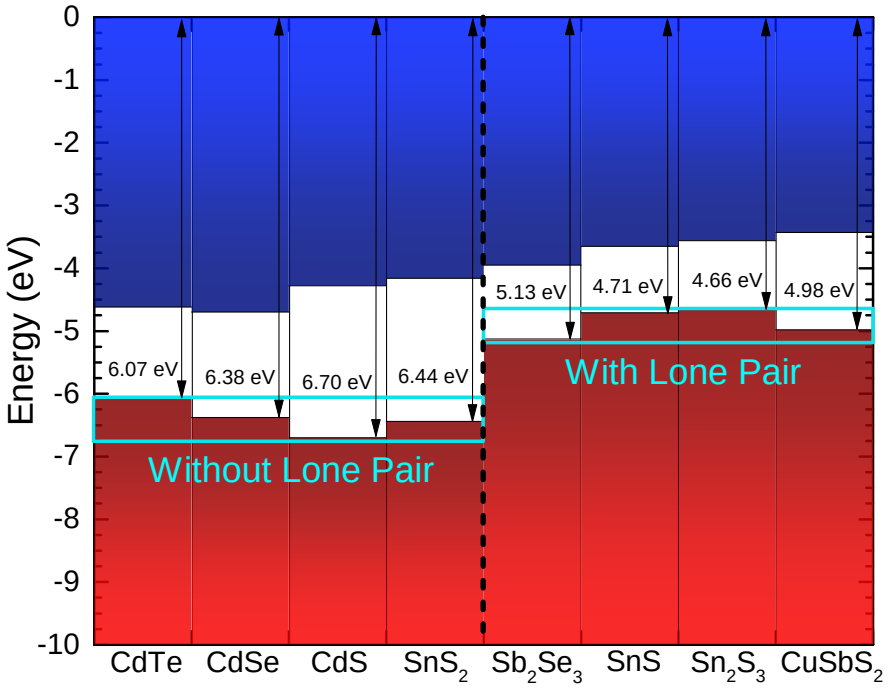

Figure 5.10 Ionisation potential for Sb_2Se_3 from the photoemission results in Figure 6, compared with literature values for other materials. [96, 146, 174, 190] The zero of the energy scale corresponds to the vacuum level. The materials are labelled as without or with lone pair ns^2 electrons.

5.3 Part 2 - Band Bending

In this study, the differing depth profiles of UPS, XPS and HAXPES were used to plot a profile of the change in VBM to E_F separation as a function of depth from the surface. These three data points could be fitted with a solution to Poisson's equation for surface band bending, providing an insight into the likely bulk carrier density as well as the surface band bending profile of the material. This also provided an interesting view on the influence of dopants on the band bending and band positions of Sb_2Se_3.

5.3.1 Background

Doping of Sb_2Se_3

As mentioned in Chapters 2 and 4, the devices produced by our group were found to have n-type conductivity, contrary to the majority of the literature. As detailed by Hobson *et al.* [62], this n-type conductivity is the result of unintentional Cl contamination in the source material used in the CSS deposition. As shown in Chapter 4, these devices still work well via an isotype junction with n-type window layers. However, given that Sb_2Se_3 is conventionally thought of as a p-type semiconductor, there was some interest in studying p-type Sb_2Se_3 to observe any differences. In pursuit of this, T. D. C. Hobson fabricated highly-oriented bulk crystals using pure Sb, Se and a small quantity of Sn to produce bulk crystals of p-type Sn:Sb_2Se_3.

Photoemission data was used to measure the valence band to Fermi level energy separation of the Cl:Sb_2Se_3 crystal, and this was included in the analysis by Hobson *et al.* in proving the n-type nature of Cl:Sb_2Se_3 [62]. As discussed in section 3.2, UPS, XPS and HAXPES have very different depth sensitivities as a result of the different photon energies used and the resulting difference in photoelectron inelastic mean free path. Preliminary analysis produced a solution to the Poisson equation to be fitted to the data points provided by the photoemission results (see Figure 5.11), however the fit was imperfect due to the use of approximate constants for the carrier effective mass and dielectric constant [62]. In this study we have used DFT calculated values for these quantities in each of Sb_2Se_3's different planar directions, allowing for a more rigorous fit of the Cl:Sb_2Se_3 results as well as the Sn:doped crystal.

Semiconductor Carrier Statistics

The number of electrons available for carrier transport in the conduction band is given by equation 5.2. $f(E)$ is the Fermi-Dirac distribution function which described the probability that a state at energy E is occupied or unoccupied. At $T = 0$ K this function takes the form of an abrupt step, with a probability of 0 that a state with energy greater than E_F will be occupied and a probability of 1 that a state below E_F will be occupied. At higher temperatures, however, this step becomes more gradual as some carriers have a probability of being excited into the conduction band by the thermal energy in the system.

$$\mathrm{n} = \int_{E_C}^{\infty} f\left(E\right)\, g_C\left(E\right)\, dE \tag{5.2}$$

$$f\left(E\right) = \frac{1}{1 + e^{\frac{E - E_F}{k_B T}}} \tag{5.3}$$

$$g_C\left(E\right) = \frac{8\sqrt{2}\pi m_e^{*3/2}}{h^3}\sqrt{E - E_C} \tag{5.4}$$

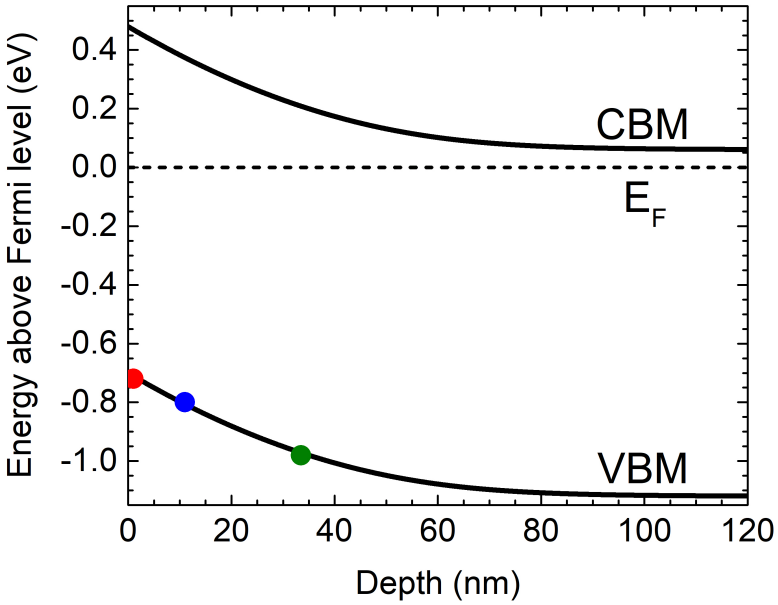

Figure 5.11 Solution to Poisson's equation as calculated for n-type Sb_2Se_3 by Hobson *et al.* [62]

$g_C(E)$ gives the DOS in the conduction band. For an energy level above the conduction band minimum, E_C, the number of available energy states is calculated according to the carrier effective mass, m_e^*. Due to the relatively narrow band gap of Sb_2Se_3 the conduction band exhibits a degree of non-parabolicity as a result of interactions between the valence and conduction band states. This is accounted for using the α-approximation (as explained in Appendix 7.2.3), and the carrier density is given by:

$$\mathrm{n} = \int_{E_C}^{\infty} \frac{1}{1 + e^{\frac{E - E_F}{k_B T}}} \times \frac{8\sqrt{2}\pi m_e^{*3/2}}{h^3} \times \sqrt{\frac{E}{E_g} + 1} \times \left(\frac{2\mathrm{E}}{E_g} + 1\right) \times \sqrt{E - E_C} \qquad (5.5)$$

in which k_B is Boltzmann's constant and h is Planck's constant.

Solving Poisson's Equation

The existence of a space charge layer at the surface is common for any semiconductor and is a result of the formation of surface electronic states at the surface of the material. These surface states will influence the Fermi level position at the surface and, due to the significant screening lengths in semiconductors compared to metals, lead to a space charge region in which the conduction and valence bands bend relative to the Fermi level. The physical origin of this space charge region is the introduction of acceptor or donor states that lead to the depletion or accumulation of majority carriers near the surface. For example, in an n-type semiconductor, the presence of negatively (positively) charged

surface states at the surface introduces a region of ionised acceptor (donor) states to retain charge neutrality (Figure 5.13). This leads to the depletion (accumulation) of electrons near the surface, causing the bands to bend upward (downward), as illustrated in Figure 5.12. In a p-type semiconductor, a depletion (accumulation) layer will occur with the introduction of donor (acceptor) states near the surface and will result in downward (upward) band bending.

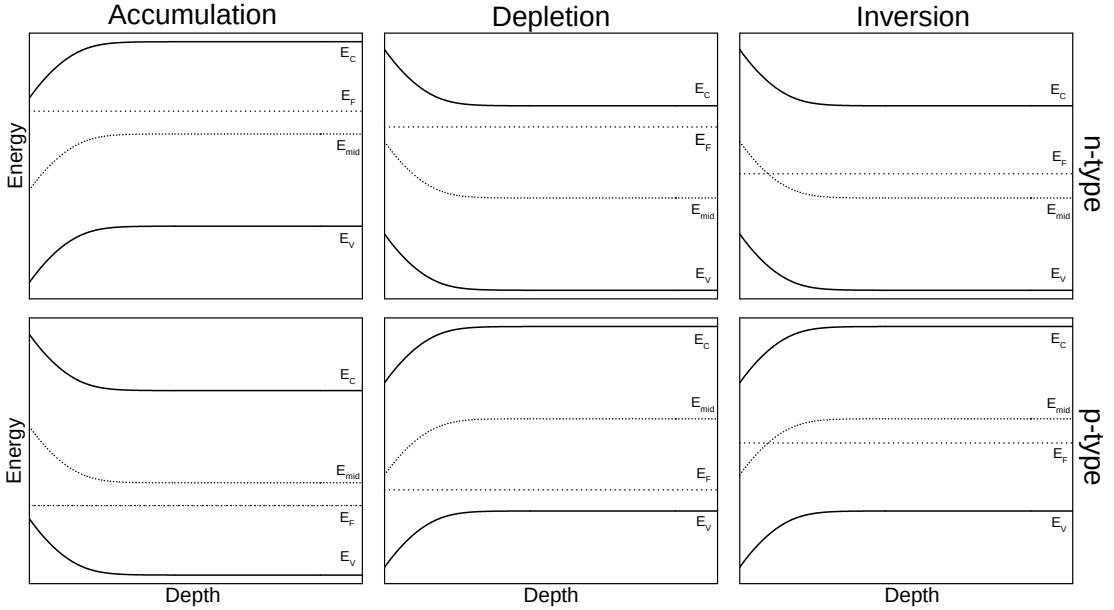

Figure 5.12 Illustration of the different types of surface space charge layer that can occur in n-type and p-type semiconductors.

The spatial variation of the charge introduced by the band bending is described by Poisson's equation.

$$\frac{d^2V}{dz^2} = -\frac{e}{\epsilon_z \epsilon_0}\left[N_d^+ - N_a^- - n(z) + p(z)\right] \tag{5.6}$$

where e is the electronic charge, ϵ_z is the static dielectric constant and ϵ_0 is the permittivity of free space. The left-hand side of Poisson's equation, $\frac{d^2V}{dz^2}$, describes the rate of change of the gradient of the potential with depth into the material (or distance from the surface), z. The right-hand side describes the distribution of charges inside the material. N_d^+ and N_a^- are the density of charged donors or acceptors present in the material. $n(z)$ and $p(z)$ describe the density of free electrons and holes in the material as a function of depth. Solving Poisson's equation and Schrodinger's equation self-consistently is computationally complex, especially when conduction band non-parabolicity is included. Therefore an approximation is used to numerically determine the distribution of charges within the space-charge region. This approximation assumes that electrons are distributed evenly within each increment of space charge dV and therefore for each

increment of depth into the surface of a material, the electron density can be calculated. It is therefore possible, with an initial estimate of $V(z)$ and $\frac{dV(z)}{dz}$, to calculate and plot the potential at incremental steps into the material's surface using Poisson's equation.

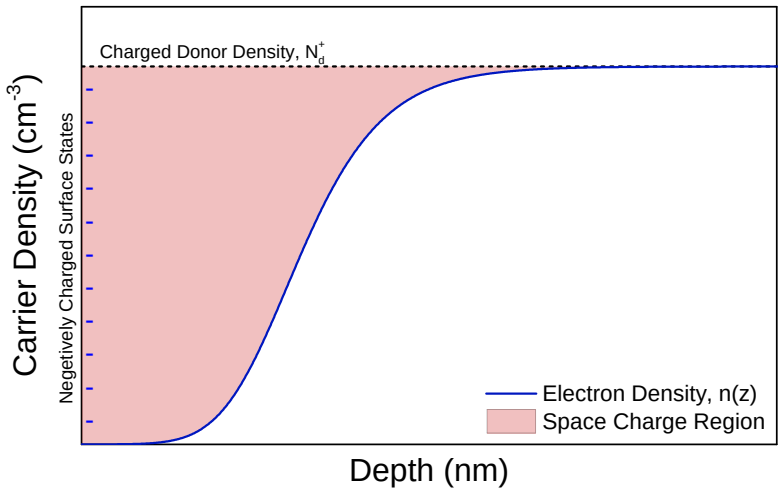

Figure 5.13 An illustration of the formation of a depletion layer in an n-type semiconductor in terms of carrier density with increasing depth.

In an n-type doped material it is assumed that the number of bulk acceptor states is negligible in relation to the number of donors and that the hole density is likewise very low. Therefore, equation 5.6 can be written as:

$$\frac{d^2V}{dz^2} = -\frac{e_0}{\epsilon_z \epsilon_0}\left[n(z) \text{ - } N_d^+\right] \tag{5.7}$$

The density of charged donors is assumed to be equal to the bulk carrier density, making $N_d^+ = n$, where n is the bulk carrier density. To calculate $n(z)$ at a given depth a potential is added to the expression $E - E_F$ to give:

$$n(z) = \frac{8\sqrt{2}\pi m_e^{*3/2}}{h^3}\int_{E_C}^{\infty} \frac{\sqrt{\mathrm{E}}\,\sqrt{\frac{E}{E_g}+1}\,\left(\frac{2\mathrm{E}}{E_g}+1\right)}{1+e^{\frac{E-E_F+V(z)}{k_B T}}}dE \tag{5.8}$$

$V(z)$ is the potential at a given depth, z, and is one of the input parameters to the function. However, additional correction factors are required to produce an accurate solution, taking into account quantum mechanical effects. For accumulation layers, an additional correction is included to model the surface potential barrier resulting from the vanishing carrier density at the surface [191–194]. This is essential only for accumulation or inversion layers but is not required in depletion regions [195].

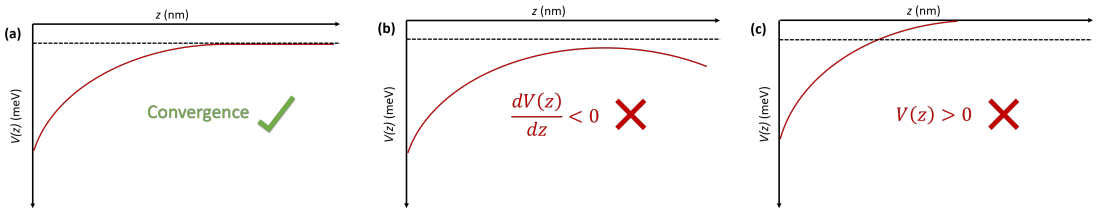

Figure 5.14 Example of (a) successful convergence, and (b & c) the two conditions for convergence being contradicted for a depletion layer in a p-type material.

$$f_{MTFA}(z) = 1 - \text{sinc}\left(\frac{2z}{L}\sqrt{1+\frac{E}{E_g}}\sqrt{\frac{E}{k_BT}}\right) \tag{5.9}$$

where $\mathrm{L} = \hbar/(2m_0k_B\mathrm{T})^{1/2}$. Equation 5.8 then becomes equation 5.10 which is known as the modified Thomas-Fermi approximation (MTFA).

$$n(z)_{mtfa} = \frac{8\sqrt{2}\pi m_e^{*3/2}}{h^3}\int_{E_C}^{\infty}\frac{\sqrt{\mathrm{E}}\,\sqrt{\frac{E}{E_g}+1}\,\left(\frac{2\mathrm{E}}{E_g}+1\right)}{1+e^{\frac{E-E_F+V(z)}{k_BT}}}f_{MTFA}(z)\;dE \tag{5.10}$$

Having a way of calculating both N_d^+ and $n(z)$ means that Poisson's equation can be solved for $\frac{d^2V}{dz^2}$. The code designed for this project was based upon the combination of using the MTFA to solve Poisson's equation and using an interval bisection method to find the optimum solution to this equation within some selected constraints. Using initial estimates for $V(z)$ and $\frac{dV}{dz}$ at the surface ($z = 0$), each quantity was calculated for a step deeper into the material, plotting the band bending in incremental steps until a convergence criteria was violated. These convergence criteria were governed by simple assumptions on the overall shape of the band bending profile. One limit was that the band bending profile could not double back on itself, or in other words, the gradient could not change sign and still converge (see Figure 5.14b). The other was that the carrier density would not increase/decrease past the bulk carrier density (see Figure 5.14c). If one of these conditions was violated the initial values of $V(z)$ and $\frac{d^2V}{dz^2}$ were then adjusted accordingly and the process repeated until convergence was achieved.

A more detailed description of the code is included in Appendix B.

5.3.2 Experimental Details

Photoemission

The photoemission results for this study were acquired using three photon energies with significantly different surface sensitivities. As discussed in Chapter 4, this surface sensi-

tivity is dependent on the IMFP of the photo-excited electrons. The IMFP of valence electrons excited in Sb_2Se_3 is shown in Figure 5.15. The TPP-2M equation was not designed to calculate the IMFP of electrons for kinetic energy lower than 50 eV and seems to break down at the lower energy limit but by extrapolating backwards the IMFP of UPS has been estimated at ~0.5 nm [109]. XPS and HAXPES have IMFPs of approximately 3 nm and 10 nm for this kinetic energy. The total probing depth, as previously discussed, can be considered to be approximately three times this IMFP, from which 95% of the total signal will originate. However, it is important to remember that the total signal is a superposition of signal from the full range of these depths and that this signal will be dominated by electrons nearer the surface. It is not straightforward, therefore, when measuring the valence band position for a given depth to determine which specific depth the valence band edge measured is indicative of. It is safe to assume that the measured VBM is not a true indication of the VBM at 3×IMFP, however one IMFP would neglect 33% of the acquired signal. For this reason, and after some trial fitting of the data with the Poisson's equation solver, it was decided that 2×IMFP was a reasonable estimation of the measured VBM depth.

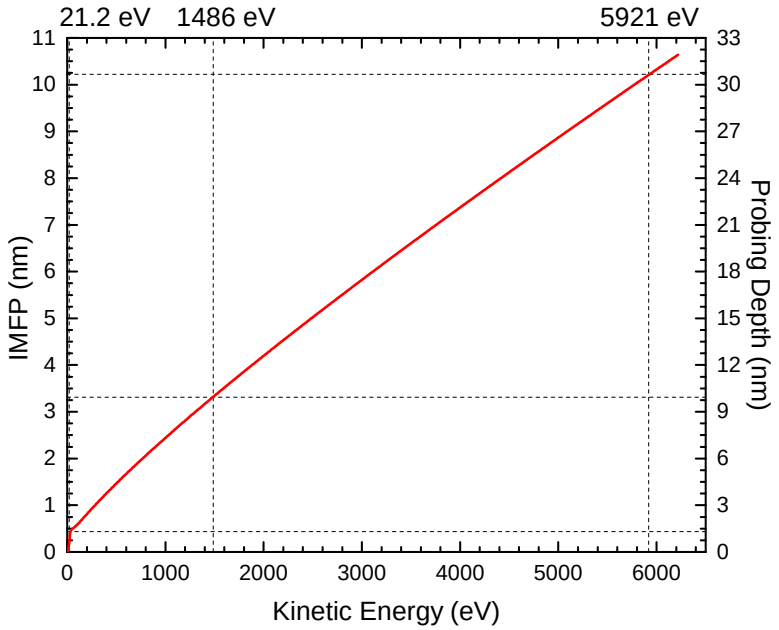

Figure 5.15 IMFP of an electron travelling through Sb_2Se_3 as a function of its kinetic energy. Dashed lines show the photon energies used for UPS, XPS and HAXPES and the corresponding IMFP.

UPS measurements were acquired using a He(I) discharge lamp as the UV source and the same acquisition method as used for XPS (see section 3.2.7). The HAXPES and XPS data was the same as that used in Part 1.

5.3.3 Results

The solution to the Poisson equation was calculated using the Python script explained in Appendix B. The input parameters that were common to both doping types were the band gap (known to be 1180 meV [54]) and the temperature (300 K), the approximate room temperature which the photoemission measurements were taken at. The dielectric constant value used was 3.5 - the DFT calculated value for the *b* plane (Table 2.1) which is the one measured.

n-type

The valence band spectra of the n-type crystal as measured by UPS, XPS and HAXPES are shown in Figure 5.16. The VBM - E_F separation for the valence bands in Figure 5.16 were determined by finding the intercept of straight lines fitted to the steepest part of the valence band edge and the flattest part of the background. VBM positions are consistent with n-type behaviour at the surface with lower binding energies measured by the more surface sensitive techniques. This indicates upward band bending of the valence band towards the surface which corresponds to an electron depletion layer (as shown in Figure 5.12).

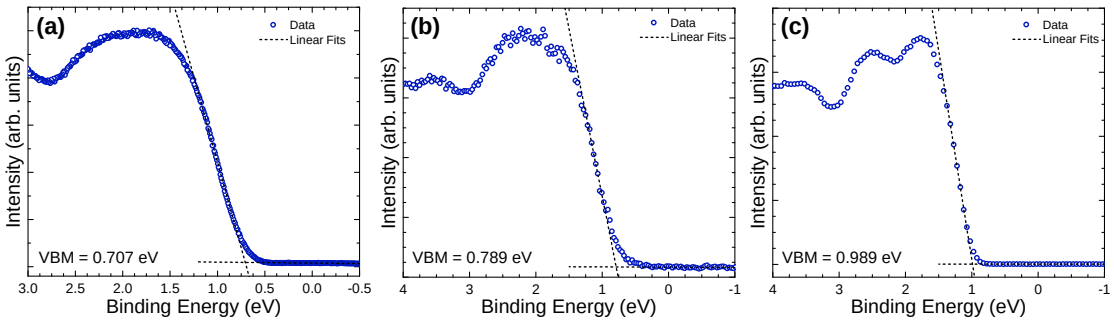

Figure 5.16 Valence band spectra of the n-type bulk Sb_2Se_3 crystal as measured by (a) UPS, (b) XPS and (c) HAXPES with linear fits used to determine the VBM-E_F separation.

These photoemission results are plotted as data points in Figure 5.17a at the estimated depths that they represent (as explained above). Superimposed onto these points are the conduction and valence bands altered to incorporate the Poisson's equation solution for the surface potential. Figure 5.17b shows the electron density on a log scale with respect to depth into the material. The 'bulk' carrier density (calculated from the VBM - E_F separation at the plateau of the band bending solution, 135 meV) is equal to 1.77×10^{17} cm^{-3}, consistent with the levels of doping measured by Hobson *et al.* ($\sim10^{17}$ cm^{-3}). The total amount of band bending is equal to 360 meV, significantly less than that required by Hobson *et al.* (420 meV). This is a result of the different effective mass and relative permittivity values used - in the previous work the Fermi level was placed

higher in the gap in order to allow for enough band bending to fit the data points. In this work, the updated values for effective mass and relative permittivity result in band bending over a much shallower depth for the same Fermi level position, meaning that the Fermi level is placed lower in the gap and the band bending required to fit the data is less.

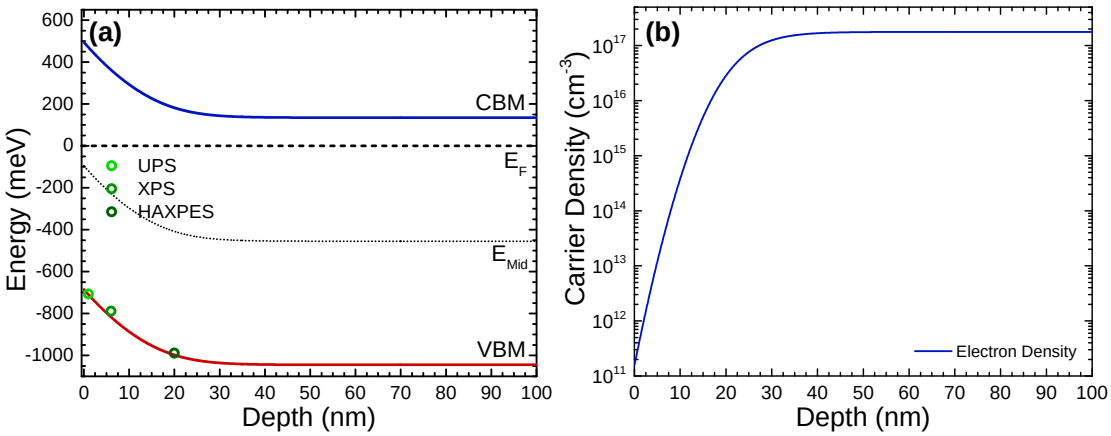

Figure 5.17 (a) Band structure and (b) carrier density plots from the solution to Poisson's equation for VBMs measured by linear extrapolation from different photoemission techniques at estimated depths.

It is noticeable that the XPS data point does not line up well with the Poisson equation solution, something that could not be rectified by adjusting the input parameters because the depth over which the band bending takes place is dictated by the carrier effective mass and the Fermi level position (which is somewhat constrained by the position of the HAXPES data point). However it is simple to explain this discrepancy - XPS has a lower instrumental resolution than both UPS and HAXPES (see section 3.2.3) which would likely lead to an underestimation of the VBM - E_F separation. This can be addressed by using a fitting method that takes into account the different resolutions of the photoemission methods.

As introduced in Part 1, DFT calculated DOS can be aligned to the valence band data acquired from photoemission measurements. This DOS is broadened using the known Gaussian instrumental broadening of the technique used (as well as the Lorentzian lifetime broadening). The DOS is calculated by DFT with the valence band maximum at 0 eV, meaning that whatever shift is necessary to align the DOS to the data is a good measurement of the true VBM - E_F separation. This alignment procedure was applied to the same three valence band spectra shown in Figure 5.16 and the results are shown in Figure 5.18. The total shift required to align the DOS to the data is included alongside a straight line to show this point on the x-axis.

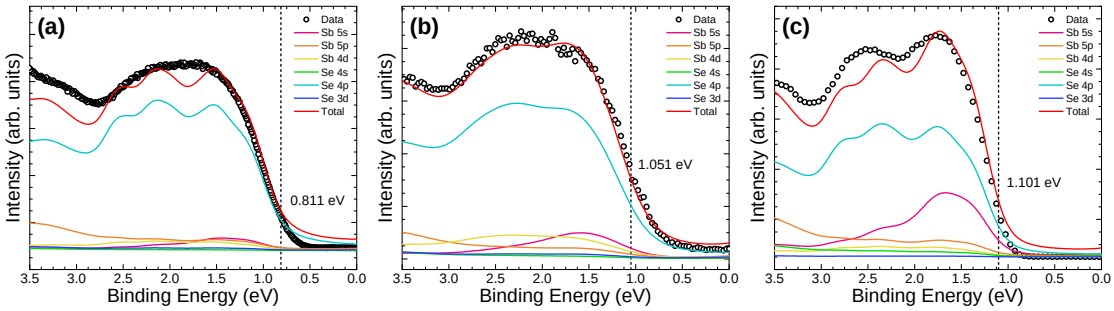

Figure 5.18 Valence band spectra of the n-type bulk Sb_2Se_3 crystal as measured by (a) UPS, (b) XPS and (c) HAXPES with broadened DOS fits used to determine the VBM-E_F separation.

It is clear from examining Figure 5.18 that the difference between the 'foot' of the valence band and the true position of the valence band maximum is particularly pronounced for the XPS data, whereas it is reasonably similar for UPS and HAXPES. This supports the theory that the fit in Figure 5.17a is poor due to the poorer resolution of XPS. It is also clear that the DOS alignment result indicated a more strongly n-type Fermi level position in the Cl doped Sb_2Se_3. The Poisson equation was solved again to fit these new VBM energies, as shown in Figure 5.19a.

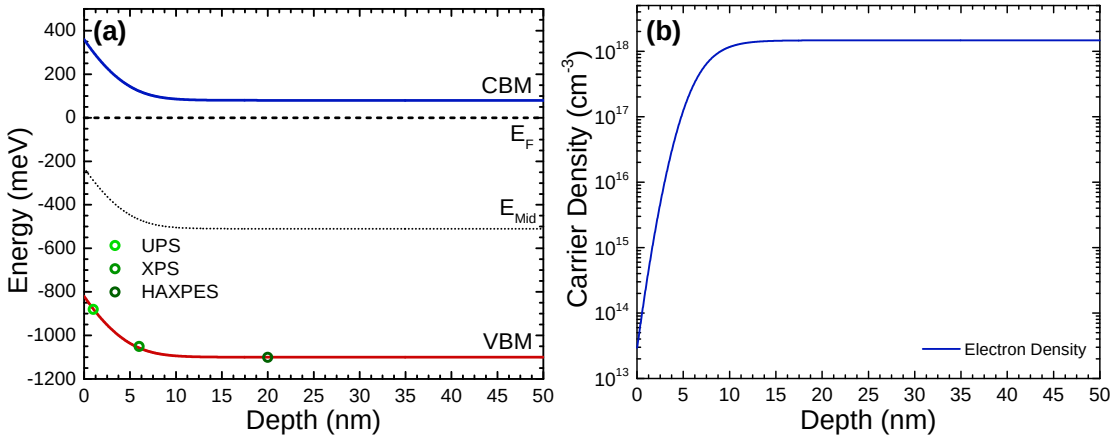

Figure 5.19 (a) Band structure and (b) carrier density plots from the solution to Poisson's equation for VBMs measured by DOS fitting from different photoemission techniques at estimated depths.

The fit obtained for the DOS fitted photoemission points is far better, with the valence band comfortably passing through all three data points. The total amount of band bending was 280 meV. The band bending takes place over a far shallower depth which is a result of the much smaller VBM - E_F separation (80 meV). This is consistent

with the very similar VBM energies calculated from XPS and HAXPES when using the DOS fitting method, and interestingly indicates that the VBM position measured from HAXPES is representative of the bulk band position. Indeed, the bulk position is unlikely to be any closer to the Fermi level because this would begin to approach unrealistic levels of doping. The calculated carrier density for this Fermi level position in the band gap is 1.46×10^{18} cm^{-3} (Figure 5.19b), an order of magnitude higher than what was obtained from the linear extrapolation data. This is quite high and a little higher than expected but generally consistent with the mid-10^{17} cm^{-3} measured by Hobson *et al.* The higher than expected value could be a consequence of the slightly wider fundamental gap in the *b* direction as opposed to the smallest fundamental gap which is found in the *c* direction. Given that there are no experimentally determined values for this electronic gap and that it would be difficult to obtain one, the well established value of 1.18 eV has been used in this work and it is likely only slightly smaller than the true gap in the *b* direction.

p-type

The same photoemission measurements were performed on an *in situ* cleaved crystal that was doped p-type with Sn. The valence band spectra are shown in Figure 5.20. Figure 5.20 also shows the linear extrapolation of the valence band edge used to determine the VBM and the calculated values. These values were again used to find a solution to Poisson's equation that fit the photoemission data, shown in Figure 5.21a. The decreasing VBM - E_F separation with increasing depth indicates hole depletion, however the separation of 0.614 eV is in fact greater than half the band gap which means that this crystal exhibits type inversion at the surface (from p-type to n-type). This inversion is illustrated by the carrier density plots in Figure 5.21b. Near the interface the depletion of holes is so severe that electrons become the majority carrier type.

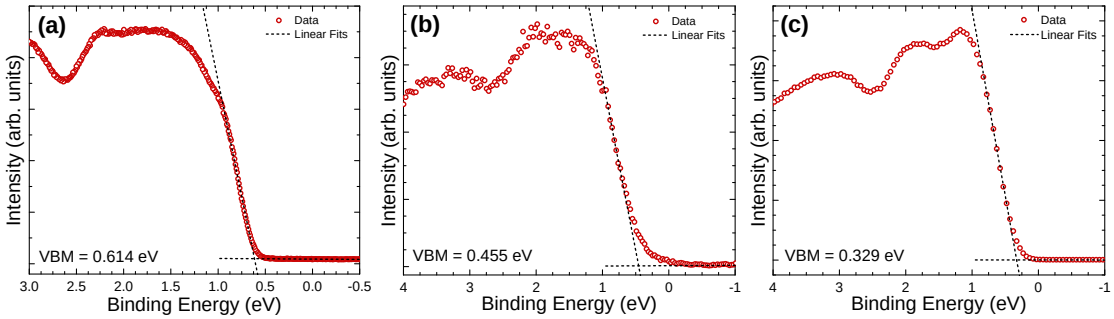

Figure 5.20 Valence band spectra of the p-type bulk Sb_2Se_3 crystal as measured by (a) UPS, (b) XPS and (c) HAXPES with linear fits used to determine the VBM-E_F separation.

The total amount of band bending was 470 meV and the carrier density associated with the determined bulk Fermi level position is 9.68×10^{16} cm^{-3}. Once again, the VBM - E_F determined from XPS seemed to be underestimated and it was difficult to achieve

a fit that passed cleanly through all three data points. This further supports the earlier theory that the difference in resolution for the XPS measurement, compared to UPS and HAXPES, means that the separation is underestimated and a good fit difficult to achieve.

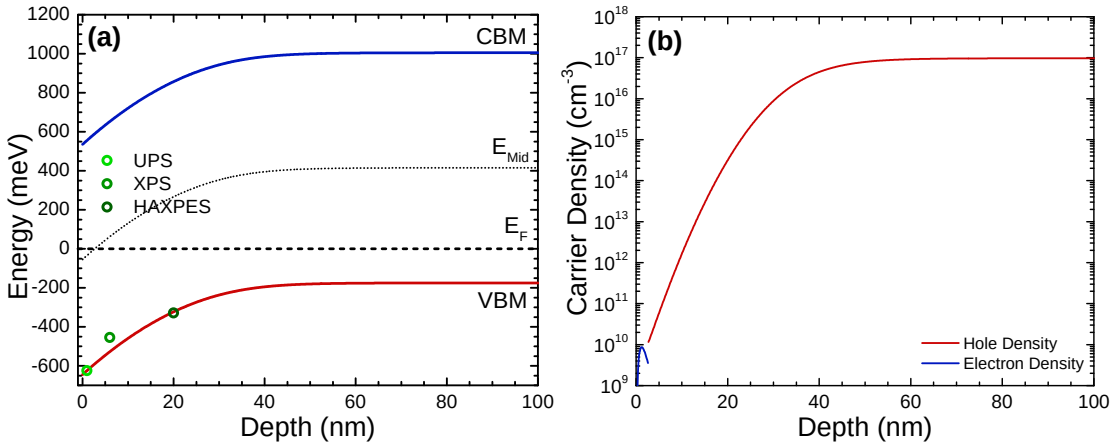

Figure 5.21 (a) Band structure and (b) carrier density plots from the solution to Poisson's equation for VBMs measured by linear extrapolation from different photoemission techniques at estimated depths.

The DOS alignment method was employed for the p-type valence band spectra as well and the results are shown in Figure 5.22. There is little difference between these fits and those shown in Figure 5.18 except for the shifts on the binding energy scale, consistent with expectation. The XPS data is again significantly broader than the UPS and HAXPES valence bands which accounts for the difficulty in achieving a good fit in Figure 5.21a. The solution to Poisson's equation fitted to these DOS aligned VBM values is shown in Figure 5.23a. As can be seen, the fit is much better for these values. The bulk Fermi level position required for this fit was further from the valence band, corresponding to a lower bulk carrier density of 2.06×10^{16} cm^{-3}. A lower hole density is more consistent with our expectations for this sample given the expected self-compensation of Sn as a p-type dopant, which will be discussed further below. The total amount of band bending was 500 meV, similar but slightly greater than that required for the linear extrapolation data. This fit also indicates the presence of an inversion layer at the surface but with a more n-type surface and transition from p-type to n-type taking place deeper in the material (Figure 5.23b).

5.3.4 Discussion

The photoemission measurements of the valence band to Fermi level energy separation provides one of the most reliable measurements of the conductivity type of the Sb_2Se_3 crystals. Hall effect and C-V measurements performed as part of the work by Hobson *et*

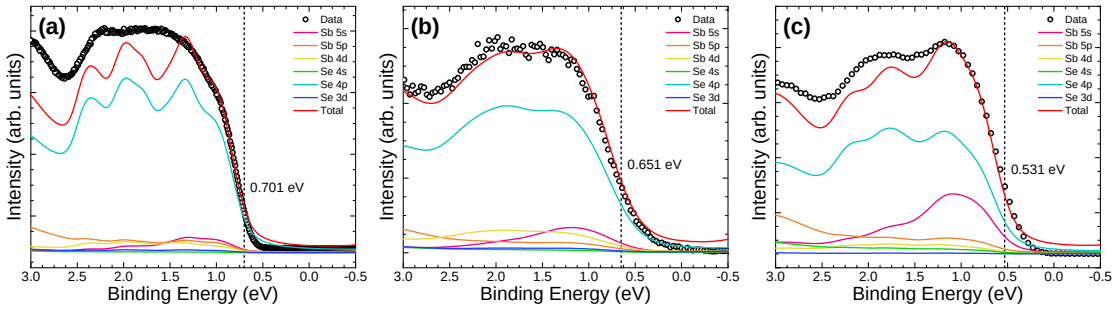

Figure 5.22 Valence band spectra of the p-type bulk Sb_2Se_3 crystal as measured by (a) UPS, (b) XPS and (c) HAXPES with broadened DOS fits used to determine the VBM-E_F separation.

al. provided good indication of the carrier type - Hall effect measurements of the n-type crystal indicated n-type conductivity with an electron density of $\sim 4\times10^{16}$ cm^{-3} [34, 62]. However, it is possible for Hall effect measurements to be misleading if inversion layers or buried junctions exist within the material. Capacitance-voltage (C-V) measurements were also used for electronic characterisation and supported this measurement of the carrier density - a range of 5-10 $\times10^{16}$ cm^{-3} measured for different frequencies [34]. Unfortunately, C-V measurements can also suffer from some ambiguity over carrier type. The photoemission measurements of the valence band energy relative to the Fermi level do not suffer from such ambiguity. When properly calibrated and used in combination with a well known band gap value, the position of the Fermi level within the gap can be determined beyond doubt.

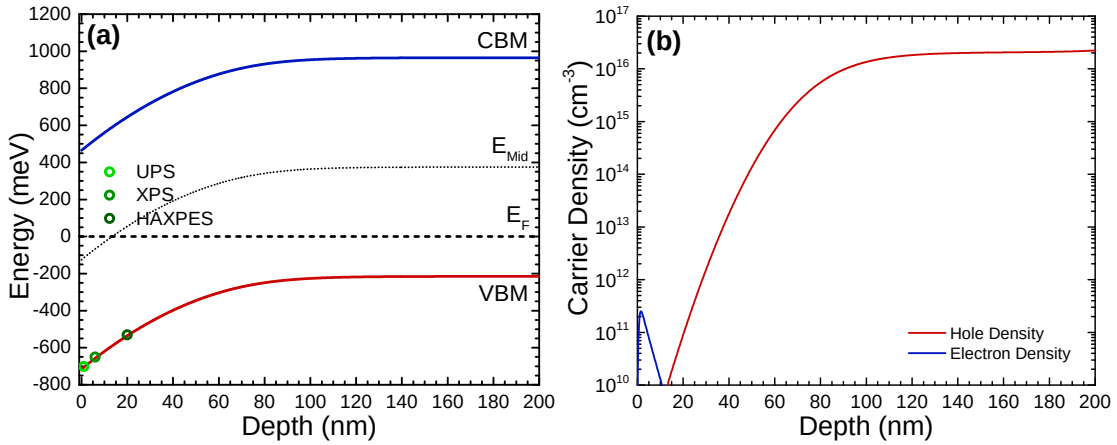

Figure 5.23 (a) Band structure and (b) carrier density plots from the solution to Poisson's equation for VBMs measured by DOS fitting from different photoemission techniques at estimated depths.

There are limitations to the photoemission method for determining conductivity type. The surface sensitivity of XPS is the most obvious - a single XPS measurement in isolation could hide a significant amount of surface band bending (as seen in the p-type crystal). The use of three different photon energies removes this possibility and, as utilised in this work, introduces the potential to predict the bulk carrier density. The results of this study do not match the results of the Hall effect and C-V measurements exactly. In the case of the n-type crystal, the predicted carrier density from the photoemission measurements is approximately an order of magnitude higher than that measured by Hobson *et al.*. This is likely a consequence of the photoemission measurements' surface sensitivity. While the Poisson equation solution does converge towards a 'bulk' carrier density, this is calculated over a depth of 100-200 nm, whereas 'bulk' characteristics of a complete thin film encompass a depth of $\sim$2 μm.

The p-type crystals in particular have proven difficult to measure with Hall effect and C-V. Hobson *et al.* found that no carrier density could be obtained from Hall effect measurements and that C-V measurements gave a wide range of carrier densities between 10^{15} - 10^{17} cm^{-3}. In light of this, even with the limitations of surface sensitivity, the photoemission results provide a wealth of information on the carrier density and the inversion layer at the surface. The presence of an inversion layer at the surface of Sn:Sb_2Se_3, could be the reason for such difficulty in measuring the carrier density by other methods. It could also have implications for contacting of Sn:Sb_2Se_3, although that would be heavily influenced by the difference in work functions between the Sb_2Se_3 and contact layer. The weakly doped nature of the p-type crystal also points to a non-ideal dopant. Given the amount of Sn in the source material ($\sim$1 at%, although not all this Sn can be assumed to be incorporated during crystal growth and there was no Sn signal present in the XPS) it seems likely that compensation begins to limit the carrier density after relatively low amount of doping. This is supported by DFT calculations of the formation energy energies of defects under Sn doping.

The formation energies of the different defects under Sn and Cl doping are shown in Figures 5.24 and 5.25. For the most relevant insight the Sn-doped defects were calculated in the Se-rich regime (which the crystals were deliberately grown in [34]) and the Cl-doped defects were calculated in the Se-poor regime (which Sb_2Se_3 is known to tend towards, as discussed in section 2.2.2). An examination of the two diagrams indicates that Sn would be a far less effective dopant than Cl. In Figure 5.24, at the mid-gap point, Sn_{Sb} substitutional defects have the lowest formation energy, acting as acceptors. However, at approximately 0.4eV above the valence band, this effect is compensated by the Sn_{Sb} switching to behave as donors, along with the formation of Se_{Sb} antisite donors becoming equally favourable. This would pin the Fermi level at this point 0.4 eV above the valence band. Meanwhile, in Figure 5.25, Cl_{Se} substitutional defects have very low formation energy and are not compensated by V_{Sb} until approximately 1.1 eV above the valence band (or 0.1 eV below the conduction band). This is significantly higher in terms of doping potential and is in line with the much higher levels of doping seen in the n-type

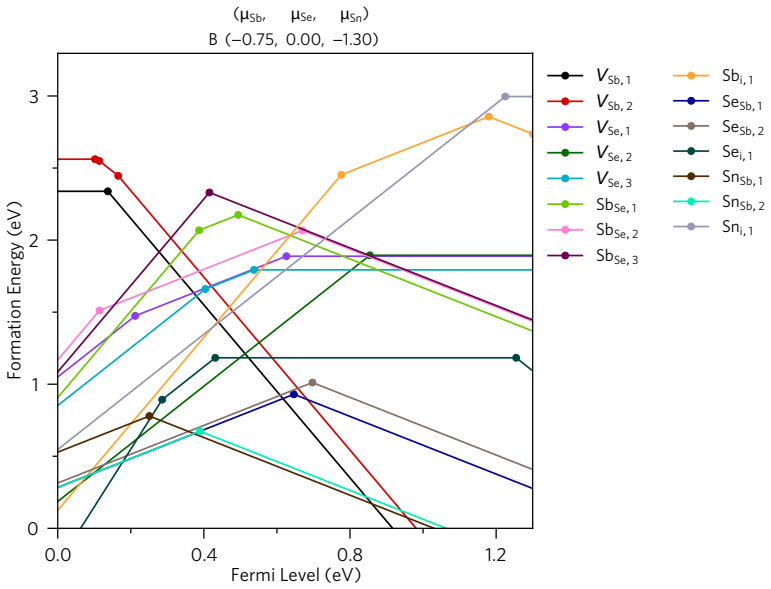

Figure 5.24 DFT predicted formation energies of different defects with respect to Fermi level position above the valence band for Se-rich Sb_2Se_3 doped with Sn [58].

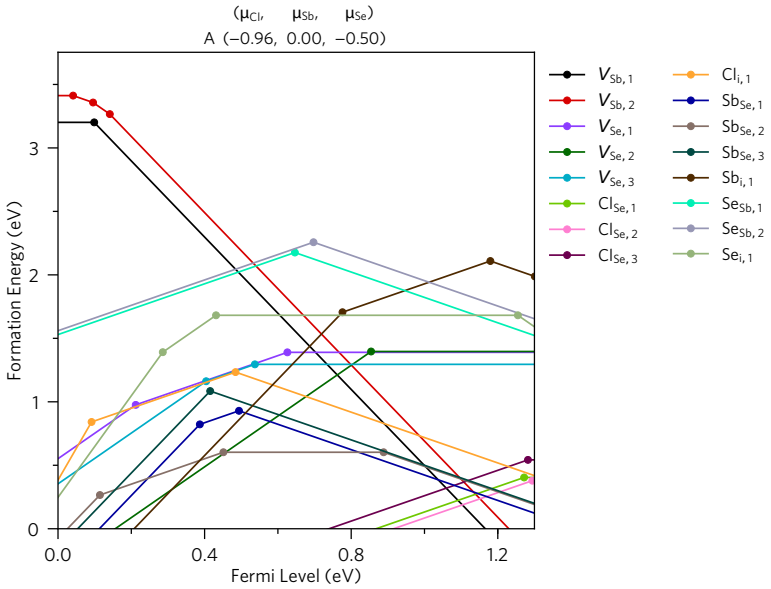

Figure 5.25 DFT predicted formation energies of different defects with respect to Fermi level position above the valence band for Se-poor Sb_2Se_3 doped with Cl [58].

crystal than the p-type crystal. Whether or not this is due to Sb_2Se_3 being easier to dope n-type than p-type or Sn being a poor p-type dopant is a question that will need answering if the best use of Sb_2Se_3 is to be found.

5.4 Conclusion

This study, similarly to the band alignment study in Chapter 4, utilised a powerful combination of both hard and soft x-ray photoemission techniques to gain an in-depth understanding of the electronic structure of Sb_2Se_3. In this case, rather than examining the band alignments from a practical, device-focused perspective, a more fundamental understanding was sought. The Sb $5s^2$ lone pair had been previously predicted by theoretical studies, and its effect on the structure and material properties of Sb_2Se_3 discussed. In this work the presence of the lone pair was shown experimentally. Furthermore the effects of contamination were shown and the implications of lone pairs on band alignments studied.

Core level spectra of the Sb and Se regions collected using HAXPES showed the presence of a Sb_2O_3 layer on the surface, a result of the surface's exposure to air. This is accompanied by a certain amount of free elemental selenium. Both were not present in the *in situ* cleaved sample, showing that this contamination is localised to the surface and doesn't affect the bulk. The implications of this contamination on device performance is not discussed here but will be explored in detail in Chapter 6.

Using the energy dependence of photoionisation cross-sections, shifts in valence band photoemission features have been linked to bonding mechanisms. The agreement observed between the theoretical VB DOS and the experimental photoemission data near the VBM provides strong evidence that Sb_2Se_3 exhibits contributions to the VB spectra from a lone pair of electrons in the Sb 5s state. This Sb 5s state hybridises with the Se 4p state, consequently bringing this state to the valence band edge as well. This has the effect of raising the valence band edge on an absolute energy scale and lowering the ionisation potential of the material. The IP of 5.23 eV groups Sb_2Se_3 with other chalcogenide materials containing lone pairs as having a lower IP and band gap than similar materials that do not possess lone pairs.

The implications of these conclusions to device applications cannot be underestimated. Band alignment engineering is a crucial aspect of solar cell design and development and this work shows how the band positions of materials are heavily influenced by the make-up of the valence band, particularly in the case of lone pair materials. The position of the valence band could even be considered to be at the root of all the results obtained in Chapter 4.

Measurement of the VBM - E_F separation of both a Cl- and Sn-doped Sb_2Se_3 bulk crystal was carried out using the three different photon energies of UPS, XPS and HAX-

PES. These values were used as data points in a depth profile of the VBM - E_F that was used to inform a solution to Poisson's equation for surface space charge layers. The use of linear extrapolation fitting of the VBM did not provide satisfactory results whereas VB DOS fitting provided good solutions.

The results indicated that Cl doped Sb_2Se_3 exhibited strong n-type conductivity in the region of 10^{17}-10^{18} cm^{-3}, whereas Sn was less effective in doping Sb_2Se_3 p-type, with a predicted bulk carrier density of 10^{16}-10^{17} cm^{-3}. n-type crystals exhibited surface electron depletion whereas p-type crystals presented surface inversion layers, with hole depletion giving way to a shallow n-type layer at the surface.

These results represent an important first step in experimental understanding of extrinsic doping of Sb_2Se_3. The significant influence of chemical impurities on the conductivity strength and type of Sb_2Se_3 means that this is a quantity that will likely have to be well understood and controlled in future optimisation of solar cells. Good control over this phenomenon could provide a platform to improve devices beyond 10% in the future by optimising device structure and controlling defects and band alignments.

Chapter Six

Antimony Selenide Back Contacts: Chemical Etching and Band Alignments

Parts of this work are published as:

H. Shiel & O. S. Hutter *et al.*, "Chemical etching of Sb_2Se_3 solar cells: surface chemistry and back contact behaviour", *Journal of Physics: Energy*, **1**, 4 (2019), DOI:10.1088/2515-7655/ab3c98

H. Shiel *et al.*, "Band alignment of Sb_2O_3 and Sb_2Se_3", *Journal of Applied Physics* ***129**, 235301 (2021), DOI: 10.1063/5.0055366*

6.1 Introduction

A thin film solar cell is made up of a number of layers, each usually of a different material. The combining of these materials is not always straightforward and many losses can occur from poor band alignment (as discussed in chapter 4), lattice mismatch or intermixing. To further complicate the matter, in a standard laboratory setup each layer is exposed to atmospheric contamination in between fabrication processes. This can lead to issues with materials that are unstable in air such as with most perovskites. While Sb_2Se_3 is very stable in air, it does undergo surface oxidation when exposed to air for even a short time (a process likely exacerbated by the sample being heated during deposition), something which was thought to have a negative impact on device performance [38, 39]. The natural response was to etch away the contaminants prior to the next step in device fabrication, the deposition of Au contacts. However, introducing a chemical etchant to the back surface of the Sb_2Se_3 could have a wider impact than simply removing an unwanted oxide, such as altering the chemical composition of the surface, changing the surface morphology or depositing another contaminant onto the surface.

In the first part of this chapter, the effect of two chemical etches on the surface

chemistry of Sb_2Se_3 thin films is investigated and paired with a thorough study of the effect of etching on device performance. The results are then used to infer the impact of the original contaminant, filling in a number of gaps in the existing literature and providing clarity on some conflicting results from previous work. The results from this study led to further work within the group investigating the implications of the chemical composition of the Sb_2Se_3 back surface (which is reported elsewhere [115]) and that in turn led to the second part of this study, in which the band alignment between the Sb_2Se_3 and the contaminant layer present at the back contact is quantified for the first time.

6.2 Part 1 - Chemical Etching of Sb_2Se_3 Back Contacts

6.2.1 Background

It is well established in other technologies that surface modification prior to back contacting can lead to performance improvement. In CdTe, for example, the nitric-phosphoric acid [33, 196–198], bromine methanol [199], methyl ammonium iodide [200] or hydrogen iodide [201] etching steps often improve device characteristics through the creation of a more Te-rich layer prior to back contacting. This is a key step because back contact losses are known to be a major limiting factor in CdTe due to the issue of CdTe's high work function [202]. This high work function leads to a widely reported back contact barrier between the CdTe and the metal contact. However, by leaving a tellurium-rich back surface, this effect can be lessened [203]. Understanding the chemical composition of the free back surface is a key component in developing such a process.

In works published by the Tang group in 2017, it was stated that the presence of Sb_2O_3 and elemental Se contamination at the back contact of superstrate Sb_2Se_3 devices was detrimental to performance and that chemical etchants solved the problem. In 2017, Wang *et al.* stated that the removal of free elemental selenium using a carbon disulphide (CS_2) chemical etchant was successful in increasing the FF of their Sb_2Se_3 devices [39] and Chen *et al.* reported that the use of an ammonium sulphide ($(NH_4)_2S$) chemical etch was effective in removing both Sb_2O_3 and Se contamination. In both these cases, an improvement in device performance was shown via an increased FF, along with XPS analysis of the back surface before and after etching (Figure 6.1). However, the discussion of these changes amounted to only a single sentence in each work. The sporadic use of chemical etchants on the devices made within our research group however showed mixed results and therefore it was decided that some clarification of the effects of chemical etching was needed.

In the work by Wang *et al.* it is stated that "CS_2 treatment removes excess amorphous Se on the back surface, thus eliminating the contact barrier and improving FF significantly...". However, no experimental evidence is given for a back contact barrier. Chen *et al.* stated that "The low FF is largely caused by Sb_2O_3 and elemental Se at the back surface, which increase the contact resistance and impede carrier transport".

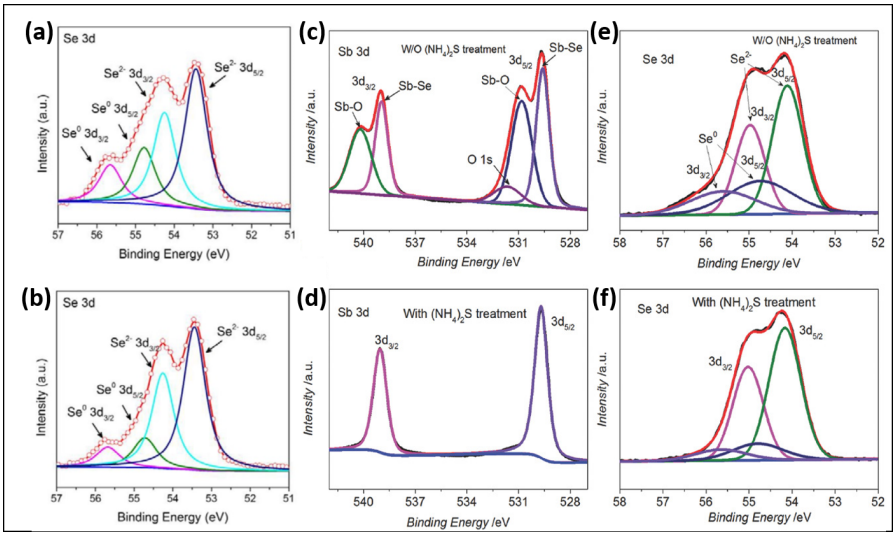

Figure 6.1 XPS results from the works by Wang *et al.* (a-b) and Chen *et al.* (c-f). Figures show selenium 3d region (a) before and (b) after CS_2 rinse, the antimony 3d region (c) before and (d) after an $(NH_4)_2S$ etch and the selenium 3d region (e) before and (f) after an $(NH_4)_2S$ etch. Reproduced from Refs [39] with permission from Nature and [38] with permission from Wiley.

While plausible, no experimental evidence is given for this and in some works it has been claimed that the exposure to air and resultant oxidation or selenisation of the Sb_2Se_3 film is in fact beneficial to device performance [115]. The XPS analysis performed by Wang *et al.* showed a reduction in Se levels at the surface following the etch treatment and Chen *et al.* similarly quoted XPS analysis as evidence of a reduction in Sb_2O_3 and Se after etching. However, the XPS interpretation was not consistent across the two studies (despite coming from the same group), with there being a large discrepancy in the assigned positions of the chemically shifted contaminant peaks. It is also significant that the effectiveness of the two etches has never been directly compared in a consistent study, given that the two etches were used in different works with differing devices, and it is therefore unclear if one etch offers superior benefits or performance over the other. The exact mechanism of the etching processes are unclear - there have been reports on the use of $(NH_4)_2S$ to dissolve Sb-chalcogenides [204] however, to the best of our knowledge, there are no reports on the mechanism of CS_2 as an etchant for Sb_2Se_3. It is noteworthy that CS_2 has not been used in any other reports of Sb_2Se_3 solar cell fabrication, whereas the $(NH_4)_2S$ treatment has been used in some but is far from widespread [205]. Indeed, only a handful of papers reported from within that same research group quote the use of an $(NH_4)_2S$ chemical etch, suggesting that the benefits are not universal for all Sb_2Se_3 cells.

The aim of this work was to explore in more depth the effect of these etches on the back

contact chemical composition using rigorous XPS analysis on a set of samples identical in every way except for the chemical etching treatment. The Sb_2Se_3 samples were deposited by CSS (see section 2.2.2) and were left as an unetched control sample, or were treated with either a CS_2 or an $(NH_4)_2S$ chemical etch to modify the surface chemistry prior to back contacting [38, 39, 206] (Figure 6.2). In addition, the film morphology and crystallinity were examined using XRD and SEM. Crucially, the XPS analysis was related to the back contact barrier and device performance by temperature dependent current-voltage, J-V and EQE measurements, allowing for a more thorough investigation of the influence of these chemical etchants on the back contacting mechanism. The knowledge gleaned in the study was used to inform the development of the chemical etching process.

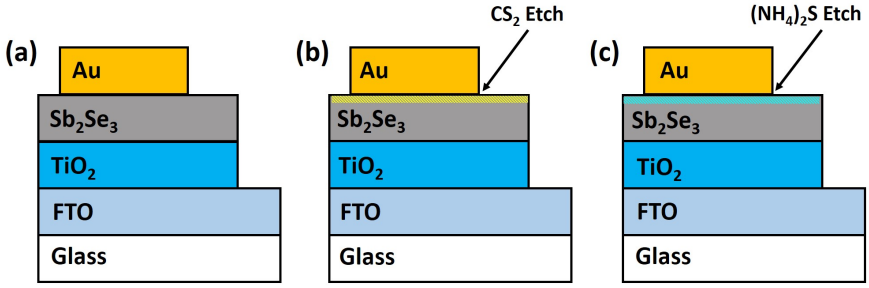

Figure 6.2 Schematics of device structure for the three studied samples: (a) unetched control sample, (b) CS_2-etched sample and (c) $(NH_4)_2S$-etched sample.

6.2.2 Methods

Film, Surface and Device Preparation

TiO_2 films were deposited by spin casting titanium isopropoxide onto fluorine-doped tin dioxide coated glass substrates (TEC10 FTO, NSG Group) prior to annealing in air, via an established two-step process [144]. Sb_2Se_3 was then deposited via a multi-step CSS process [81] utilising a seed layer deposited at a pressure of 10^{-2} mbar, followed by a thicker layer with a source temperature of 470°C for 15 minutes at a pressure of 13 mbar N_2 to give a total layer thickness of ~2 μm. This process was developed to generate layers with a more compact grain structure. In addition to an unetched control sample, two surface treatments were used, these being a CS_2 etch and an $(NH_4)_2S$ etch. For the CS_2 etch, a 25 mm × 25 mm sample was rinsed with 3 ml of CS_2 as carried out by Wang *et al.* [39]. For the $(NH_4)_2S$-etched sample, 3 ml of 0.3 mmol.dm^{-3} $(NH_4)_2S$ (aqueous), and subsequently 3 ml of H_2O, was applied to the substrate using a spin coater at 2500 rpm, as described by Chen *et al.* [38]. For completion of devices, 100 nm thick Au back contacts were then thermally evaporated through a shadow mask, creating $N = 16$ cells per sample type, each having an active area of 0.1 cm^2. Figure 6.2 shows a schematic diagram of the device structure.

Materials and Device Characterisation

SEM images were taken using a JEOL 7001F with an acceleration voltage of 5 kV. XRD was performed with a Rigaku SmartLab x-ray diffractometer in a parallel beam configuration. XPS measurements were performed inside an ultra-high vacuum chamber operating at a pressure less than 4×10^{-9} mbar. The surface composition was probed using core level XPS with an unmonochromated Mg Kα x-ray source (hν = 1253.6 eV) operating at 200 W and a hemispherical Scienta SES200 electron energy analyser comprised of a double channel plate and phosphor screen with a CCD camera. The resolution was determined from the FWHM of a Ag $3d_{5/2}$ peak of a Ag calibration sample to be 0.7 eV, allowing binding energy determination with a precision of $\pm$ 0.1 eV.

Device performance was measured under simulated AM1.5 illumination at 1000 Wm^{-2} using a TS Space Systems solar simulator and a Keithley 2400 source-meter. The Au/Sb_2Se_3 back-contact barrier height, ϕ_b, was determined from dark J-V measurements as a function of temperature (J-V-T) using a CTI-cryogenics cryostat in the range 250-350K, with J-V curves taken using a Keithley 2400 source-meter over the range -1 to 1 V. Using the method proposed by Bätzner *et al.* [21], the series resistance, R_s, is determined at forward bias above open-circuit voltage (V_{oc}) as a function of temperature i.e. the slope method. $R_s(T)$ may then be separated into an invariant, an Ohmic and an exponential component, the latter resulting from the passage of the carriers over the back contact via thermionic emission. R_s is thereby expressed as follows:

$$R_s = R_{\Omega 0} + \frac{\partial R_{\Omega 0}}{\partial T}T + \frac{C}{T^2}exp\left(\frac{\phi_b}{\mathrm{k}_B T}\right) \tag{6.1}$$

where C is a fitting parameter, $R_{\Omega 0}$ is the Ohmic resistance, and k_B is the Boltzmann constant. As shown by Al Turkestani [125], at low temperature the exponential term is much greater than the first two terms. Hence, for this experiment, the third term is deemed sufficient and the expression is simplified to:

$$R_s \approx \frac{C}{T^2}exp\left(\frac{\phi_b}{\mathrm{k}_B T}\right) \tag{6.2}$$

6.2.3 Results

Film Morphology

SEM images of as-deposited and etched films are shown in Figure 6.3. SEM was employed to investigate any significant alteration to the texture or damage to the surface layer by the etches that may affect the metal contacting. It is also a good indicator of the quality of the Sb_2Se_3 films. It can be seen from Figure 6.3 that the films have large and reasonably uniform grains (up to 2 µm across), with some cavities visible at the surface owing to the large grain structure. These cavities are not uncommon in CSS grown Sb_2Se_3 and it has been shown that they do not directly correspond to shunting pathways [75], being a product of a very uneven surface rather than a gap in the entire film. The etches have

little obvious impact on the surface morphology, aside from some loss of delineation of the grain boundaries following the $(NH_4)_2S$ etch (Figure 6.3c). This delineation is more likely a result of poorer image resolution than any effect of the etches on grain boundaries.

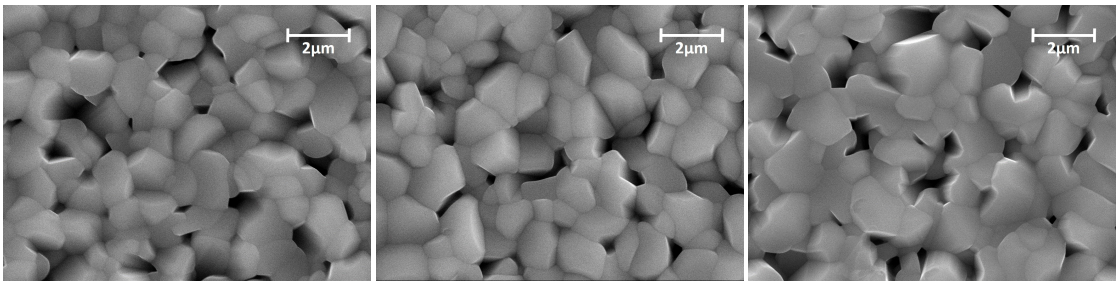

Figure 6.3 SEM micrographs of (a) unetched control, (b) CS_2-etched and (c) $(NH_4)_2S$-etched Sb_2Se_3 films.

Similar to SEM analysis, XRD patterns (Figure 6.4) show no significant differences between the samples, with all three patterns showing prominent peaks at 28.2°, 31.2°, 32.2° and 45.6° that are characteristic of the (211), (221), (301) and (002) planes respectively (using the Pbnm space-group labelling convention [57]). These planes are representative of nanoribbons lying at 37°, 44°, 46° and 0° from normal to the substrate for the (211), (221), (301) and (002) planes respectively. As discussed in section 2.2.2, growth of nanoribbons normal to the substrate surface would be expected to optimise both vertical conduction along the nanoribbon axes and also increase the fraction of van der Waals-bonded rather than covalent-bonded grain boundaries, both of which are expected to be beneficial to photovoltaic performance [54, 78]. Even the ∼45° angle of the (221) and (301) planes from normal is not expected to impede carrier transport due to the size of the grains in this material. It is also noted that there were no peaks at 15° and 17°, showing the lack of detrimental orientations in these films. It is reasonable to assume that the majority of the grains, and therefore the nanoribbons, span from the bottom to the top of the film [54, 57]. There is a small difference in the peak at 26.6°. However, this is attributed to an additional Sb_2Se_3 (021) orientation [54] and is therefore not indicative of any significant change at the surface.

Overall the SEM and XRD studies revealed that the etching processes introduced no significant morphological or crystallographic change that was detectable using these methods. This was consistent with expectations; the chemical etches had been reported to have a purely surface specific effect on the films and therefore any deeper structural changes would have been surprising. The reported influence of the etches was on a compositional level and evidenced with XPS, but without sufficient rigour to determine for certain the full picture of the effect of the etches. Therefore, the surface sensitivity of XPS was required here to detect the important chemical changes in the films and to examine the differences in the performances of the CS_2 and $(NH_4)_2S$ etches.

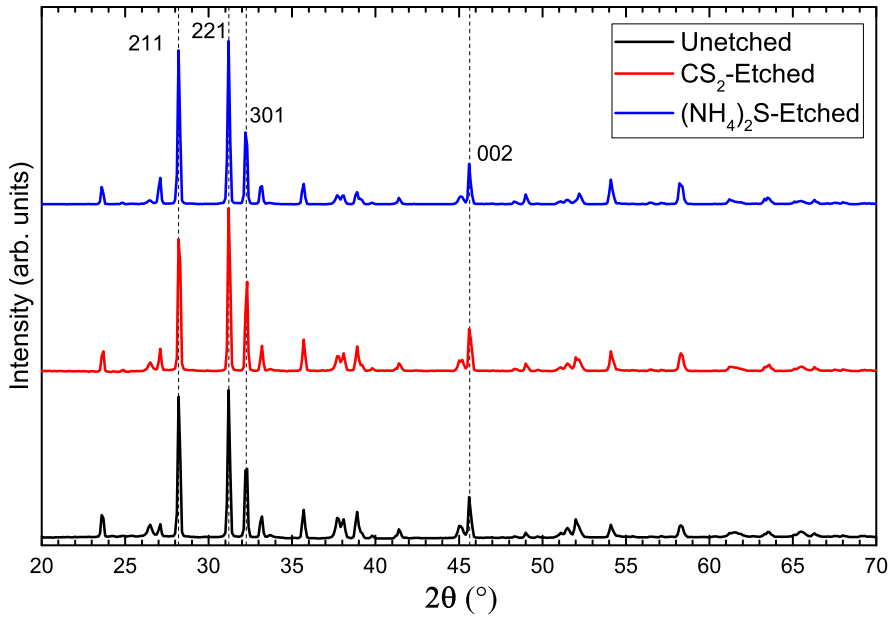

Figure 6.4 XRD patterns of unetched, CS_2-etched, and $(NH_4)_2S$-etched Sb_2Se_3 samples showing prominent peaks at 28.2°, 31.2°, 32.2° and 45.6°.

Surface Chemistry

The analysis of core level spectra using XPS is a powerful tool for investigating surface chemistry. However, it has its limitations, which will be briefly discussed here as well as the methodology used in the analysis. XPS can give a great deal of information on surface chemistry (as laid out in section 3.2.6), particularly the different chemical environments of each element. However, the exact ratios of the varying elements and chemical states cannot be accurately determined. This is primarily due to the varying photoionisation cross-sections of different elements making XPS more sensitive to some elements than others. It is also important to consider that different regions on the binding energy scale have different levels of surface sensitivity (see Figure 4.6), meaning that careful consideration must be taken of what depth of material a peak will give information on. This meant that for this XPS study no hard conclusions could be made on the exact amount of contamination present at the surface, but it was possible to look at the relative change in contamination under etching if all samples were exposed to the exact same conditions.

To ensure consistency in the results, the films were grown in the same CSS run and cut into quarters. As one piece was transferred immediately to the XPS for analysis the others were stored in an inert N_2 atmosphere to prevent any surface contamination. The chemical etches were applied immediately before each sample was transferred to the XPS for analysis in order to ensure consistency in the amount of time the etches had to change the Sb_2Se_3 surface.
Figures 6.5 and 6.6 show the XPS spectra for the Sb 4d (30 - 38 eV) and Se 3d (51 -

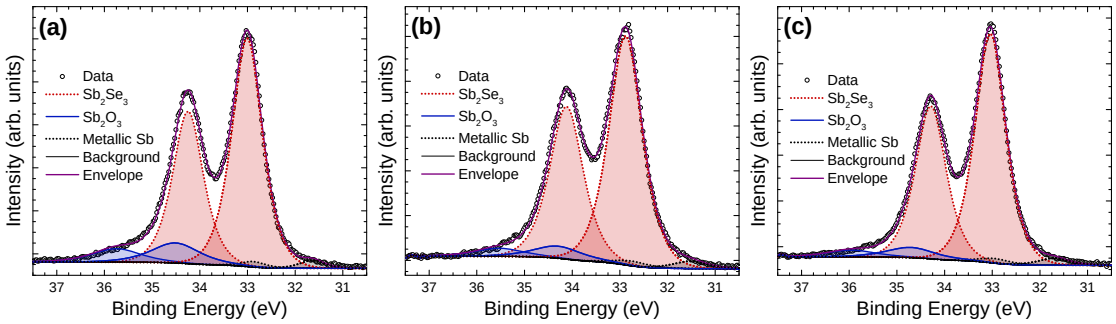

Figure 6.5 XPS spectra of Sb 4d regions for (a) unetched (b) CS_2-etched and (c) $(NH_4)_2S$-etched Sb_2Se_3 films. It can be seen that the relative amount of Sb_2O_3 is reduced with etching. There is also a low, unchanged metallic antimony signal in all three samples.

58 eV) regions respectively, for each of the unetched, CS_2-etched and $(NH_4)_2S$-etched samples. All contamination levels are presented as percentages of the Se or Sb present at the surface in each of their chemical environments (Table 6.2 & Figure 6.7). For example, the amount of free elemental selenium present is characterised as the amount of free elemental selenium as a percentage of total selenium detected in all its environments.

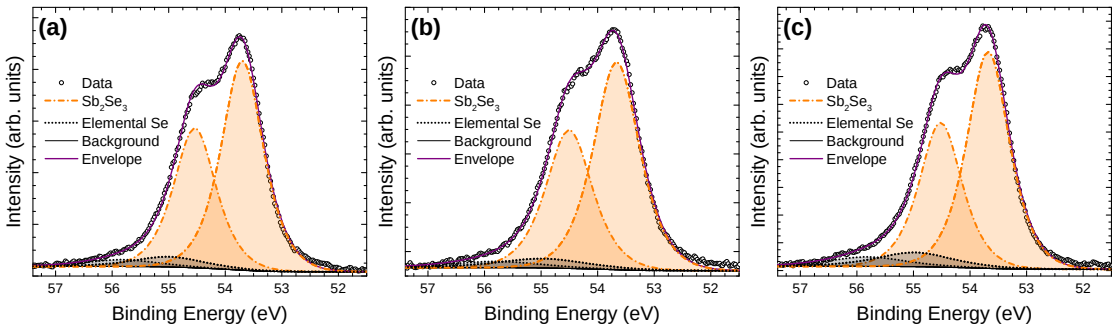

Figure 6.6 XPS spectra of Se 3d regions for (a) unetched (b) CS_2-etched and (c) $(NH_4)_2S$-etched Sb_2Se_3 films. It can be seen that the relative amount of free elemental selenium rises with the $(NH_4)_2S$ etch but is unchanged by the CS_2 etch.

For the Sb 4d region, three chemical species were identified: Sb_2Se_3, Sb_2O_3 and metallic Sb [111, 207–209]. The oxide component was determined to be Sb_2O_3 and not Sb_2O_5 or a mix of the two species due to a clear difference in chemical shift (~1 eV) for the two species relative to Sb_2Se_3 [111, 208]. For the Se 3d region, two chemical species were identified: Sb_2Se_3 and free elemental Se [39, 111, 210, 211]. The binding energies of the components are displayed in Table 6.1 and were determined using the fitting procedure laid out in Chapters 2 and 4.

Peak	Measured Binding Energy (eV)	FWHM (eV)
Sb(Se) $4d_{5/2}$	33.0	0.8
Sb(Se) $4d_{3/2}$	34.2	0.8
Sb(O) $4d_{5/2}$	34.5	1.1
Sb(O) $4d_{3/2}$	35.7	1.1
Sb $4d_{5/2}$	31.6	0.7
Sb $4d_{3/2}$	32.9	0.7
Se(Sb) $3d_{5/2}$	53.7	0.9
Se(Sb) $3d_{3/2}$	54.5	0.9
Se $3d_{5/2}$	55.0	1.5
Se $3d_{3/2}$	55.8	1.5

Table 6.1 Identified peaks in the XPS spectra for Sb_2Se_3 samples.

In Figure 6.5, although the magnitude of the signal is understandably dwarfed by the Sb_2Se_3 signal, it is noticeable that the Sb_2O_3 peaks are reduced in size after etching with both CS_2 and $(NH_4)_2S$, indicating removal of the oxide via etching. However, it is also noted that here the level of contamination is already very low in the unetched sample compared with the other unetched samples previously reported by Wang *et al.* and Chen *et al.* (see Figures 6.1, 6.5 and 6.6) [38, 39]. This is likely because the CSS deposition technique used in this work, unlike the RTE process used by the Tang group, uses an inert nitrogen atmosphere. Additionally, samples were exposed to air for minimal time (< 30 minutes) between deposition and XPS measurement. A low level of contamination is therefore consistent with our expectations.

Contaminant	Unetched (%)	CS_2-etched	$(NH_4)_2S$-etched
Free elemental selenium	7.6 ($\pm$0.2)	8.0 ($\pm$0.5)	10.5 ($\pm$0.3)
Sb_2O_3	11.9 ($\pm$1.2)	6.9 ($\pm$1.0)	5.4 ($\pm$0.4)

Table 6.2 Percentage of the Se and Sb_2O_3 contaminant signals as a percentage of total Se- and Sb-related signals, respectively, for unetched, CS_2-etched and $(NH_4)_2S$-etched films.

The levels of Se and Sb_2O_3 contamination are summarised in Table 6.2 and Figure 6.7. It is clear that both etching processes reduce the level of Sb_2O_3 contamination, with the $(NH_4)_2S$ etch being marginally more effective. However, while the CS_2 etch has little or no effect on the amount of free elemental selenium at the back contact surface, the $(NH_4)_2S$ etch increases the proportion of free elemental selenium at the surface. This indicates that the etches do not selectively remove selenium and in the case of the $(NH_4)_2S$ etch it in fact produces a more selenium rich surface. In this work, by ensuring consistency in the fitting procedure used to analyse the effect of both etches, we show beyond doubt that the primary result of the etch process is Sb_2O_3 removal and not Se removal. This is contrary to previous work, in which inconsistencies in the XPS fitting procedure led to misidentification of Se removal as the primary result of the CS_2 etching

process [38, 39] (as discussed in section 6.2.4). The next step is then to determine what impact this has on the device contacting and performance.

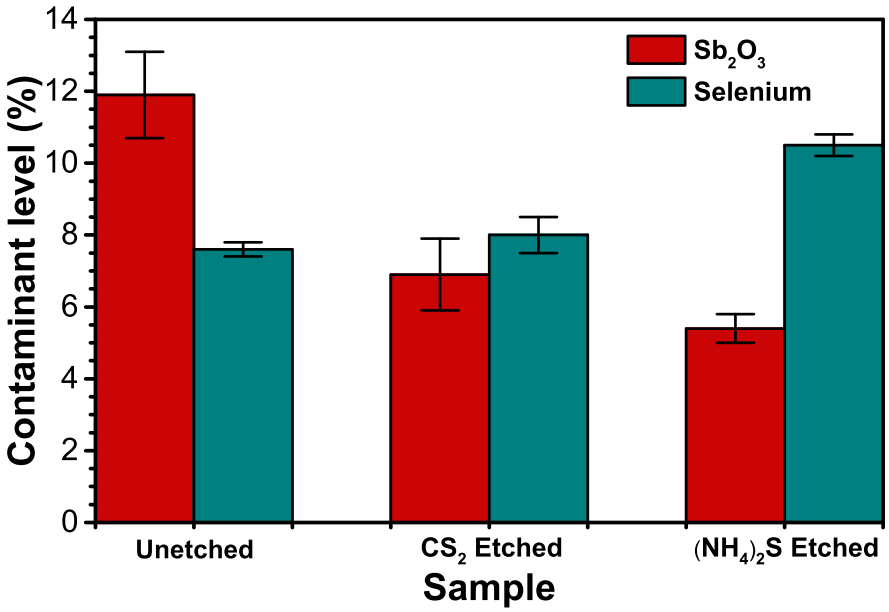

Figure 6.7 Sb_2O_3 and selenium contamination levels with different etches. Both etches reduce the proportion of oxide contamination, while relative levels of free elemental selenium rise slightly with the $(NH_4)_2S$ etch but are unchanged by the CS_2 etch.

Device Performance and Barrier Height Determination

A series of complete cells was produced with absorber layers and etching steps identical to those used for XPS analysis to allow direct comparison. Average and peak device performance parameters extracted from J-V analysis are shown in Tables 6.3 & 6.4 for an unetched sample and samples etched by CS_2 and $(NH_4)_2S$. Here it can be seen that chemical etching has a negative effect on both the average and peak performances of the devices.

The CS_2 etch reduces the average efficiency by 25%, with the V_{oc} significantly reduced but no significant change in the FF and J_{sc}, contrary to expectation based on literature. The $(NH_4)_2S$ etch, on the other hand, led to a significant drop in both the average V_{oc} and J_{sc}, while the average FF was unaffected. However, looking at averaged device parameters takes into account both good and bad cells which could be affected differently by the etch. The peak efficiency characteristics tell a slightly different story. In the peak performing cell, the effect of the CS_2 etch on efficiency is still negative but by a smaller margin ($\sim$3% decrease), with an increase in FF being the most significant difference. This

Device	PCE (%)	V_{oc} (V)	J_{sc} (mA.cm^{-2})	FF (%)
Unetched	5.00 (±0.46)	0.42 (±0.01)	28.2 (±2.1)	42.4 (±1.1)
CS_2	4.27 (±1.68)	0.36 (±0.09)	27.1 (±2.8)	40.7 (±8.2)
$(NH_4)_2S$	3.73 (±1.58)	0.37 (±0.11)	21.8(±5.4)	42.2 (±8.0)

Table 6.3 Average J-V results and standard deviations for devices with different chemical etch treatments ($N = 16$ per device type).

is accompanied by a slight drop in R_s. However, these improvements are counteracted by a slight lowering of both V_{oc}, J_{sc}. The $(NH_4)_2S$ etch again causes a greater drop in peak efficiency than the CS_2 etch (∼14% decrease), but also produces an improvement in FF and R_s.These improvements are counteracted by significant decreases in J_{sc} and R_{sh}.

Device	PCE (%)	V_{oc} (V)	J_{sc} (mA.cm^{-2})	FF (%)	R_s (Ω.cm^{-2})	R_{sh} (Ω.cm^{-2})
Unetched	5.70	0.42	30.7	44.2	5.0	73.5
CS_2	5.55	0.40	29.2	47.5	4.8	72.3
$(NH_4)_2S$	4.89	0.42	25.1	46.4	3.9	68.2

Table 6.4 Peak J-V results for devices with different chemical etch treatments.

The improvement in FF and R_s in the peak devices correlates well with the previously reported theory that the removal of a resistive layer at the back contact improves conductivity. However, the drop in J_{sc} and R_{sh} indicate that the film is damaged by these etches and increase the amount of shunt leakage in the devices. It is possible that the more drastic decrease in the average performance is an extension of this, with weaker cells experiencing more harm from the etches than good. The negative impact on the V_{oc} is also unexpected, and could be an indicator of some positive influence of the contaminants on the overall band structure and built-in voltage of the devices. This is discussed further in section 6.3.

The motivation for back contact treatments in CdTe is usually to reduce the back contact barrier caused by the unfavourable alignment between the work function of CdTe and the work function of the metal contact. This back contact barrier is evident in the J-V curves of CdTe devices by the existence of 'rollover' - an increase in series resistance at high forward bias. At lower temperatures this rollover becomes more prominent, due to the decreasing probability of thermionic emission of carriers over this barrier. J-V-T can be used to measure the change in series resistance with temperature and, by fitting one of a variety of models to the data, determine the magnitude of the back-contact barrier, ϕ_b. J-V-T analysis was carried out on all Sb_2Se_3 devices, in order to determine whether the chemical etching had a similar influence in Sb_2Se_3 devices as in CdTe.
R_s values were measured in the dark via the slope method for a range of temperatures

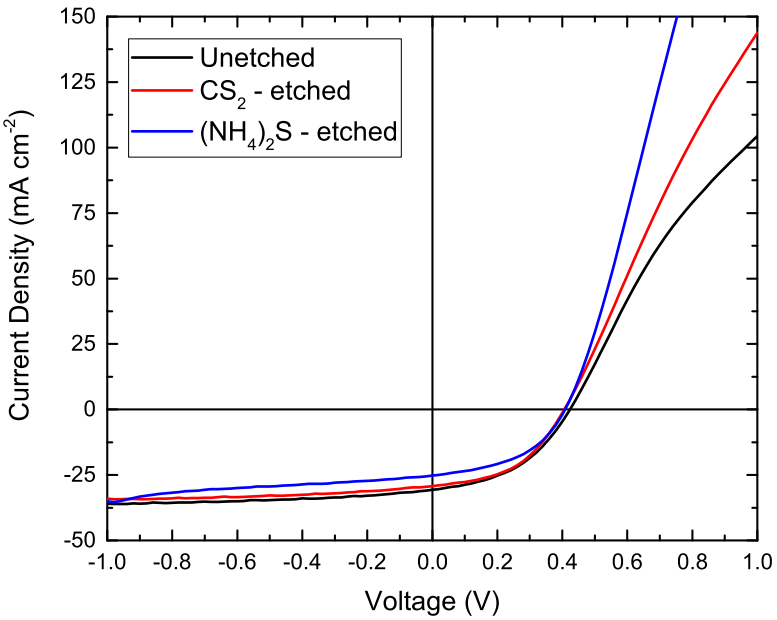

Figure 6.8 J-V scans for the best performing Sb_2Se_3 devices with no etching treatment, CS_2 etch and $(NH_4)_2S$ etch.

Sb_2Se_3 Surface Treatment	Barrier Height (eV)
Unetched	0.43 ±0.01
CS_2-etched	0.26 ±0.01
$(NH_4)_2S$-etched	0.29 ±0.01

Table 6.5 Measured back contact barriers for Sb_2Se_3 devices.

(250 - 350 K) for all devices prior to fitting them using equation 6.2. The fits can be found in Figure 6.9 and the results of the fitting are shown in Table 6.5. The results show that the barrier height is lowered by both etches, with a similar decrease for both the $(NH_4)_2S$ etch and the CS_2 etch (albeit slightly larger for the CS_2). This correlates well with the XPS results and the device results, indicating that a removal of the oxide layer is beneficial to the back contact performance [38, 39].

6.2.4 Discussion

The impact of $(NH_4)_2S$ etch and CS_2 etching on Sb_2Se_3 identified here is notably different from prior reports [38, 39]. Wang *et al.* [39] suggested CS_2 improved FF by dramatically reducing the proportion of free elemental selenium at the back contact. However, in this work we observe a reduction in Sb_2O_3 and not elemental selenium to be the primary role of CS_2 etching. This discrepancy in the effect on selenium can be explained, in part, by the much lower selenium contamination levels in our devices (Figure 6.6) due to use of a CSS process rather than rapid thermal evaporation (as used by Wang *et al.* and

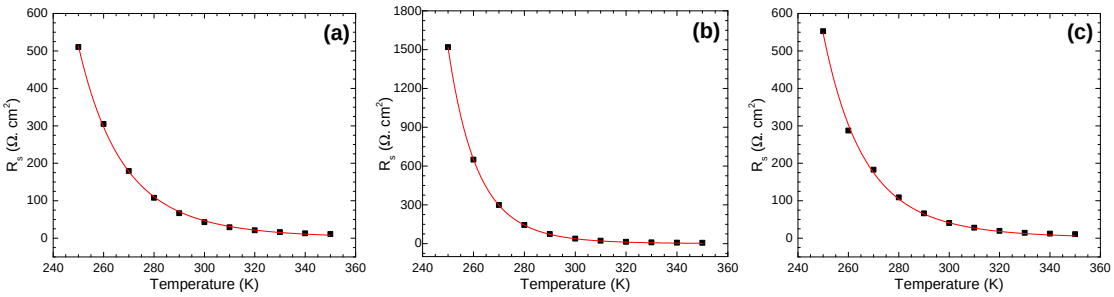

Figure 6.9 R_s data with exponential fit used to calculate back contact barrier height in (a) unetched, (b) CS_2-etched and (c) $(NH_4)_2S$-etched Sb_2Se_3 devices.

Chen *et al*) and may be the reason why they see a greater influence on device performance [38, 39]. Chen *et al.* reported that the $(NH_4)_2S$ etch effectively removes both Sb_2O_3 and free elemental selenium from the back contact [38]. However, the XPS peak fitting of the Se region by Chen *et al.* was dramatically inconsistent with both Wang *et al.*[39] and this work. In this work, the binding energy separation between elemental Se and Sb_2Se_3 in the Se region is ~1.3 eV, consistent with Wang *et al.*, and other reports [39, 111, 210]. However, Chen *et al.* [38] state this separation as ~0.6 eV, combined with a very broad line shape for the alleged elemental Se component. Given the 0.1 eV precision of binding energy determination in XPS, this difference casts doubt over the validity of these assignments, and therefore it cannot be concluded from their work that the $(NH_4)_2S$ treatment is in fact effective in removing free elemental selenium. Indeed our results show there to be no removal of elemental selenium and the improvement they observed in device performance is most likely due to removal of Sb_2O_3, which would be consistent with the work carried out in this study. Furthermore, Wang *et al.*, while demonstrating XPS fitting that reliably shows a reduction in elemental Se, show no XPS spectra of the Sb region that would have shown a reduction in Sb_2O_3, meaning that it is insufficient evidence to conclude that the removal of Se was the cause of the performance improvement. It is also possible that a more dramatic reduction in sb_2O_3 could mean a more Se-rich back surface after etching.

Our results indicate that while these chemical etches have led to an improvement in device performance in previous studies they are in some cases harmful [38, 39]. The removal of Sb_2O_3 from the back contact decreases the barrier height and lowers the series resistance. However, the decrease in J_{sc} and R_{sh} in J-V measurements can be explained by damage to the film upon etching. Whilst it is likely that the removal of a resistive Sb_2O_3 layer would benefit device performance by lowering of the series resistance and increasing the FF, there are clear differences in the initial level of contamination on the surfaces of our samples compared to those of Wang *et al.* and Chen *et al.* [38, 39]. Our samples show very low levels of Sb_2O_3 and free elemental selenium contamination compared to those shown in the previous studies, presumably due to the different deposition method. For

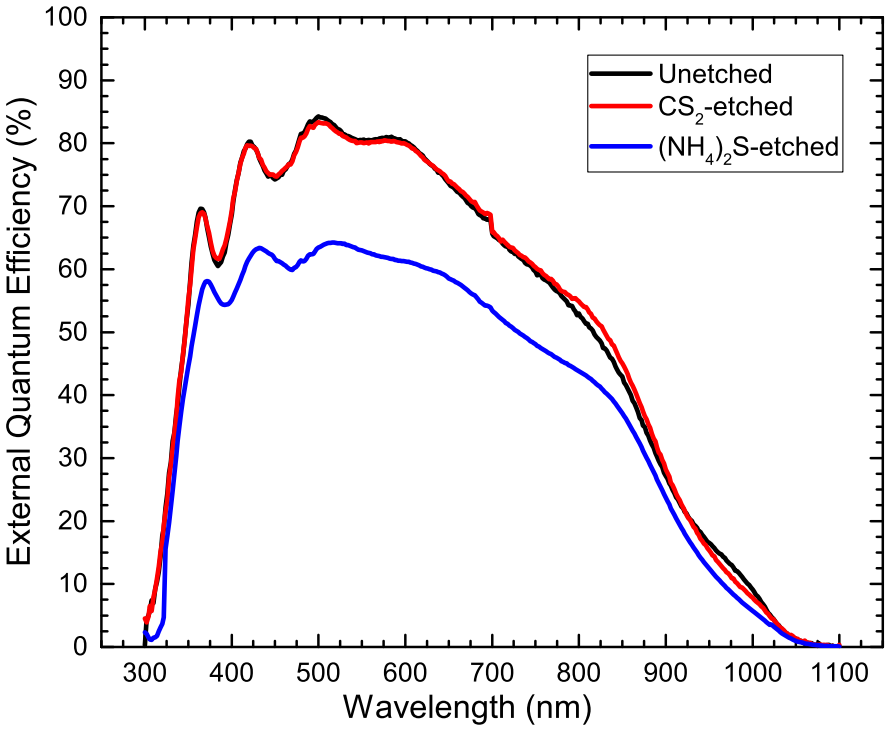

Figure 6.10 EQE spectra of an unetched reference, CS_2-etched and $(NH_4)_2S$-etched Sb_2Se_3 solar cells. The spectra show no noticeable change in shape with the exception of the $(NH_4)_2S$-etched spectrum being lower, as expected from the lower J_{sc} in Tables 6.3 & 6.4.

example, the RTE process uses no inert gas during deposition and also deposits at a much higher rate than CSS and at a different pressure ($\sim$ 0.01 mbar rather than $\sim$ 13 mbar) [78]. Additionally, in the RTE process the Sb_2Se_3 melts before evaporating, whereas in CSS the material directly sublimes onto the substrate which could lead to differences in contamination from the source material [78]. It seems likely therefore that the state of the as-deposited Sb_2Se_3 surface plays a major role in the effectiveness of these chemical etches. We postulate that if the sample has a thick layer of Sb_2O_3 contamination then the etches are effective in reducing the thickness of a resistive layer, thereby improving the fill factor of the device. However, if the Sb_2O_3 layer is very thin, the reduction in R_s is counteracted by a more significant decrease in R_{sh} and J_{sc} that lowers the overall performance of the cell. This is supported by the fact that EQE measurements show that the $(NH_4)_2S$-etched sample has uniformly lower EQE across all wavelengths whilst showing no change in shape in the EQE spectrum (Figure 6.10).

According to the work carried out in this study, the factor counteracting the benefits of Sb_2O_3 removal at the back contact was the aggressiveness of the etch, potentially also removing Sb_2Se_3. It was therefore decided that a more dilute version of the most

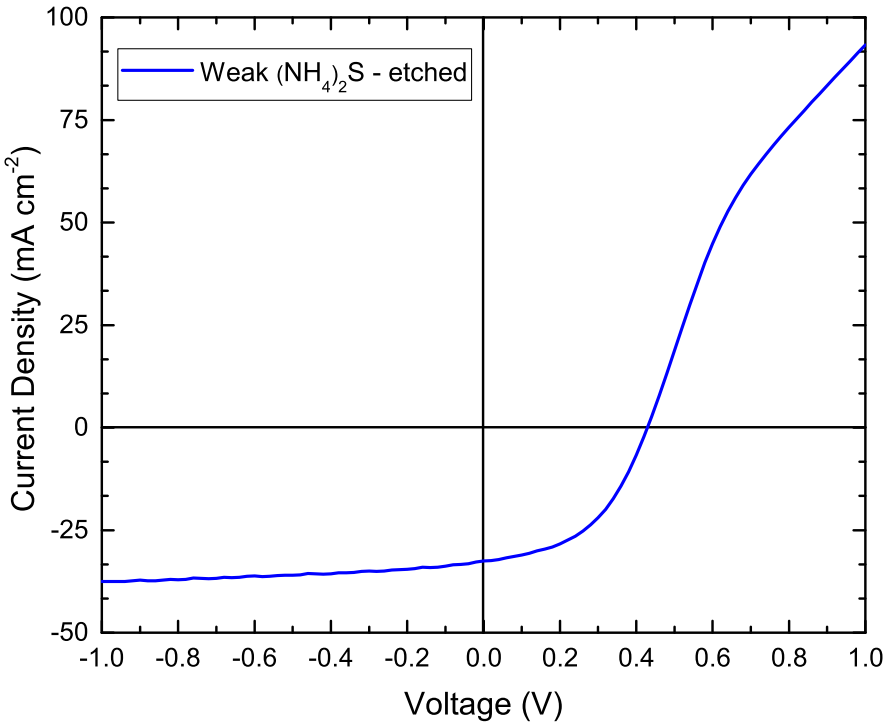

Figure 6.11 J-V curve of a device etched with a more dilute (0.03 mmol.dm^{-3}) solution of $(NH_4)_2S$, showing improved performance from that shown in Figure 6.8.

commonly used etch, $(NH_4)_2S$, would be used on a similar Sb_2Se_3 solar cell to test this hypothesis. The etch was made 10 times weaker. This succeeded in improving the device performance to over 6.6%, as shown in Figure 6.11 (PCE = 6.63%, V_{oc} = 0.42 V, J_{sc} = 32.5 mA.cm^{-2}, FF = 48.5), which further supports the conclusions of this work. It is noted that the concentration used in the earlier part of the study matched exactly the conditions laid out by Chen *et al.* [38] in the work in which they reported an improvement in device performance. It is likely that the difference in concentration required is another result of the difference in contamination levels immediately post-deposition.

6.3 Part 2 - Band Alignments

6.3.1 Background

The publication of the study on chemical etching of the back contact contamination led to further work within the PV research group, carried out in collaboration with this project. In particular, it had been noticed that the exposure of Sb_2Se_3 solar cells to air led to an improvement in device performance over the span of a few hours. This coupled interestingly with the conclusions of the chemical etch study that the removal of

very thin contaminant layers was actually detrimental to device performance. This was studied in detail by Fleck *et al.* [115]. This work was closely linked to the work of this chapter, although not a part of it, and will therefore be discussed here for context.

The study by Fleck *et al.* showed that over a 23 hour period following the first measurement of device performance (carried out as soon after completion of the device as possible) the efficiency of the cell increased by approximately 10%. This improvement manifested itself primarily through an increase in fill factor (FF) and a decrease in 'rollover' in the J-V curve. Rollover is a well known indicator of a back contact barrier in CdTe solar cells, indicating an unfavourable band alignment between the surface of the Sb_2Se_3 layer and the back contact metal (Au). Fleck *et al.* showed that samples exposed to air experienced this improvement whereas samples stored in vacuum did not. This, coupled with XPS analysis of the back surface, showed that the improvement in device performance was linked to the growth of Sb_2O_3 contamination on the back surface and the accompanying formation of elemental selenium, Se.

Measurement of the secondary electron cut-off of the films immediately after deposition and after exposure to air and vacuum revealed that the growth of a native oxide decreased the work function of the surface from 4.9 eV to 4.3 eV. This is consistent with the established concepts in the CdTe literature of decreasing back contact barrier height by lowering the work function of the back surface. However, it is important to remember that the Sb_2Se_3 thin films studied are n-type rather than p-type and that the PV devices consist of a n-n^+ junction [62]. It was also postulated that the positioning of the valence and conduction bands of the Sb_2O_3 in between those of Sb_2Se_3 and the Fermi level of Au would act as a passivation layer to suppress carrier recombination at the back contact.

This was tested by depositing ultra-thin (2 nm) layers of both Sb_2O_3, Se and a combination of both via thermal evaporation. Both layers were shown to improve device performance, but it was the Se layer and the combination of Sb_2O_3 and Se that had the greater impact. This supports the conclusions of the chemical etch study in Part 1 of this chapter, in which the etch that removed Sb_2O_3 and left a Se rich back contact was the most beneficial. It also supports the theory that a very thin layer of oxide is not detrimental and that only thicker layers of contamination are deleterious to device performance. Layers thicker than 2 nm were also tested by Fleck *et al.* but these were found to reduce efficiency via a loss in J_{sc}. This supports the conclusions in the chemical etch study in Part 1 of this chapter - that the additional resistance from the oxide layer is the primary source of efficiency loss introduced by the contamination.

In order to further examine the role of oxide at the back contact, it was necessary to measure the band alignments between Sb_2Se_3 and an Sb_2O_3 contaminant layer. The device results and J-V-T measurements from the work by Fleck *et al.* suggest that the oxide layer forms a barrier to carrier extraction from the Sb_2Se_3 to the Au contact, but that this can be tunnelled through by holes if the layer is sufficiently thin and simulta-

neously acts as an electron reflection barrier [115]. It is desirable, therefore, to acquire a measurement of the band offset between the Sb_2Se_3 crystalline film and the contaminant layer of Sb_2O_3, to corroborate this theory.

In this study, two different methods were used to measure the band alignment between Sb_2Se_3 and Sb_2O_3. The first used a novel method of measuring the valence band difference spectrum between an air-exposed, oxidised bulk crystal of Sb_2Se_3 (the same n-type crystal as used in Chapter 5) and finding the valence band offset between this difference spectrum and the pristine, cleaved bulk crystal. The second method used was the same as that used in Chapter 4, with the Kraut method applied to a thermally evaporated thin film of Sb_2O_3 deposited onto CSS grown Sb_2Se_3, similar to (but thicker than) the one used by Fleck *et al.* when attempting to replicate the effects of surface oxidation [115].

6.3.2 Methods

Film and Crystal Fabrication

As well as the bulk crystal (discussed in detail in Chapter 5), three thin film samples were used in this work. A $\sim$2 μm thick Sb_2Se_3 film was deposited onto a TiO_2 substrate (matching the usual solar cell structure [57, 62]) via CSS. A two stage process was used - 2 minutes with a source temperature of 390°C, substrate heating at 360°C and a pressure of $\sim$0.05 mbar followed by 15 minutes with a source temperature of 470°C at a pressure of 13 Torr. A $\sim$75 nm thick film of Sb_2O_3 was deposited via thermal evaporation onto a fluorine doped SnO_2 coated glass substrate. A thin Sb_2O_3 film was deposited onto Sb_2Se_3 for the interface measurement. Sb_2O_3 thickness was limited to 22 nm, as determined using atomic force microscopy and the Sb_2Se_3 layer was identical to the thick Sb_2Se_3 sample.

The Sb_2Se_3 bulk crystals were fabricated via the Bridgman melt-growth technique, as already covered in Chapter 5 . A more detailed description of the process and characterisation of the crystals is provided elsewhere [62, 97, 175, 176, 212].

Photoemission

Hard x-ray photoemission spectroscopy was carried out at the I09 beamline at the Diamond Light Source facility, as laid out in section 3.2.7. Following the initial, as-received measurement, the crystals were cleaved in-situ to expose a pristine (010) surface (in the Pbnm space group setting [50]), as demonstrated in Chapter 5 and by Hobson *et al.* and Don *et al.* in previous works by our group [62, 212]. The crystals were cleaved by affixing a metal stud to the crystal surface with an epoxy and then knocking it off with a wobble-stick once inside the UHV system. All peak positions from curve fitting are reported with an error of ±0.05 eV. HAXPES core level spectra were curve fitted using CASAXPS software with Voigt lineshapes after subtracting a Shirley background [178].

6.3.3 Results

Valence Band Difference Spectrum

Figure 6.12 shows a reproduction of Figure 5.7 from Chapter 5. The spectra show some difference in intensity at binding energies above 3 eV and this difference is particularly pronounced between 3 and 4 eV. As previously discussed in Chapter 5, this intensity difference is attributed to a surface layer of Sb_2O_3 that is known to grow on the surface of Sb_2Se_3 upon exposure to air. The two spectra have been normalised to be matching in intensity at ~1.7 eV [213]. This point was chosen for the normalisation for two reasons - firstly the shapes of the valence bands are very similar up to ~2 eV, with the shape of the uncleaved beginning to differ towards higher binding energy. By normalising to this point there is no negative intensity in the difference spectrum [213], with the contribution from the Sb_2O_3 beginning to show from ~2 eV. This point also corresponds to the binding energy at which the Sb 5s orbital has a significant contribution in the Sb_2Se_3 density of states [212]. It therefore corresponds to a peak in the valence band density of states (rather than background intensity or a peak shoulder/edge), making it more reliable. Secondly, at this point no contribution from Sb_2O_3 would be expected (due to its wide band gap and n-type conductivity), meaning that the intensity at this point originates solely from Sb_2Se_3 in both spectra. No energy shift was necessary to align the two samples, which lent weight to the assumption that the valence band edge position was representative of the Sb_2Se_3's VBM-E_F separation in both the oxidised and pristine states. By subtracting the valence band spectrum of the cleaved sample from that of the uncleaved sample, the remaining intensity, called the difference spectrum, should originate from this Sb_2O_3 layer [213]. This is shown by the black circular data points in Figure 6.12b and will henceforth be referred to as 'Sb_2O_3-sub'.

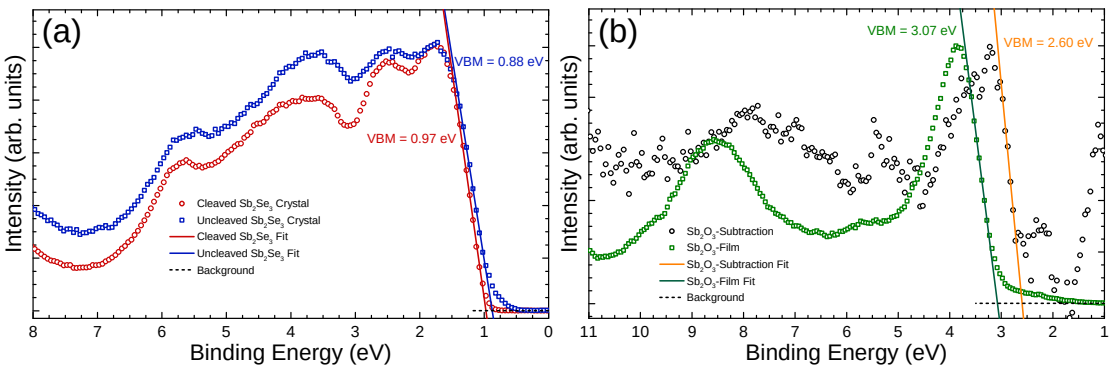

Figure 6.12 (a) Valence band spectra of (red) cleaved Sb_2Se_3 crystal and (blue) uncleaved Sb_2Se_3 crystal and (b) valence band spectra of (green) Sb_2O_3 thin film and (black) valence band subtracted Sb_2O_3. All spectra are shown with linear fits and measured VBM energies.

To ascertain whether this method was successful in isolating the contribution from the contamination, the Sb_2O_3-sub spectrum was compared to the valence band spectrum of a thin film of Sb_2O_3 (henceforth referred to as 'Sb_2O_3-film'). This is a thermally evaporated thin film deposited onto Sb_2Se_3 but with a thickness of 75 nm. This data is represented by the green data points on Figure 6.12b and shows good agreement with the Sb_2O_3-sub data. Both exhibit a peak in intensity at the edge of the valence band, with another broader feature at 5-6 eV below the valence band edge. However, the two spectra do not line up in energy, with the Sb_2O_3-film valence band lying roughly 0.5 eV to higher binding energy than Sb_2O_3-sub. There is also a peak in the Sb_2O_3-sub data at 1 eV, corresponding exactly with the edge of the Sb_2Se_3 data. This spike is attributed to a difference in mid-gap states between the air exposed crystal and the *in situ* cleaved crystal [214, 215]. Again using linear fits, the VBM energies were determined to be 3.07 eV and 2.60 eV respectively for the Sb_2O_3-film and Sb_2O_3-sub. This highlights a difference between the deposited film and the native oxide, although whether this is due to a difference in thickness or has a different origin is unclear (as discussed below). Using the valence band edge of the Sb_2O_3-sub, it is possible to determine the band alignment between the valence band of Sb_2Se_3 and Sb_2O_3 contamination.

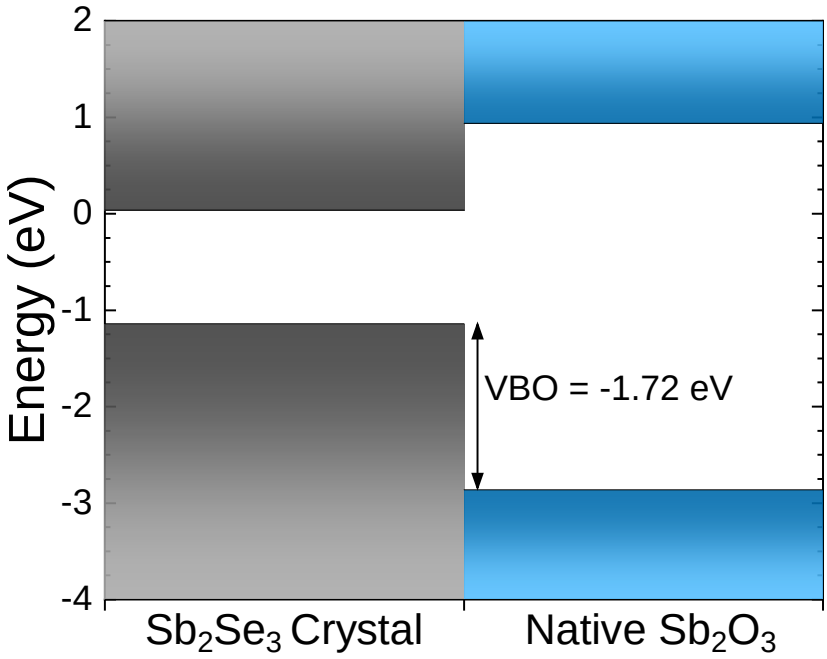

Figure 6.13 Band alignment between Sb_2Se_3 bulk crystal and its native Sb_2O_3 determined by valence band subtraction. Conduction band energies have been determined by adding the known band gap values for Sb_2Se_3 and Sb_2O_3 of 1.18 eV and 4 eV.

The band gap of Sb_2Se_3 is well known to be 1.18 eV [54] while there is a range of

reported band gap values for Sb_2O_3, from ~3.5 eV to ~4 eV [216–218]. For this study a DFT calculated band gap of 4 eV was used [219]. This was calculated using the HSE06 functional which is known to achieve accurate band gap values and is in line with many values reported in the literature [216–218]. This is towards the upper limit of the range reported in the literature but, as will be shown later, any smaller values within the reported range would have no bearing on the conclusions of this work - the nature of the conduction band offset is the same for all reasonable values of the Sb_2O_3 band gap. Using the valence band subtraction method, the VBO between Sb_2Se_3 and Sb_2O_3 can be measured as the difference in the two valence band edge energies of the uncleaved crystal and the native oxide from the Sb_2O_3-sub spectrum. Figure 6.13 shows the resulting experimentally determined band alignment between Sb_2Se_3 and its native oxide. The VBO of -1.72 eV shown in Figure 6.13 implies a straddling alignment (where both the CBM and VBM of one material lie within the band gap of the other), as would be expected with two materials of such different band gaps. An uncertainty of 0.14 eV was determined for the linear fitting procedure, which is not sufficient to change the straddling nature of the alignment.

The Kraut Method

In order to verify the nature of the alignment between Sb_2Se_3 and Sb_2O_3, the VBO between thin films of Sb_2Se_3 and Sb_2O_3 was measured via the Kraut method. This method is explained in detail in Chapter 4 as well as the advantages and disadvantages of using HAXPES instead of regular XPS. For this measurement, an Sb_2O_3 layer was deposited to a thickness of 22 nm onto a 1.5 µm thick layer of Sb_2Se_3. Separate, thicker layers of Sb_2Se_3 (2 µm) and Sb_2O_3 (75 nm) were also necessary for the measurement, of which the thick Sb_2O_3 sample was the same as Sb_2O_3-film used in Figure 6.12b.

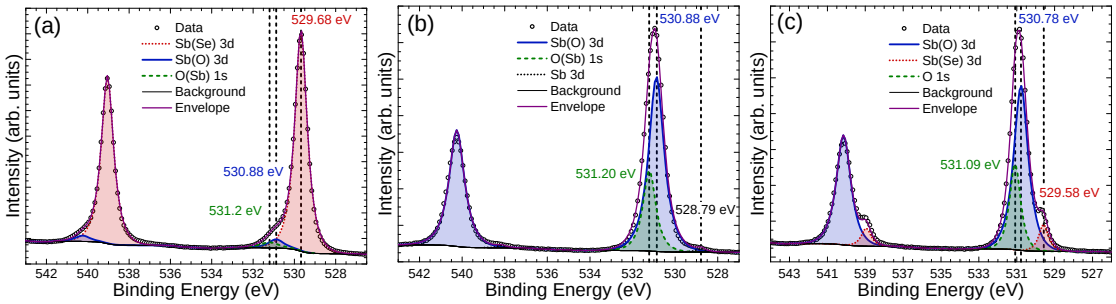

Figure 6.14 Core level spectra of the Sb 3d and O 1s region for (a) Sb_2Se_3 thin film, (b) Sb_2O_3 thin film and (c) Sb_2O_3/Sb_2Se_3 interfacial sample.

Figure 6.14 shows the HAXPES core level spectra of the Sb 3d and O 1s region for the Sb_2Se_3, Sb_2O_3 and Sb_2O_3/Sb_2Se_3 interface thin films. The spectrum from the Sb_2Se_3 film (Figure 6.14a) is, as expected, dominated by Sb bonded to Se, with a very small

contribution from Sb bonded to O. This is a result of oxidation of the surface when the sample was briefly exposed to air. The signal is so small that it does not indicate a complete layer of Sb_2O_3, such as the one removed by *in situ* cleaving [212]. The spectrum from the Sb_2O_3 film (Figure 6.14b) is dominated by Sb bonded to O, as well as the overlapping O 1s peak. This sample also shows some trace contamination from metallic Sb at 528.79 eV, likely a by-product of the deposition process or some slight oxygen deficiency in the source material. The interfacial sample (Figure 6.14c) shows signals from both Sb_2Se_3 and Sb_2O_3 with the oxide signal dominating as expected for the uppermost layer. Other core levels used for the Kraut method calculations as well as valence band spectra for the thin films are included in Figures 6.16 - 6.19.

	Binding Energy (eV)			
Peaks Used	O(Sb) 1s	Sb(O) 3d	Sb(O) 4s	Sb(O) 4d
Sb(Se) $3d_{5/2}$	-1.91	-1.93	-2.02	-2.00
Se(Sb) $3p_{3/2}$	-1.89	-1.90	-2.00	-1.98
Se(Sb) $3d_{5/2}$	-1.63	-1.65	-1.74	-1.72
Sb(Se) $4d_{5/2}$	-1.96	-1.97	-2.06	-2.04

Table 6.6 Table showing the valence band offset calculated by the Kraut method using different combinations of core level peaks from Sb_2O_3 (columns) and Sb_2Se_3 (rows).

Figure 6.15 shows the VBO as measured by the Kraut method. The measured VBO was -1.90 eV, taken as an average of the different valence band offsets calculated using different combinations of core level peaks (see Table 6.6). The error on the measurement was taken as the standard deviation of the different calculated values and was determined to be 0.13 eV. The offset of -1.90±0.13 eV is consistent with that determined by the subtraction method and would also signify a straddling alignment. The different band offsets measured using different core level peak combinations is shown in Table 6.6. It is noticeable that the band offsets calculated using the Se 3d peak in the Sb_2Se_3 spectrum are consistently lower than those calculated from other peaks. The reason for this is difficult to determine. It is possible that the presence of the plasmon lines from the Sb 4d interferes with the determination of the binding energy, but as shown in Figure 5.5 these features have been fitted and accounted for. It is unlikely that the measured peak is present in a different oxidation state because the peak positions match literature reported values as well as those measured elsewhere in this thesis very well [37, 111, 220]. Common photoemission effects such as recoil shift or charging can also be discounted. Recoil shift is unlikely due to the absence of a similar effect seen for the oxygen in Sb_2O_3 or the sulfur or oxygen measured in Chapter 4. Similarly, differential charging is known not to have occurred due to the correct binding energies of peaks being measured at either end of the spectrum. Ultimately, this trend has to be attributed to a random quirk of the measurement and is assumed to be accounted for by averaging all calculated VBOs. A detailed breakdown of core level peak positions is included in Table 6.7 at the end of the chapter and an account of the fitting procedure is included in Chapters 2 and

4.

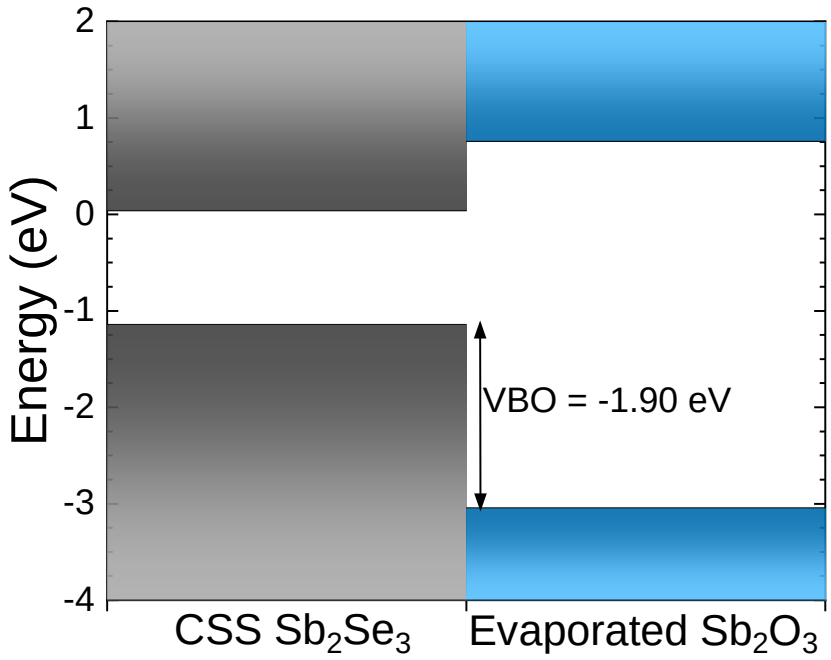

Figure 6.15 Band alignment between CSS-deposited Sb_2Se_3 and a thermally evaporated Sb_2O_3 thin film determined using the Kraut method. Conduction band energies have been determined by adding the known band gap values for Sb_2Se_3 and Sb_2O_3 of 1.18 eV and 4 eV.

6.3.4 Discussion

While the two VBO values determined for the native oxide on Sb_2Se_3 crystal and the evaporated Sb_2O_3 on Sb_2Se_3 film are consistent with each other, there are several possible reasons for any small differences. These include how the native oxide forms on the surface, which occurs under very different conditions from a thermally evaporated film, and has been shown to be accompanied by elemental selenium at the surface (equation 6.3) [115]. Additionally, the crystal surface studied is made up of only one crystal orientation, whereas the polycrystalline film's surface includes multiple different orientations [57, 62, 81]. Ultimately, however, the two results can be considered consistent with each other taking into account the uncertainty on the values, which was taken as the standard deviation in the calculated values (0.13 eV) for the Kraut method results and as 0.14 eV for the subtraction method (determined from the uncertainty in the linear extrapolation of the valence band onsets).

$$2\,Sb_2Se_3 + 3\,O_2 \longrightarrow 2\,Sb_2O_3 + 3\,Se_2 \tag{6.3}$$

These results have implications for Sb_2Se_3's use as a PV material due to the great difficulty in avoiding Sb_2O_3 formation at the back surface, as reported by Fleck *et al.* [115]. The presence of Sb_2O_3 between the Sb_2Se_3 layer and the back contact had a significant effect on the degree of 'rollover' (a feature in J-V curves indicative of a back contact potential barrier) in Sb_2Se_3 solar cells and the formation of Ohmic contacts. Attempts to remove this Sb_2O_3 contamination have also been shown to have mixed effects on the performance of the PV devices, as discussed in Part 1 of this chapter [37, 38]. Fleck *et al.* also attempted to replicate the effects of Sb_2O_3 contamination by depositing ultra-thin films of Sb_2O_3 onto the back contact via thermal evaporation. They reported that a thin layer of Sb_2O_3 could suppress recombination at the interface between Sb_2Se_3 and Au provided the holes could tunnel through the Sb_2O_3 layer. Thicker layers of Sb_2O_3, even up to 5 nm, were found to be detrimental to device performance. This is supported by the conclusions of this work, which shows that any significant thickness of Sb_2O_3 would provide a significant barrier to hole transport through the back contact due to the magnitude of the negative VBO.

The significant offset between the two valence bands can be explained by looking in greater detail at the valence orbital density of states for the two materials. Antimony chalcogenides are known to exhibit strong cation s - anion p orbital mixing, leading to the existence of a stereochemically-active lone pair of electrons at the valence band edge [51, 212]. The mixing of the cation s states with the anion p states results in the formation of bonding and anti-bonding states. The anti-bonding states in turn hybridise with the cation p orbitals to form bonding and anti-bonding states that make up the edges of the valence and conduction bands respectively. The configuration energies of the anion p-orbitals therefore play a significant role in determining the position of the valence band maximum on an absolute energy scale and this has been shown to result in a lower ionisation potential in materials containing these lone pairs compared to those without. Both Sb_2Se_3 and Sb_2O_3 are predicted to undergo this lone pair formation (experimentally evidenced for Sb_2Se_3 in Chapter 5 and by Don *et al.* [212]) but, as shown in Figure 5.1b, there is a significant 'jump' in the orbital energies when going from sulphur to oxygen in the chalcogenide series, with the selenium orbital energies being similar to those of sulphur [221]. The valence band of Sb_2O_3 would therefore be expected to sit significantly lower (or have a higher ionisation potential) than that of Sb_2Se_3, as seen experimentally in this work.

6.4 Conclusion

This study aimed primarily to clarify the impact of two chemical etches both on the surface chemistry of Sb_2Se_3 and on the performance characteristics of Sb_2Se_3 solar cells. A particular focus was put on the linking of these two approaches, as is seldom done, as well as filling in the gaps and clarifying the inconsistencies in the existing literature. The films used for structural and surface chemistry analysis were again identical to the films used in the devices, and the devices made were of high quality. These factors were all

deliberately ensured so that this study was as relevant to device fabrication as possible. The etching processes used were identical to the procedure laid out by Wang *et al.* and Chen *et al.* [38, 39]

The XRD patterns from the three films showed minimal difference, as did the SEM analysis. This result was expected if the existing literature was to be believed. However it was important to show beyond doubt that the improvements to the device performance were not a result of some recrystallisation, grain boundary modification or even of some unintentional additional deposition onto the back contact by the etches.

XPS analysis was central to the study in understanding how the introduction of a chemical etchant at the back contact affected the chemical environment. It was lent further importance because the conclusions drawn in the existing literature relied on XPS analysis, in which there were inconsistencies and gaps in the work presented that this study aimed to clarify [38, 39]. In order to ensure as consistent and relevant a study as possible, great care was taken to keep all samples identical, exposed to ambient conditions for the same amount of time and the data fitted to be consistent across all samples. The results supported some of the claims made previously, but also disproved others. It was found that the etches were indeed effective in removing Sb_2O_3 contamination from the back contact and that the $(NH_4)_2S$ was marginally more effective in doing so. On the other hand, there was no evidence of elemental Se being removed from the back contact, at least not preferentially. In fact, the $(NH_4)_2S$ left a higher percentage of elemental Se at the back contact then the unetched control sample, signifying that it was more effective in removing Sb_2Se_3 than Se.

As important to this study as the XPS analysis were the device performance characteristics. In the work in which these etches were proposed, only the FF was shown to improve, with other important quantities such as V_{oc} and J_{sc} not shown [38, 39]. In this work, it was found that for the best devices, this improvement in FF was replicated, along with a lowering of the R_s. J-V-T analysis showed a reduced back contact barrier, fitting in well with the reduced R_s. However these were counteracted by a significant drop in J_{sc} and R_{sh} (particularly in the $(NH_4)_2S$-etched sample), which lead to the overall efficiency of the devices being lowered by etching. EQE measurements showed that this lowering in J_{sc} was uniform across the light spectrum, indicating that it was not a result of a more fundamental change in the quality of the absorber. The lowered R_{sh} indicated an increase in shunting that tied in well with the hypothesis that the etches (in particular the $(NH_4)_2S$ etch) were etching Sb_2Se_3 as well as the contaminants.

The overall conclusion of the work therefore, was that the effect of the etches was more nuanced than initially suggested by Wang *et al.* and Chen *et al.* [38, 39]. The removal of contaminants at the back contact does reduce the series resistance, however the etches can also damage the Sb_2Se_3 film itself, meaning that for films with a low level of contamination the etches do more harm than good. This conclusion was strengthened by

the use of a much more dilute $(NH_4)_2S$ etch that ultimately led to an improved device performance from 5.70 to 6.63%.

These conclusions led to further work within the group to investigate the nuanced role of Sb_2O_3 at the back contact of Sb_2Se_3 solar cells and to investigate why some evidence suggested that some level of surface oxidation was in fact beneficial to device performance. Following the discovery of the beneficial effects of an electron reflection barrier caused by the Sb_2O_3 layer at the back contact it was decided to pursue the topic further by measuring quantitatively the band alignment between Sb_2Se_3 and Sb_2O_3.

By measuring the valence band difference spectrum of cleaved and uncleaved Sb_2Se_3 bulk crystals an alignment could be found between the Sb_2Se_3 contamination and the pristine Sb_2Se_3 crystal. The significant conduction band offset confirmed the expected electron reflection barrier, while the large valence band offset indicated that there would be a barrier to holes unless the layer was thin enough for them to tunnel through. The result was compared to the band alignment between Sb_2Se_3 and Sb_2O_3 thin films measured using the Kraut method and the two results were found to be consistent, validating the result obtained from the novel technique of using the difference spectrum. The origin of the large valence band offset was also discussed. As studied in Chapter 5, the p orbital energies of the chalcogenide series are known to play a prominent role in determining the ionisation potentials of the materials in the series. The large jump in orbital energies going from O to S & Se accounts for such a large valence band offset.

The two parts of this chapter show the beginning and end points of a continuous study over a number of years to better understand the effects of surface contamination on the performance of Sb_2Se_3 back contacts. Given the difficulty in avoiding this oxidation of the Sb_2Se_3 surface, a proper understanding of the effects is crucial for optimising the device fabrication process.

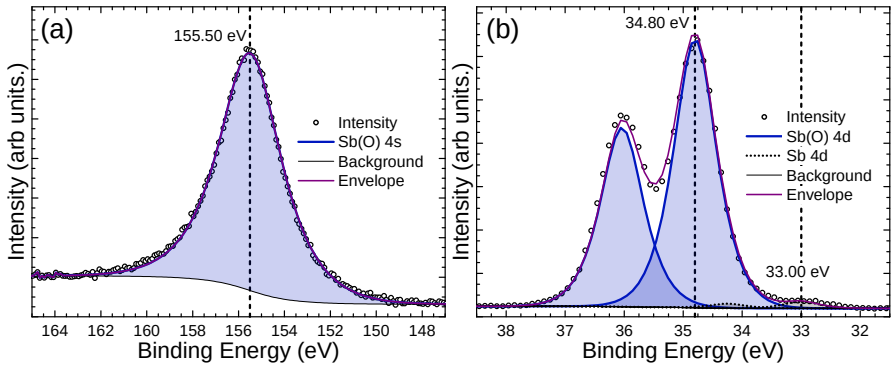

Figure 6.16 Core level spectra of (a) Sb 4s and (b) Sb 4d for the Sb_2O_3 thin film.

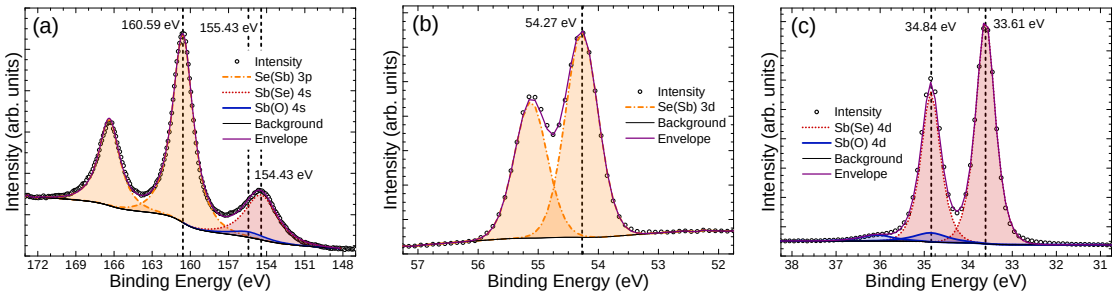

Figure 6.17 Core level spectra of (a) Se 3p & Sb 4s (b) Se 3d and (c) Sb 4d for the Sb_2Se_3 thin film.

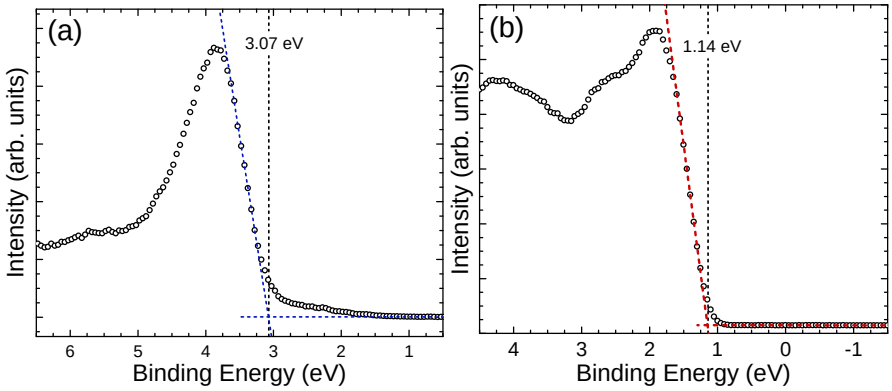

Figure 6.18 Valence band spectra of (a) Sb_2O_3 and (b) Sb_2Se_3 thin films.

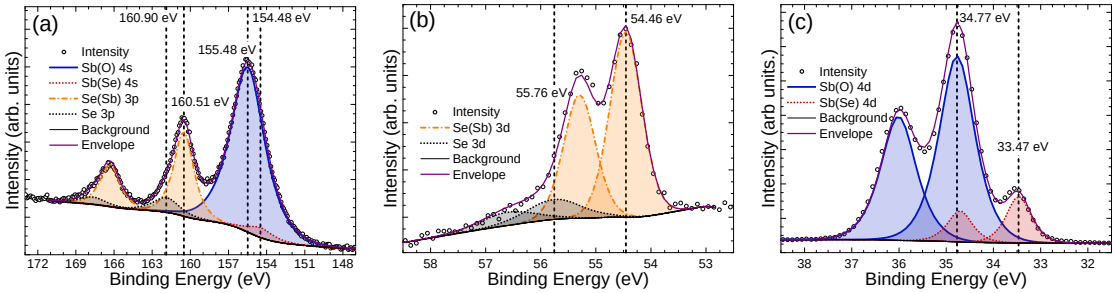

Figure 6.19 Core level spectra of (a) Se 3p & Sb 4s (b) Se 3d and (c) Sb 4d for the interfacial Sb_2O_3/Sb_2Se_3 film.

Sample	Peak	Energy (eV)
Sb_2Se_3 Film	Sb(Se) $3d_{5/2}$	529.68
	Se(Sb) $3p_{3/2}$	160.59
	Se(Sb) $3d_{5/2}$	54.27
	Sb(Se) $4d_{5/2}$	33.61
	VB	1.14
Sb_2O_3 Film	O(Sb) 1s	531.21
	Sb(O) $3d_{5/2}$	530.88
	Sb(O) 4s	155.49
	Sb(O) $4d_{5/2}$	34.80
	VB	3.07
Sb_2O_3/Sb_2Se_3	O(Sb) 1s	531.07
	Sb(O) $3d_{5/2}$	530.77
	Sb(Se) $3d_{5/2}$	529.93
	Se(Sb) $3p_{3/2}$	160.51
	Sb(O) 4s	155.48
	Se(Sb) $3d_{5/2}$	54.46
	Sb(O) $4d_{5/2}$	34.77
	Sb(Se) $4d_{5/2}$	33.47

Table 6.7 Peak positions of core levels measured for use in the Kraut method calculations.

Chapter Seven

Conclusions & Future Work

7.1 Summary of Research Outcomes

The aim of this project was to develop an understanding of the role band alignments play in the performance of Sb_2Se_3 solar cells. The terms 'band alignments' covers a wide range of properties and interfaces within a solar cell. In this work a number of different quantities have been investigated relating to the band alignments of the Sb_2Se_3 absorber layer. In Chapter 4, the crucial band alignment between the Sb_2Se_3 absorber and the window layer was investigated for both CdS and TiO_2. This band alignment was measured via two different methods and the differences in the results discussed. In Chapter 5, the fundamental electronic properties and band structure of Sb_2Se_3 was investigated, along with the effects of different dopants, and conductivity types on the electronic properties. Finally, in Chapter 6, the back contact of the Sb_2Se_3 absorber prior to Au deposition was rigorously measured, both chemically, in terms of contamination, and electronically, in terms of work function and band alignments. This work, therefore, covers the band alignments of Sb_2Se_3 from front contact to bulk material and to back contact within the device structure.

The secondary priority in this work was to maintain a constant dialogue between the fundamental properties measured using photoemission techniques (often used in isolation) and the performance characteristic of Sb_2Se_3 solar cells. To carry out detailed photoemission measurements on samples that are subject to the sometimes complex processes of device optimisation is not straightforward, and understanding how the results of photoemission experiments can be applied to systems as complex as a full solar cell is likewise non-trivial. Where possible during this work, the results of the photoemission characterisation have been linked to device performance characteristics. The understanding of both Sb_2Se_3 solar cells and Sb_2Se_3 as a material has continually developed over the time-frame of this project and has in many cases been influenced by the work included herein.

7.1.1 Heterojunction Band Alignments

In Chapter 4, the band alignments between Sb_2Se_3 and CdS and between Sb_2Se_3 and TiO_2 were investigated. The natural band alignments of CdS, TiO_2 and Sb_2Se_3 were measured using XPS and, using Anderson's rule, the band alignments were predicted. These band alignments predicted a small spike-like offset in both the case of Sb_2Se_3 with CdS and Sb_2Se_3 with TiO_2. However, Anderson's method for predicting band alignments does not take into account certain effects such as charge transfer and so the band offsets were directly measured using HAXPES and the Kraut method used for calculating the valence band offset. HAXPES was used to overcome the challenges of growing the ultra-thin films required to carry out the Kraut method with conventional Al Kα XPS, by increasing the probing depth of the measurement and allowing for thicker films of Sb_2Se_3 to be used. The result of the Kraut method measurements showed an almost flat alignment between Sb_2Se_3 and CdS, consistent with the result of Anderson's rule, whereas the band offset between Sb_2Se_3 and TiO_2 was cliff-like. This difference is attributed to the much greater difference in electronegativity between Sb_2Se_3 and TiO_2 than between Sb_2Se_3 and CdS.

The implications of these results are important to the development of Sb_2Se_3 solar cells due to the other factors in achieving a good heterojunction. The band alignment between CdS and Sb_2Se_3 was superior to that of Sb_2Se_3 and TiO_2. However, in many cases (including within this group), TiO_2 based devices perform better due to the deleterious intermixing at Sb_2Se_3-CdS interfaces. This intermixing is somewhat specific to deposition techniques such as CSS that operate at high temperatures, but these depositions techniques are also the ones achieving the best efficiencies currently (see section 2.2.2). Meanwhile, the band alignment of Sb_2Se_3 with TiO_2 is sub-optimal and therefore future work should seek to find a better solution.

7.1.2 Fundamental Electronic Properties

In Chapter 5, in-depth photoemission analysis was used to investigate some of the fundamental electronic properties of Sb_2Se_3 bulk crystals. The use of *in situ* cleaving/exfoliating, multiple different photon energies and DFT calculations allowed for certain properties to be understood well beyond what has previously been achieved. In the first part, a bulk crystal, cleaved *in situ* was measured using HAXPES and XPS and the valence band spectra aligned to DFT calculated density of states. The different cross sections of different orbitals under different photoemission photon energies allowed the contribution of the Sb 5s lone pair of electrons to the valence band density of states to be experimentally observed for the first time, validating the hypothesis that Sb_2Se_3 possesses a stereochemically active lone pair, as laid out in the revised lone pair model [51]. The implications of this lone pair were shown by comparing the ionisation potential of Sb_2Se_3 (measured using XPS) compared to that of other similar chalcogenide materials, some possessing lone pairs and others not. This comparison illustrated how the presence of a lone pair of electrons at the valence band edge reduces the ionisation potential,

playing a significant role in the natural band alignments of Sb_2Se_3.

The second part of Chapter 5 looked at the effects of extrinsic doping on the electronic properties of Sb_2Se_3. The understanding of the role of impurities in determining the conductivity of Sb_2Se_3 developed significantly over the period of this project, with the photoemission results in this thesis playing a key role in developing the understanding. The valence band of bulk crystals, cleaved or exfoliated *in situ* were measured using three different photoemission techniques (UPS, XPS and HAXPES) of varying surface sensitivity. The energy separation between valence band and Fermi level was in itself informative on the position of the Fermi level within the band gap (and therefore the carrier density of the material). By solving Poisson's equation to match the depth profile of this valence band energy, further insight was obtained into the surface space charge layers and the bulk carrier density. The results showed Cl doping to result in n-type Sb_2Se_3 with a bulk electron density of $\sim 10^{17}$-10^{18} cm^{-3}, whereas Sn doping resulted in p-type Sb_2Se_3 with a bulk hole density of $\sim 10^{16}$-10^{17} cm^{-3}. The n-type Sb_2Se_3 showed a surface electron depletion layer, whereas the p-type crystal presented weak inversion at the surface.

7.1.3 Back Contact Contamination

The examination of the back contact contamination and its effect on the performance of Sb_2Se_3 solar cells was a study that spanned the entirety of this project and made up both the first and last publications finished within that time. The first part of Chapter 6 studies the effect of two back contact chemical etches on the performance of Sb_2Se_3 solar cells. This work was motivated by contradictory reports in the literature and sought to clarify both the impact on device performance and the changes in surface chemical composition when the $(NH_4)_2S$ and CS_2 etches were applied to Sb_2Se_3 prior to Au back contact deposition. The central result was that both etches were effective in removing Sb_2O_3 contamination but that neither removed Se (as previously reported [39]). Furthermore, the effect on device performance was not straightforward. While reducing the back contact barrier (as measured by J-V-T), the resulting improvement (reduction) in series resistance was balanced by a decrease in shunt resistance, meaning that device performance was in fact poorer following etching. It was concluded that the removal of Sb_2O_3 was beneficial as long as the original layer of contamination was relatively thick, but that the etches' damage to the underlying Sb_2Se_3 layer proved more harm than good if the level of contamination was low.

On the back of this study, more work was carried out (outside the scope of this thesis [115]) showing that the initial growth of Sb_2O_3 contamination at the back contact in fact led to a slight improvement in device performance over completely fresh surfaces. This was due to improved band alignments at the back contact due to a reduction in the work function of the Sb_2Se_3 surface upon oxidation. However, thicker layers of Sb_2O_3 led to a reduced efficiency as a result of increased series resistance. Following this study, the second part of Chapter 6 measured the band alignment between Sb_2Se_3 and this

contaminant layer. Once again making use of bulk crystals cleaved *in situ*, the difference spectrum between the valence bands of the contaminated and cleaved crystal was used to measure the band alignment between the contaminated surface and the pristine Sb_2Se_3 surface. This showed a straddling alignment between the two with a VBO of -1.72 eV. This was supported by Kraut method measurements of the VBO between a CSS Sb_2Se_3 film and a thermally evaporated Sb_2O_3 film as -1.90 eV.

7.2 Suggestions for Future Work

7.2.1 Heterojunction Band Alignments

The evidence that the band alignment between Sb_2Se_3 and CdS is far better than that between Sb_2Se_3 and TiO_2 suggests the need to find a solution to the intermixing that is so harmful to CSS-Sb_2Se_3-on-CdS devices. As mentioned in Chapter 4, the current record efficiency in Sb_2Se_3 photovoltaics is held by a cell that utilised an ultra-thin TiO_2 layer (deposited by ALD) between the Sb_2Se_3 and CdS layers. While many other differences exist between said device and those made at Liverpool, it is surely an avenue worth exploring. ALD layers of TiO_2 and Al_2O_3 were briefly experimented with during this project, but were not pursued to great lengths due to the need to potentially alter then entire deposition process to accommodate the different growth dynamics of Sb_2Se_3 on such a different substrate. However, the use of ultra-thin buffer layers between Sb_2Se_3 and CdS could prove incredibly beneficial if these layers can be incorporated properly into the current device structure.

Other options include attempting to find another window layer with similar band alignments and performance to CdS but without such a tendency to intermix with Sb_2Se_3. A few have been tried (as discussed in section 2.2.2) but very few (if any) have been subject to the level of optimisation that CdS and TiO_2 have benefited from. This is in large part due to the wealth of research already carried out on CdS and TiO_2 as window layers in other solar cell technologies, meaning that they are very well understood and the fabrication process optimised. However, given the evidence that neither CdS or TiO_2 is an ideal window layer it may be worth pursuing alternative window layers such as the tuneable magnesium zinc oxide recently incorporated into CdTe solar cells [106].

7.2.2 Fundamental Electronic Properties

Extrinsic doping of Sb_2Se_3 could become a key avenue of research in optimising Sb_2Se_3 solar cells. Currently, many groups utilise different deposition methods and different source materials (i.e. sputtering targets, solutions, source material for CSS or evaporation) The extrinsic dopant present in these varying sources could lead to drastic differences in device performance and the optimum cell structure. At Liverpool, Sb_2Se_3 solar cells had been optimised for over 3 years before the discovery of unintentional Cl contamination in the purchased source material. The revelation that the FTO/TiO_2/Sb_2Se_3/Au device

structure was in fact forming an n-n^+ junction meant having to adjust our entire perception of what was the best way to improve the devices. However, the fabrication of bulk crystals with controlled Sn doping highlighted a way forward with controlled doping of the source material.

It seems inevitable that at some point, the optimum dopant, doping type, and doping concentration for Sb_2Se_3 will have to be identified. Before this is done, optimisation of the rest of the device structure could quite likely be aiming at a moving set of goalposts, with different studies and different groups working with different conductivities and by extension different band alignments in their Sb_2Se_3. While Sn has been used in this work as a p-type dopant, there are many other available elements that could be trialled. The use of a p-type layer, optimally doped could increase the performance of the current device structure used in Liverpool significantly. Furthermore, the Cl doped crystals studied in this work were fabricated from the same purchased source material as used in the high efficiency devices. The level of Cl in this source material is not controlled by us and comes with no guarantee of consistency from the manufacturer (given that it is not advertised as containing Cl). It may be that Sb_2Se_3 can reach far higher carrier densities with n-type doping but it is far from certain that the level of Cl currently being used is optimal. Controlled n-type doping of Sb_2Se_3 should therefore also be researched.

7.2.3 Back Contact Contamination

Through the course of this work, the role of surface contamination on the back contact performance of Sb_2Se_3 has been made reasonably clear. However, it has highlighted that there is an opportunity for significant optimisation through back contact engineering. The effects of the surface oxidation are beneficial to device performance but only if limited to a certain amount. Any over-oxidation has been shown to harm device performance [115]. It would be beneficial, therefore, to develop a process to replicate this effect but in a controlled way. This could be with a surface treatment (such as chemical etching) or through the deposition of an intermediate layer. Fleck *et al.* attempted to reproduce the effects by evaporating thin films of Sb_2O_3 onto the back surface, with limited success. Many other hole transport layers have also been utilised in certain studies (as discussed in section 2.2.2), but none have yet seen widespread use. However, it is clear that, similarly to CdTe, Sb_2Se_3 has a high work function and therefore surface treatments or transport layers will likely be an integral part of the optimisation of device structure going forwards.

APPENDIX

Appendix A - Semiconductor Statistics

A1 Semiconductor Statistics

To understand how Poisson's equation can be solved to model the surface space charge layers in semiconductors (as in Chapter 5), one must first understand how semiconductor band structures and carrier statistics can be approximated. This appendix will provide a brief introduction to these concepts, building on the basic understanding of electronic band structure in semiconductors outlined in section 2.1.1.

The electronic properties of a semiconductor are governed largely by the Fermi level, and the electrons occupying the band edges. The behaviour of electrons in a many-body system is given by the solution to the many-body Schrödinger equation:

$$\mathrm{H}\Psi = \mathrm{E}\Psi \tag{A1}$$

where H is the Hamiltonian, ψ is the eigenfunction of H and E is the eigenvalue. However, the complexity of the many-body problem, arising from electrons interacting with both ions and other electrons means that a number of approximations are employed to simplify the computation of these energy states. These approximations are outlined in brief here and discussed in more detail elsewhere [195].

- **Born-Oppenheimer (Adiabatic) Approximation**: This approximation assumes that, given the very high masses of the ions relative to the electrons, the ions can be considered stationary in the electrons' frame of reference. The electrons therefore see an overall time-averaged adiabatic potential.
- **One-Electron Approximation**: This assumes that each independent electron-electron interaction can be averaged into a constant repulsive component in the Hamiltonian.
- **Mean-Field Approximation**: This approximation addresses the fluctuating positions of the ions by assuming that every electron experiences an identical average potential.

With these approximations, equation A1 can be written as:

$$\left(\frac{\boldsymbol{P}^2}{2m_0} + \mathrm{V}(\boldsymbol{r})\right)\phi_n(\boldsymbol{r}) = E_n\phi_n(\boldsymbol{r}) \tag{A2}$$

where $\phi_n(\boldsymbol{r})$ and E_n are the wavefunction and energy of an electron in the eigenstate n, $\boldsymbol{P}$ is the momentum operator, m_0 is the electron mass and $\mathrm{V}(\boldsymbol{r})$ is the periodic potential of the lattice. The eigenstates in equation A2, $\phi_n(\boldsymbol{r})$, will have the form of a Bloch wavefunction:

$$\phi_{nk}(\boldsymbol{r}) = u_{nk}(\boldsymbol{r})exp(i\boldsymbol{k}.\boldsymbol{r}) \tag{A3}$$

where $\boldsymbol{k}$ is the wavevector of the electron in the first Brillouin zone. The Bloch wavefunctions have the same periodicity as the lattice so that:

$$u_{nk}(\boldsymbol{r} + \boldsymbol{R}) = u_{nk}(\boldsymbol{r}) \tag{A4}$$

While the solution to equation A2 is incredibly complex for the entire Brillouin zone, the band extrema are by far the most relevant to the electronic properties of a material, as these are the first to be filled or vacated during carrier transport. The band extrema can be simplified somewhat further: in most semiconductors, about the high symmetry points (such as the Γ point) the band dispersion can be approximated closely by a parabolic function, expanded as a Taylor series from the dispersion relation about the high-symmetry point. The simplest form of the dispersion relation for states about the band extrema is:

$$E_{e,h}(k) = E_{e,h}(0) \pm \frac{\hbar^2k^2}{2m^*} \tag{A5}$$

where $E_{e,h}(0)$ is the zero energy of the band, $\hbar$ is the reduced Planck constant and m^* is the carrier effective mass. This parabolic relation is reasonably accurate very near the band extrema or in very wide band gap semiconductors where there is no interaction between the valence and conduction band states. However, in narrow band gap semiconductors, inter-band transitions are more common and the bands take on a degree of non-parabolicity. This effect is accounted for by including a $\boldsymbol{k.p}$ perturbation in the Schrödinger equation, as demonstrated by Kane [222]. This approach adds first and second order perturbations to the Hamiltonian as well as a perturbation for spin-orbit splitting. A detailed breakdown of this approach can be found in other works [195, 223]. However the solution to this model remains non-trivial and so additional simplifications can be introduced for a case where the energy eigenvalues and the spin-orbit splitting are small relative to the band gap. The dispersion relation can be simplified, and is known as the alpha, α-approximation:

$$E(1 + \alpha E) = \frac{\hbar^2k^2}{2m_0^*} \tag{A6}$$

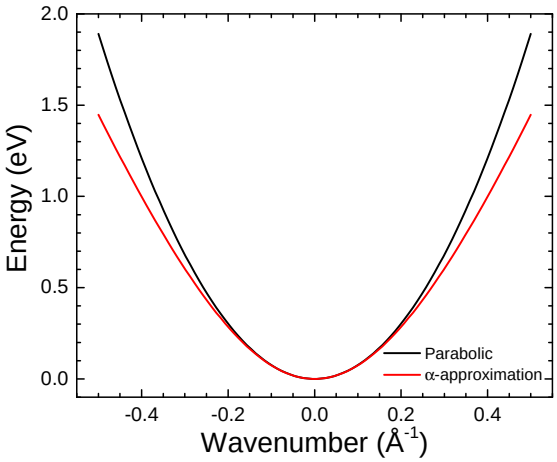

Figure A1 Dispersion of the conduction band in a narrow band gap semiconductor as calculated using the parabolic band approximation (black) and the α-approximation (red).

where $\alpha = (1/E_g)\,(1 - m^*/m_0)^2$, m^* is the carrier effective mass and m_0 is the electron mass. The differences between the simple parabolic band model and the α-approximation can be visualised by plotting the band dispersion of the conduction band, as shown in Figure A1. This band dispersion was calculated for the case of Sb_2Se_3, with a band gap of 1.18 eV and an effective mass of $0.5m_e$ (the average conduction band effective mass). The α-approximation produces a much more disperse band edge than the parabolic band model. The impact of this can be seen in Figures A2 & A3. The wider band edge in the α-approximation leads to an increase in the density of states nearer the band edge and in turn, higher carrier densities at lower Fermi level energies.

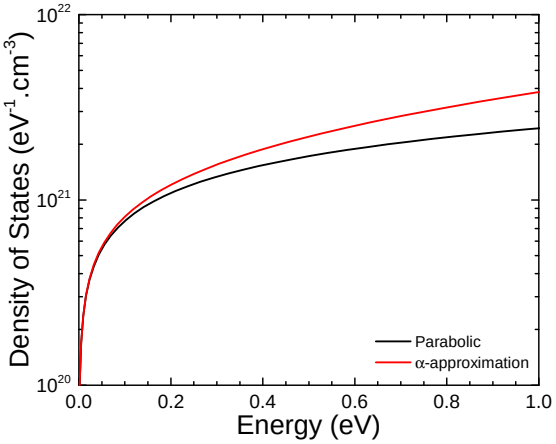

Figure A2 Density of states as a function of energy above the conduction band minimum in a narrow band gap semiconductor as calculated using the parabolic band approximation (black) and the α-approximation (red).

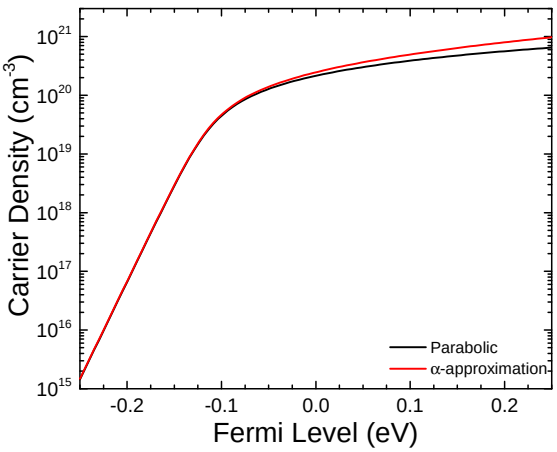

Figure A3 Carrier density as a function of the position of the Fermi level above the conduction band minimum in a narrow band gap semiconductor as calculated using the parabolic band approximation (black) and the α-approximation (red).

Appendix B - Python Code for Solving Poisson's Equation

The code was divided into three subroutines and one main code. The three subroutines were used to calculate the bulk carrier density, calculate the right hand side of Poisson's equation for a given potential and gradient, and to calculate the band bending with increasing depth into the material, while the main code carried out the interval bisection. In this section, these four parts of the code will be described. All code used for the project is included in Appendix B.

B1 Code Method

B1.1 Calculating Bulk Carrier Density, $f_n(x)$

This function, $f_n(x)$, calculates the bulk carrier density in a material with a given band gap, E_g, Fermi level energy, E_F and carrier effective mass, m_e^*, at a given temperature, T using equation B1.

$$\mathrm{n} = \sum_{E_C}^{E_\infty} f\left(E\right) \times g_C\left(E\right) \times dE \tag{B1}$$

B1.2 Solving Poisson's Equation, $f_U(x)$

A function, $f_U(x)$, was created in Python to calculate the left-hand side of Poisson's equation using the modified Thomas-Fermi approximation. This function requires user input values for the band gap, E_g, Fermi level energy, E_F and carrier effective mass, m_e^*, at a given temperature, T, the same as $f_n(x)$. Additional inputs were required for the static dielectric constant, ϵ_z, the depth, z (in m), and the potential, $V(z)$ (in meV).

B1.3 Plotting band bending, $f_P(x)$

From experimental data a reasonably good approximation/guess can be obtained for the potential at the surface (i.e. the amount of band bending). This therefore gives us a good guess for the potential, $V(z)$, at zero depth, $V(0)$. It is also given naturally that $V(\infty) = 0$. The third subroutine function, $f_P(x)$ plots the band bending from the surface to a given depth, z, that is assumed will be beyond the surface space-charge region, given certain user-defined values for $V(0)$ and the initial gradient $\frac{dV}{dz}$, henceforth referred to as U.

To track the band bending into the material a 'for' loop was used with each loop taking a step further into the material. This step size, δz, was set to 0.5 Å. At the first 0.5 Å step from the surface the potential can be calculated according to:

$$V(z_i) = V(z_{i-1}) + U(z_{i-1}) \tag{B2}$$

where i represents the step and $U(z_{i-1})$ in the case of the first step is a user defined initial guess. For subsequent steps, however, the gradient must be calculated according to the MTFA. For each iteration the left hand side of Poisson's equation (which gives the change in gradient of the potential) is obtained by calling on $f_U(x)$ to solve Poisson's equation for $\frac{d^2V(z_i)}{dz^2}$, henceforth referred to as $\frac{dU(z_i)}{dz}$. This can then be used to calculate $U(z_i)$ and at this point it is also prudent to determine $n(z_i)$ for later use.

$$U(z_i) = U(z_{i-1}) + \frac{dU(z_{i-1})}{dz} \tag{B3}$$

$$n(z_i) = N_d^+ - \frac{\epsilon_z}{C}\,\frac{dU(z_i)}{dz} \tag{B4}$$

There are certain conditions that can be placed on the curve to ensure that the code is working towards a physical result. Firstly, it can be assumed that the potential $V(z)$ would not change sign, and that the bands bend gradually towards the bulk band positions. Similarly, it can be safely assumed that the gradient of the band bending, $U(z)$ would not change sign either. These conditions are used in the main code to perform an interval bisection (see below).

A flowchart has been included to depict the logic used by the $f_P(x)$ function to plot the band bending and detect any discrepancies from the expected result. Key to the loop is the options to break if one of the aforementioned conditions is satisfied. Should the potential or the potential gradient change sign (the conditions in the flowchart are for the case of depletion layers in n-type material) the loop will break and a value for P will be returned from the function indicating which condition was met. Unless either of these conditions is met the loop will continue to iterate for steps deeper and deeper into the material until the maximum depth is reached.

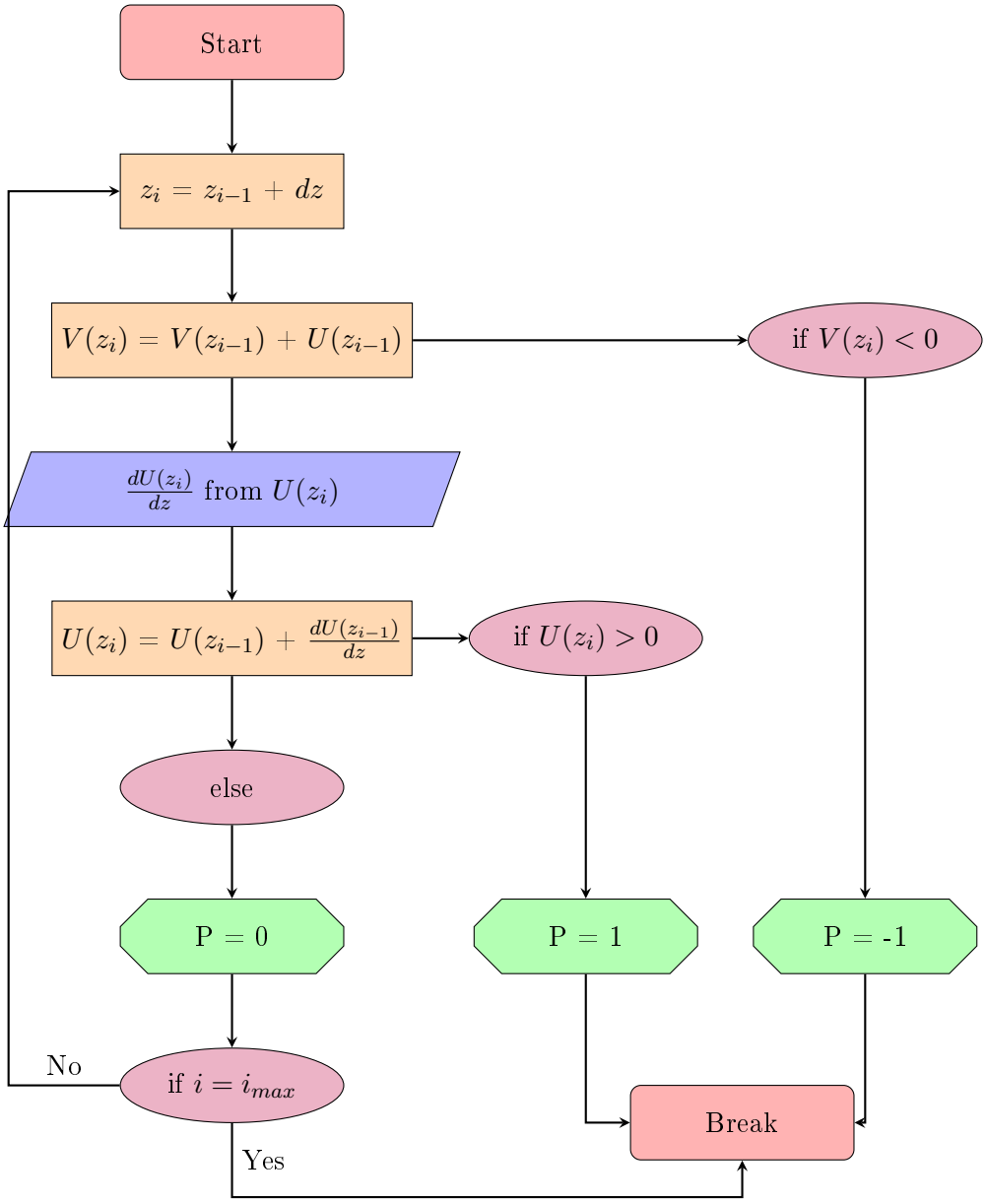
Start
$z_i = z_{i-1} + dz$
$V(z_i) = V(z_{i-1}) + U(z_{i-1})$
if $V(z_i) < 0$
$\frac{dU(z_i)}{dz}$ from $U(z_i)$
$U(z_i) = U(z_{i-1}) + \frac{dU(z_{i-1})}{dz}$
if $U(z_i) > 0$
else
P = 0
P = 1
P = -1
No
if $i = i_{max}$
Break
Yes

B1.4 Main Code

The main code for modelling the band bending in the space-charge region relies chiefly on an interval bisection. This works by specifying an upper and lower limit to the initial guess of the potential gradient. Based on the result/feedback of an attempt to plot the band bending using the middle point of these two limits the attempted gradient will replace the upper or lower limit for the next iteration. In this way the code should converge on a potential gradient value that will not break the conditions set in the plotting function (see above).

Being the master function, this script first requires that all relevant constant and user defined variable be defined for all the functions. These include the case specific but fixed variables; the band gap, E_g, Fermi level, E_F, effective mass, M_e^*, low frequency dielectric constant, ϵ_z and temperature, T. The bulk carrier density, N_d^+, is also calculated by calling the carrier density function, $f_n(x)$. It is also possible to enter the desired depth into the material over which the band bending will be plotted.

Setting up the initial parameters of the interval bisection is also done at the beginning of the script. Firstly J_{max}, the maximum number of attempts to find the correct band bending, was set to a generous but not impractical value of 500. $V(0)$ could be guessed with reasonable accuracy by following the trajectory of the photoemission results plotted with respect to depth. The gradient upper and lower limit, $U_{max}(0)$ and $U_{min}(0)$, can be set reasonably broadly (the interval bisection will narrow it rapidly at the beginning) but not so wide as to waste time. In this case they were set to $U_{max}(0) = -1\times10^{10}$ and $U_{min}(0) = -1\times10^{6}$. To check that the initial gradients straddle the correct result a simple test is carried out to ensure that one of gradients is too steep and the other not steep enough. The outputs from the band bending function, $f_P(x)$, are set to be $+1$ if the potential changes sign (i.e. the initial gradient is too steep) and -1 if the gradient changes sign (i.e. the gradient is not steep enough). Therefore the product of the output from this function for the upper (P_{max}) and lower (P_{min})limit should equal -1 if the desired outcome is achieved. Conversely, if both the upper and lower limit result in the bands bending back on themselves or crossing the bulk band energy, the product of P_{max} and P_{min} will be $+1$. If this is the case the code will abort and instruct the user to enter new values for U_{max} and U_{min}. A flowchart is included below depicting the processes and logics of the main code while carrying out the interval bisection.

Having defined all necessary parameters the program will converge on the best initial gradient for plotting the band bending so that it reaches a flat plateau. An extra constraint is placed on the interval bisection to break once the difference between U_{min} and U_{max} reaches a certain lower limit in order to save wasted time. In some cases it is possible it will fail to find a flat plateau in which case this accuracy can be increased or the depth over which the band bending is plotted increased. It is important to note that while the interval bisection will optimise U_0 for a given set of input parameters, the values for V_0 and E_f are not known for certain. At this stage it is therefore necessary to

make adjustments to these values informed by the photoemission data.

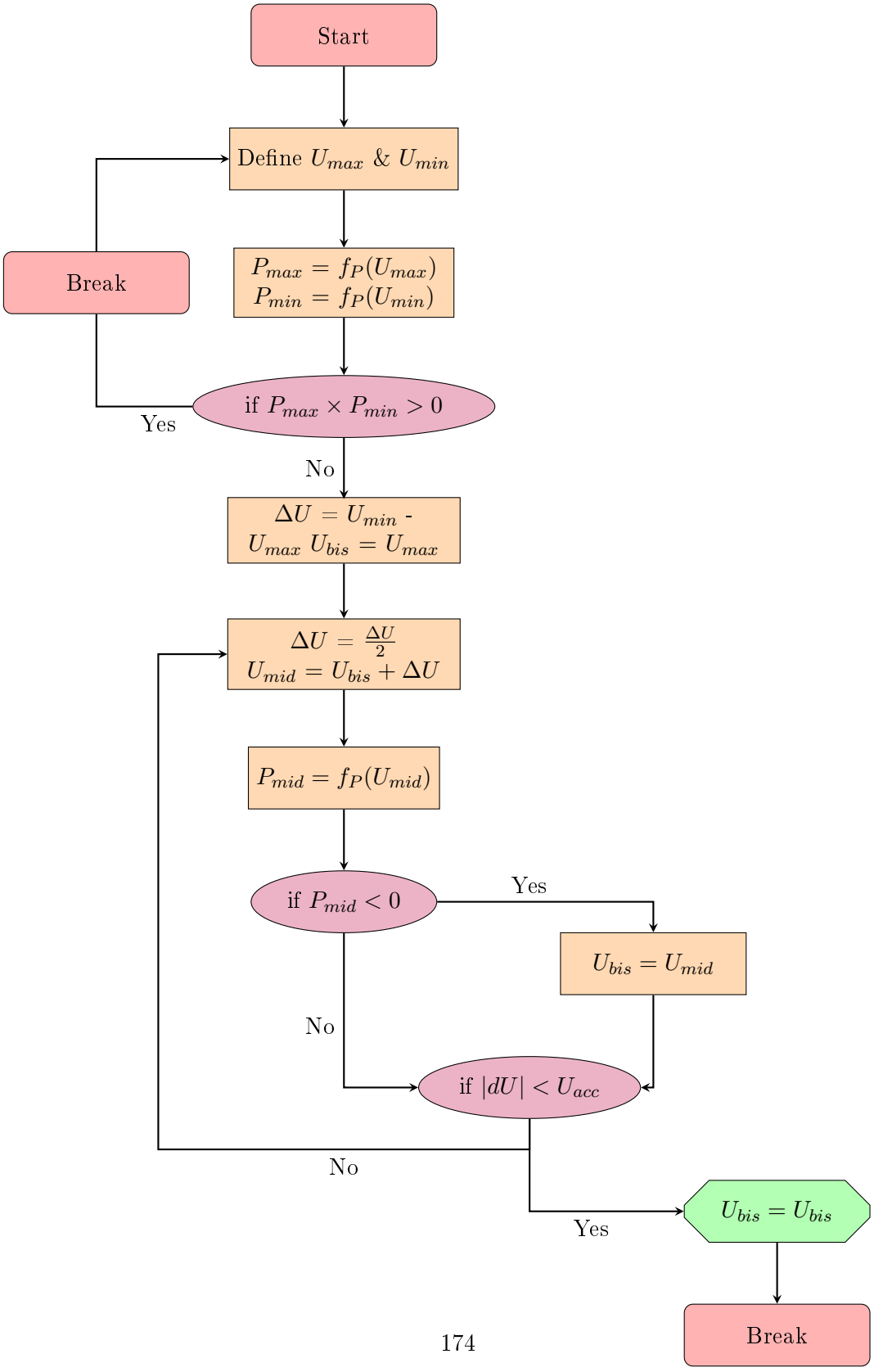
Start
Define U_{max} & U_{min}
Break
$P_{max} = f_P(U_{max})$
$P_{min} = f_P(U_{min})$
if $P_{max} \times P_{min} > 0$
Yes
No
$\Delta U = U_{min}$ -
U_{max} $U_{bis} = U_{max}$
$\Delta U = \frac{\Delta U}{2}$
$U_{mid} = U_{bis} + \Delta U$
$P_{mid} = f_P(U_{mid})$
if $P_{mid} < 0$
Yes
$U_{bis} = U_{mid}$
No
if $|dU| < U_{acc}$
No
Yes
$U_{bis} = U_{bis}$
Break

B2 Python Code - n-type

B2.1 Calculating Bulk Carrier Density, $f_n(x)$

```
def nbulk(Ef,T,m0,epsilon_z,Eg):


    prefac = 2.154E17*(m0**1.5) #prefactors calculated by Tim
    Emax = 2000
    dE=1

    jmax =int(Emax/dE)

    #E = np.zeros([jmax+1])
    #n = np.zeros([jmax+1])
    E = 0.5
    n = 0

    for j in range (0,jmax):

        g = prefac*(E**0.5) #Density of states
        f = 1/(1+np.exp(11.604*(E-Ef)/T)) #Fermi-Dirac function, 11.604 is e/k
        nonpar = 2*np.sqrt((E/Eg)+1)*((E/Eg)+0.5) #non parabolic approximation modifier
        dn = g*f*nonpar*dE #carrier concentration for specified step
        n = n + dn #sum carrier concentration
        E = E + dE #sum energy

    nbulk = n #return carrier concentration in bulk

    return nbulk
```

B2.2 Solving Poisson's Equation, $f_U(x)$

```
    def dUn(Ef,T,m0,Nd,epsilon_z,Eg,Vp,z): #dUp is equivalent to d2V/dt2 (left hand side of p

    # Integration for n at a particular value of V


    prefac = 2.154E17*(m0**1.5)
    Emax = 700
    dE=1
```

```
    jmax = int(Emax/dE)

    E = np.linspace(0.5,700.5,701)
    g = np.zeros([701])
    f = np.zeros([701])
    nonpar = np.zeros([701])
    x = np.zeros([701])
    mtfa = np.zeros([701])
    dn = np.zeros([701])

    n = np.zeros([701])

    L = 210.27E-8/((m0*T)**0.5) #prefactor = hbar/sqrt(m_elec*kB)


    g = prefac*(E**0.5)
    f = 1/(1+np.exp(11.604*(E-Ef+Vp)/T)) #Fermi-Dirac function, 11.604 is e/k
    nonpar = 2*np.sqrt((E/Eg)+1)*((E/Eg)+0.5) #non parabolic approximation modifier
    #x = (2*z/L)*((E*11.604/T)**0.5)*((1+(E/Eg)))**0.5 #x for sinc(x) in mtfa modifier
    #mtfa = 1-((np.sin(x))/x) #modified thomas-fermi approximation using sinc(x)
    dn = g*f*nonpar*dE#mtfa*dE #carrier concentration for specified step to add this it

    for j in range (0,jmax-1):
        n[j+1] = n[j] + dn[j] #sum carrier concentration


    dUn = -(1.8093517E-3/epsilon_z)*(n[jmax-1]-Nd) #Returns dUp. const is e/epsilon0
    #print(dUp)
    return dUn
```

B2.3 Plotting Band Bending, $f_P(x)$

```
    steps = 2000

V = np.zeros([steps+1])
U = np.zeros([steps+1])
dU = np.zeros([steps+1])
nz = np.zeros([steps+1])

def poisson(Ef,Vbb,Ubb,Eg,T,m0,epsilon_z,depth):

    V[0] = Vbb #initial potential
    U[0] = Ubb #initial gradient of band bending
```

```
    Nd = nbulk(Ef,T,m0,epsilon_z,Eg) #return carrier concentration in bulk

    dz = depth/steps  # depth step size. units in cm
    #nss = (5.5268414E2)*epsilon_z*U[0] #surface state density (const is eps0/e)
    z = np.linspace(0,depth,steps+1)
    znm = z*1E7

    dU[0] = dUn(Ef,T,m0,Nd,epsilon_z,Eg,V[0],1E16)
    nz[0] = Nd - ((5.5268414E2*epsilon_z)*dU[0])

    #complicated derivative bit
    for j in range (1,steps+1):
        V[j]= V[j-1] + U[j-1]*dz #potential at given depth
        if (np.abs(Eg-Ef)) > (Eg/2):
            dU[j] = dUn(Ef,T,m0,Nd,epsilon_z,Eg,V[j-1],z[j]) #d2V/dt2 for given step (left ha
        else:
            dU[j] = dUp(Ef,T,Nd,epsilon_z,Eg,V[j-1],z[j])
        U[j] = U[j-1] + dU[j-1]*dz #gradient of potential at given depth
        #if statements for Ef >/< Eg/2
        nz[j] = Nd - ((5.5268414E2*epsilon_z)*dU[j]) #carrier density as a function of depth
        #print('V=',V[zj])
        if V[j]<0: #loop tells main code which way to go for a better solution
           poisson = -1
        elif U[j]>0:
           poisson = 1
        if V[j] > 0 and U[steps] < 0:
            poisson = 0
    #print('V=',V[jmax],' and pmid=',poisson)
    return poisson,znm,V,nz
```

B2.4 Main Code

```
    #main code - solves interval bisection calling nbulk, dUp and poisson

#####Inputs######
T = 300 #temperature
q = 1.6E-19 ##charge
Eg =  1180 #band gap in meV
m0 = 1.135 #effective mass
epsilon_z = 3.5 #static dielectric constant - from Tim
epsilon_inf = 14.3 # #high frequency dielectric constant
Ef = -135 #bulk fermi level wrt conduction band in meV
#Ef = -80 for DOS
```

```
#Ef = -135 for LE
Nd = nbulk(Ef,T,m0,epsilon_z,Eg) #return carrier concentration in bulk
print('Bulk Carrier Density = ',Nd)

depth = 10E-6
####################

jmax = 500 #number of attempts to find best fit

Uacc = 1E-8 #accuracy with which U must be found
Umin = -1E6 #initial min slope guess
Umax = -1.0E10 #initial max slope guess
Vbb = 360 #band bending potential at z=0
#Vbb = 280 for DOS
#Vbb = 360 for LE
p_min = poisson(Ef,Vbb,Umin,Eg,T,m0,epsilon_z,depth) #band bending using Umin
p_max = poisson(Ef,Vbb,Umax,Eg,T,m0,epsilon_z,depth) #band bending using Umax



#print('Pmin=',p_min[0])
#print('Pmax=',p_max[0])

#####Interval bisection#########

#extracts relevant values from poisson subroutine tuple
pp = p_min[0]*p_max[0]


if pp>0:
   print('Error: Utrue must be bracketed by Umin and Umax.') #initial conditions must s
   sys.exit('Error: Utrue must be bracketed by Umin and Umax.')
if p_min[0] < 0: #if pmin doesn't go back on itself pmid will be found from pmin
    Ubis = Umin
    dU = Umax - Umin
else: #if pmin does go back on itself pmid if found from pmax
    Ubis = Umax
    dU = Umin - Umax



for j in range (0,jmax):
    dU = 0.5*dU #Halves for each loop as the separation between pmid and pmin
```

```
    Umid = Ubis + dU #Sets Umid to be the line in between pmin and pmax
    p_mid = poisson(Ef,Vbb,Umid,Eg,T,m0,epsilon_z,depth) #calculates pmid
    pmid = p_mid[0] #picks out poisson value of -1,0,1 from tuple
    if pmid < 0: #if pmid crosses 0 sets as Ubis for next iteration of for loop.
        Ubis = Umid
    if np.abs(dU) < Uacc: #If dU is smaller than required accuracy breaks loop and returns fi
        Ubis = Ubis
        print("Break at iteration ",j,"at",datetime.datetime.now()) #last run 1t 15:09 to (14
        break

print('Ubis = ',Ubis)

#extract values from tuple for plotting with
znm = p_mid[1]
nz = p_mid[3]
Vfinal = p_mid[2]

Ec = Vfinal - Ef
Ev = Vfinal - (Eg + Ef)

#plot potential as a function of depth
fig = plt.figure(1,figsize=(16,9))
plt.plot(znm,Vfinal)
pylab.ylabel('Potential (meV)')
pylab.xlabel('Depth (nm)')

#plot carrier density as a function of depth
fig2 = plt.figure(2,figsize=(16,9))
plt.plot(znm,nz)
pylab.ylabel('nz')
pylab.xlabel('Depth (nm)')

#plot carrier density on a log scale as a function of depth
fig3 = plt.figure(3,figsize=(16,9))
plt.semilogy(znm,nz)
pylab.ylabel('nz')
pylab.xlabel('Depth (nm)')


#Linear Extrapolation Values
Udepth = 1
Uvbm = -707
Xdepth = 6
```

```
Xvbm = -789
Hdepth = 20
Hvbm = -989
filename = 'ntypeBandBending_linear.jpg'

"""
#DOS Fitting Values
Udepth = 1
Uvbm = -881
Xdepth = 6
Xvbm = -1051
Hdepth = 20
Hvbm = -1101
filename = 'ntypeBandBending_DOS.jpg'
"""

#plot bands as a function of depth
fig4 = plt.figure(4,figsize=(16,9))
#plt.plot(znm,Vfinal)
plt.plot(znm,Ec)
plt.plot(znm,Ev)
plt.plot(Udepth,Uvbm,'k*')
plt.plot(Xdepth,Xvbm,'k*')
plt.plot(Hdepth,Hvbm,'k*')
plt.axhline(linestyle='--',color='black')
pylab.ylabel('Energy (meV)')
pylab.xlabel('Depth (nm)')
#fig4.savefig(filename)

P = np.array([znm,Vfinal,Ec,Ev,nz]).transpose()
np.savetxt('ntype_Vfinal_LE.csv',P,delimiter=',')
```

B3 Python Code - p-type

B3.1 Calculating Bulk Carrier Density, $f_n(x)$

```
def pbulk(Ef,T,m0,epsilon_z,Eg):

    prefac = 2.154E17*(m0**1.5)
    Emin = 2001
    dE = 1

    hmin = int(Emin/dE)
```

```
    E = np.linspace(0,2000,2001)
    g = np.zeros([2001])
    f = np.zeros([2001])
    nonpar = np.zeros([2001])
    dn = np.zeros([2001])
    n = np.zeros([2001])

    g = prefac*(E**0.5)
    f = 1/(1+np.exp(11.604*(E-Ef)/T))
    #nonpar = 2*np.sqrt((E/Eg)+1)*((E/Eg)+0.5)
    dn = g*(f)*dE#*nonpar

    for h in range (0,hmin-1):
        n[h+1] = n[h] + dn[h]

    nbulk = n[hmin-1]

    return nbulk
```

B3.2 Solving Poisson's Equation, $f_U(x)$

```
T = 300 #temperature
Eg =  1180 #band gap in meV


########################## Second Step - Poisson's Equation ##########################

def dUp(Ef,T,m0,Na,epsilon_z,Vp):
    Emax = 1000
    dE = 1

    prefac = 2.154E17*(m0**1.5)

    jmax = int(Emax/dE)

    E = np.linspace(0.05,1000.05,1001)
    g = np.zeros([1001])
    f = np.zeros([1001])
    dn = np.zeros([1001])

    n = np.zeros([1001])
```

```
    g = prefac*(E**0.5)
    f = 1/(1+np.exp(11.604*(E-Ef-Vp)/T)) #Fermi-Dirac function, 11.604 is e/k
    nonpar = 2*np.sqrt((E/Eg)+1)*((E/Eg)+0.5) #non parabolic approximation modifier
    #x = (2*z/L)*((E*11.604/T)**0.5)*((1+(E/Eg)))**0.5 #x for sinc(x) in mtfa modifier
    #mtfa = 1-((np.sin(x))/x) #modified thomas-fermi approximation using sinc(x)
    dn = g*f*dE*nonpar #carrier concentration for specified step to add this iteration

    for j in range (0,jmax-1):
        n[j+1] = n[j] + dn[j] #sum carrier concentration

    dUp = -(1.8093517E-3/epsilon_z)*(-n[jmax-1]+Na) #Returns dUp. const is e/epsilon0

    return dUp
```

B3.3 Plotting Band Bending, $f_P(x)$

```
T = 300 #temperature
Eg =  1180 #band gap in meV
me = 1.135



########################## Third Step - Band Bending ##########################
steps = 2000

V = np.zeros([steps+1])
U = np.zeros([steps+1])
dU = np.zeros([steps+1])
nz = np.zeros([steps+1])


def poisson(Ef,Vbb,Ubb,Na,epsilon_z,m0,depth):

    V[0] = Vbb
    U[0] = Ubb

    #Na = pbulk(-Ef,T,m0,epsilon_z,Eg)
    Nd = nbulk(Ef,T,me,epsilon_z,Eg)

    dz = depth/steps #cm units
    z = np.linspace(0,depth,steps+1) #0 - 80 nm in steps of dz cm units
    znm = z*1E7
```

```
    dU[0] = dUp(-Ef,T,m0,Na,epsilon_z,V[0])
    nz[0] = -Na - ((5.5268414E2*epsilon_z)*dU[0])

    for i in range (1,steps+1):
        V[i] = V[i-1] + U[i-1]*dz
        if (Ef-V[i]) > Eg/2:
            dU[i] = dUn(Ef-Eg,T,Na,epsilon_z,V[i-1],z[i])
            #nz[i] = Nd - ((5.5268414E2*epsilon_z)*dU[i])
        else:
            dU[i] = dUp(-Ef,T,m0,Na,epsilon_z,V[i-1])
        nz[i] = -Na - ((5.5268414E2*epsilon_z)*dU[i])
        U[i] = U[i-1] + dU[i-1]*dz
        poisson = 0
    if V[i] > 0:
        poisson = -1
    if U[i] < 0:
        poisson = 1
    if V[i] < 0 and U[steps] > 0:
        poisson = 0
    return poisson
```

B3.4 Main Code

```
T = 300 #temperature
Eg =  1180 #band gap in meV
m0 = 2.246 #effective mass
epsilon_z = 3.5 #static dielectric constant - from Tim
#epsilon_inf = 14 # #high frequency dielectric constant
Ef = 175 #bulk fermi level wrt valence band in meV
#Ef = 175 for ptype linear fits
#Ef = 215 for ptype DOS fits
prefac = 2.154E17*(m0**1.5)

Na = pbulk(-Ef,T,m0,epsilon_z,Eg)
print('Bulk Carrier Density = ',Na)

kmax = 400 #number of attempts to find best fit

############################################################

Uacc = 1E-16 #accuracy with which U must be found
Umin = 1E3 #initial min slope guess
Umax = 1E9 #initial max slope guess
Vbb = -470 #band bending potential at z=0
```

```
#Vbb = -470 for ptype linear fits
#Vbb = -500 for ptype DOS fits
depth = 2E-5

############################################################

p_min = poisson(Ef,Vbb,Umin,Na,epsilon_z,m0,depth) #band bending using Umin
p_mid = poisson(Ef,Vbb,Umax,Na,epsilon_z,m0,depth) #band bending using Umax

#extracts relevant values from poisson subroutine tuple
pp = p_min*p_mid


if p_min < 0: #if pmin doesn't go back on itself pmid will be found from pmin
    Ubis = Umin
    deltaU = Umax - Umin
else: #if pmin does go back on itself pmid if found from pmax
    Ubis = Umax
    deltaU = Umin - Umax

#print('p_min = ',p_min)
#print('p_max = ',p_mid)
#print('pp = ',pp)
#print('Ubis = ',Ubis)
#print('deltaU = ',deltaU)

if (pp)>0:
   print('Error: Utrue must be bracketed by Umin and Umax.') #initial conditions must s
   sys.exit('Error: Utrue must be bracketed by Umin and Umax.')

for k in range (0,kmax):
    #if k%10 == 0:
    #    print("No. of iteratons so far = ",k)
    deltaU = 0.5*deltaU #Halves for each loop as the separation between pmid and pmin
    Umid = Ubis + deltaU #Sets Umid to be the line in between pmin and pmax
    pmid = poisson(Ef,Vbb,Umid,Na,epsilon_z,m0,depth) #calculates pmid
    #pmid = p_mid[0] #picks out poisson value of -1,0,1 from tuple
    #print('pmid=',pmid)
    if pmid < 0: #if pmid crosses 0 sets as Ubis for next iteration of for loop.
        Ubis = Umid
    if np.abs(deltaU) < Uacc: #If dU is smaller than required accuracy breaks loop and
        Ubis = Ubis
        print("Break at iteration ",k,"at",datetime.datetime.now()) #last run 1t 15:09
```

```
        break

print('Ubis=',Ubis)
#print('deltaU=',deltaU)
Vfinal = Vfinal(Ef,Vbb,Ubis,Na,epsilon_z,m0,depth)
#extract values from tuple for plotting with
znm = Vfinal[1]
nz_h = Vfinal[2]
dU = Vfinal[3]
Vfinal = Vfinal[0]

Ec = Vfinal -Ef + Eg
Ev = Vfinal - Ef

#plot potential as a function of depth
fig = plt.figure(1,figsize=(16,9))
plt.plot(znm,Vfinal)
pylab.ylabel('Potential (meV)')
pylab.xlabel('Depth (nm)')
#plt.xlim(-5,20)



#plot carrier density as a function of depth
fig2 = plt.figure(2,figsize=(16,9))
plt.plot(znm,-nz_h)
pylab.ylabel('nz')
pylab.xlabel('Depth (nm)')
fig2.savefig('ptype_LE_nz.jpg')

#plot carrier density on a log scale as a function of depth
fig3 = plt.figure(3,figsize=(16,9))
plt.semilogy(znm,-nz_h)
pylab.ylabel('nz')
pylab.xlabel('Depth (nm)')
fig3.savefig('ptype_LE_lognz.jpg')
#P = np.array([znm,Vfinal]).transpose()
#np.savetxt('Vfinal.csv',P,delimiter=',')


#Linear Extrapolation Values
Udepth = 1
Uvbm = -625
```

```
Xdepth = 6
Xvbm = -455
Hdepth = 20
Hvbm = -329
filename = 'ptypeBandBending_linear.jpg'
"""

#DOS Fitting Values
Udepth = 1
Uvbm = -701
Xdepth = 6
Xvbm = -651
Hdepth = 20
Hvbm = -531
filename = 'ptypeBandBending_DOS.jpg'

"""

#plot bands as a function of depth
fig4 = plt.figure(4,figsize=(16,9))
#plt.plot(znm,Vfinal)
plt.plot(znm,Ec)
plt.plot(znm,Ev)
plt.plot(Udepth,Uvbm,'k*')
plt.plot(Xdepth,Xvbm,'k*')
plt.plot(Hdepth,Hvbm,'k*')
plt.axhline(linestyle='--',color='black')
pylab.ylabel('Energy (meV)')
pylab.xlabel('Depth (nm)')
fig4.savefig(filename)

#fig5 = plt.figure(5,figsize=(16,9))
#plt.plot(znm,-nz_e)
#pylab.ylabel('nz')
#pylab.xlabel('Depth (nm)')
#fig5.savefig('ptype_LE_nz.jpg')

P = np.array([znm,Vfinal,Ec,Ev,nz_h]).transpose()
np.savetxt('ptype_Vfinal_LE.csv',P,delimiter=',')
```

REFERENCES

[1] *Statistical Review of World Energy*. 2020. URL: https://www.bp.com/content/dam/bp/business-sites/en/global/corporate/pdfs/energy-economics/statistical-review/bp-stats-review-2020-full-report.pdf.

[2] United Nations. *Paris Agreement*. 2015. URL: https://unfccc.int/sites/default/files/english_paris_agreement.pdf.

[3] Chris Skidmore - Minister of State. *The Climate Change Act 2008 (2050 Amendment) Order*. 2019. URL: https://www.legislation.gov.uk/uksi/2019/1056/made.

[4] Energy Department for Business and Industrial Strategy. *Press Release: UK sets ambitious new climate target ahead of UN Summit*. Dec. 2020. URL: https://www.gov.uk/government/news/uk-sets-ambitious-new-climate-target-ahead-of-un-summit.

[5] Rafael M. Almeida et al. "Reducing greenhouse gas emissions of Amazon hydropower with strategic dam planning". In: *Nature Communications* 10.1 (Sept. 2019), p. 4281. ISSN: 2041-1723. DOI: 10.1038/s41467-019-12179-5.

[6] International Energy Agency. *Projected costs of generating electricity 2020*. 2020. URL: https://www.iea.org/reports/projected-costs-of-generating-electricity-2020.

[7] Thomas J. Whittles. "Electronic characterisation of Earth-abundant sulphides for solar photovoltaics". PhD thesis. University of Liverpool, July 2017.

[8] Stuart J. C. Irvine, ed. *Materials Challenges. Inorganic Photovoltaic Solar Energy*. Energy and Environment Series. The Royal Society of Chemistry, 2014, P001–343. ISBN: 978-1-84973-187-4. DOI: 10.1039/9781849733465.

[9] Peter Yu and Manuel Cardona. *Fundamentals of Semiconductors: Physics and Material Properties*. Springer, 2010.

[10] Jenny Nelson. *The Physics of Solar Cells*. Imperial College Press, 2003.

[11] B. L. Sharma and R. K. Purohit. *Semiconductor Heterojunctions*. Pergamon, 1974.

[12] William Shockley and Hans J. Queisser. "Detailed Balance Limit of Efficiency of p-n Junction Solar Cells". In: *Journal of Applied Physics* 32.3 (1961), pp. 510–519. DOI: 10.1063/1.1736034.

[13] Sven Rühle. "Tabulated values of the Shockley-Queisser limit for single junction solar cells". In: *Solar Energy* 130 (2016), pp. 139–147. ISSN: 0038-092X. DOI: https://doi.org/10.1016/j.solener.2016.02.015.

[14] First Solar. *First Solar Series 6 Plus™ PV Module*. Tech. rep. MPD-00540-06-P. First Solar, Oct. 2020.

[15] Martin A. Green et al. "Solar cell efficiency tables (version 56)". In: *Progress in Photovoltaics: Research and Applications* 28.7 (2020), pp. 629–638. DOI: https://doi.org/10.1002/pip.3303.

[16] Office of Energy Efficiency and Renewable Energy. *Copper Indium Gallium Selenide*. URL: https://www.energy.gov/eere/solar/copper-indium-gallium-diselenide.

[17] Thomas P. Shalvey. Private Communication.

[18] Antoine Kahn. "Fermi level, work function and vacuum level". In: *Mater. Horiz.* 3 (1 2016), pp. 7–10. DOI: 10.1039/C5MH00160A.

[19] D. Cahen and A. Kahn. "Electron Energetics at Surfaces and Interfaces: Concepts and Experiments". In: *Advanced Materials* 15.4 (2003), pp. 271–277. DOI: 10.1002/adma.200390065.

[20] Hisao Ishii et al. "Energy Level Alignment and Interfacial Electronic Structures at Organic/Metal and Organic/Organic Interfaces". In: *Advanced Materials* 11.8 (1999), pp. 605–625. DOI: https://doi.org/10.1002/(SICI)1521-4095(199906)11:8<605::AID-ADMA605>3.0.CO;2-Q.

[21] D. L. Bätzner et al. "Device analysis methods for physical cell parameters of CdTe/CdS solar cells". In: *Thin Solid Films* 361 (2000), pp. 288–292. ISSN: 00406090. DOI: 10.1016/S0040-6090(99)00862-7.

[22] D. Kraft et al. "Characterization of tellurium layers for back contact formation on close to technology treated CdTe surfaces". In: *Journal of Applied Physics* 94.5 (2003), pp. 3589–3598. ISSN: 00218979. DOI: 10.1063/1.1597757.

[23] E. Becquerel. "Memoire sur les effets electriques produits sous l'influence des rayons solaires". In: *Comptes Rendus* 9 (1839), pp. 561–567.

[24] C. E. Fritts. "On a new form of selenium cell, and some electrical discoveries made by its use". In: *American Journal of Science* 26.156 (Oct. 1883), pp. 465–472. DOI: 10.2475/ajs.s3-26.156.465.

[25] C.E. Fritts. "On the Fritts selenium cells and batteries". In: *Journal of the Franklin Institute* 119.3 (1885), pp. 221–232. ISSN: 0016-0032. DOI: https://doi.org/10.1016/0016-0032(85)90426-0.

[26] D. M. Chapin, C. S. Fuller, and G. L. Pearson. "A New Silicon p-n Junction Photocell for Converting Solar Radiation into Electrical Power". In: *Journal of Applied Physics* 25.5 (1954), pp. 676–677. DOI: 10.1063/1.1721711.

[27] Fraunhofer Institute for Solar Energy Systems. *Photovoltaics Report*. Nov. 2019.

[28] A. Jager-Walday. *PV Status Report 2019*. 2019. DOI: doi:10.2760/326629.

[29] Hitoshi Sai et al. "Impact of silicon wafer thickness on photovoltaic performance of crystalline silicon heterojunction solar cells". In: *Japanese Journal of Applied Physics* 57.8S3 (July 2018), 08RB10. DOI: 10.7567/jjap.57.08rb10.

[30] National Renewable Energy Laboratories. *What is the energy payback for PV*. 2004. URL: https://www.nrel.gov/docs/fy05osti/37322.pdf.

[31] B. Goldstein. "Properties of Photovoltaic Films of CdTe". In: *Phys. Rev.* 109 (2 Jan. 1958), pp. 601–603. DOI: 10.1103/PhysRev.109.601.2.

[32] Jinqing Peng, Lin Lu, and Hongxing Yang. "Review on life cycle assessment of energy payback and greenhouse gas emission of solar photovoltaic systems". In: *Renewable and Sustainable Energy Reviews* 19 (2013), pp. 255–274. ISSN: 1364-0321. DOI: https://doi.org/10.1016/j.rser.2012.11.035.

[33] J. D. Major et al. "A low-cost non-toxic post-growth activation step for CdTe solar cells". In: *Nature* 511.7509 (2014), pp. 334–337. ISSN: 14764687. DOI: 10.1038/nature13435.

[34] Theodore D. C. Hobson. "Growth and properties of bulk CZTSSe and Sb_2Se_3 for solar cells". PhD thesis. University of Liverpool, May 2020.

[35] Andriy Zakutayev et al. "Emerging inorganic solar cell efficiency tables (version 2)". In: *Journal of Physics: Energy* 3.3 (Apr. 2021), p. 032003. DOI: 10.1088/2515-7655/abebca.

[36] Kai Zeng, Ding-Jiang Xue, and Jiang Tang. "Antimony selenide thin-film solar cells". In: *Semiconductor Science and Technology* 31.6 (Apr. 2016), p. 063001. DOI: 10.1088/0268-1242/31/6/063001.

[37] Huw Shiel et al. "Chemical etching of Sb_2Se_3 solar cells: surface chemistry and back contact behaviour". In: *Journal of Physics: Energy* 1.4 (Oct. 2019), p. 045001. DOI: 10.1088/2515-7655/ab3c98.

[38] Chao Chen et al. "Accelerated optimization of TiO_2/Sb_2Se_3 thin film solar cells by high-throughput combinatorial approach". In: *Advanced Energy Materials* 7.20 (2017), p. 1700866. ISSN: 16146832. DOI: 10.1002/aenm.201700866.

[39] Liang Wang et al. "Stable 6%-efficient Sb_2Se_3 solar cells with a ZnO buffer layer". In: *Nature Energy* 2.4 (2017), p. 17046. ISSN: 20587546. DOI: 10.1038/nenergy.2017.46.

[40] Weihuang Wang et al. "The effects of SnS_2 secondary phases on Cu_2ZnSnS_4 solar cells: a promising mechanical exfoliation method for its removal". In: *J. Mater. Chem. A* 6 (7 2018), pp. 2995–3004. DOI: 10.1039/C7TA08242H.

[41] Ashish K. Singh et al. "Phase evolution during the electrodeposition of Cu-Sn-Zn metal precursor layers and its role on the Cu_2S impurity phase formation in Cu_2ZnSnS_4 thin films". In: *Solar Energy* 155 (2017), pp. 627–636. ISSN: 0038-092X. DOI: https://doi.org/10.1016/j.solener.2017.06.063.

[42] Zhongjie Guan, Wenjun Luo, and Zhigang Zou. "Formation mechanism of ZnS impurities and their effect on photoelectrochemical properties on a Cu_2ZnSnS_4 photocathode". In: *CrystEngComm* 16 (14 2014), pp. 2929–2936. DOI: 10.1039/C3CE42373E.

[43] Zhiqiang Li et al. "9.2%-Efficient Core-Shell Structured Antimony Selenide Nanorod Array Solar Cells". In: *Nature Communications* 10.125 (2019), pp. 1–9. ISSN: 2041-1723. DOI: 10.1038/s41467-018-07903-6.

[44] Rong Tang et al. "Highly efficient and stable planar heterojunction solar cell based on sputtered and post-selenized Sb_2Se_3 thin film". In: *Nano Energy* 64 (2019), p. 103929. ISSN: 2211-2855. DOI: https://doi.org/10.1016/j.nanoen.2019.103929.

[45] Xiaomin Wang et al. "Interfacial engineering for high efficiency solution processed Sb_2Se_3 solar cells". In: *Solar Energy Materials and Solar Cells* 189 (2019), pp. 5–10. ISSN: 0927-0248. DOI: https://doi.org/10.1016/j.solmat.2018.09.020.

[46] Xixing Wen et al. "Vapor transport deposition of antimony selenide thin film solar cells with 7.6% efficiency". In: *Nature Communications* 9 (2018), p. 2179. ISSN: 2041-1723. DOI: 10.1038/s41467-018-04634-6.

[47] B. O'Neill. "Indium market forces, a commercial perspective". In: *2010 35th IEEE Photovoltaic Specialists Conference*. 2010, pp. 000556–000559.

[48] U. S. Geological Survey. *Mineral commodity summaries 2020*. 2020. DOI: https://doi.org/10.3133/mcs2020.

[49] Royal Society of Chemistry. *Royal Society of Chemistry - Periodic Table*. 2021. URL: https://www.rsc.org/periodic-table/.

[50] T.D.C. Hobson and K. Durose. "Protocols for the Miller indexing of Sb_2Se_3 and a non-x-ray method of orienting its single crystals". In: *Materials Science in Semiconductor Processing* 127 (2021), p. 105691. ISSN: 1369-8001. DOI: https://doi.org/10.1016/j.mssp.2021.105691.

[51] Aron Walsh et al. "Stereochemistry of post-transition metal oxides: revision of the classical lone pair model". In: *Chemical Society Reviews* 40.9 (2011), pp. 4455–4463.

[52] Jean-Yves Raty et al. "A Quantum-Mechanical Map for Bonding and Properties in Solids". In: *Advanced Materials* 31.3 (2019), p. 1806280. DOI: 10.1002/adma.201806280.

[53] Chao Chen et al. "Optical properties of amorphous and polycrystalline Sb_2Se_3 thin films prepared by thermal evaporation". In: *Applied Physics Letters* 107.4 (2015), p. 043905. ISSN: 0003-6951. DOI: 10.1063/1.4927741.

[54] Max Birkett et al. "Band gap temperature-dependence of close-space sublimation grown Sb_2Se_3 by photo-reflectance". In: *APL Materials* 6.8 (2018), p. 084901. DOI: 10.1063/1.5027157.

[55] Faiazul Haque et al. "Annealing induced microstructure engineering of antimony tri-selenide thin films". In: *Materials Research Bulletin* 99 (2018), pp. 232–238. ISSN: 0025-5408. DOI: https://doi.org/10.1016/j.materresbull.2017.11.014.

[56] Arturo Morales-Acevedo. "Thin film CdS/CdTe solar cells: Research perspectives". In: *Solar Energy* 80.6 (2006). SREN 05 - Solar Renewable Energy News Conference, pp. 675–681. ISSN: 0038-092X. DOI: https://doi.org/10.1016/j.solener.2005.10.008.

[57] Laurie J. Phillips et al. "Current enhancement via a TiO_2 window layer for CSS Sb_2Se_3 solar cells: performance limits and high V_{oc}". In: *IEEE Journal of Photovoltaics* 9.2 (2019), pp. 544–551.

[58] Chris N Savory. Private Communication.

[59] X Liu et al. "Thermal evaporation and characterisation of Sb_2Se_3 thin films for substrate Sb_2Se_3/CdS solar cells". In: *ACS Applied Materials and Interfaces* 6.13 (2014), pp. 10687–10695. ISSN: 1944-8244. DOI: 10.1021/am502427s.

[60] N. Cifuentes et al. "Electronic Conduction Mechanisms and Defects in Polycrystalline Antimony Selenide". In: *The Journal of Physical Chemistry C* 124.14 (2020), pp. 7677–7682. DOI: 10.1021/acs.jpcc.0c00398.

[61] Xinsheng Liu et al. "Enhanced Sb_2Se_3 solar cell performance through theory-guided defect control". In: *Progress in Photovoltaics: Research and Applications* 25.10 (2017), pp. 861–870. DOI: 10.1002/pip.2900.

[62] Theodore D. C. Hobson et al. "Isotype Heterojunction Solar Cells Using n-Type Sb_2Se_3 Thin Films". In: *Chemistry of Materials* 32.6 (2020). DOI: 10.1021/acs.chemmater.0c00223.

[63] Chao Chen et al. "Characterization of basic physical properties of Sb_2Se_3 and its relevance for photovoltaics". In: *Frontiers of Optoelectronics* 10.1 (Mar. 2017). DOI: 10.1007/s12200-017-0702-z.

[64] Adrien Stoliaroff et al. "Deciphering the Role of Key Defects in Sb_2Se_3, a Promising Candidate for Chalcogenide-Based Solar Cells". In: *ACS Applied Energy Materials* 3.3 (2020), pp. 2496–2509. DOI: 10.1021/acsaem.9b02192.

[65] Oliver S. Hutter et al. "CSS antimony selenide film morphology and high efficiency PV devices". In: *WCPEC-7 Conference Paper* (2018). DOI: 10.1109/PVSC.2018.8547653.

[66] Xiaobo Hu et al. "5.91%-efficient Sb_2Se_3 solar cells with a radio-frequency magnetron-sputtered CdS buffer layer". In: *Applied Materials Today* 16 (2019), pp. 367–374. ISSN: 2352-9407. DOI: https://doi.org/10.1016/j.apmt.2019.06.001.

[67] Deng-Bing Li et al. "Stable and efficient CdS/Sb_2Se_3 solar cells prepared by scalable close space sublimation". In: *Nano Energy* 49 (2018), pp. 346–353. ISSN: 2211-2855. DOI: 10.1016/j.nanoen.2018.04.044.

[68] Liping Guo et al. "Interface Engineering via Sputtered Oxygenated CdS:O Window Layer for Highly Efficient Sb_2Se_3 Thin-Film Solar Cells with Efficiency Above 7%". In: *Solar RRL* 3.10 (2019), p. 1900225. DOI: 10.1002/solr.201900225.

[69] Xinsheng Liu et al. "Improving the performance of Sb_2Se_3 thin film solar cells over 4% by controlled addition of oxygen during film deposition". In: *Progress in Photovoltaics: Research and Applications* 23.12 (2015), pp. 1828–1836. DOI: 10.1002/pip.2627.

[70] Zhiqiang Li et al. "Sb_2Se_3 thin film solar cells in substrate configuration and the back contact selenization". In: *Solar Energy Materials and Solar Cells* 161 (2017), pp. 190–196. ISSN: 0927-0248. DOI: https://doi.org/10.1016/j.solmat.2016.11.033.

[71] Xiaoyang Liang et al. "Effect of deposition pressure on the properties of magnetron sputtering-deposited Sb_2Se_3 thin-film solar cells". In: *Applied Physics A* 125 (May 2019), p. 381. DOI: 10.1007/s00339-019-2677-7.

[72] Kanghua Li et al. "Improved efficiency by insertion of $Zn_{1-x}Mg_xO$ through sol-gel method in ZnO/Sb_2Se_3 solar cell". In: *Solar Energy* 167 (2018), pp. 10–17. ISSN: 0038-092X. DOI: https://doi.org/10.1016/j.solener.2018.03.081.

[73] Taifeng Ju et al. "Enhanced photovoltaic performance of solution-processed Sb_2Se_3 thin film solar cells by optimizing device structure". In: *Current Applied Physics* 20.2 (2020), pp. 282–287. ISSN: 1567-1739. DOI: 10.1016/j.cap.2019.11.018.

[74] Wen-Jian Shi et al. "Antimony Selenide Thin Film Solar Cells with an Electron Transport Layer of Alq_3". In: *Chinese Physics Letters* 37.10 (Oct. 2020), p. 108401. DOI: 10.1088/0256-307x/37/10/108401.

[75] Rhys E. Williams et al. "Evidence for Self-healing Benign Grain Boundaries and a Highly Defective Sb2Se3–CdS Interfacial Layer in Sb2Se3 Thin-Film Photovoltaics". In: *ACS Applied Materials & Interfaces* 12.19 (2020), pp. 21730–21738. DOI: 10.1021/acsami.0c03690.

[76] Peter J. Yates. "Emerging Absorber Materials for Sustainable Photovoltaics". PhD thesis. University of Liverpool, Nov. 2018.

[77] Meiying Leng et al. "Selenization of Sb_2Se_3 absorber layer: An efficient step to improve device performance of CdS/Sb_2Se_3 solar cells". In: *Applied Physics Letters* 105.8 (2014), p. 083905. DOI: 10.1063/1.4894170.

[78] Ying Zhou et al. "Thin-film Sb_2Se_3 photovoltaics with oriented one-dimensional ribbons and benign grain boundaries". In: *Nature Photonics* 9.6 (2015), pp. 409–415. ISSN: 17494893. DOI: 10.1038/nphoton.2015.78.

[79] Nicolae Spalatu et al. "Screening and optimization of processing temperature for Sb_2Se_3 thin film growth protocol: Interrelation between grain structure, interface intermixing and solar cell performance". In: *Solar Energy Materials and Solar Cells* 225 (2021), p. 111045. ISSN: 0927-0248. DOI: https://doi.org/10.1016/j.solmat.2021.111045.

[80] Chao Chen et al. "6.5% Certified Efficiency Sb_2Se_3 Solar Cells Using PbS Colloidal Quantum Dot Film as Hole-Transporting Layer". In: *ACS Energy Letters* 2 (2017), pp. 2125–2132. DOI: 10.1021/acsenergylett.7b00648.

[81] Oliver S. Hutter et al. "6.6% efficient antimony selenide solar cells using grain structure control and an organic contact layer". In: *Solar Energy Materials Solar Cells* 188 (2018), pp. 177–181. ISSN: 0927-0248. DOI: 10.1016/j.solmat.2018.09.004.

[82] Chunsheng Guo et al. "1D/3D Alloying Induced Phase Transition in Light Absorbers for Highly Efficient Sb_2Se_3 Solar Cells". In: *Solar RRL* 4.4 (2020), p. 2000054. DOI: 10.1002/solr.202000054.

[83] Yan-Di Luo et al. "An effective combination reaction involved with sputtered and selenized Sb precursors for efficient Sb_2Se_3 thin film solar cells". In: *Chemical Engineering Journal* 393 (2020), p. 124599. ISSN: 1385-8947. DOI: https://doi.org/10.1016/j.cej.2020.124599.

[84] Guang-Xing Liang et al. "Sputtered and selenized Sb_2Se_3 thin-film solar cells with open-circuit voltage exceeding 500 mV". In: *Nano Energy* 73 (2020), p. 104806. ISSN: 2211-2855. DOI: https://doi.org/10.1016/j.nanoen.2020.104806.

[85] Christopher N. Savory and David O. Scanlon. "The complex defect chemistry of antimony selenide". In: *J. Mater. Chem. A* 7 (17 2019), pp. 10739–10744. DOI: 10.1039/C9TA02022E.

[86] Ying Zhou et al. "Solution-Processed Antimony Selenide Heterojunction Solar Cells". In: *Advanced Energy Materials* 4.8 (2014), p. 1301846. DOI: 10.1002/aenm.201301846.

[87] Jiahua Tao et al. "Solution-processed SnO_2 interfacial layer for highly efficient Sb_2Se_3 thin film solar cells". In: *Nano Energy* 60 (2019), pp. 802–809. ISSN: 2211-2855. DOI: https://doi.org/10.1016/j.nanoen.2019.04.019.

[88] Jing Zhou et al. "Dual-function of $CdCl_2$ treated SnO_2 in Sb_2Se_3 solar cells". In: *Applied Surface Science* 534 (2020), p. 147632. ISSN: 0169-4332. DOI: https://doi.org/10.1016/j.apsusc.2020.147632.

[89] Gang Li et al. "Improvement in Sb_2Se_3 Solar Cell Efficiency through Band Alignment Engineering at the Buffer/Absorber Interface". In: *ACS Applied Materials and Interfaces* 11 (2019), pp. 828–834. DOI: 10.1021/acsami.8b17611.

[90] Xiaohai Guo et al. "Low-temperature deposited SnO_2 used as the buffer layer of Sb_2Se_3 solar cell". In: *Materials Letters* 222 (2018), pp. 142–145. ISSN: 0167-577X. DOI: https://doi.org/10.1016/j.matlet.2018.03.141.

[91] Zhiwen Chen et al. "Efficiency improvement of Sb_2Se_3 solar cells based on La-doped SnO_2 buffer layer". In: *Solar Energy* 187 (2019), pp. 404–410. ISSN: 0038-092X. DOI: https://doi.org/10.1016/j.solener.2019.05.026.

[92] Ying Zhou et al. "Buried homojunction in CdS/Sb_2Se_3 thin film photovoltaics generated by interfacial diffusion". In: *Applied Physics Letters* 111.1 (2017), p. 013901. DOI: 10.1063/1.4991539.

[93] Qingfei Cang et al. "Enhancement in the efficiency of Sb_2Se_3 solar cells by adding low lattice mismatch $CuSbSe_2$ hole transport layer". In: *Solar Energy* 199 (2020), pp. 19–25. ISSN: 0038-092X. DOI: https://doi.org/10.1016/j.solener.2020.02.008.

[94] Liping Guo et al. "Stable and efficient Sb_2Se_3 solar cells with solution-processed NiO_x hole-transport layer". In: *Solar Energy* 218 (2021), pp. 525–531. ISSN: 0038-092X. DOI: https://doi.org/10.1016/j.solener.2021.02.063.

[95] Cong Liu et al. "Back contact interfacial modification in highly-efficient all-inorganic planar n-i-p Sb_2Se_3 solar cells". In: *ACS Applied Materials and Interfaces* 12.34 (2020), pp. 38397–38405. DOI: 10.1021/acsami.0c10629.

[96] J.D. Major et al. "P3HT as a pinhole blocking back contact for CdTe thin film solar cells". In: *Solar Energy Materials and Solar Cells* 172 (2017), pp. 1–10. ISSN: 0927-0248. DOI: https://doi.org/10.1016/j.solmat.2017.07.005.

[97] Theodore D. C. Hobson et al. "Defect properties of Sb_2Se_3 thin film solar cells and bulk crystals". In: *Applied Physics Letters* 116.26 (2020), p. 261101. DOI: 10.1063/5.0012697.

[98] Rokas Kondrotas, Chao Chen, and Jiang Tang. "Sb_2S_3 Solar Cells". In: *Joule* 2.5 (2018), pp. 857–878. ISSN: 2542-4351. DOI: https://doi.org/10.1016/j.joule.2018.04.003.

[99] Rongfeng Tang et al. "Hydrothermal deposition of antimony selenosulfide thin films enables solar cells with 10% efficiency". In: *Nature Energy* (July 2020). ISSN: 2058-7546. DOI: 10.1038/s41560-020-0652-3.

[100] Kai Shen et al. "Efficient and stable planar n-i-p Sb_2Se_3 solar cells enabled by oriented 1D trigonal selenium structures". In: *Advanced Science* (2020), p. 2001013. DOI: https://doi.org/10.1002/advs.202001013.

[101] Jun Zhang et al. "Alternative back contacts for Sb_2Se_3 solar cells". In: *Solar Energy* 182 (2019), pp. 96–101. ISSN: 0038-092X. DOI: https://doi.org/10.1016/j.solener.2019.02.050.

[102] Liping Guo et al. "Improved stability and efficiency of $CdSe/Sb_2Se_3$ thin-film solar cells". In: *Solar Energy* 188 (2019), pp. 586–592. ISSN: 0038-092X. DOI: https://doi.org/10.1016/j.solener.2019.06.042.

[103] Kunal J. Tiwari et al. "Tailoring doping of efficient Sb_2Se_3 solar cells in substrate configuration by low temperature post deposition selenization process". In: *2018 IEEE 7th World Conference on Photovoltaic Energy Conversion (WCPEC) (A Joint Conference of 45th IEEE PVSC, 28th PVSEC and 34th EU PVSEC)* (2018), pp. 1858–1860.

[104] Miao Luo et al. "Thermal evaporation and characterization of superstrate CdS/Sb_2Se_3 solar cells". In: *Applied Physics Letters* 104.17 (2014), p. 173904. ISSN: 0003-6951. DOI: 10.1063/1.4874878.

[105] Angus Rockett. *The Materials Science of Semiconductors*. Springer, 2008. ISBN: 978-0-387-25653-5. DOI: 10.1007/978-0-387-68650-9.

[106] Tom Baines. "Optimisation of $CdTe_{1-x}Se_x$ and $Mg_xZn_{1-x}O$ layers for CdTe PV devices". PhD thesis. University of Liverpool, Sept. 2019.

[107] Jonathan Major. "CdTe solar cells: growth phenomena and device performance". PhD thesis. Durham University, Dec. 2008.

[108] Jennifer C. Green and Piero Decleva. "Photoionization cross-sections: a guide to electronic structure". In: *Coordination Chemistry Reviews* 249.1 (2005), pp. 209–228. ISSN: 0010-8545. DOI: https://doi.org/10.1016/j.ccr.2004.02.012.

[109] S. Tanuma, C. J. Powell, and D. R. Penn. "Calculations of electron inelastic mean free paths. III. Data for 15 inorganic compounds over the 50-2000 eV range". In: *Surface and Interface Analysis* 17.13 (1991), pp. 927–939. DOI: 10.1002/sia.740171305.

[110] S. Tanuma, C. J. Powell, and D. R. Penn. "Calculation of electron inelastic mean free paths (IMFPs) VII. Reliability of the TPP-2M IMFP predictive equation". In: *Surface and Interface Analysis* 35.3 (2003), pp. 268–275. DOI: 10.1002/sia.1526.

[111] John F. Moulder et al. *Handbook of X-ray Photoelectron Spectroscopy*. Perkin-Elmer Corporation, (1992), p. 261. ISBN: 9780962702624.

[112] C. Calderón et al. "Phase identification and XPS studies of Cu(In,Ga)Se_2 thin films". In: *Microelectronics Journal* 39.11 (2008), pp. 1324–1326. ISSN: 0026-2692. DOI: https://doi.org/10.1016/j.mejo.2008.01.071.

[113] Gabriel P. López, David G. Castner, and Buddy D. Ratner. "XPS O 1s binding energies for polymers containing hydroxyl, ether, ketone and ester groups". In: *Surface and Interface Analysis* 17.5 (1991), pp. 267–272. DOI: https://doi.org/10.1002/sia.740170508.

[114] M.C. Davies et al. "An analysis of the surface chemical structure of polymethacrylate (Eudragit) film coating polymers by XPS". In: *International Journal of Pharmaceutics* 57.3 (1989), pp. 183–187. ISSN: 0378-5173. DOI: https://doi.org/10.1016/0378-5173(89)90205-6.

[115] Nicole Fleck et al. "How Oxygen Exposure Improves the Back Contact and Performance of Antimony Selenide Solar Cells". In: *ACS Applied Materials and Interfaces* 12.47 (2020), pp. 52595–52602. DOI: 10.1021/acsami.0c14256.

[116] Lee A. Burton et al. "Electronic and optical properties of single crystal SnS_2: an earth-abundant disulfide photocatalyst". In: *J. Mater. Chem. A* 4 (4 2016), pp. 1312–1318. DOI: 10.1039/C5TA08214E.

[117] Christophe Nicolas and Catalin Miron. "Lifetime broadening of core-excited and -ionized states". In: *Journal of Electron Spectroscopy and Related Phenomena* 185.8 (2012). Special Issue in honor of Prof. T. Darrah Thomas: High-Resolution Spectroscopy of Isolated Species, pp. 267–272. ISSN: 0368-2048. DOI: https://doi.org/10.1016/j.elspec.2012.05.008.

[118] Casa Software Ltd. *CasaXPS Manual 2.3.15*. 2009.

[119] XPS Simplified. 2020. URL: https://xpssimplified.com/UPS.php.

[120] Anna Regoutz et al. "A novel laboratory-based hard X-ray photoelectron spectroscopy system". In: *Review of Scientific Instruments* 89 (2018), p. 073105. DOI: 10.1063/1.5039829.

[121] Diamond Light Source. *The Diamond Machine*. 2020. URL: https://www.diamond.ac.uk/Science/Machine/Components.html.

[122] Tien-Lin Lee and David A. Duncan. "A Two-Color Beamline for Electron Spectroscopies at Diamond Light Source". In: *Synchrotron Radiation News* 31.4 (2018), pp. 16–22. DOI: 10.1080/08940886.2018.1483653.

[123] J.J. Yeh and I. Lindau. "Atomic subshell photoionization cross sections and asymmetry parameters". In: *Atomic Data and Nuclear Data Tables* 32.1 (1985), pp. 1–155. ISSN: 0092-640X. DOI: https://doi.org/10.1016/0092-640X(85)90016-6.

[124] J. H. Scofield. "Theoretical photoionization cross sections from 1 to 1500 keV". In: (Jan. 1973).

[125] M. Al Turkestani. "CdTe solar cells: key layers and electrical effects". PhD thesis. Durham University, 2010.

[126] Chao Ding et al. "Effect of the conduction band offset on interfacial recombination behavior of the planar perovskite solar cells". In: *Nano Energy* 53 (2018), pp. 17–26. ISSN: 2211-2855. DOI: https://doi.org/10.1016/j.nanoen.2018.08.031.

[127] J.M. Kephart et al. "Band alignment of front contact layers for high-efficiency CdTe solar cells". In: *Solar Energy Materials and Solar Cells* 157 (2016), pp. 266–275. ISSN: 0927-0248. DOI: 10.1016/j.solmat.2016.05.050.

[128] Suzanne K. Wallace et al. "Finding a junction partner for candidate solar cell absorbers enargite and bournonite from electronic band and lattice matching". In: *Journal of Applied Physics* 125.5 (2019), p. 055703. DOI: 10.1063/1.5079485.

[129] M.G. Helander et al. "Pitfalls in measuring work function using photoelectron spectroscopy". In: *Applied Surface Science* 256.8 (2010), pp. 2602–2605. ISSN: 0169-4332. DOI: 10.1016/j.apsusc.2009.11.002.

[130] R Schlaf, H Murata, and Z.H Kafafi. "Work function measurements on indium tin oxide films". In: *Journal of Electron Spectroscopy and Related Phenomena* 120.1 (2001), pp. 149–154. ISSN: 0368-2048. DOI: 10.1016/S0368-2048(01)00310-3.

[131] S Kraut et al. "Precise determination of the valence band edge in x-ray photoemission spectra: application to measurement of semiconductor interface potentials". In: *Physical Review Letters* 44 (24 1980), pp. 1620–1623. DOI: 10.1103/PhysRevLett.44.1620.

[132] P. D. C. King et al. "InN/GaN valence band offset: High-resolution x-ray photoemission spectroscopy measurements". In: *Phys. Rev. B* 78 (3 2008), p. 033308. DOI: 10.1103/PhysRevB.78.033308.

[133] R. L. Anderson. "Germanium-Gallium Arsenide Heterojunctions [Letter to the Editor]". In: *IBM Journal of Research and Development* 4.3 (1960), pp. 283–287. ISSN: 0018-8646. DOI: 10.1147/rd.43.0283.

[134] Andreas Klein. "Energy band alignment at interfaces of semiconducting oxides: A review of experimental determination using photoelectron spectroscopy and comparison with theoretical predictions by the electron affinity rule, charge neutrality levels, and the common anion rule". In: *Thin Solid Films* 520.10 (2012). 7th International Symposium on Transparent Oxide Thin Films for Electronics and Optics (TOEO-7), pp. 3721–3728. ISSN: 0040-6090. DOI: 10.1016/j.tsf.2011.10.055.

[135] Andreas Klein. "Energy band alignment in chalcogenide thin film solar cells from photoelectron spectroscopy". In: *Journal of Physics: Condensed Matter* 27.13 (Mar. 2015), p. 134201. DOI: 10.1088/0953-8984/27/13/134201.

[136] D. W. Niles and G. Margaritondo. "Heterojunctions: Definite breakdown of the electron affinity rule". In: *Phys. Rev. B* 34 (4 Aug. 1986), pp. 2923–2925. DOI: 10.1103/PhysRevB.34.2923.

[137] R. Schlaf et al. "Band lineup of layered semiconductor heterointerfaces prepared by van der Waals epitaxy: Charge transfer correction term for the electron affinity rule". In: *Journal of Applied Physics* 85.5 (1999), pp. 2732–2753. DOI: 10.1063/1.369590.

[138] S. Tanuma, C. J. Powell, and D. R. Penn. "Calculation of electron inelastic mean free paths (IMFPs) VII. Reliability of the TPP-2M IMFP predictive equation". In: *Surface and Interface Analysis* 35.3 (2003), pp. 268–275. DOI: 10.1002/sia.1526.

[139] Chizhu Ou et al. "Bandgap tunable CdS:O as efficient electron buffer layer for high-performance Sb_2Se_3 thin film solar cells". In: *Solar Energy Materials and Solar Cells* 194 (2019), pp. 47–53. ISSN: 0927-0248. DOI: https://doi.org/10.1016/j.solmat.2019.01.043.

[140] Sebastian Siol et al. "Band alignment engineering at Cu_2O/ZnO heterointerfaces". In: *ACS Applied Materials and Interfaces* 8.33 (2016), pp. 21824–21831. DOI: 10.1021/acsami.6b07325.

[141] Sebastian Siol et al. "Combinatorial In Situ Photoelectron Spectroscopy Investigation of Sb_2Se_3/ZnS Heterointerfaces". In: *Advanced Materials Interfaces* 3.24 (2016), p. 1600755. DOI: 10.1002/admi.201600755.

[142] Shuaicheng Lu et al. "In situ investigation of interfacial properties of Sb_2Se_3 heterojunctions". In: *Applied Physics Letters* 116.24 (2020), p. 241602. DOI: 10.1063/5.0008879.

[143] Jiabin Dong et al. "Boosting V_{oc} of antimony chalcogenide solar cells: A review on interfaces and defects". In: *Nano Select* (2021). DOI: https://doi.org/10.1002/nano.202000288.

[144] Silvia Mariotti et al. "Stability and performance of $CsPbI_2Br$ thin films and solar cell devices". In: *ACS Applied Materials and Interfaces* 10.4 (2018), pp. 3750–3760. ISSN: 1944-8244. DOI: 10.1021/acsami.7b14039.

[145] Christian Dette et al. "TiO_2 Anatase with a Bandgap in the Visible Region". In: *Nano Letters* 14.11 (2014), pp. 6533–6538. DOI: 10.1021/nl503131s.

[146] Thomas J. Whittles et al. "Core levels, band alignments, and valence-band states in $CuSbS_2$ for solar cell applications". In: *ACS Appl. Mater. Inter.* 9.48 (2017), pp. 41916–41926.

[147] A.I. Oliva et al. "Formation of the band gap energy on CdS thin films growth by two different techniques". In: *Thin Solid Films* 391.1 (2001), pp. 28–35. ISSN: 0040-6090. DOI: https://doi.org/10.1016/S0040-6090(01)00830-6.

[148] S. Bechlaghem, B. Zebentout, and Z. Benamara. "The major influence of the conduction-band-offset on Zn(O,S)/$CuIn_{0.7}Ga_{0.3}Se_2$ solar cells". In: *Results in Physics* 10 (2018), pp. 650–654. ISSN: 2211-3797. DOI: https://doi.org/10.1016/j.rinp.2018.07.006.

[149] A. O. Pudov et al. "Secondary barriers in CdS-$CuIn_{1-x}Ga_xSe_2$ solar cells". In: *Journal of Applied Physics* 97.6 (2005), p. 064901. DOI: 10.1063/1.1850604.

[150] Rajiv Ramanujam Prabhakar et al. "Sb_2S_3/TiO_2 Heterojunction Photocathodes: Band Alignment and Water Splitting Properties". In: *Chem. Mater.* (). **2020**, https://doi.org/10.1021/acs.chemmater.0c01581.

[151] Winfried Mönch. *Semiconductor Surfaces and Interfaces*. Springer, (1993), p. 548. ISBN: 3540679022.

[152] A R Miedema, F R de Boer, and P F de Chatel. "Empirical description of the role of electronegativity in alloy formation". In: *Journal of Physics F: Metal Physics* 3.8 (Aug. 1973), pp. 1558–1576. DOI: 10.1088/0305-4608/3/8/012.

[153] A.R. Miedema, P.F. de Châtel, and F.R. de Boer. "Cohesion in alloys - fundamentals of a semi-empirical model". In: *Physica B+C* 100.1 (1980), pp. 1–28. ISSN: 0378-4363. DOI: https://doi.org/10.1016/0378-4363(80)90054-6.

[154] Winfried Mönch. *Electronic Properties of Semiconductor Interfaces*. Springer, (1986), p. 263. ISBN: 978-3-642-05778-6.

[155] J. J. Carey, D. O. Allen J. P. Scanlon, and G. W. Watson. "The electronic structure of the antimony chalcogenide series: Prospects for optoelectronic applications". In: *J. Sol. State Chem.* 213 (2014), pp. 116–125.

[156] J.D. Dunitz and L.E. Orgel. "Stereochemistry of Ionic Solids". In: ed. by H.J. Emeleus and A.G. Sharpe. Vol. 2. Advances in Inorganic Chemistry and Radiochemistry. Academic Press, 1960, pp. 1–60. DOI: https://doi.org/10.1016/S0065-2792(08)60186-7.

[157] G. W. Watson and S. C. Parker. "Origin of the Lone Pair of α-PbO from Density Functional Theory Calculations". In: *The Journal of Physical Chemistry B* 103.8 (1999), pp. 1258–1262. DOI: 10.1021/jp9841337.

[158] G. W. Watson, S. C. Parker, and G. Kresse. "Ab initio calculation of the origin of the distortion of α-PbO". In: *Phys. Rev. B* 59 (13 Apr. 1999), pp. 8481–8486. DOI: 10.1103/PhysRevB.59.8481.

[159] Graeme W. Watson. "The origin of the electron distribution in SnO". In: *The Journal of Chemical Physics* 114.2 (2001), pp. 758–763. DOI: 10.1063/1.1331102.

[160] Aron Walsh and Graeme W. Watson. "Electronic structures of rocksalt, litharge, and herzenbergite SnO by density functional theory". In: *Phys. Rev. B* 70 (23 Dec. 2004), p. 235114. DOI: 10.1103/PhysRevB.70.235114.

[161] Alex M. Ganose, Christopher N. Savory, and David O. Scanlon. "Beyond methylammonium lead iodide: prospects for the emergent field of ns2 containing solar absorbers". In: *Chem. Commun.* 53 (1 2017), pp. 20–44. DOI: 10.1039/C6CC06475B.

[162] Riley E. Brandt et al. "Identifying defect-tolerant semiconductors with high minority-carrier lifetimes: beyond hybrid lead halide perovskites". In: *MRS Communications* 5.2 (2015), pp. 265–275. DOI: 10.1557/mrc.2015.26.

[163] Andriy Zakutayev et al. "Defect Tolerant Semiconductors for Solar Energy Conversion". In: *The Journal of Physical Chemistry Letters* 5.7 (2014), pp. 1117–1125. DOI: 10.1021/jz5001787.

[164] Wan-Jian Yin, Tingting Shi, and Yanfa Yan. "Superior Photovoltaic Properties of Lead Halide Perovskites: Insights from First-Principles Theory". In: *The Journal of Physical Chemistry C* 119.10 (2015), pp. 5253–5264. DOI: 10.1021/jp512077m.

[165] Hidenori Noguchi et al. "Characterization of vacuum-evaporated tin sulfide film for solar cell materials". In: *Solar Energy Materials and Solar Cells* 35 (1994), pp. 325–331. ISSN: 0927-0248. DOI: https://doi.org/10.1016/0927-0248(94)90158-9.

[166] Leanne A. H. Jones et al. "Sn5s^2 lone pairs and the electronic structure of tin sulphides: A photoreflectance, high-energy photoemission, and theoretical investigation". In: *Phys. Rev. Materials* 4 (7 July 2020), p. 074602. DOI: 10.1103/PhysRevMaterials.4.074602.

[167] R.E. Banai, M.W. Horn, and J.R.S. Brownson. "A review of tin (II) monosulfide and its potential as a photovoltaic absorber". In: *Solar Energy Materials and Solar Cells* 150 (2016), pp. 112–129. ISSN: 0927-0248. DOI: https://doi.org/10.1016/j.solmat.2015.12.001.

[168] Lydia H Wong et al. "Emerging inorganic solar cell efficiency tables (Version 1)". In: *Journal of Physics: Energy* 1.3 (July 2019), p. 032001. DOI: 10.1088/2515-7655/ab2338.

[169] Philip A. E. Murgatroyd et al. "GeSe: Optical Spectroscopy and Theoretical Study of a van der Waals Solar Absorber". In: *Chemistry of Materials* 32.7 (2020), pp. 3245–3253. DOI: 10.1021/acs.chemmater.0c00453.

[170] Ding-Jiang Xue et al. "GeSe Thin-Film Solar Cells Fabricated by Self-Regulated Rapid Thermal Sublimation". In: *Journal of the American Chemical Society* 139.2 (2017), pp. 958–965. DOI: 10.1021/jacs.6b11705.

[171] Shun-Chang Liu et al. "An antibonding valence band maximum enables defect-tolerant and stable GeSe photovoltaics". In: *Nature Communications* 12.1 (Jan. 2021), p. 670. ISSN: 2041-1723. DOI: 10.1038/s41467-021-20955-5.

[172] Luisa Whittaker-Brooks et al. "Bi_2S_3 nanowire networks as electron acceptor layers in solution-processed hybrid solar cells". In: *J. Mater. Chem. C* 3 (11 2015), pp. 2686–2692. DOI: 10.1039/C4TC02534B.

[173] Arup K. Rath et al. "Solution-Processed Heterojunction Solar Cells Based on p-type PbS Quantum Dots and n-type Bi2S3 Nanocrystals". In: *Advanced Materials* 23.32 (2011), pp. 3712–3717. DOI: 10.1002/adma.201101399.

[174] Thomas J. Whittles et al. "Band alignments, valence bands, and core levels in the tin sulfides SnS, SnS_2, and Sn_2S_3: experiment and theory". In: *Chem. Mater.* 28.11 (2016), pp. 3718–3726.

[175] N. Fleck et al. "Identifying Raman modes of Sb_2Se_3 and their symmetries using angle-resolved polarised Raman spectra". In: *J. Mater. Chem. A* 8 (2020), pp. 8337–8344.

[176] Theodore D. C. Hobson et al. "Growth and Characterization of Sb_2Se_3 Single Crystals for Fundamental Studies". In: *2018 IEEE 7th World Conference on Photovoltaic Energy Conversion (WCPEC) (A Joint Conference of 45th IEEE PVSC, 28th PVSEC and 34th EU PVSEC)* (2018), pp. 0818–0822.

[177] Huaibing Song et al. "Highly Anisotropic Sb_2Se_3 Nanosheets: Gentle Exfoliation from the Bulk Precursors Possessing 1D Crystal Structure". In: *Adv. Mater.* 29.29 (2017), p. 1700441. DOI: 10.1002/adma.201700441.

[178] D. A. Shirley. "High-Resolution X-Ray Photoemission Spectrum of the Valence Bands of Gold". In: *Phys. Rev. B* 5 (1972), pp. 4709–4714.

[179] G. Kresse and J. Hafner. "Ab initio molecular dynamics for liquid metals". In: *Phys. Rev. B* 47 (1 Jan. 1993), pp. 558–561. DOI: 10.1103/PhysRevB.47.558.

[180] G. Kresse and J. Hafner. "Ab initio molecular-dynamics simulation of the liquid-metal–amorphous-semiconductor transition in germanium". In: *Phys. Rev. B* 49 (20 May 1994), pp. 14251–14269. DOI: 10.1103/PhysRevB.49.14251.

[181] G. Kresse and J. Furthmüller. "Efficient iterative schemes for ab initio total-energy calculations using a plane-wave basis set". In: *Phys. Rev. B* 54 (16 Oct. 1996), pp. 11169–11186. DOI: 10.1103/PhysRevB.54.11169.

[182] G. Kresse and J. Furthmüller. "Efficiency of ab-initio total energy calculations for metals and semiconductors using a plane-wave basis set". In: *Computational Materials Science* 6.1 (1996), pp. 15–50. ISSN: 0927-0256. DOI: https://doi.org/10.1016/0927-0256(96)00008-0.

[183] Aliaksandr V. Krukau et al. "Influence of the exchange screening parameter on the performance of screened hybrid functionals". In: *The Journal of Chemical Physics* 125.22 (2006), p. 224106. DOI: 10.1063/1.2404663.

[184] S. Grimme. "Accurate Description of van Der Waals Complexes by Density Functional Theory Including Empirical Corrections". In: *Journal of Computational Chemistry* 25 (12 2004), pp. 1463–1473. DOI: 10.1002/jcc.20078.

[185] Wang Jianqi et al. "An investigation of the flame retardation mechanism of polypropylene containing a chlorine flame retardant system by XPS (ESCA)". In: *Polymer Degradation and Stability* 31.2 (1991), pp. 129–140.

[186] René Delobel et al. "X-ray photoelectron spectroscopy study of uranium and antimony mixed metal-oxide catalysts". In: *Journal of the Chemical Society, Faraday Transactions 1: Physical Chemistry in Condensed Phases* 79.4 (1983), pp. 879–891.

[187] C. D. Wagner, D. A. Zatko, and R. H. Raymond. "Use of the oxygen KLL Auger lines in identification of surface chemical states by electron spectroscopy for chemical analysis". In: *Analytical Chemistry* 52.9 (1980), pp. 1445–1451.

[188] L. Ley et al. "Total valence-band densities of states of III-V and II-VI compounds from x-ray photoemission spectroscopy". In: *Phys. Rev. B* 9.2 (1974), p. 600.

[189] L. A. Burton and A. Walsh. "Band Alignment in SnS Thin-Film Solar Cells: Possible Origin of the Low Conversion Efficiency". In: *Appl. Phys. Lett.* 102 (2013), p. 132111.

[190] Vladan Stevanović et al. "Assessing capability of semiconductors to split water using ionization potentials and electron affinities only". In: *Phys. Chem. Chem. Phys.* 16 (8 2014), pp. 3706–3714. DOI: 10.1039/C3CP54589J.

[191] J.-P. Zöllner et al. "A novel self-consistent theory of the electronic structure of inversion layers in InSb MIS structures". In: *physica status solidi (b)* 134.2 (1986), pp. 837–845. DOI: https://doi.org/10.1002/pssb.2221340245.

[192] Timothy D. Veal. "High-Resolution Electron-Energy-Loss Spectroscopy of Narrow Gap III-V Semiconductor Surfaces and Interfaces". PhD thesis. University of Warwick, Mar. 2002.

[193] G. Paasch and H. Übensee. "A Modified Local Density Approximation. Electron Density in Inversion Layers". In: *physica status solidi (b)* 113.1 (1982), pp. 165–178. DOI: https://doi.org/10.1002/pssb.2221130116.

[194] G. Paasch and H. Übensee. "Carrier Density near the Semiconductor-Insulator Interface. Local Density Approximation for Non-Isotropic Effective Mass". In: *physica status solidi (b)* 118.1 (1983), pp. 255–266. DOI: https://doi.org/10.1002/pssb.2221180131.

[195] Sepehr V. Farahani. "Optical and electronic properties of defects and dopants in oxide semiconductors". PhD thesis. University of Warwick, May 2013.

[196] Tom Baines et al. "Incorporation of CdSe layers into CdTe thin film solar cells". In: *Solar Energy Materials and Solar Cells* 180 (2018), pp. 196–204. ISSN: 0927-0248. DOI: 10.1016/j.solmat.2018.03.010.

[197] Y. Y. Proskuryakov et al. "Admittance spectroscopy of CdTe/CdS solar cells subjected to varied nitric-phosphoric etching conditions". In: *Journal of Applied Physics* 101.1 (2007), p. 014505. DOI: 10.1063/1.2402961.

[198] Yongbeom Kwon et al. "Bifacial CdS/CdTe thin-film solar cells using a transparent silver nanowire/indium tin oxide back contact". In: *Opt. Express* 26.2 (Jan. 2018), A30–A38. DOI: 10.1364/OE.26.000A30.

[199] S. Girish Kumar and K. S. R. Koteswara Rao. "Physics and chemistry of CdTe/CdS thin film heterojunction photovoltaic devices: fundamental and critical aspects". In: *Energy Environ. Sci.* 7 (1 2014), pp. 45–102. DOI: 10.1039/C3EE41981A.

[200] S. C. Watthage et al. "Selective Cd Removal From CdTe for High-Efficiency Te Back-Contact Formation". In: *IEEE Journal of Photovoltaics* 8.4 (July 2018), pp. 1125–1131. ISSN: 2156-3381. DOI: 10.1109/JPHOTOV.2018.2830302.

[201] Rasha A. Awni et al. "The Effects of Hydrogen Iodide Back Surface Treatment on CdTe solar Cells". In: *Solar RRL* 3.3 (2019), p. 1800304. DOI: 10.1002/solr.201800304.

[202] S.H. Demtsu and J.R. Sites. "Effect of back-contact barrier on thin-film CdTe solar cells". In: *Thin Solid Films* 510.1 (2006), pp. 320–324. ISSN: 0040-6090. DOI: https://doi.org/10.1016/j.tsf.2006.01.004.

[203] Dean Levi, David Albin, and David King. "Influence of surface composition on back-contact performance in CdTe/CdS PV devices". In: *Progress in Photovoltaics: Research and Applications* 8.6 (2000), pp. 591–602. DOI: https://doi.org/10.1002/1099-159X(200011/12).

[204] Zhe Xia et al. "Generalized Water-Processed Metal Chalcogenide Complexes: Synthesis and Applications". In: *Chemistry of Materials* 27.23 (2015), pp. 8048–8057. DOI: 10.1021/acs.chemmater.5b03614.

[205] Chao Chen et al. "Efficiency Improvement of Sb_2Se_3 Solar Cells via Grain Boundary Inversion". In: *ACS Energy Letters* 3.10 (2018), pp. 2335–2341. DOI: 10.1021/acsenergylett.8b01456.

[206] Perrin Walker and William H Tarn. *Handbook of Metal Etchants*. CRC Press, 1991, p. 972. ISBN: 0849336236.

[207] Dae-Hwan Kim et al. "Highly reproducible planar Sb_2S_3-sensitized solar cells based on atomic layer deposition". In: *Nanoscale* 6.23 (2014), pp. 14549–14554. ISSN: 2040-3364. DOI: 10.1039/C4NR04148H.

[208] C. D. Wagner. "Chemical shifts of Auger lines, and the Auger parameter". In: *Faraday Discussions of the Chemical Society* 60 (1975), pp. 291–300. ISSN: 03017249. DOI: 10.1039/DC9756000291.

[209] Wayne E. Morgan, Wojciech J. Stec, and John R. Van Wazer. "Inner-orbital binding-energy shifts of antimony and bismuth compounds". In: *Inorganic Chemistry* 12.4 (1973), pp. 953–955. ISSN: 1520510X. DOI: 10.1021/ic50122a054.

[210] Rutvik J. Mehta et al. "High electrical conductivity antimony selenide nanocrystals and assemblies". In: *Nano Letters* 10.11 (2010), pp. 4417–4422. ISSN: 15306984. DOI: 10.1021/nl1020848.

[211] G Malmsten et al. "Selenium compounds studied by means of ESCA". In: *Physica Scripta* 3.2 (1971), p. 96.

[212] Christopher H. Don et al. "Sb $5s^2$ lone pairs and band alignment of Sb_2Se_3: a photoemission and density functional theory study". In: *J. Mater. Chem. C* 8 (36 2020), pp. 12615–12622. DOI: 10.1039/D0TC03470C.

[213] Andrew. Proctor and Peter M. A. Sherwood. "Data analysis techniques in x-ray photoelectron spectroscopy". In: *Analytical Chemistry* 54.1 (1982), pp. 13–19. DOI: 10.1021/ac00238a008.

[214] Benjamin A. D. Williamson et al. "Resonant Ta Doping for Enhanced Mobility in Transparent Conducting SnO_2". In: *Chemistry of Materials* 32.5 (2020), pp. 1964–1973. DOI: 10.1021/acs.chemmater.9b04845.

[215] Jack E. N. Swallow et al. "Resonant doping for high mobility transparent conductors: the case of Mo-doped In_2O_3". In: *Mater. Horiz.* 7 (1 2020), pp. 236–243. DOI: 10.1039/C9MH01014A.

[216] N. Tigau, V. Ciupina, and G. Prodan. "The effect of substrate temperature on the optical properties of polycrystalline Sb_2O_3 thin films". In: *Journal of Crystal Growth* 277.1 (2005), pp. 529–535. ISSN: 0022-0248. DOI: https://doi.org/10.1016/j.jcrysgro.2005.01.056.

[217] C. Wood, B. van Pelt, and A. Dwight. "The Optical Properties of Amorphous and Crystalline Sb_2O_3". In: *physica status solidi (b)* 54.2 (1972), pp. 701–706. DOI: https://doi.org/10.1002/pssb.2220540234.

[218] B. Wolffing and Z. Hurych. "Photoconductivity in crystalline and amorphous Sb_2O_3". In: *physica status solidi (a)* 16.2 (1973), K161–K163. DOI: https://doi.org/10.1002/pssa.2210160256.

[219] Jack E. N. Swallow et al. *Role of Sb $5s^2$ lone pairs on the electronic structure of Sb-Chalcogenides (Sb_2O_3, Sb_2S_3, Sb_2Se_3 and Sb_2Te_3).*

[220] Huw Shiel et al. "Natural Band Alignments and Band Offsets of Sb_2Se_3 Solar Cells". In: *ACS Applied Energy Materials* 3.12 (2020), pp. 11617–11626. DOI: 10.1021/acsaem.0c01477.

[221] Joseph B. Mann, Terry L. Meek, and Leland C. Allen. "Configuration Energies of the Main Group Elements". In: *Journal of the American Chemical Society* 122.12 (2000), pp. 2780–2783. DOI: 10.1021/ja992866e.

[222] Evan O. Kane. "Band structure of indium antimonide". In: *Journal of Physics and Chemistry of Solids* 1.4 (1957), pp. 249–261. ISSN: 0022-3697. DOI: https://doi.org/10.1016/0022-3697(57)90013-6.

[223] Wojciech M. Linhart. "Electron accumulation and doping in InN and InGaN alloys". PhD thesis. University of Warwick, Feb. 2012.